

AD A 082990

LEVEL

12

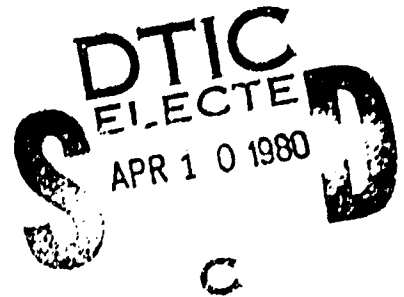
RADC-TR-79-277
Final Technical Report
February 1980



MILLIMETER WAVE APPLICATIONS OF LARGE APERTURE SYSTEMS

The Charles Stark Draper Laboratory, Inc.

Sponsored by
Defense Advanced Research Projects Agency (DoD)
ARPA Order No. 3537



APPROVED FOR PUBLIC RELEASE; DISTRIBUTION UNLIMITED

The views and conclusions contained in this document are those of the authors and should not be interpreted as necessarily representing the official policies, either expressed or implied, of the Defense Advanced Research Projects Agency or the U.S. Government.

ROME AIR DEVELOPMENT CENTER
Air Force Systems Command
Griffiss Air Force Base, New York 13441

DDC FILE COPY

80 4 10 090

This report has been reviewed by the RADC Public Affairs Office (PA) and is releasable to the National Technical Information Service (NTIS). At NTIS it will be releasable to the general public, including foreign nations.

RADC-TR-79-277 has been reviewed and is approved for publication.

APPROVED:



ROBERT F. Ogrodnik
Project Engineer

If your address has changed or if you wish to be removed from the RADC mailing list, or if the addressee is no longer employed by your organization, please notify RADC (OCTM), Griffiss AFB NY 13441. This will assist us in maintaining a current mailing list.

Do not return this copy. Retain or destroy.

MILLIMETER WAVE APPLICATIONS OF LARGE APERTURE SYSTEMS

Francois Ayer

Contractor: The Charles Stark Draper Lab, Inc.
Contract Number: F30602-78-C-0128
Effective Date of Contract: 30 June 1978
Contract Expiration Date: 30 March 1979
Short Title of Work: MM Wave Applications
Program Code Number: 9E20
Period of Work Covered: June 1978 - March 1979

Principal Investigator: Francois Ayer
Phone: 617 258-4659

Project Engineer: Robert Ogrodnik
Phone: 315 330-4431

Approved for public release; distribution unlimited.

This research was supported by the Defense Advanced Research Projects Agency of the Department of Defense and was monitored by Robert Ogrodnik, (OCTM), Griffiss AFB NY under Contract F30602-78-C-0128.

UNCLASSIFIED

SECURITY CLASSIFICATION OF THIS PAGE (When Data Entered)

19 REPORT DOCUMENTATION PAGE		READ INSTRUCTIONS BEFORE COMPLETING FORM
1. REPORT NUMBER RADC-TR-79-277	2. GOVT ACCESSION NO.	3. RECIPIENT'S CATALOG NUMBER
4. TITLE (and Subtitle) MILLIMETER WAVE APPLICATIONS OF LARGE APERTURE SYSTEMS.	5. TYPE OF REPORT & PERIOD COVERED Final Technical Report. June 1978 - March 1979	6. PERFORMING ORG. REPORT NUMBER R-1381
7. AUTHOR(s) Francois/Ayer	8. CONTRACT OR GRANT NUMBER(s) F30602-78-C-0128	9. PROGRAM ELEMENT, PROJECT, TASK AREA & WORK UNIT NUMBERS 62301E C5370001
10. PERFORMING ORGANIZATION NAME AND ADDRESS The Charles Stark Draper Laboratory, Inc. Cambridge MA, 02139	11. CONTROLLING OFFICE NAME AND ADDRESS Defense Advanced Research Projects Agency 1400 Wilson Blvd Arlington VA 22209	12. REPORT DATE February 1980
13. MONITORING AGENCY NAME & ADDRESS (if different from Controlling Office) Rome Air Development Center (OCTM) Griffiss AFB NY 13441	14. SECURITY CLASS. (of this report) UNCLASSIFIED	15. NUMBER OF PAGES 164
16. DISTRIBUTION STATEMENT (of this Report) Approved for public release; distribution unlimited.		15a. DECLASSIFICATION/DOWNGRADING SCHEDULE N/A
17. DISTRIBUTION STATEMENT (of the abstract entered in Block 20, if different from Report) Same		
18. SUPPLEMENTARY NOTES RADC Engineer: Robert F. Ogrodnik (OCTM)		
19. KEY WORDS (Continue on reverse side if necessary and identify by block number) Packaging and Deployment Approaches Large Space Structure: model and analysis Orbital Environment Assessment Hexagonal Reflector Panel Design		
20. ABSTRACT (Continue on reverse side if necessary and identify by block number) This study proposes a structural design for the millimeter wave (MMW) antenna concept offered by Aerojet/NTL. It performs an assessment of the structural behavior of the satellite as it proceeds along its 500 km orbit. This effort concentrated on the definition and quantification of critical disturbances expected in the orbital environment. The design of a thermal blanket is arrived at through a number of thermal model analyses. The modeling of structural components and substructuring approaches are presented. The responses are evaluated for thermal loadings and dynamic disturbances. Based		

DD FORM 1 JAN 73 1473

UNCLASSIFIED

(Con: 1)

SECURITY CLASSIFICATION OF THIS PAGE (When Data Entered)

408386

LB

A

UNCLASSIFIED

SECURITY CLASSIFICATION OF THIS PAGE(When Data Entered)

Item 20 (Cont'd)

on the antenna deformational state, the performance is evaluated in terms of point-spread functions (antenna loss of gain) and line-of-sight errors. A packaging and deployment technique is suggested for the surface panels, the back-up trusses and the feed tower to fit into the cargo bay of a single shuttle. Although the satellite is relatively heavy at 8800 kg, it is expected to perform satisfactorily in an almost completely passive manner. The evaluation of orbital dynamics shows the need for substantial propellant (2000 kg) to maintain the 500 km orbit.

UNCLASSIFIED

SECURITY CLASSIFICATION OF THIS PAGE(When Data Entered)

ACKNOWLEDGMENT

The work reported herein was performed by the Charles Stark Draper Laboratory, Inc. (CSDL). The research was supported by the Advanced Research Projects Agency of the Department of Defense, and was monitored by USAF/AFSC, Rome Air Development Center under Contract No. F30602-78-C-0128. This report covers the period from 30 June 1978 through 31 March 1979. The technical monitor was Mr. Robert Ogrodnik of RADC.

Francois Ayer was the Project Manager and Principal Investigator; the study was performed within the Large Space Structures Division (LSSD), Dr. Keto Soosaar, manager. The LSSD is a part of the CSDL Advanced Systems Department, headed by Mr. David Hoag.

Major contributors to this study have been Dr. Vini Mahajan, Timothy Henderson, Stephen Gates, Roland Crin and Dr. Leslie Matson, et. al., whose assistance is gratefully acknowledged.

Accession For	
NTIS GRA&I	<input checked="checked" type="checkbox"/>
DDC TAB	<input type="checkbox"/>
Unannounced	<input type="checkbox"/>
Justification	
By	
Distribution/	
Availability Codes	
Dist	Availand/or special
A	

TABLE OF CONTENTS

<u>Section</u>	<u>Page</u>
1 INTRODUCTION, OBJECTIVE, AND SUMMARY.....	1
2 ANTENNA DESCRIPTION.....	6
2.1 Antenna Selection and Description.....	6
2.2 Structural Concept and Design.....	10
3 DISTURBANCE IDENTIFICATION.....	19
3.1 Introduction and Approach.....	19
3.2 Orbital Thermal Disturbances.....	21
3.3 Atmospheric Drag.....	32
3.4 Solar Radiation.....	38
3.5 Gravity Gradient.....	43
3.6 Dynamic On-Board Disturbance.....	50
4 STRUCTURAL MODEL AND ANALYSIS.....	55
4.1 Introduction and Approach.....	55
4.2 Model Description of Trusses/Tower Assembly.....	56
4.3 Panel Design and Analysis.....	70
5 RESPONSE EVALUATION.....	77
5.1 Introduction and Approach.....	77
5.2 Response to Sun Thermal Flux (68°).....	77
5.3 Approximate Distortion Calculations.....	83
5.4 Dynamic Responses.....	86
6 DEGRADATION OF ANTENNA PERFORMANCE DUE TO SOLAR FLUX	102
6.1 Introduction.....	102
6.2 Antenna Description.....	102
6.3 Point-Spread Function Evaluation.....	104
6.4 Antenna Aberrations Due to Solar Flux.....	106
6.5 Results.....	110
6.6 Discussions and Conclusions.....	115
7 PACKAGING AND DEPLOYMENT.....	130
7.1 Introduction and Issues.....	130
7.2 Packaging Concept for the MMW Antenna Structure.....	131
8 CONCLUSIONS.....	136
COMPUTER SIMULATION OF A LARGE ADAPTIVE OPTICAL SYSTEM, (reprint from The Proceedings of the SPIE, Volume 172).....	139

LIST OF FIGURES

<u>Figure</u>	<u>Page</u>
1-1 Flow chart for structural design analysis and performance evaluation tasks.....	5
2-1 Pushbroom microwave satellite imager.....	7
2-2 Single surface antenna candidate.....	9
2-3 Response minimization by passive means.....	12
2-4 View of reflector surface.....	14
2-5 Main features of antenna surface panel.....	15
2-6 Structural arrangement of antenna components.....	17
2-7 Mass moments of inertia.....	18
3-1 Thermal analysis tool integration.....	22
3-2 Antenna panel and truss thermal model.....	24
3-3 Preliminary design trade-offs.....	26
3-4 Temperatures at center of antenna (run 4).....	27
3-5 Temperatures at center of antenna (run 3).....	29
3-6 Run 4 antenna temperatures, corrected for curvature.....	30
3-7 Tower structure thermal model.....	31
3-8 Tower structure temperature results.....	33
3-9 Atmospheric drag at 500 km orbit.....	39
3-10 Radiation pressures (N/m^2) on three different surfaces due to an incident radiation flux intensity $H(W/m^2)$ arriving at an angle to surface normal.....	41
3-11 Solar, maximum albedo and earth IR radiation pressures on a flat black plate as a function of altitude.....	42
3-12 Solar radiation resultants.....	44
3-13 Reference and body axes for a body in a circular orbit about the earth.....	46
3-14a Definition of satellite axes for gravity-gradient torque evaluation.....	48
3-14b Definition of satellite axes for gravity-gradient torque evaluation.....	49

LIST OF FIGURES (Cont.)

<u>Figure</u>		<u>Page</u>
4-1a	MMW antenna mathematical model.....	57
4-1b	MMW antenna mathematical model.....	58
4-2a	Millimeter wave antenna.....	61
4-2b	Millimeter wave antenna.....	62
4-2c	Millimeter wave antenna.....	63
4-2d	Millimeter wave antenna.....	64
4-2e	Millimeter wave antenna.....	65
4-2f	Millimeter wave antenna.....	66
4-2g	Millimeter wave antenna.....	67
4-2h	Millimeter wave antenna.....	68
4-2i	Millimeter wave antenna.....	69
4-3	Mathematical model of the reflector surface panel.....	73
5-1	Reflector surface distortion calculation.....	78
5-2	Thermal loading for sun at 68° with z-axis.....	80
5-3	Reflector z-displacement of trusses due to thermal loading (68° sun), lines A, B, and C.....	82
5-4	Receiver support tower thermal distortions (sun in z-y plane)...84	
5-5	Steady-state temperatures on a spherical mirror from a thermal flux.....	85
5-6	Description of dynamic loading.....	88
5-7	Response characteristics to a unit step impulse.....	89
5-8	Truss/tower model. Joints identification numbers.....	91
5-9	z-displacement (m) histories for the first 1.2 s of response to 86 N thruster's impulse.....	92
5-10a	z-displacement (m) histories for the first 1.2 s of response to 86 N thruster's impulse.....	93
5-10b	z-displacement (m) histories for the first 1.2 s of response to 86 N thruster's impulse.....	94
5-11	Tower tip displacements (m) histories for the first 1.2 s of response to 86 N thruster's impulse.....	95
5-12	Simple oscillator parameter definition.....	96
5-13	Reflector center line response to harmonic disturbance (2 dis- placements at 3 times).....	99
5-14	Reflector extreme points 3i1 and 3i2 Δz steady-state response cycle (0.1 s). Disturbance: 15 N at 10 Hz.....	100

LIST OF FIGURES (Cont.)

<u>Figure</u>		<u>Page</u>
5-15	Tower tip joint 801 displacements for 1 cycle steady-state response to harmonic excitation (15 N at 10 Hz).....	101
6-1	Elliptic torus 30 x 60 m segmented antenna. The total number of segments is 124.....	103
6-2	Thermal loading due to sun.....	107
6-3	Antenna segment showing distribution of points at which deformations were calculated. There are 30 points on a segment..	108
6-4	Distribution of pupil points. The total number of points inside a circle of 30 m diameter is 1575. The spacings between two adjacent points along the u and v axes are $\Delta u = 0.675$ m and $\Delta v = 0.650$ m.....	109
6-5	Pupil locations on the antenna.....	111
6-6	Aberration-free and degraded PSFs for graphite-epoxy antenna...	112
6-7	Aberration-free and degraded PSFs for aluminum antenna.....	113
6-8	PSF profile along the x axis. The central value is unity. The linear and angular units of the horizontal scale are 0.52 mm and 7.4 μ rad, respectively.....	116
6-9a	Sidelobe structure for graphite-epoxy antenna under solar flux. PSF x-profile for pupil position 1.....	117
6-9b	PSF y-profile position 1. The linear and angular units of the horizontal scale are 0.54 mm and 18 μ rad, respectively.....	118
6-9c	PSF x-profile for pupil position 2.....	119
6-9d	PSF y-profile for pupil position 2.....	120
6-9e	PSF x-profile for pupil position 3.....	121
6-9f	PSF y-profile for pupil position 3.....	122
6-10a	Sidelobe structure for aluminum antenna under solar flux. PSF x-profile for pupil position 1.....	123
6-10b	PSF y-profile for pupil position 1.....	124
6-10c	PSF x-profile for pupil position 2.....	125
6-10d	PSF y-profile for pupil position 2.....	126
6-10e	PSF x-profile for pupil position 3.....	127
6-10f	PSF y-profile for pupil position 3.....	128
6-11	PSF power on a centered detector as a function of its size.....	129

LIST OF FIGURES (Cont.)

<u>Figure</u>		<u>Page</u>
7-1	MMW antenna packaged in one Shuttle cargo bay.....	134
7-2	Packaging and deployment schemes for back-up vertical trusses (preliminary).....	135

LIST OF TABLES

<u>Table</u>		<u>Page</u>
2-1	Tolerances on reflector surface and feed.....	10
3-1	Disturbances identification.....	20
3-2	$\bar{F}_{10.7} = 150$	35
3-3	$\bar{F}_{10.7} = 250$	36
3-4	External disturbance forces and torques.....	50
3-5	Thrust displacement for attitude control.....	52
4-1	Cross-sectional properties and member characteristics.....	59
4-2	Characteristics of other possible material candidates.....	60
4-3	Natural frequencies and mode shapes (MMW).....	70
4-4	Hexagonal reflector panel - design characteristics.....	74
4-5	Reflector panel designs - thermal and dynamic characteristics...	75
5-i	Trusses and panel temperatures ($^{\circ}\text{K}$) (sun incidence angle of 68 $^{\circ}$ with respect to z axis).....	81
6-1	System parameters.....	103
6-2	Antenna aberrations in millimeters due to solar flux.....	110
6-3	PSF evaluation parameters.....	114
7-1	Structural, packaging and deployment issues.....	132

SECTION 1

INTRODUCTION, OBJECTIVE, AND SUMMARY

The role of the Charles Stark Draper Laboratory, Inc. (CSDL) in this study has been to assist the government (USAF/RADC) in assessing the viability of a space based millimeter wave (MMW) antenna. While several other contractors were involved with the study of the various aspects of the design of a MMW antenna system, CSDL's responsibility was to provide technical support in the areas of structures, dynamics, and control for a specific antenna concept. The results of these studies provide information for use in comparing a MMW surveillance satellite with other surveillance satellites using visual or infrared wavelengths.

The objective of the CSDL work is therefore to design, analyze, and evaluate the performance of a MMW antenna system concept. The base line was selected from the Aerojet/NTL study. The design should rely on a traditional approach using state-of-the-art technology for materials and spacecraft design techniques. More specifically, this study is limited in scope to the generic truss constructions that are generally proposed for large satellites requiring high precision for their optical components. The truss structure used in the design of the MMW antenna can be compared to an alternate structural concept employing an electrostatically shaped reflector. Figures of merit for both systems will be compared in order to assess their relative desirability.

In designing the structure of the satellite, all avenues are explored in order to obtain an adequate performance while using passive means of control only. An active system could be advocated for instance, on the basis of comparison between the advantages of weight saving and problems associated with the added complexity. The decision between active and passive approaches depends mainly on reflector size and its associated deformational tolerance requirements. Among the passive means of controlling the antenna deformations, the judicious design of thermal blankets appears to be the most promising approach. This is a direct consequence of the fact that the thermal effect of the solar radiation constitutes the more severe disturbance.

In the present study, the numerous issues involving packaging and deployment are also considered as they impact the structural design. For a reflector of the size considered ($\sim 1600 \text{ m}^2$) a relatively high packaging ratio is also needed if the satellite is to be stowed into the cargo of a single shuttle. This very desirable requirement restricts the freedom of the structural designer.

In earlier studies, done by other contractors, the most promising candidate sensor configurations have been identified. The present satellite design is based on the single surface antenna concept described in the report by Aerojet ElectroSystems Company, (AESC) and NTL, Inc.* The elliptical torus

* Investigation of Passive Microwave Sensing from Satellite (31 Oct. 78) AESC

reflector is rectangular in projection, with side dimensions of approximately 60 m and 30 m. The feed surface, about 30 m above the reflector is supported by a tower designed in a way that its members do not interfere with the incoming rays.

This report presents the approach to the design and the analysis of a structural system capable of supporting the millimeter wave antenna concept suggested by AESC/NTL. The structural distortions resulting from environmental disturbances and on-board dynamic loadings have been translated into antenna performance indices. Line-of-sight errors and loss of gain have been calculated for various beam-pointing directions which use different portions of the antenna surface. It appears that it is possible for the performance to fall within acceptable limits, provided that the surface panels are fabricated with graphite-epoxy composites because of their high modulus of elasticity and low coefficient of thermal expansion. The design of the thermal blanket insured small temperature excursions and negligible gradient such that the surface of the panels was only slightly distorted. The motions of the receiver supported at the tip of the tower were more significant. Some active positioning scheme as a function of time along the orbit path might be required, unless some judicious compensation technique is designed to provide thermal insensitivity for the 30 m open tower. Because of the 500 km orbit that was tentatively selected, the atmospheric drag causes a substantial orbital decay rate, thus creating a need for additional propellant. Preliminary estimates put the needed propellant at 2000 kg. The structural design concept, including 124 surface panels, the back-up truss assembly and the receiver tower can be packaged into a single shuttle cargo bay. While the packaging scheme presented is still preliminary, the use of open cross-sections for the truss construction greatly increases the packaging ratio without endangering the stability of the individual members. As is usually the case for large high precision satellites, the total mass of 8800 kg makes this design volume limited with respect to shuttle capabilities.

This report sequentially covers the steps involved in identifying the problem, designing the structure, constructing a mathematical model, quantifying disturbances, obtaining the structural response and evaluating the corresponding performance. It explains the approaches used, with their assumptions and limitations. It is important to recognize that the performance of the antenna structure has been evaluated as the satellite responds to typical static and dynamic disturbances expected along a 500 km altitude circular orbit. The main objective of this study was to check whether a satellite of this size (60 m \times 30 m) could be designed to perform adequately at a 3 mm wavelength in a purely passive way. The report includes an introduction, followed by six sections and a conclusion. An outline of the content of each section is presented below.

Section 1 above defined the problem and the objectives of the study. The approach chosen in order to provide a useful answer to the problem was explained with the assumptions and the reasons involved. A summary of the important results is included.

Section 2 deals with the structural design for the millimeter wave antenna based on a concept suggested by AESC/NTL. It describes the approach followed in selecting the truss configuration and the structural materials, the stiffness needs, and stability criteria. Some design optimization under the constraints of packaging and deployment requirements have also been attempted. A summary of the mechanical and inertia properties of the satellite components is presented.

Section 3 addresses the problem of disturbance identification and quantification. Steady-state and transient thermal loadings are calculated for a number of thermal models in order to minimize the expected responses. Models of the reflector assembly and the receiver tower have been analyzed separately. An evaluation of the atmospheric drag is presented for two extreme solar activities. The effect of solar radiation pressures were obtained along the entire orbit and expressed in terms of force and torque resultants. Because of its asymmetrical configuration, the satellite is subject to additional torquing from the effects of gravity gradient. All these force and moment resultants translated into dynamic disturbances of thrusters needed to compensate for loss of pointing accuracy and for station keeping requirements. Other mechanical disturbances such as the harmonic forcing function of a refrigeration unit have been identified.

Section 4 discusses the approaches to structural modeling. While the model for static analysis derives its simplicity from the permissible decoupling of the surface panels and the back-up trusses, the dynamic analysis is less rigorous since the decoupling is based on the frequency separation of relatively rigid panels and flexible main structure. Two distinct models, (a) the back-up trusses with the receiver tower, and (b) the typical surface panel, have been constructed, and modal analysis furnished information on their dynamic characteristics. For the surface panels, several materials and construction approaches have been considered so as to suggest the most efficient solution.

Section 5 explains the choice of static and dynamic disturbances believed to be critical for the antenna performance. The thermal loading due to the sun flux at 68° incidence angle with the pointing axis was treated in detail. Four different zones on the reflector were subjected to four different temperature excursions and gradients. The receiver tower was also analysed for several thermal conditions. Dynamic responses were calculated for three disturbances. The first two are derived from two possible means of attitude control through thrusters impulses. The third dynamic loading was a harmonic forcing function representation of a cryo-cooler machine needed for the refrigeration of the receivers. Absolute distortions of reflector surface points were obtained as a geometrical combination of individual panel distortions and back-up truss deformations, for all the loading conditions mentioned above.

Section 6 describes the degradation of point-spread-functions (PSF) of the $30\text{ m} \times 60\text{ m}$ elliptic torus antenna due to its deformations produced by solar flux. The antenna is assumed to be operating at a wavelength of 3 mm with a

cosine feed taper, and the materials considered are graphite-epoxy and aluminum. It is shown that the graphite-epoxy antenna performs much better than the aluminum antenna. Strehl ratios, line-of-sight error (LOS), power on a detector, and profiles of the PSFs are given for three regions of the antenna. Airmat antennas were also considered, but owing to their large deformations ($\sim \lambda$) under solar flux, they were not investigated in any detail.

Section 7 deals with the issues of packaging and deployment. The main objective was to limit the required volume to one shuttle cargo and suggest a deployment scheme that is as close as possible to an automatic maneuver. A packaging method presented for the back-up trusses used open cross-section members and greatly improved the packaging ratio over the more traditional use of tube members.

Section 8 summarizes the findings of the study and offers recommendations based on these results. While many refinements of the design are suggested in order to improve the spacecraft overall efficiency, it was shown that the MMW antenna structure can perform satisfactorily. This performance can be achieved with a passive structural system that can be launched by a single shuttle flight.

Before proceeding with the detailed presentation, it is helpful to consider the block diagram of Figure 1-1. It emphasizes the major possible tasks and the way they are interrelated in a flow towards the determination of the MMW antenna performance. The blocks involving active control techniques were not needed since a satisfactory performance could be achieved by use of a passive system.

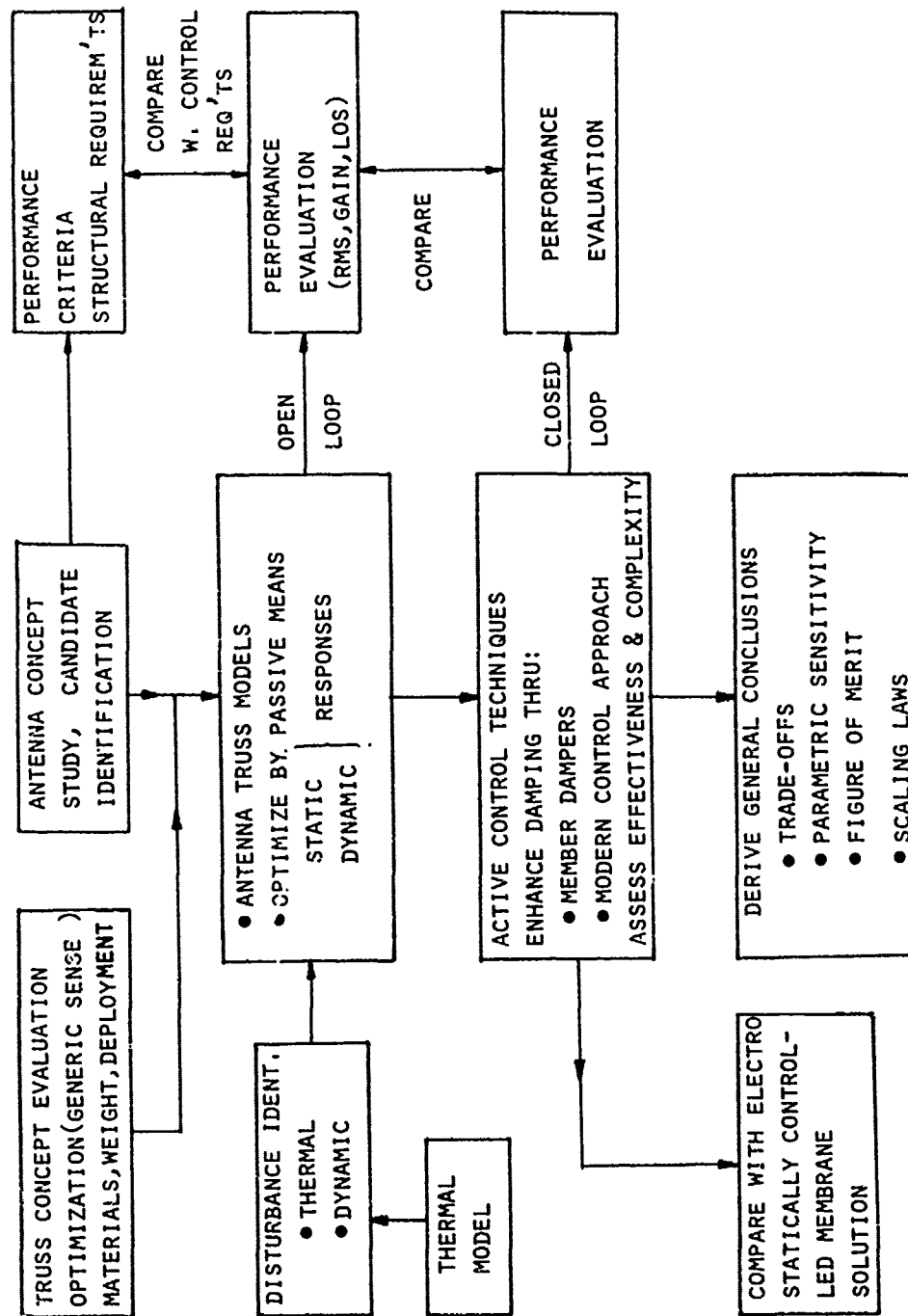


Figure 1-1. Flow chart for structural design analysis and performance evaluation tasks.

SECTION 2

ANTENNA DESCRIPTION

2.1 Antenna Selection and Description

The selection of a MMW antenna concept was based on the trade-off studies carried out by the Aerojet/NTL team. This section is a summary of their findings. It explains the merits associated with the millimeter wave sensors, their mode of operation, and suggests as a candidate a single surface antenna working at a wavelength of $\lambda = 3$ mm which corresponds to a transmission window frequency centered at 95 GHz. The following text is partially borrowed from the AESC/NTL Report.

2.1.1 MMW Antenna Characteristics

Enhancement of satellite surveillance can be derived from the cloud and weather penetration of microwave/millimeter wave sensors. Initial analyses quantitatively verified the feasibility of spacebound passive microwave technology. The effective satellite-based surveillance of strategic aircraft and naval vessels in cloud-cover and weather situations can be achieved where surveillance is presently denied by the limitations of sensors restricted to visual and infrared wavelengths.

Smoke, dust, fog, and clouds frequently prevent satellite-based observation of surface targets with visual and infrared sensors. The ability to penetrate these cover conditions and to perform equally well by night or day makes microwave passive sensing an attractive candidate to significantly extend the capabilities of satellite based observations beyond their present limitations.

Passive microwave sensors respond to millimeter wavelength thermal radiation emitted by all objects in proportion to their physical temperature T_h and surface emissivity ϵ . Useful sensing of military targets results predominantly from high contrasts of target emissivity with respect to background surface.

Oxygen and water vapor are the only atmospheric gasses with significant absorptions at millimeter wavelengths. These combine to establish the clean air transmission windows centered at frequencies of 35 GHz, 95 GHz, 140 GHz, and 230 GHz.

Design of a microwave pushbroom sensor, shown in Figure 2-1, is based on optical principles. A satellite altitude R requires an antenna diameter $D_a = \lambda R d_c^{-1}$ to achieve a surface resolution d_c . The sensor wavelength, λ , in millimeters is related to frequency, f , in GHz by $\lambda = 300 f^{-1}$. A "pushbroom" of N contiguous surface resolution cells results in an instantaneous crosstrack coverage swath width of dimension W_s . As a consequence of the satellite ground velocity v_g , the sensor has an earth surface area search rate $\dot{A} = W_s \times v_g$.

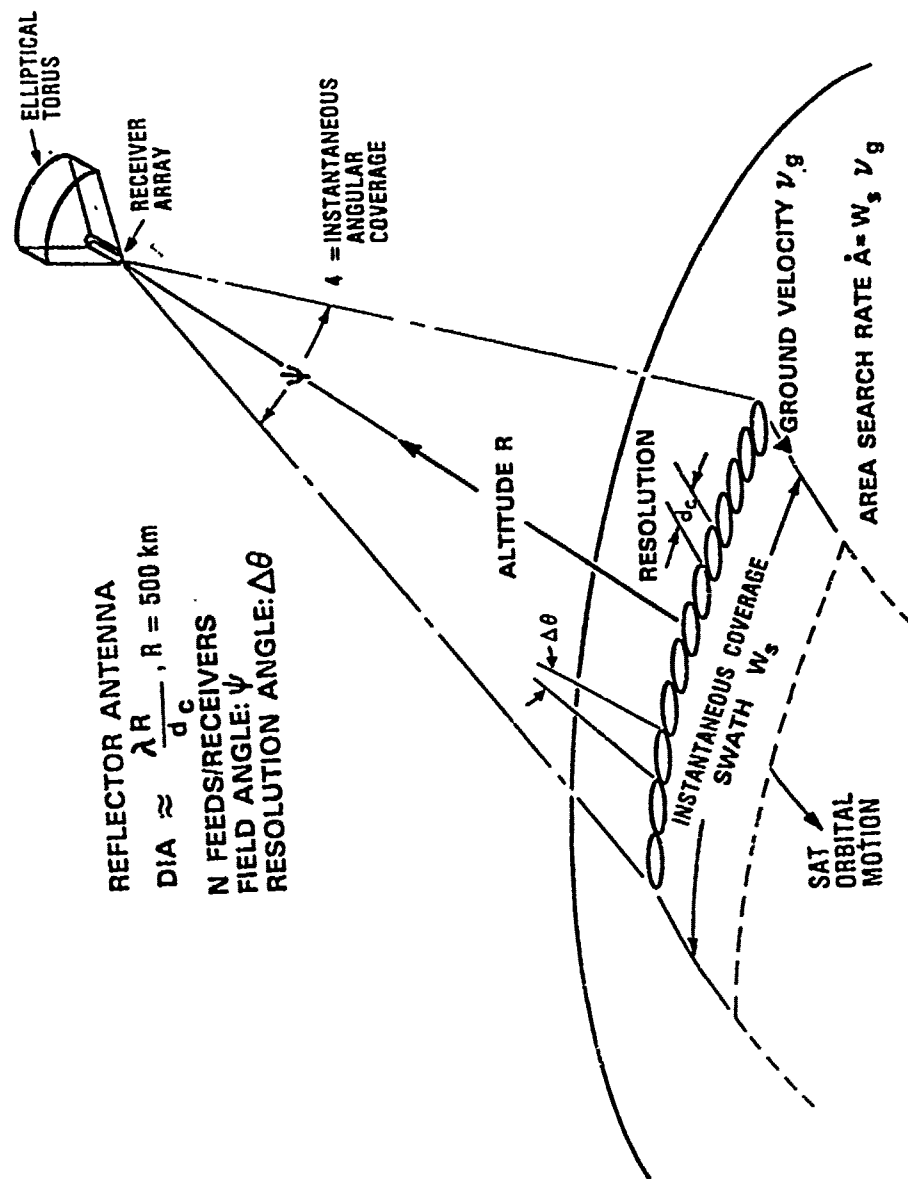


Figure 2-1. Pushbroom microwave satellite imager.

The filled pushbroom sensor is configured with a number M of feed/receiver modules which sample the entire crosstrack swath at distance intervals equal to the surface resolution cell diameter d_c . The antenna beam associated with the individual feed/receiver modules are situated at fixed pointing angles in the crosstrack plane. Thus satellite motion scans each feed/receiver module to sweep along a continuous inline track of width d_c . The outputs of all feed/receiver modules are sampled at intervals $\tau_i = d_c v_g^{-1}$ (the dwell time).

Conceptually the satellite based passive microwave imager resembles quite closely in form that of an infrared imaging system. A reflecting system focuses the radiation of individual surface resolution cells onto the feed apertures situated at the focal surface.

As in the case of an infrared sensor the detected output from the microwave receiver output varies with time, having a magnitude which is directly proportional to the incoming radiation intensity. An analog signal processor and digital data processor serve the same functions as in the case of an infrared mosaic imaging system.

2.1.2 Description of Selected Concept

Figure 2-2 shows the general form of the reflector antenna selected. The microwave antenna features efficient performance and the reflector surface is an elliptic torus. The feed horns are deployed on a cylindrical surface passing through the focal circle of the ellipses. The other focal circle lies on the surface of the earth. The design of the feed horns provides compensation for the aberration caused by the circular crosstrack reflector profile. Each horn accepts incident energy from approximately half of the reflecting surface and provides for side lobe control through proper tapering of the energy accepted.

The elliptical torus reflector is not a perfect collimator so "point source" feed horns are not adequate for maintaining pattern gain and quality. Oversized feeds with the ability of controlling the amplitude and phase over an extended focal region are used to maintain antenna performance levels. These feeds can be small arrays of horn radiators, multimode horn feeds such as the scalar feed or corrugated horn feeds or horn/reflector combinations.

Tolerance limits must be imposed on the positions and orientations of the antenna feeds relative to the reflector surface. RMS limits on surface roughness and surface deviations due to operational disturbances are provided as preliminary requirements for satisfactory performance. Table 2-1 summarizes the various tolerance limits.

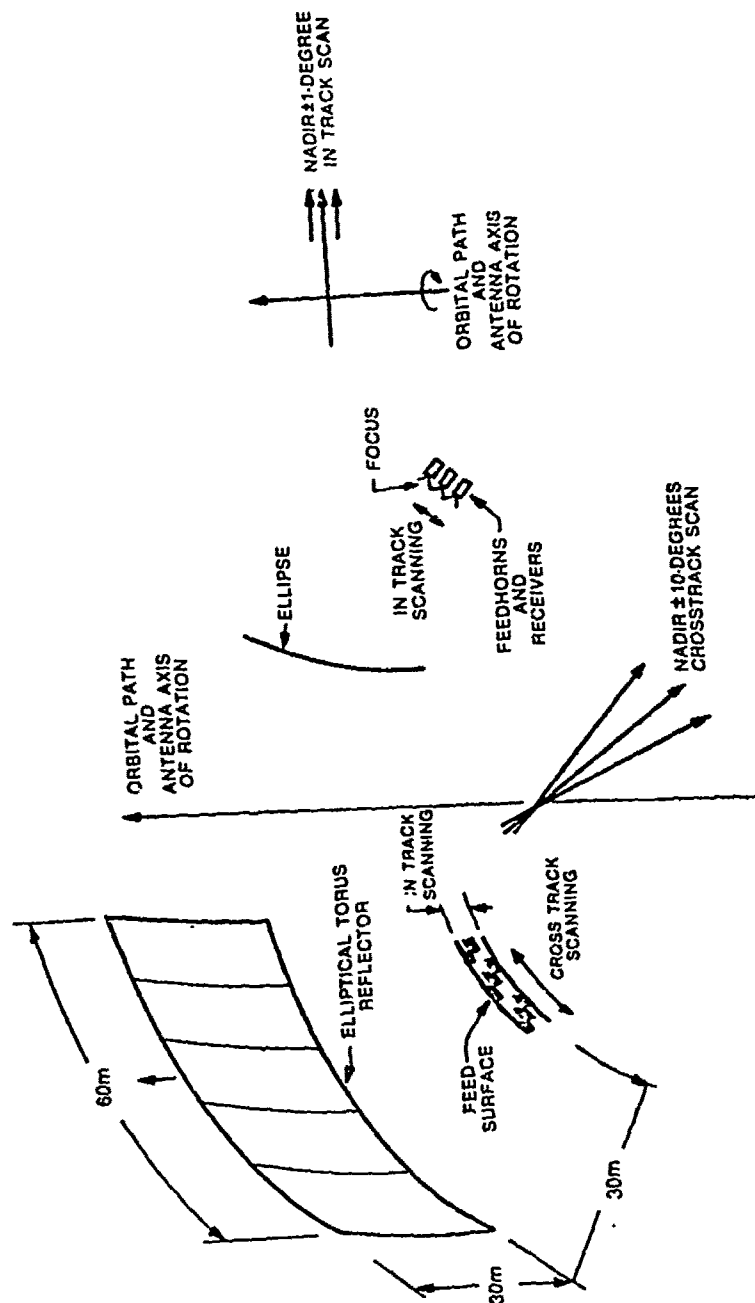


Figure 2-2. Single surface antenna candidate.

Table 2-1. Tolerances on reflector surface and feed

$\lambda = 3\text{mm}$		
Primary Reflector Surface	RMS Surface Deviation	0.15mm
	RMS Surface Quality	0.05mm
Feed Tolerances	Torsional	1°
	Axial	1.0mm
	Decenter	0.15mm
Pointing	Drift	50.0 μrad
	Accuracy	1.5 μrad

2.2 Structural Concept and Design

2.2.1 Introduction and Objective

The task of the structural designer is to provide a support structure to the millimeter wave antenna configuration such that the structural system will perform within tolerable limits when exposed to orbital environment. In designing a space structure compatible with the geometry of the large optical system, it is important to generate sufficient stiffness with a minimum amount of structural mass. Since these needs are basically in conflict, the structural design will emerge as a result of trade-off studies and optimization techniques. Many constraints emanating from optical, structural and environmental sources cannot be ignored in the optimization process. In addition, the size of the shuttle cargo bay will impose constraints on the structural design associated with the specific packaging and deployment technique.

The objective of the CSDL work was to suggest an antenna design that uses conventional, state-of-the-art structural concepts and technology. More precisely, the overall structural design approaches have been limited to the solution space involving truss construction only. Although this traditional concept requires a relatively larger amount of mass when compared to more advanced systems, it offers the advantages of simplicity and reliability and thus, provides a desirable level of confidence. The figure of merits of this design and its performance characteristics will be contrasted with, and compared with, those of an alternate structural concept, i.e., an electrostatically shaped membrane reflector proposed by another contractor. Some parameters such as total mass and packaging ratio are easily assessed, others involving control complexity and ultimate reliability do not lend themselves to quantitative measures of comparison.

2.2.2 Approach to Antenna Structure Design

Designing a large structure that performs to the required stringent optical performance is challenging and the task is further complicated by the space shuttle launch constraints. It was stipulated that the entire satellite will be packaged into the cargo bay of a single shuttle. This requirement limits the designer in his freedom to select the various structural components, their size, shape and dimensions. A third tentative requirement, that the antenna have a satisfactory performance without the help of active means of control, only compounds the difficulties in an already complicated situation.

The large size of the reflector dictated segmentation into panels for the "rigid" surface structure. In order to take best advantage of the shuttle cargo dimensions (4.57 m in diameter) and at the same time have an efficient assemblage pattern, a panel of hexagonal shape with a diameter of 4.5 m appeared most advantageous. The 124 panels are supported on kinematic mounts by an orthogonal system of graphite-epoxy trusses. This interface between panel and back-up trusses allows for structural decoupling in response calculation to static loadings, while the choice of a relatively high fundamental frequency of the panels should permit the assumption of mild dynamic coupling between the panel and the back-up truss assembly. Another major structural component consists of the receiver support tower that extends some 30 m above the reflector surface. Because of the undesirability of optical blockage, this structure was designed in such a way that it does not obstruct any incoming or outgoing signals. In order to achieve an acceptable bending stiffness, the tower space frame construction increases in depth from the top down to extend about 8 m beyond the reflector's edge. The design of a large passive reflector that performs within given tolerances is limited by state-of-the-art technology in structures and materials. With today's technology, the ratio between reflector diameter and surface accuracy can reach approximately 10^5 for a passive structure exposed to a typical orbital environment. The present design goes beyond this number, since the ratio equals 10^6 for a reflector of 50 m (equivalent) diameter requiring a surface accuracy of 0.05 mm.

In order to achieve this goal, many avenues capable of optimizing the structure have been explored. In this attempt the overall structure was viewed as a time-invariant mechanical system acted upon by environmental disturbance inputs. The distortion of the system is the output from which the antenna performance is evaluated. The wide range of options at the designer's disposal to optimize the structural system must be exercised subject to existing constraints. Figure 2-3 attempts to list such options, many of which have been used to minimize the structural distortions of the back-up truss assembly. A special effort was made to design an efficient thermal blanket over the reflector's back-face since it was determined that the sun and earth thermal radiation effects translated into the most deleterious distortions. The thermal model of this structure and this thermal shield was used for trade-off studies. The results are discussed in detail in Section 3.3.

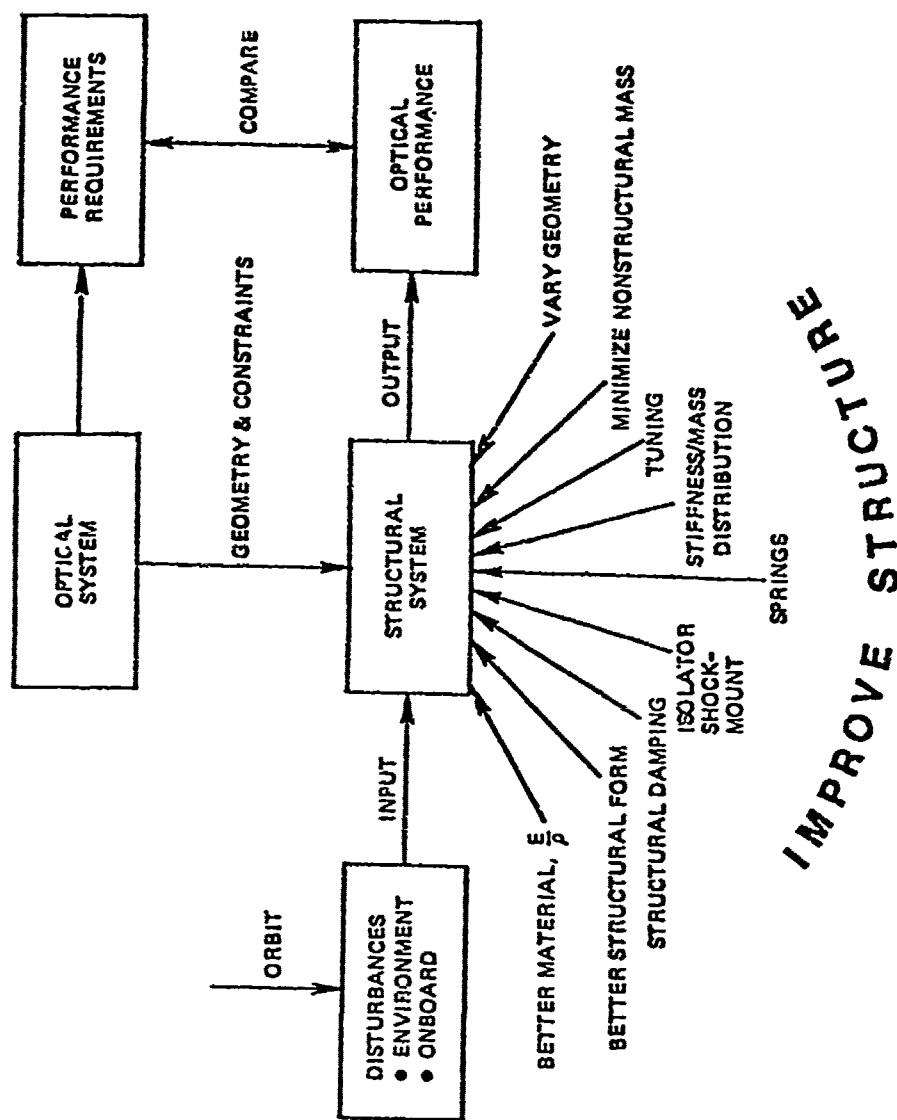


Figure 2-3. Response minimization by passive means.

In the selection of structural materials, whether for truss members or panel egg-crate construction, graphite-epoxy composites invariably emerged as the most desirable candidate. This choice hinges on the excellent E/ρ ratio (modulus of elasticity over density) which advantageously affects the stiffness while keeping the structural mass to a minimum. At the same time, graphite-epoxy exhibits a very low coefficient of thermal expansion α , usually assumed to be 0.2×10^{-6} m/m $^{\circ}$ K. This value can be decreased in one privileged direction of the material, if the proper combination of plys can be achieved in its construction.

2.2.3 Antenna Structure Description

The millimeter wave antenna selected for this study includes a large reflector surface in the shape of an elliptical torus and a feed horn deployed on a cylindrical surface passing through the focal circle of the ellipses. In projection the reflector is approximately rectangular in shape with side dimensions of 60 m and 30 m. Since the area of the reflector employed by each receiver is a circle of approximately 30 m in diameter the corner areas of the rectangular surface are not needed and therefore, have been removed. Figure 2-4 shows a projected view of the reflector surface and illustrates the arrangement of 124 of the hexagonal panels. These panels are each supported by three kinematic mounts located at the intersections of longitudinal and transverse back-up trusses. At about 30 m above the reflector a slender 11 m long box housing the feed horn equipment is supported by space frame tower. The design geometry of the tower structure was dictated by the need for non-obscuration of the reflector. For that reason the entire tower structure extends beyond the reflector's edge and its triangular shape is needed in order to develop the bending stiffness required. Its attachment to the reflector back-up trusses attempts to avoid localized reactions. Two main oversized trusses underneath the reflector insure a gradual interaction of tower and back-up trusses. A perspective view in Figure 2-6 illustrates the main features of the antenna structures. Details of relative dimensions, elements shapes, sizes and material properties are given below.

The entire reflector surface is provided by 124 hexagonally shaped graphite-epoxy panels. The largest dimension of the panels was limited to 4.5 m so that the panel can fit into the shuttle cargo-bay diameter of 4.57 m. In order to preserve good dynamic characteristics it was important to design a relatively stiff and therefore, deep panel. Limitations, however, were imposed by the packaging requirements and the choice for the panel depth was finally set at 6 cm. In this way it is possible to stack the 124 panels in about 7.8 m length of the shuttle cylindrical cargo. The hexagonal panel is an egg-crate construction, using thin graphite-epoxy face sheets and an orthogonal grid of webs. It weighs just under 4 kg/m 2 . To minimize the mass, the back face sheet and the webs have cut-outs as shown in Figure 2-5. The three kinematic mounts are located along radial lines, 120 $^{\circ}$ apart, and preserve the symmetry of the hexagon. In the present layout the back-up trusses offer hard-point supports at the apex of the hexagonal panels, but it might be desirable to move these supports inward along the panel radial lines, in order to increase the panel fundamental frequency. Comparative studies have been made and are reported on later in this report.

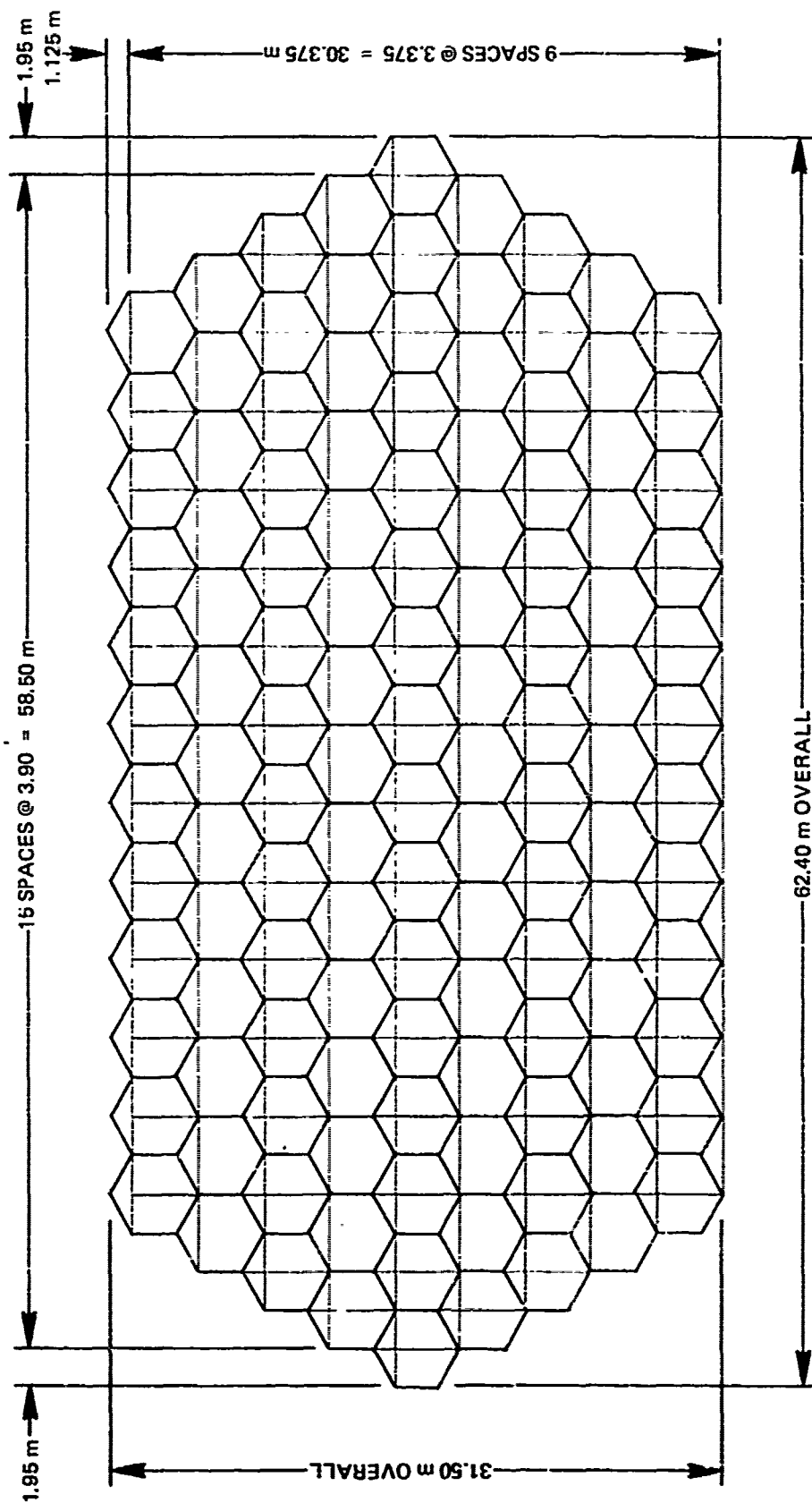


Figure 2-4. View of reflector surface.

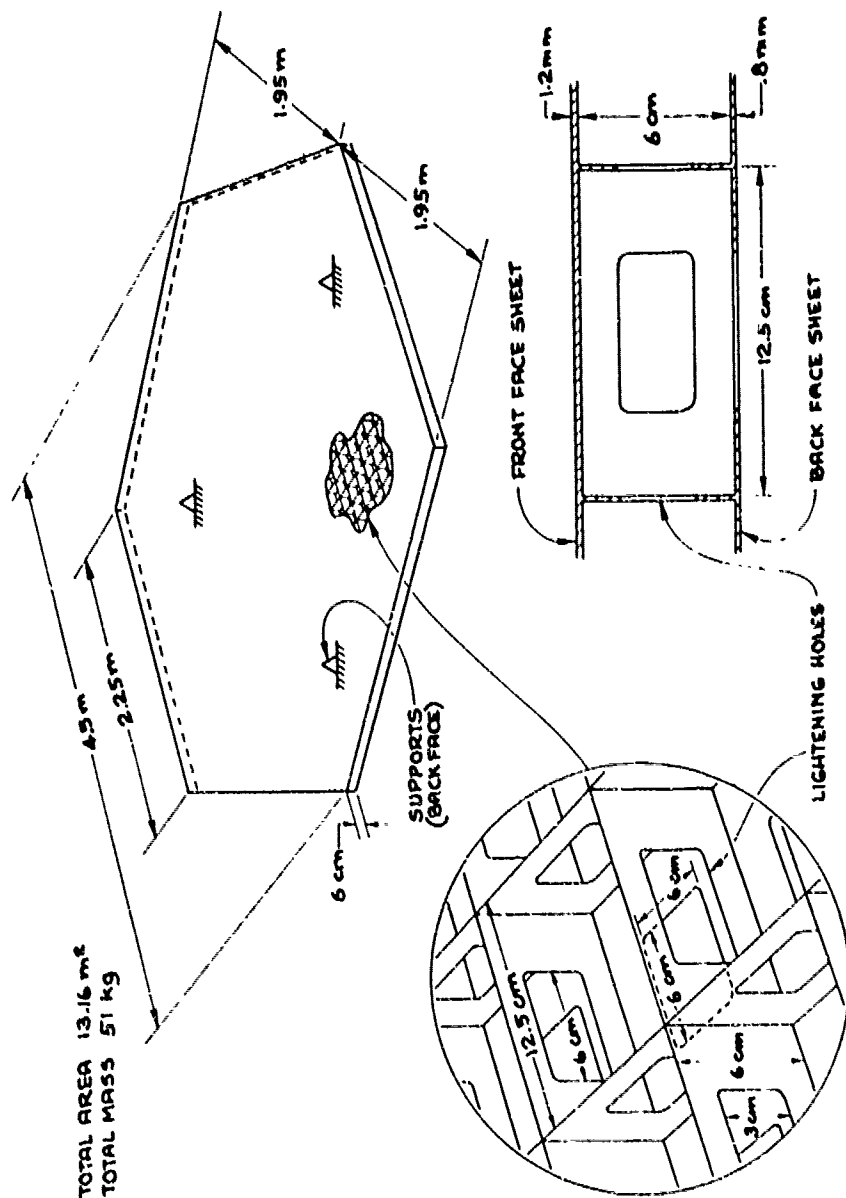


Figure 2-5. Main features of antenna surface panel.

The back-up trusses were designed as an orthogonal set of 1.5 m deep trusses and spaced such that their intersections coincide with the corners of hexagonal panels. There are 9 longitudinal trusses at 3.375 m on center and 16 transverse trusses at 3.9 m spacing. Their length varies and some have outriggers in order to accommodate the irregular arrangement of the peripheral panels. Diagonal members in the top and bottom faces provide the necessary lateral stability of the assembly. The individual truss member's area has been selected so that the bending stiffness of the platform would be sufficient to result in a fundamental natural frequency of 1 Hz. The individual truss members, usually are designed with the traditional thin-wall tube section, because this section is most efficient in terms of member bending stiffness, natural frequency, and stability. In this design an open thin-wall section was suggested since it offered the advantage of very efficient packaging for the trusses. Because of the angle shape of all its constitutive members, a truss can be nested into another one by adding to the package only slightly more than the 0.2 cm of its section's wall thickness. The packaging ratio is approximately 10 times the one corresponding to a similar packaging of trusses using tube members. The stability study of a typical truss member showed that it would require a relatively high stress (or equivalently, axial force) to reach the calculated buckling load. Under normal conditions the existing forces are anticipated to be well below this value and the design was deemed satisfactory. The graphite-epoxy truss assembly has a mass of approximately 1 kg/m².

The 30 meter high tower supporting the receiver package was designed to impart to the structure a 10 Hz natural frequency in lateral bending. As it avoids obscuration for the reflector, the cantilevered tower, 11.7 m in width, extends beyond the reflector's edge in order to develop the necessary bending stiffness. Its triangular shape has a maximum of 8 meters at its base where it meets with the antenna surface. The individual members, longer than those of the back-up trusses, are graphite-epoxy thin wall tubes, 10 cm in diameter by 0.15 cm in thickness. Figure 2-6 illustrates the structural arrangement of the tower and its attachment to the back-up trusses' assembly.

Although it is anticipated that a substantial amount of equipment is needed for the satellite operations such as data processing, communication, power generation, it was too early to assign extra masses to the structure. The 300 kg assigned to the tip of the tower is larger than the mass required for the feed-receiver equipment and is viewed as including some of the extra equipment. The location of this mass is not favorable in terms of dynamic responses and should lead to conservative results.

2.2.4 Masses and Inertia

The summary of the masses estimated for this design is as follows:

Reflector Panels at 4 kg/m ²	=	6300 kg
Back-up Trusses at 1 kg/m ²	=	1575 kg
Feed Support Structure	=	625 kg
Equipment in Feed	=	<u>300 kg</u>
TOTAL	=	8800 kg

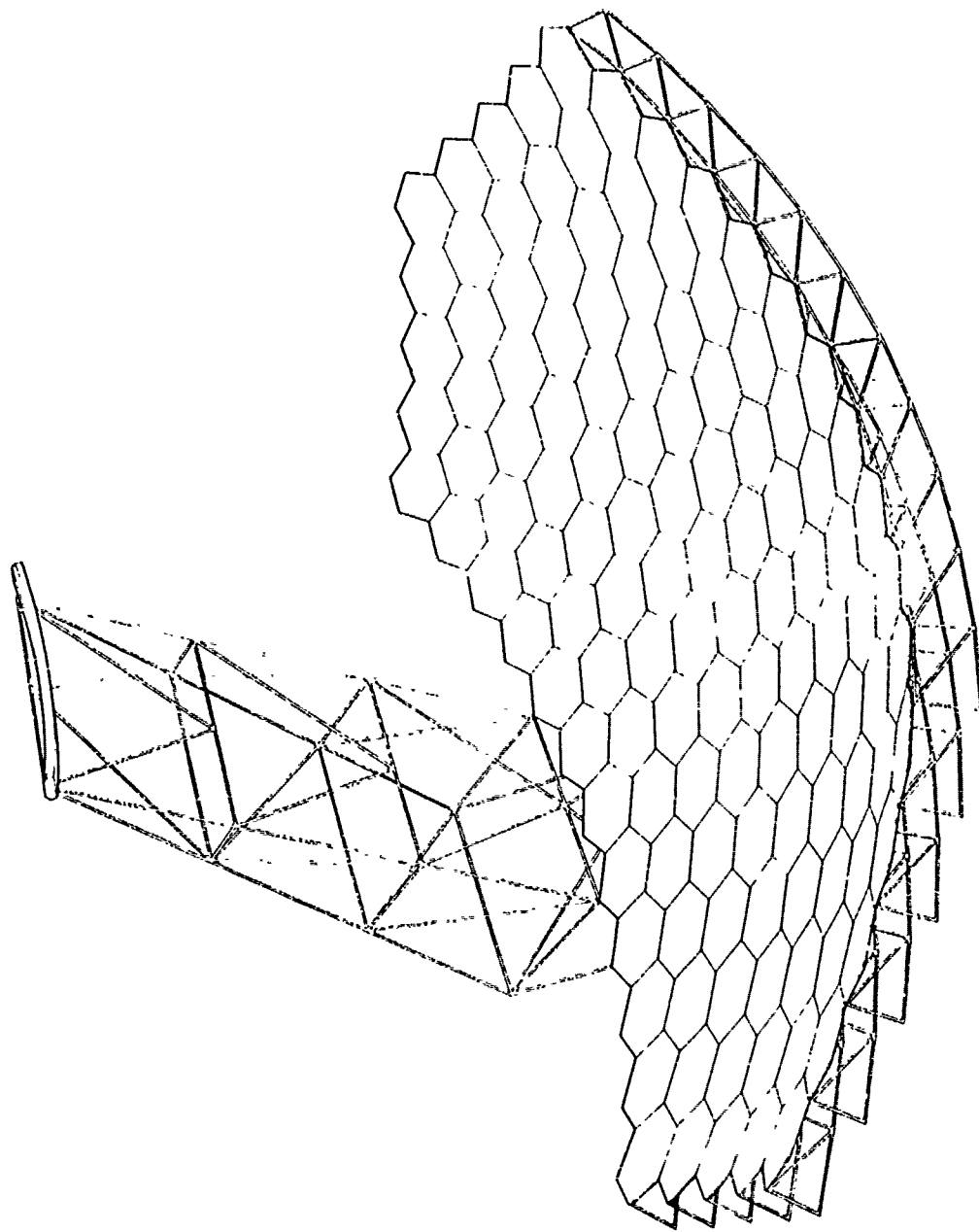
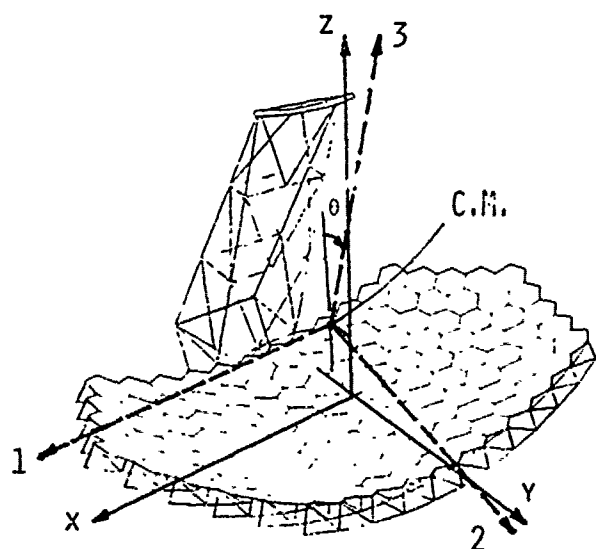


Figure 2-6. Structural arrangement of antenna components.

The mass moments of inertia have been computed with respect to the reference x,y,z system of axes located at the center surface point of the reflector. Since the overall structure is not completely symmetrical, principal axes of inertia have been determined (at the center of mass) and the associated principal mass moments of inertia have been evaluated. Figure 2-7 shows the orientation of x,y,z system and the principal axes of inertia (1,2,3) at the center of mass. The values of the various mass moments of inertia appear in the same figure.



TOTAL MASS = 8800 KG

LOCATION OF C.M.

x = 0.0
y = -1.12M
z = 4.10M

● ABOUT CENTER OF MASS

$$I_{XX} = 1.154 \cdot 10^6 \text{ KG-M}^2$$

$$I_{YY} = 2.274 \cdot 10^6 \text{ KG-M}^2$$

$$I_{ZZ} = 2.715 \cdot 10^6 \text{ KG-M}^2$$

$$I_{XY} = 0$$

$$I_{YZ} = 7.718 \cdot 10^4 \text{ KG-M}^2$$

$$I_{XZ} = 0$$

● PRINCIPAL MOMENTS OF INERTIA
W.R.T. CENTER OF MASS

$$I_1 = 1.154 \cdot 10^6 \text{ KG-M}^2$$

$$I_2 = 2.262 \cdot 10^6 \text{ KG-M}^2$$

$$I_3 = 2.728 \cdot 10^6 \text{ KG-M}^2$$

$$\theta = 9.6^\circ$$

Figure 2-7. Mass moments of inertia.

SECTION 3

DISTURBANCE IDENTIFICATION

3.1 Introduction and Approach

Disturbances affecting the structural performance of the MMW antenna system derive from various external and internal sources. The external sources of disturbance consist of solar and terrestrial related effects. The resultant torques and forces applied to the structure are functions of the satellite's position in its orbit, and its size, shape, and mass distribution. While the identification and quantification of these external loadings can be analyzed through well understood derivations and available programs, the internal loadings generated by satellite components are more difficult, at this point, to identify and evaluate. They might include torques and forces from reaction wheel mass imbalances and bearings, drive mechanisms, solar array drives and compensating jet thrusters. Since the satellite design is yet to be finalized, many of its mechanical part characteristics have not been identified. As an example, the effects of the movable solar panels and communication antennas can only be estimated.

From a structural analyst's point of view, it is desirable to categorize the disturbances by their frequency content. Once the dynamic characteristics of the structure have been determined, the various loadings can usually be classified into quasi-static and dynamic (vibrational) disturbances. In the first case, a static analysis is sufficient to predict the structural distortions, whereas a more involved dynamic analysis is required for evaluating responses to dynamic disturbances. Table 3-1 attempts to identify and classify under quasi-static and dynamic headings most of the loadings expected to ultimately affect the structural performance.

Since this study is mainly concerned with the structural behavior of the satellite, it appears natural at first to identify only a few of these disturbances that are most likely to be critical and will furnish meaningful response information. In other words, this analysis does not pretend to offer exact responses to all exactly identified disturbances, but it will evaluate the effects of some selected representative loadings on the structural performance in a behavioral sense. While the disturbances are usually approximated, the structure will be faithfully modelled so as to make it possible to assess the viability of the structural concept.

With this approach in mind, some dominant disturbances arising during the orbit period of approximately 1.56 hours have been established. In the following sections, the procedures used in evaluating the effects of solar and earth thermal fluxes, atmospheric drag, solar-radiation-pressure and gravity gradient are discussed. The approaches usually employ simplified models and the assumptions used, as well as the effects neglected, are carefully defined, so that the results can be meaningfully interpreted and discussed.

Table 3-1. Disturbances identification

SOURCES

- External or environmental
- Configuration dependent
- Attitude/position system
- Cryo-system (if required)

GROUPED BY FREQUENCY CONTENT

QUASI-STATIC

- Thermal loadings (steady state) from various sun angles, eclipsing, earth radiation
- Solar & earth radiation pressures
- Gravity gradient
- Solar panel motion reaction torques
- Geomagnetic field
- Solar wind
- Atmospheric drag

DYNAMIC

- Thrusters transients for attitude control, station keeping
- Thermal shock (transient) from eclipsing
- Solar array drive
- Communication antenna motion
- Refrigeration machinery
- Coolant mass shift
- Turbulence in pipes

3.2 Orbital Thermal Disturbances

3.2.1 Introduction

A satellite in earth orbit is exposed to internal heat sources, as well as to several thermal radiation fluxes emanating from different external sources. While the solar flux is the predominant one, its reflection from the earth, known as albedo, and the IR flux irradiated from a warm earth may also be significant. Incident flux levels on the satellite vary as a function of orbit geometry, satellite orientation, and time. Such variations give rise to time-varying temperature distributions, which in turn, cause time-varying deformations of the structure. It is the task of the analyst to make suitable assumptions in building a mathematical model capable of adequately predicting the thermal behavior of the spacecraft. From this model, temperature distributions which are a function of both spatial coordinates and time are predicted throughout the structure.

Since the orbital thermal environment and the satellite temperature responses thereto are time-varying, thermal storage effects are generally very significant. Therefore, suitable mathematical modeling requires the inclusion of thermal storage capacitances for each subdivision of the satellite structure. The degree of fineness in subdividing the structure, necessary for adequate modeling accuracy, is an important trade-off and is an item requiring experience and intuitive judgement of the analyst.

As the satellite experiences the various external radiation fluxes, three modes of thermal exchange can take place between its subdivisions and to space: conduction, convection and radiation. In space applications, gas convection and conduction between structural components is negligible because of the rarefied atmosphere and, therefore, is disregarded.

Solid conduction is easily included in thermal models, but its contribution to temperature changes depends largely on the particular problem. It is found to be very small, for example, along typical truss members because of the thinness of their wall sections. In the design of high precision mirrors, conduction becomes a significant factor because it establishes thermal gradients across the plate thickness and, thus, has a predominant contribution to the surface distortions. In some cases conductance couplings parallel to the mirror surface are negligible, while in other cases they are significant.

By far the most important mode of thermal exchange for the large space structure is radiation. A satellite structure can be viewed as an aggregate of members and surfaces that are exposed to external incident radiant energy but at the same time emit radiant energy. All these surfaces interact with each other to some degree which for typical diffuse surfaces is accounted for by the use of gray-body radiation exchange view-factors. Special methods are used for specular surfaces. As the satellite progresses along its orbital path, the angles of incidence of the incident fluxes are changing constantly (including shadowing effects) while individual surfaces usually remain in constant orientation with respect to one another. There exists a number of thermal analyzer computer programs capable of generating thermal models and calculating the temperatures for any predefined orbit. CSDL uses a combination of programs shown in Figure 3-1.

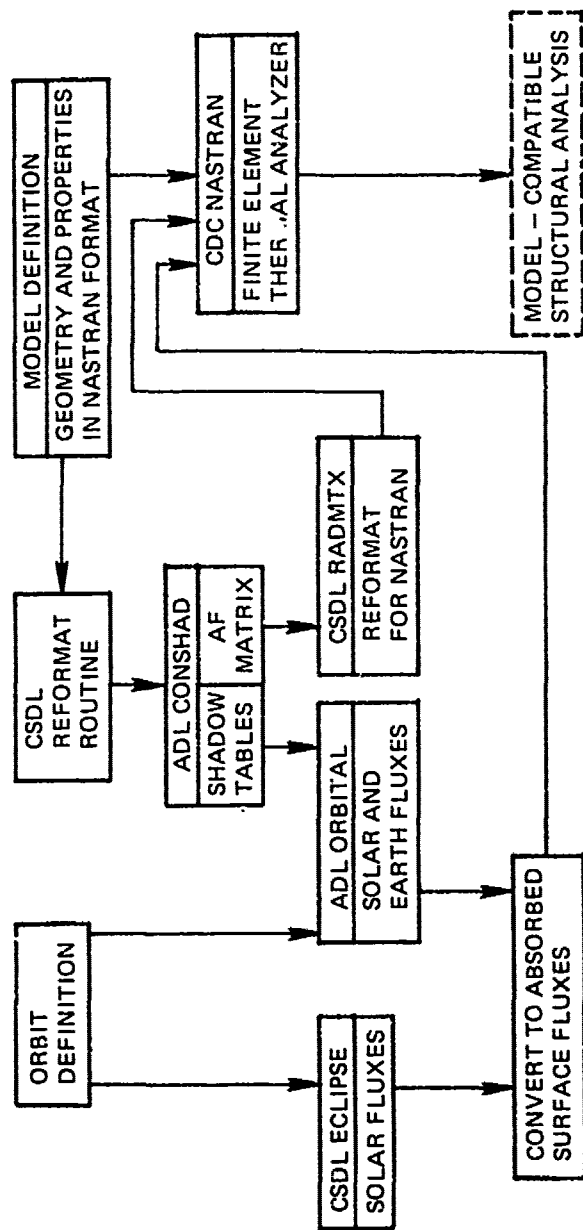


Figure 3-1. Thermal analysis tool integration.

Since the characteristics of each orbit cycle change relatively slow with time, it is expected that the thermal disturbance will become cyclic. After several revolutions the initial transient effects will disappear and the temperature histories of satellite surfaces will become almost identical for each subsequent orbit. This quasi-steady-state cyclic condition usually provides a good measure of the expected thermal fluctuations, and will give rise to slowly changing mechanical responses which are calculated using static structural analysis. Under special conditions, however, the effect of rapidly changing thermal conditions must be calculated by a dynamic mechanical analysis method. This could be created, for example, by the sudden passage from total eclipse to sunlight incident to surfaces of low modal frequencies.

For this specific study of the MMW satellite, many simplifying assumptions were made in order to obtain feasibility assessment of the design, while minimizing costly detailed thermal modeling.

Because the structure is composed of thin sheet materials of large surface areas, or of thin-walled truss tubing of large lengths, thermal solid conductances along the surfaces or truss element axes are negligible in comparison to radiative couplings, and were ignored. The repetitive design pattern of the antenna structure allowed simplified one-dimensional analyses which ignore edge effects (these effects can be minimized by suitable edge shielding). Also, truss members were treated as being isothermal through their cross-sections at any particular axial location.

The orbital thermal inputs were for a 500-km altitude equatorial orbit, with the satellite oriented with the antenna beam always directed toward the center of the earth. Orbital geometry was simplified by the worst-case assumption that the solar vector rotated in the plane of a principal axis of the satellite. The orbit period is 1.58 hours, of which 38% of the time the sun is eclipsed by the earth. For this study the combined earth IR and albedo flux was taken as a constant value, intended only as an aid in achieving approximate absolute temperature levels. The disturbances due to earth flux variations are minor in comparison to those due to direct solar loading. This constant flux incident to the satellite was taken to be 344 watts/m^2 , while the solar incident flux was taken as 1350 watts/m^2 .

3.2.2 Antenna Panels and Trusses

3.2.2.1 Model Definition

Thermal modeling of the antenna panels and trusswork was based on the general arrangement of Figure 3-2. The radiative effects of cross members between nodes 4 and 5 of the trusswork were ignored, and the reflector panels were treated as being continuous over the whole antenna. By ignoring curvature and edge effects for the whole antenna, the treatment was vastly simplified to the one-dimensional 7-node problem shown. Curvature effects are approximately accounted for separately, and edge effects can be minimized by suitable shielding.

The thermal blanket is composed of top (7) and bottom (6) layers of

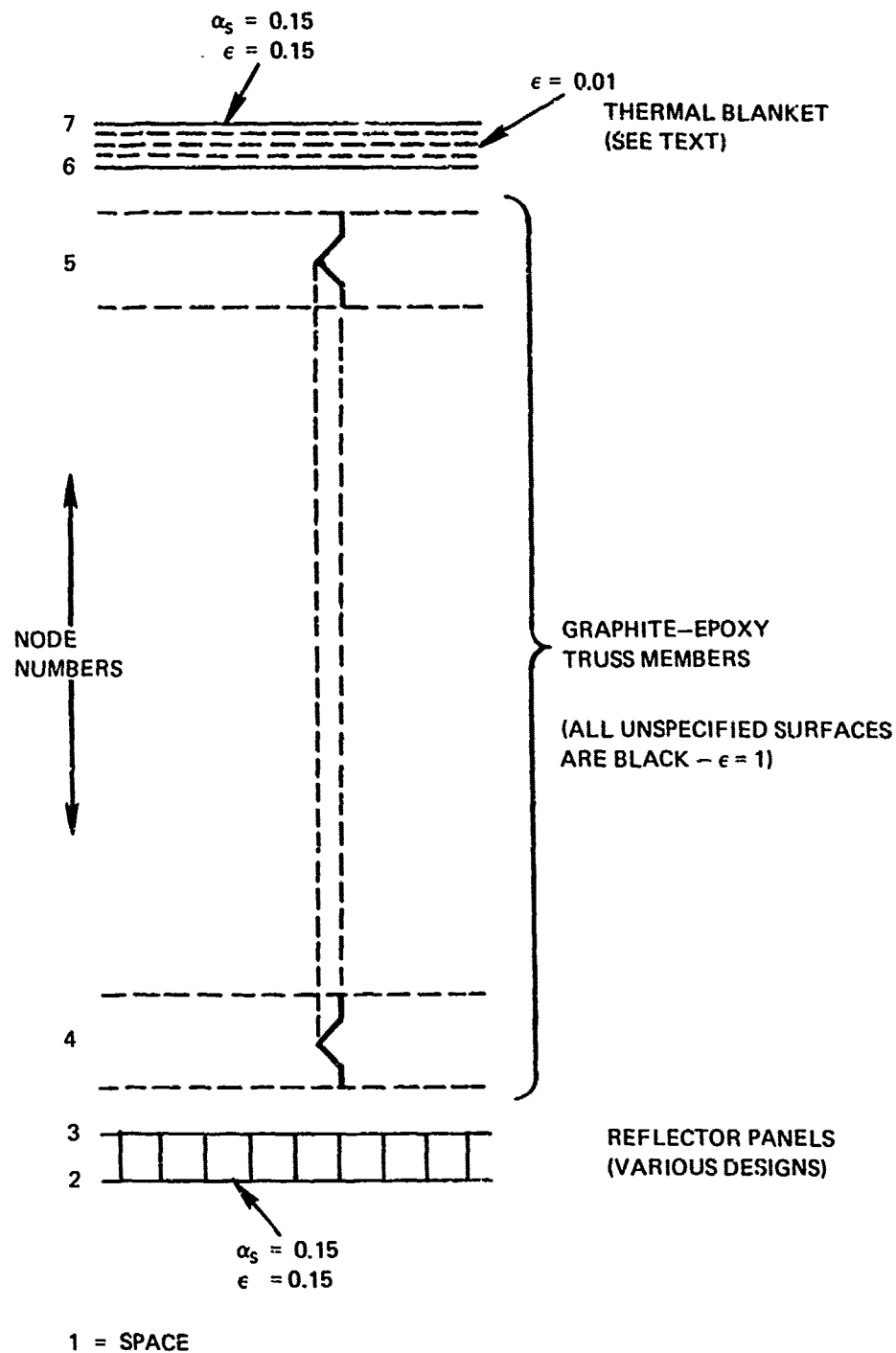


Figure 3-2. Antenna panel and truss thermal model.

0.1 mm thick teflon or other fabric covers, separated by alternating layers of dacron "bridal veil" separators and 0.01 mm thick aluminized mylar shields (possibly 5 layers). The exterior surface of the top cover is metalized to achieve reasonably low solar absorptivity and emissivity (this could be a radiatively selective surface for temperature level adjustment). In some cases analyzed, the blanket shielding layers were "short-circuited", essentially making nodes 6 and 7 a single node, to represent a simpler and less-costly single sheet of material.

A number of different design alternatives were studied for the reflector panels. The alternatives are described in their variations from a baseline design used for final analysis. This baseline design consists of a sandwich panel, all made of graphite-epoxy. The reflector sheet (2) is 1.5 mm thick, while the back sheet (3) is 1 mm thick. The core is comprised of webs of 1 mm thickness spaced in a square matrix on 88 mm centers. Web graphite fiber orientation is assumed normal to panel sheets, for maximum thermal conductance between sheets. (The design variations are shown in Figure 3-3).

3.2.2.2 Design Trade-offs

Preliminary design trade-off studies were made, results of which are summarized in Figure 3-3. For each design condition, results are shown as three different temperature difference values, pertaining to the panels or the trusswork. The values "MAX ΔT_G " and "MIN ΔT_G " are the maximum and minimum cyclic gradient temperature differences experienced across the panels or trusswork. The node notation shown defines the calculation. For example, nodes "2-3" indicates the temperature at node 3 is subtracted from the temperature at node 2. The values "AVG ΔT_U " are the amplitudes of the cyclic temperature excursions experienced by the panels or trusswork. The values are for the excursion of the average temperatures of the two associated nodes; for example, the average of nodes 2 and 3.

For the comparison of various reflector panel designs it was desired to subject them to a large disturbance, and therefore several simulations were run without solar eclipse and without an insulation blanket. Runs 2, 3, 6 and 7 show these comparisons. It will be shown later that for small-diameter panel cells the ΔT_G values are the significant distortion influences, and so for a given material the smallest ΔT_G values result in the least distortion. Since the expansion coefficient for aluminum is much greater than for graphite-epoxy, Run 6 is not a good candidate on the basis of relative distortions. Therefore, the Run 3 design was chosen as the baseline design.

There is obviously a trade-off between panel weight and thermal distortion, as indicated by Runs 2 and 3. Another trade-off is apparent for the real orbital mission (with solar eclipse) in comparing Runs 4 and 5. Thermal distortions of both panels and trusswork may be traded for cost and weight of the insulation blanket. It was decided to use Run 4 as the case to analyze in further detail, to see if distortions would be acceptably low without the insulation blanket.

3.2.2.3 Baseline Run 4 Results

The timelines of orbital temperatures for Run 4 are shown by Figure 3-4.

TEMPERATURES (°K)						
RUN	ECLIPSE	BLANKET	PANEL TYPE	NODES	2-3	4-5
1	NO	YES	Half the web mass and conductance	MAX ΔT_G MIN ΔT_G AVG ΔT_U	+5.1 -2.4 22.3	+0.2 -0.1 15.0
2	NO	NO	Half the web mass and conductance	MAX ΔT_G MIN ΔT_G AVG ΔT_U	+8.4 -4.3 10.9	+0.9 -0.6 12.7
3	NO	NO	Baseline	MAX ΔT_G MIN ΔT_G AVG ΔT_U	+5.3 -2.7 10.8	+0.9 -0.6 11.6
4	YES	NO	Baseline	MAX ΔT_G MIN ΔT_G AVG ΔT_U	+1.8 -2.7 15.6	+0.6 -0.9 17.4
5	YES	YES	Baseline	MAX ΔT_G MIN ΔT_G AVG ΔT_U	+0.7 -0.4 2.6	+0.1 -0.1 0.7
6	NO	NO	Material all aluminum (equal mass)	MAX ΔT_G MIN ΔT_G AVG ΔT_U	+1.8 -0.9 10.8	+0.9 -0.6 11.6
7	NO	NO	Air-mat Design (equal mass)	MAX ΔT_G MIN ΔT_G AVG ΔT_U	+9.2 -7.0 10.8	+0.9 -0.6 11.6

Figure 3-3. Preliminary design trade-offs.

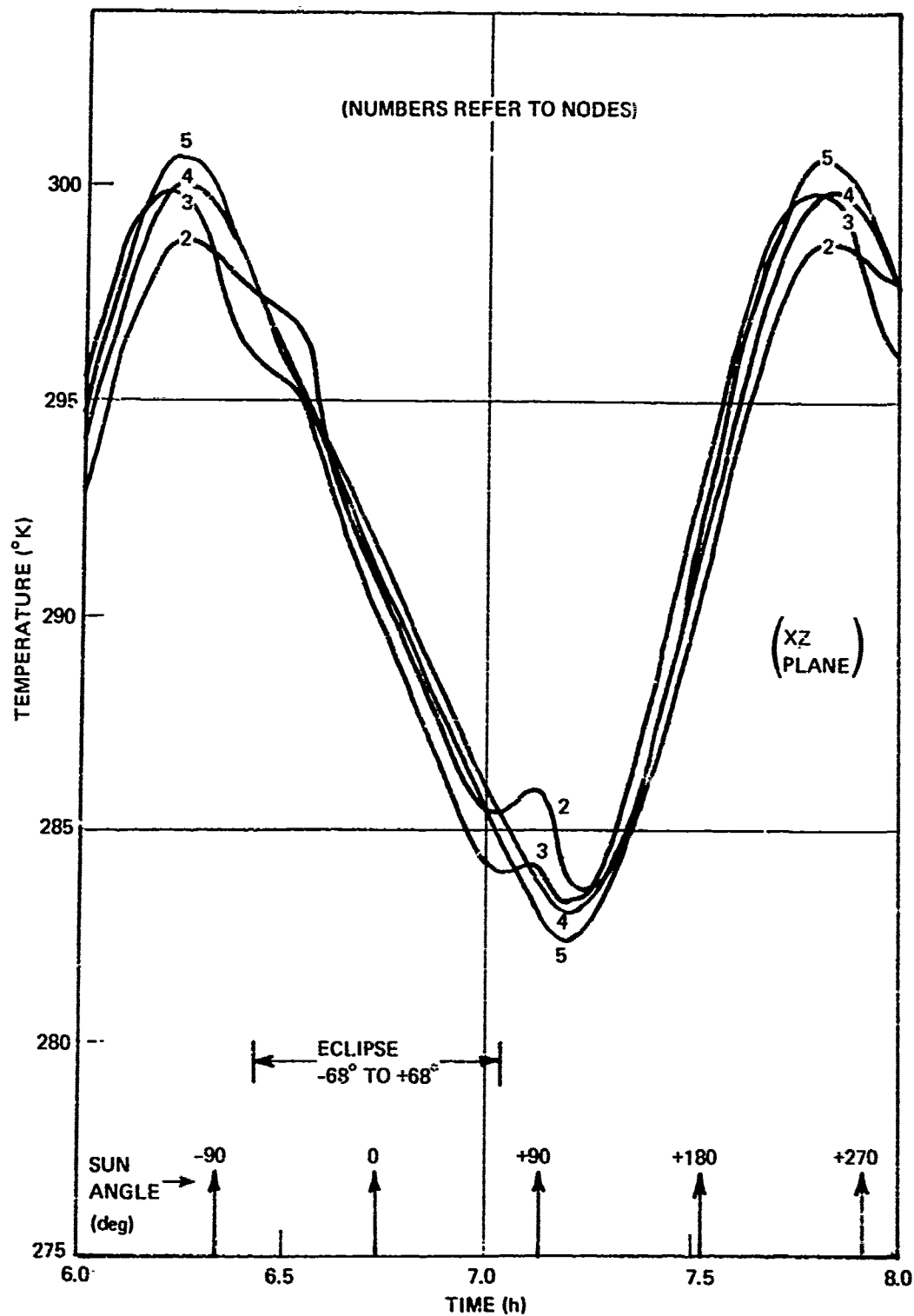


Figure 3-4. Temperatures at center of antenna (run 4).

The time scale is arbitrary, representing the fourth orbit cycle from an isothermal initial condition. As may be seen by comparison of temperatures at -90° and $+270^\circ$ of sun angle, the orbit is virtually in quasi-equilibrium. It is of interest to observe the perturbations that occur at the beginning and end of eclipse, where the sun shines on the reflector panels for a short time. This may be compared to Run 3 results, shown by Figure 3-5, which shows the effects of much greater reflector panel solar exposure when there is no eclipse.

While these results are for the center region of the antenna, based on the assumption of a flat plane, the real antenna curves through an arc of ± 30 degrees from the center, in the x-plane (60 m dimension of the antenna). An approximation was made of the effects of this curvature by adjusting the Run 4 temperature results by introducing phase angle off-sets in the results. This was done for four zones, the center of which were at angles of $+22.5$, $+7.5$, -7.5 and -22.5 degrees from the center. In addition, corrections were made in the reflector panel temperatures to account for the geometry and shadowing effects of solar loadings.

These curvature adjustments were made with the Z-axis at three sun angles of -92 , $+68$ and $+118$ degrees, estimated as being the worst thermal distortion excursion possibilities, for which distortion calculations would be made. These results are tabulated in Figure 3-6. New nodal definitions are indicated in the sketch to identify the four zones. Distortion results based on this data are reported in Section 4.5.

3.2.3 Tower Structure

3.2.3.1 Model Definition

The accurate thermal modeling of complex truss structures that are directly exposed to solar loadings is, in general, tedious and costly. For a first-order estimate of thermal distortions, a simplified model was defined for thermal analysis. Since the side tower truss sections (in the Y-Z plane) are parallel it was decided to assume a solar orbit in this plane so that one side section could be modeled, with all shadowing by truss members in that plane and with the other side responding identically by symmetry. The modeling in other solar orientations would be more difficult, but would generally be expected to produce lower total distortion excursions than for this case where the solar shadowing effects are severe in causing tower bending.

The thermal model is shown by Figure 3-7. Thermal storage capacitances are included in this model, but truss member axial solid conductances are assumed zero because they are very small relative to radiative couplings to space (members are assumed isothermal in cross-section). Also, due to the high surface reflectivities and generally small view factors between truss members, there are negligible radiative couplings between members. Each member was therefore treated independently, having only direct solar loading timelines and coupling to space. Solar loadings, including shadowing effects, were calculated in detail for each node. However, the truss members shown by dotted lines were accounted for in their shadowing effects, but not included in the thermal model. It was assumed that the major impact on tower bending was due to temperature variations of the perimeter members modeled. A more

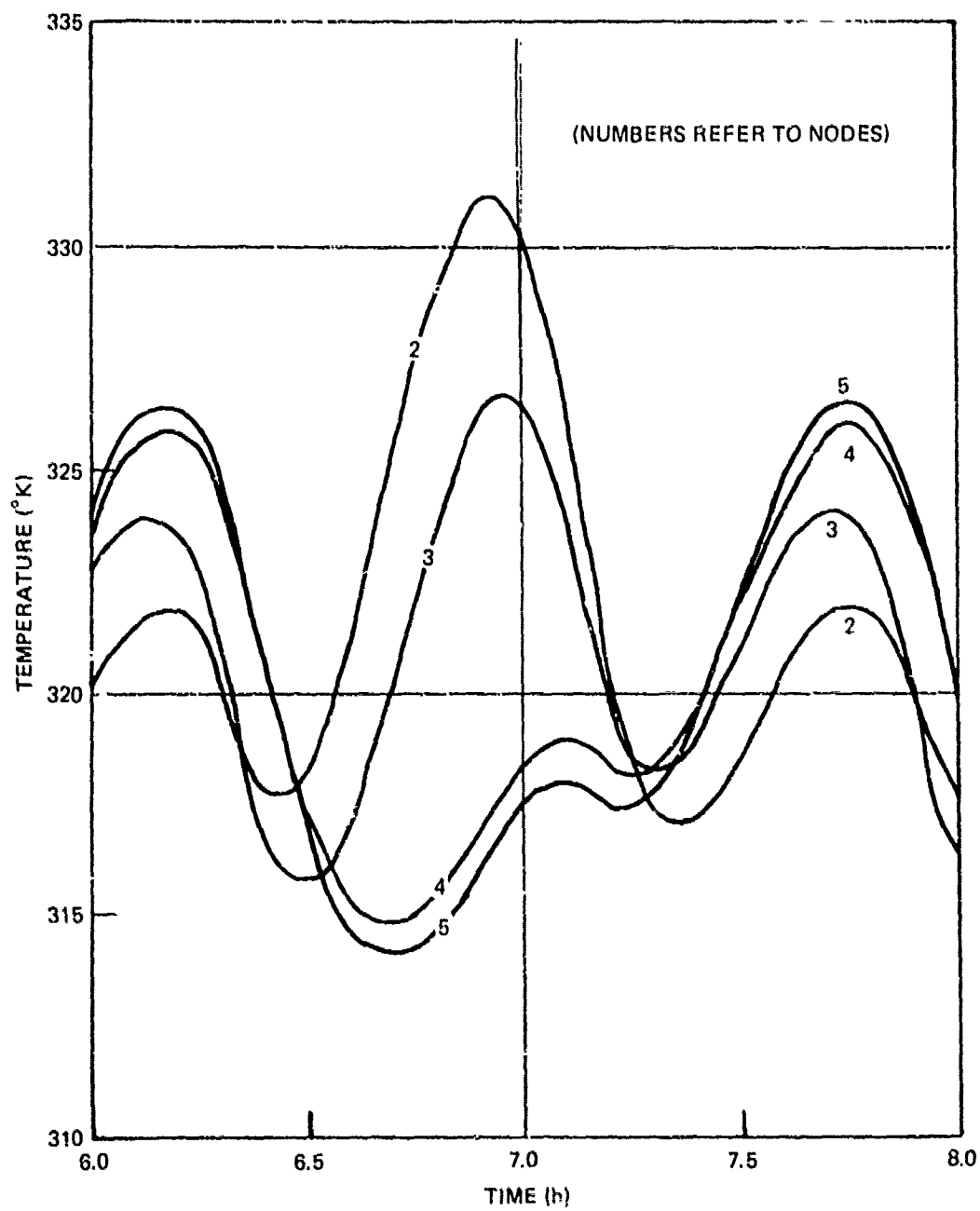


Figure 3-5. Temperatures at center of antenna (run 3).

TEMPERATURES (°K)

SUN ANGLE, degrees	-92	+68	+118
NODE 12	298.7	287.3	285.7
22	298.5	285.9	283.7
32	298.0	285.6	283.7
42	297.5	285.3	284.9
13	299.9	284.2	283.9
23	299.0	283.9	283.3
33	297.0	284.3	284.1
43	295.9	284.5	286.5
14	299.9	287.1	283.4
24	299.9	285.8	283.2
34	298.8	284.5	283.6
44	297.3	283.5	285.1
15	300.6	286.7	282.7
25	300.5	285.3	282.5
35	299.1	284.0	283.3
45	297.2	282.8	285.1

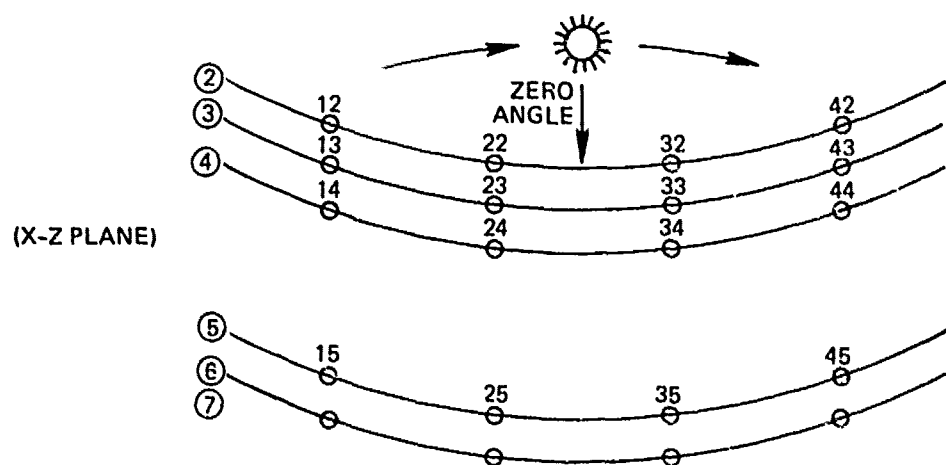


Figure 3-6. Run 4 antenna temperatures, corrected for curvature.

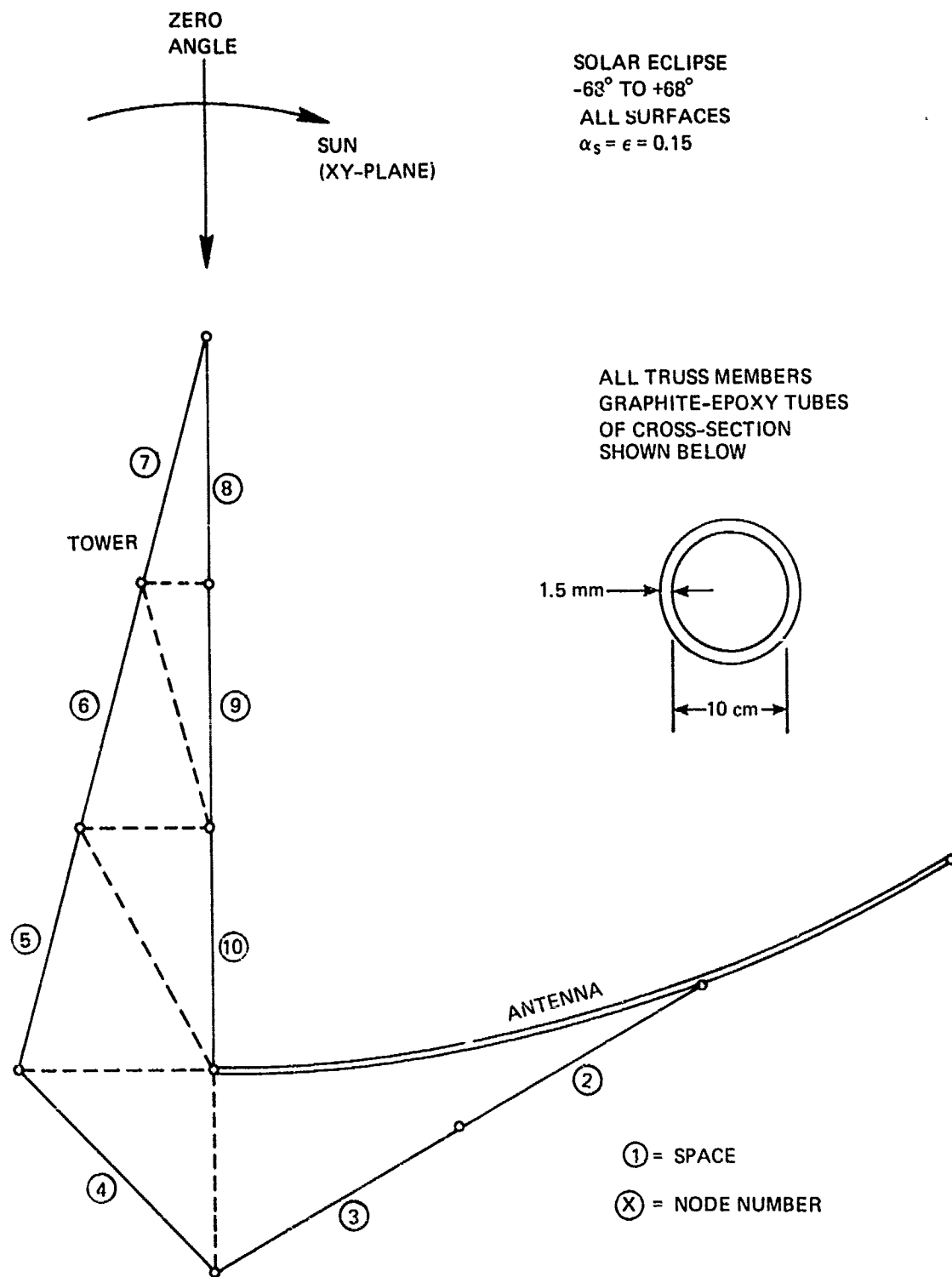


Figure 3-7. Tower structure thermal model.

significant but still minor error was introduced by omission of radiative interaction between the truss members and the antenna (which also has high reflectivity).

3.2.3.2 Tower Temperature Results

The temperature histories for the tower truss members are shown by Figure 3-8. Although the simulation was run through four orbit cycles, it is evident that temperature levels are still decreasing (compare -90 and +270 degree values). However, these results give a good approximation to the cyclic temperature excursions in quasi-equilibrium.

It is evident from Figure 3-8 that the thermal response is quite complex, this mainly being a result of the shadowed solar loading timelines. Obviously, responses would vary noticeably with orbital orientation, and these results must be considered a first-order estimate. Data from Figure 3-8 was used to calculate tower deformations at a number of different times, these being presented in Section 5.2.

3.2.4 Discussion

The thermal modeling work presented here was intended for order-of-magnitude estimation of orbital thermal distortions, to assess design feasibility and problems. It is advisable that the thermal modeling work be more comprehensive, in any future detailed design effort.

The results for the assumed baseline design antenna and associated trusswork, and for the tower trusswork, assume rather simple and passive thermal hardware. With negligible cost and weight penalties for thermal design, the resulting distortions presented in Section 5.2 are acceptable.

However, it would be quite easy to improve the thermal design further by passive means, of low cost and weight penalty. For example, it may be quite feasible to achieve lower surface emissivities on surfaces exposed to solar loadings. Also, it is obvious (from comparison of Runs 4 and 5) that great reduction of antenna distortions would result from use of an insulation blanket behind the antenna trusswork. A similarly large reduction of distortions would occur at the tower trusswork if it were enclosed in an insulation blanket, thereby transforming the large point-source solar thermal loadings into attenuated diffuse loadings.

3.3 Atmospheric Drag

3.3.1 Introduction

The MMW satellite in orbit at a height of 500 km encounters significant aerodynamic forces as it flies through the rarefied upper atmosphere. These forces create orbital perturbations that must be carefully evaluated. As a result of the braking effect of the atmosphere, the satellite experiences an orbital decay and usually a deterioration of its pointing accuracy. Although these perturbing forces are so small that the spacecraft structure is not appreciably affected in its configuration, their overall effect must be

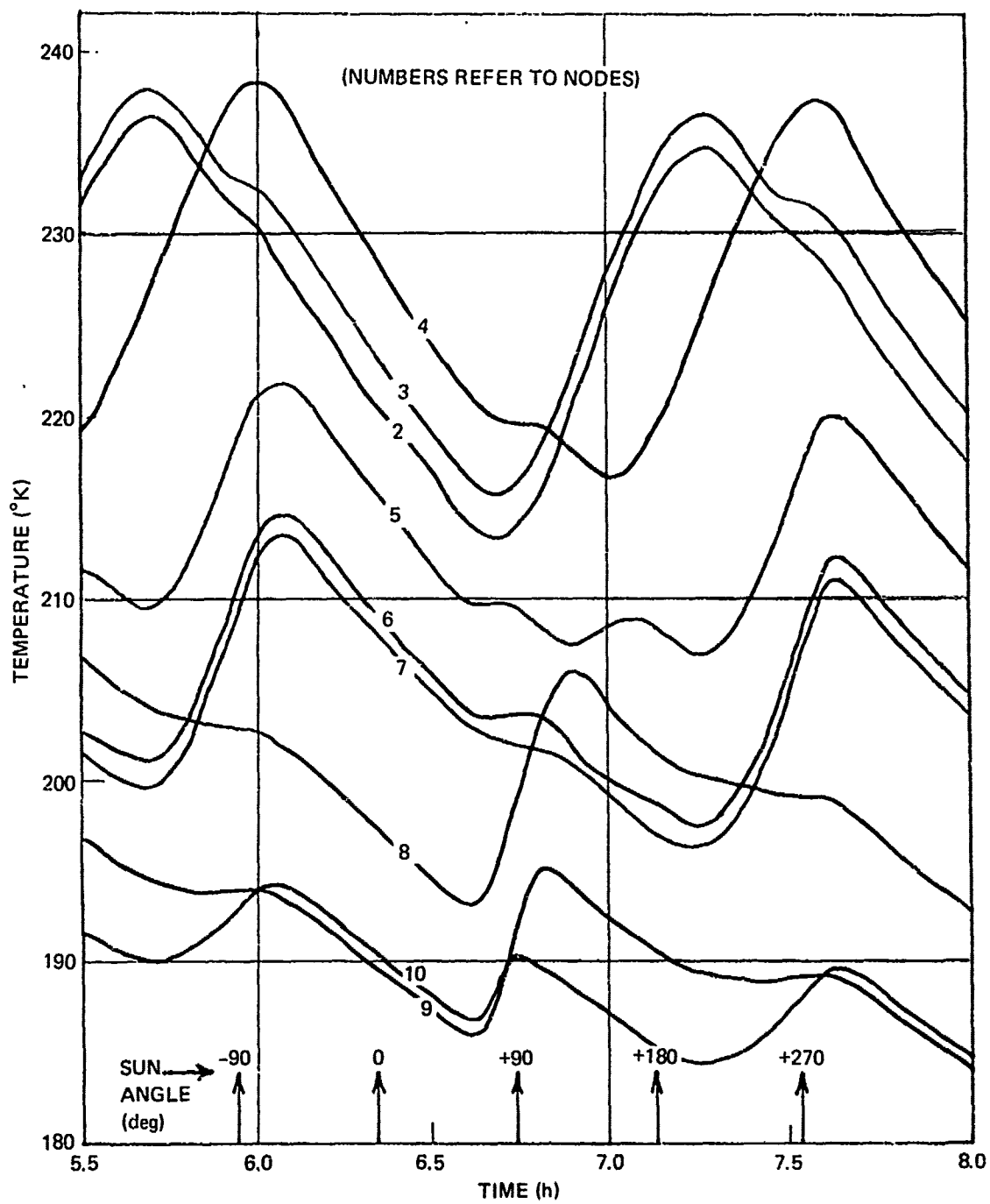


Figure 3-8. Tower structure temperature results.

counteracted by an attitude control system. It is the disturbance associated with that control law that must be carefully designed and tailored so as to minimize the dynamic structural responses of the delicate spacecraft.

This section briefly reviews the important factors entering the calculation of the upper atmosphere density used in the evaluation of drag forces and torques. A brief study of the orbital decay and the MMW antenna, performed by a special purpose computer program is also presented for two levels of solar activity. It emphasizes the problems associated with station-keeping and indicates the propulsion requirements to restore the orbit. Finally a simplified calculation of force and torque resultants with respect to the center-of-mass of the satellite is presented for some extreme cases of two atmospheric densities corresponding to an average- and a high-level of solar activities.

3.3.2 Upper Atmosphere Density Model

The determination of the upper-atmospheric density is usually based on the study of the orbital decay of a large number of earth satellites. The aim is to define a simple analytic relationship for determining the upper-atmospheric density allowing for its main variations, such as diurnal and semi-annual variations as well as its correlation with the intensity of the solar activity at the wavelength of 10.7 cm. The density ρ can be computed as a product of several factors each of them corresponding to one or other forms of the known density variations:

$$\rho = \rho_H K_1 K_2 K_3 K_4.$$

where ρ_H is a night-time vertical profile of the atmospheric density; K_1 is a factor describing the density change with the change of solar activity F at 10.7 cm relative to some average level of radiation F_0 ; K_2 is a coefficient considering the diurnal effect in the density distribution; K_3 is a correction for the semi-annual effect; K_4 is a factor taking into account the correlation between the atmospheric density variations and geomagnetic perturbations.

The coefficients change with a change of the mean level of solar activity F_0 over the eleven-year cycle of solar activity. Other density variations are not taken into account since they have a smaller influence. From the observation of the motion of existing earth satellites, the available experimental material is usually divided in groups corresponding to mean levels of solar activity F of 75, 100, 125, 150, 200, 250 units ($10^{-22} \text{ Wm}^{-2} \text{ Hz}^{-1}$).

All the K factors above are described by involved analytical relationships. With the atmospheric density information and the definition of the orbit parameters, the orbital dynamics and the station keeping requirements of the MMW antenna are evaluated with the help of a specialized computer program. The following study employed the current semi-analytical satellite theory implementation in the GTDS R/D program (Goddard Trajectory Determination System (GTDS), Research and Development version).

Orbital initial conditions and spacecraft (S/C) parameters were assumed as follows:

Initial Conditions:

semi-major axis	$a = 6878.0 \text{ km}$
eccentricity	$e = 0.001$
inclination	$i = 100^\circ$
ascending node	$\Omega = 0.0^\circ$
argument of perigee	$\omega = 0.0^\circ$
mean anomaly	$M = 0.0^\circ$
	epoch = January 31, 1979

S/C Parameters:

$A = 642.0 \text{ m}^2$
$M = 8800.0 \text{ kg}$
$C_D = 2.0$

The orbital conditions provide a 500 km, circular orbit. The orbital inclination of 100° is designed to provide global coverage and to be consistent with flight operations from WTR. The value 2.0 of the coefficient of drag (C_D) corresponds to the default option in the GTDS R/D program.

Two flight conditions have been studied. The first case takes the above data and assumes a Harris/Priester atmospheric density model corresponding to a moderate level of solar activity ($\bar{F}_{10.7} = 150$). This represents a typical flight condition over the eleven year solar cycle. The second case assumes an atmospheric density model with a high level of solar activity ($\bar{F}_{10.7} = 250$). This high level of solar activity better represents the conditions expected in 1979 and 1980.

3.3.3 Orbital Decay

For the average solar activity ($\bar{F}_{10.7} = 150$), the key elements of the orbital history are summarized in Table 3-2. The semi-major axis, a ,

Table 3-2 $\bar{F}_{10.7} = 150$

T(days)	a(km)	PH(perifocal) height, km
0	6878.	492.982
10	6872.792	493.233
20	6867.475	482.476
30	6861.969	471.230

is decreasing in a nearly linear manner due to the atmospheric drag. The perigee height is also decreasing due to the decay in a . However, there is also a long periodic oscillation due to gravitational perturbations of the orbital eccentricity (this can be seen more clearly in the GTDS print-out). Over the thirty day period,

$$\Delta a = -16.031 \text{ km}$$

$$\Delta PH = -21.752 \text{ km}$$

The average daily $\Delta a = -0.5344 \text{ km}$.

For the high solar activity ($\bar{F}_{10.7} = 250$), the key elements of the orbital history are summarized in Table 3-3. The primary difference

Table 3-3 $\bar{F}_{10.7} = 250$

T(days)	a(km)	PH(perifocal height, km)
0	6878.	492.982
10	6859.584	478.167
20	6837.117	446.441
30	6807.003	409.072

with the previous case is that the semi-major axis is decaying more rapidly due to the increased atmospheric density associated with the higher level of solar activity. The character of the decay is still nearly linear but the decay rate increases significantly over the thirty-day span. Over the thirty day period,

$$\Delta a = -70.997 \text{ km}$$

$$\Delta PH = -83.910 \text{ km}$$

The average daily $\Delta a = -2.367 \text{ km}$.

3.3.4 Stationkeeping Requirements

Active altitude control is necessary to maintain the initial orbital configuration of the MMW antenna. Nickerson et. al. provide linearized variational equations for the maneuvers about a reference circular orbit. These equations assume that the propulsive impulses are along an action line normal to the radius vector and in the plane of the orbit. These equations are

$$\Delta a = 2a_o \sqrt{\frac{a_o}{\mu}} \Delta v_T$$

$$\Delta e_x = 2 \sqrt{\frac{a_o}{\mu}} \cos \theta \Delta v_T$$

$$\Delta e_y = 2 \sqrt{\frac{a_o}{\mu}} \sin \theta \Delta v_T$$

where

Δe_x = change in $e \cos \omega$

Δe_y = change in $e \sin \omega$

μ = gravitational constant

a_o = reference circular orbit semi-major axis

ΔV_T = tangential velocity change impulse

θ = argument of latitude

Inspection of these results shows that the application of two equal impulses in the same direction, with the impulses being separated by 180° in θ , results in a net change in the semi-major axis but no change in the magnitude of the eccentricity.

For example, consider the propulsive requirements to restore the semi-major axis of the orbit for the average solar activity case ($\bar{F}_{10.7} = 150$) after thirty days. The data for the maneuvers equations is

$$\Delta a = 8.0155 \text{ km}$$

$$a_o = 6861.969 \text{ km}$$

$$\mu = 398600.8 \text{ km}^3/\text{s}^2$$

Substitution of these quantities into the first maneuvers equation gives

$$\Delta V_T = 4.45 \text{ m/s}^2$$

Thus the total ΔV requirement to restore the orbit after thirty days is 8.9 m/s. Over a five-year lifetime, the total ΔV would be approximately 542 m/s.

The ΔV requirements are much larger for the high solar activity case. The data for the maneuver equations is

$$\Delta a = 35.50 \text{ km}$$

$$a_o = 6807.003 \text{ km}$$

$$\mu = 398600.8 \text{ km}^3/\text{s}^2$$

These give

$$\Delta V_T = 19.95 \text{ m/s}$$

Thus the total ΔV requirement to restore the orbit after thirty days is 39.9 m/s. Over a five-year lifetime, the total ΔV to be applied is approximately 2428.9 m/s.

3.3.5 Density at the Orbital Altitude

The maximum density at the nominal orbital altitude is of interest in the calculation of aerodynamic torques. The values are:

Maximum density at 500 km

$$\bar{F}_{10.7} = 150 \quad 0.2042 \text{ E-2 kg/km}^3$$

$$\bar{F}_{10.7} = 250 \quad 0.5645 \text{ E-2 kg/km}^3$$

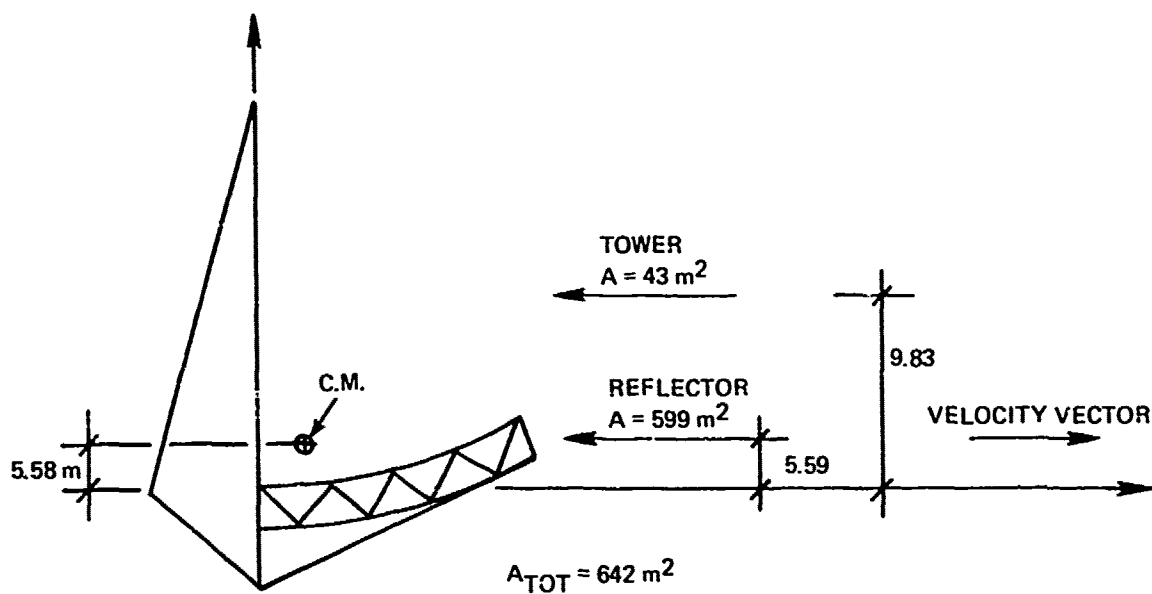
3.3.6 Forces and Torques Resultants

For the complex geometric shapes of a large satellite such as the MMW antenna, the "exact" evaluation of drag forces becomes extremely difficult and involved. First, the drag coefficient for each exposed component needs to be determined. The shape and size of the element and even the quality of its surface affect the coefficient. In addition, it is necessary to take into account the shadowing effect and possibly the multiple collision of reflected particles. While there exists specialized programs capable of accounting for some of these factors, this approach was not followed here. Because the intent was only to establish an order-of-magnitude for this highly fluctuating disturbance, a simplified model was deemed sufficient. The spacecraft y-axis was assumed to coincide with the velocity vector and the satellite was represented by only two exposed surfaces. The projection of the curved reflector into the x-y plane determined the first surface of 599 m^2 . The second surface represented the tower. Since the structure is not a continuous surface, an equivalent solid area of 43 m^2 was calculated on the basis of its solidity ratio. The relative positions of the centers of pressure of the two surfaces with respect to the center of mass of the spacecraft were used in determining the torques. In the familiar aerodynamic relations used for the drag calculation, the drag coefficient C_D was assumed to be 2.0. Sketches of the simplified model, the mathematical expressions used and the calculation results are presented in Figure 3-9. These numbers are viewed as an estimate of the typical disturbance that can result from the atmospheric drag encountered at a 500 km orbit. The design of the thruster's impulses of the attitude control system was based partially on these findings. (See Section 3.6.)

3.4 Solar Radiation Pressure

3.4.1 Introduction

Solar radiation pressure is a major disturbance to satellite attitudes since the forces are not balanced about the center of gravity. The attitude control system jets can provide the necessary corrective torque to prevent the LOS error from becoming larger than the stipulated tolerance. In order to be able to determine this disturbance, a complete time-history of the resultant solar radiation pressure torques and forces was produced for the entire orbit. This section first presents the approach to solar radiation pressure analysis where equations involving specular and diffuse reflection are discussed. Next, a model for the MMW satellite is proposed and the simplifications necessary to bring the study down to a tractable form are presented. As a result, plots of resultant forces and torques are obtained for the entire orbit time.



$$\text{DRAG } D = \frac{1}{2} \rho V^2 C_D A_{\text{TOTAL}}$$

$$\text{TORQUE } T = \frac{1}{2} \rho V^2 C_D \sum A_i D_i$$

$$V = 7.6127 \text{ km/s}$$

$$C_D = 2.0$$

$$\rho = 0.5646 \cdot 10^{-2} \text{ kg/km}^3 \text{ (HIGH)}$$

$$= 0.2042 \cdot 10^{-2} \text{ kg/km}^3 \text{ (AVERAGE)}$$

		DRAG D	TORQUE T_1
HIGH SOLAR ACTIVITY	PEAK IN ORBIT	0.210 n	0.0617 n-m
	SEVERAL-DAY AVERAGE	0.1049 n	0.030 n-m
AVERAGE SOLAR ACTIVITY	PEAK IN ORBIT	0.760 n	0.0223 n-m
	SEVERAL-DAY AVERAGE	0.0285 n	0.0081 n-m

Figure 3-9. Atmospheric drag at 500 km orbit.

3.4.2 Solar Radiation Pressure Analysis

The momentum per-unit-volume (units Nsm^{-3}) which is carried by a collimated beam of light is given by H/c^2 where H is the power per-unit-area (W m^{-2}) and c is the velocity of light (ms^{-1}). When the light is totally absorbed on a material body the force exerted on the body is the time-rate of deposition of momentum. Hence, the force per-unit-area (area is normal to the beam) exerted in the direction of travel of the light is

$$F = (\text{momentum/volume}) \times (\text{velocity of light})$$

$$F = \frac{H}{c^2} \cdot c = H/c \text{ (units } \text{N m}^{-2}\text{)}$$

For a reflecting surface, the rate-of-change of momentum of the photons can be higher because the photons leaving the surface have a component of momentum in a direction opposite to a component of the arriving photons. In computing the radiation pressure on a spacecraft it is particularly significant to determine the net resultant force per-unit-area when the incident radiation is diffusely reflected. The term "diffuse reflector" implies that the intensity of radiation leaving the surface is independent of direction and this is known as Lambert's cosine law. Because of the azimuth symmetry of the diffuse radiation, there exists only a net pressure force in a direction opposite to that of the surface normal (P_{\perp}). This component is, for normal incident light,

$$P_{\perp} = \frac{2}{3} \frac{H}{c} (1-\alpha)$$

where H is the incident radiation flux intensity (W/m^2) and α is the absorptivity of the surface.

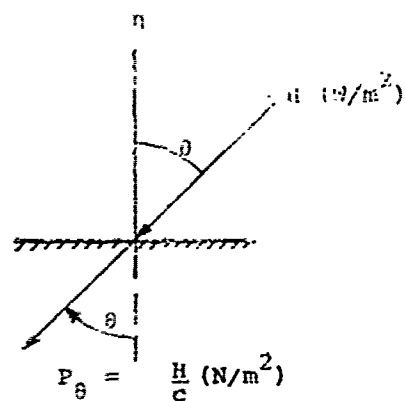
Figure 3-10 summarizes the three types of pressure forces that can be modeled as part of the orbital heat flux program. Case I represents a black (totally absorbing) surface and, as such, is just a special case of either Case II (specular surface) or Case III (diffuse surface). Figure 3-10 provides the resultant force as resolved into its components perpendicular and parallel to the surface (P_{\perp}), per unit surface area.

Figure 3-11 summarizes the radiation pressure on a flat black plate viewing the earth as a function of altitude for three sources of radiation, i.e., solar, reflected solar and earth IR. The location of the flat plate over the subsolar point of the earth was chosen to maximize the pressure force due to the sunlight reflected by the earth.

It is apparent from Figure 3-11, that the solar pressure forces on a payload can be over an order-of-magnitude higher than the pressure forces due to earth IR and reflected sunlight, particularly at the higher altitudes.

3.4.3 MMW Antenna Model and Results

The antenna structure was idealized as a simple model of a flat rectangular plate representing the slightly curved reflector. The tower structure was

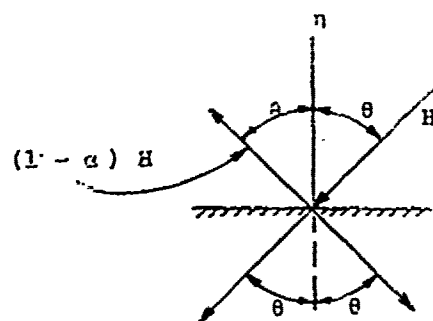


I) Black surface ($\alpha=1.0$)

$$P_{\perp} = \frac{H}{c} \cos^2 \theta$$

$$P_{\parallel} = \frac{H}{c} \cos \theta \sin \theta$$

$$P_{\theta} = \frac{H}{c} \text{ (N/m}^2\text{)}$$



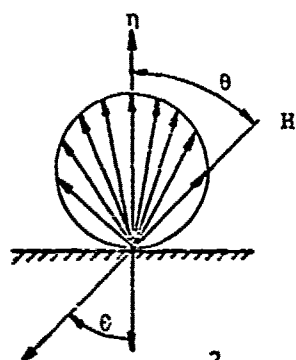
II) Specular Surface (α)

$$P_{\perp} = (2 - \alpha) \frac{H}{c} \cos^2 \theta$$

$$P_{\parallel} = \alpha \frac{H}{c} \cos \theta \sin \theta$$

$$P_{\theta} = \frac{H}{c}$$

$$P_{-\theta} = (1 - \alpha) \frac{H}{c}$$



III) Diffuse Surface (α)

$$P_{\perp} = \left[\cos^2 \theta + \frac{2}{3}(1-\alpha) \right] \frac{H \cos \theta}{c}$$

$$P_{\parallel} = \frac{H}{c} \sin \theta \cos \theta$$

$$P_{\theta} = \frac{H}{c}$$

$$P = \frac{2}{3} (1 - \alpha) \frac{H}{c} \cos \theta$$

Figure 3-10. Radiation pressures (N/m^2) on three different surfaces due to an incident radiation flux intensity $H(\text{W/m}^2)$ arriving at an angle to surface normal.

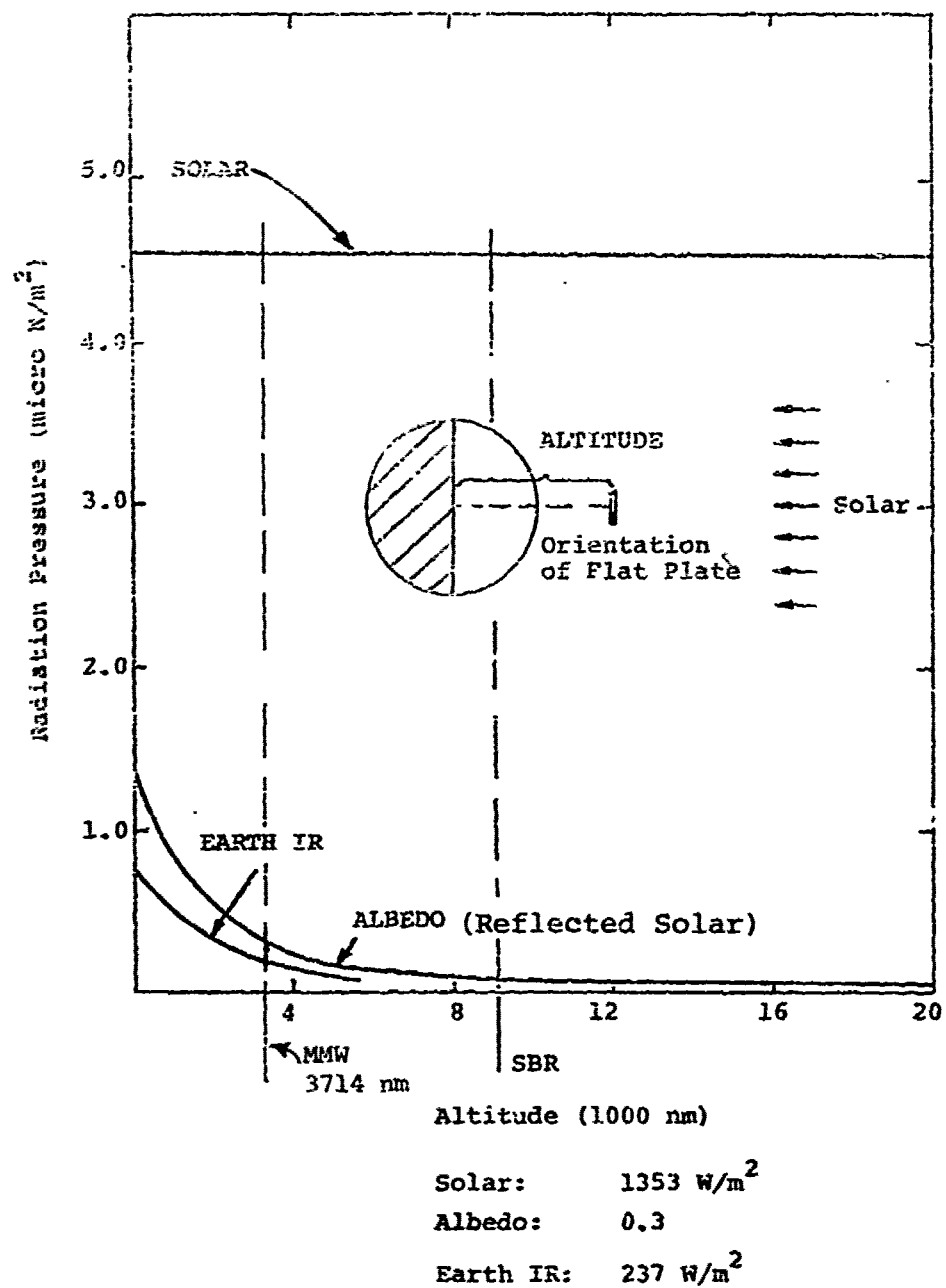


Figure 3-11. Solar, maximum albedo and earth IR radiation pressures on a flat black plate as a function of altitude.

not included in the model, since its intercepting area is negligible compared with the reflector area.

The other assumptions used in the calculation of the sun radiation pressure resultants are summarized here:

- (1) Sun radiation vector is in the circular orbit plane
- (2) Direct sun radiation only; albedo and IR effects are relatively small and are not included (See Figure 3-11)
- (3) All diffuse surfaces are assumed to have zero absorptivity ($\alpha = 0$)
- (4) No shading from tower or due to antenna curvature is accounted for

The program computes the total incident flux on the surface as a function of orbit position and spacecraft orientation. With the angle of the incoming ray known and the surface optical properties available, the magnitude and direction of the resulting force are obtained. Torques with respect to the satellite center of mass are easily calculated from geometrical relationships. Since the sun is assumed to be in the plane of the orbit, and owing to the model symmetry, only two force resultants F_x and F_z , and one torque resultant, T_y , are present. Figure 3-12 defines the various parameters describing the antenna-orbit-sun relationships. The two forces and the one torque resultants are plotted as a function of time over the entire 95 minute orbit. Due to assumption (2) above the force resultants are identically zero as the satellite moves in the earth shadow.

3.5 Gravity-Gradient

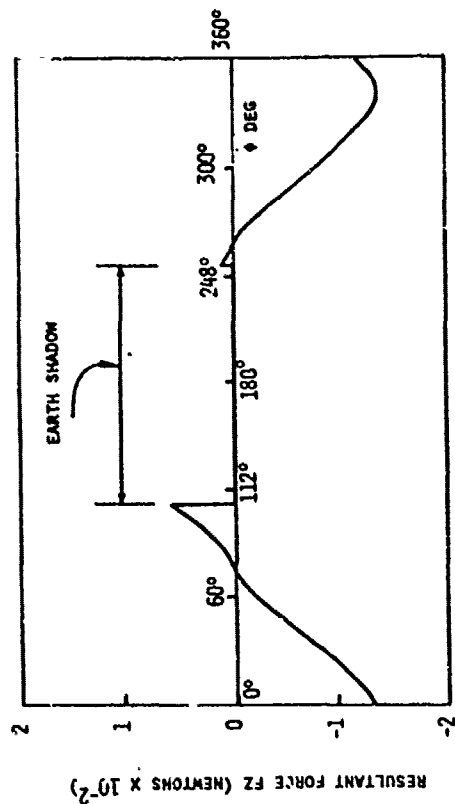
3.5.1 Introduction

The effects of gravity-gradient have often been used as a simple means of stabilizing small satellites. For large and asymmetric spacecraft such as the MMW antenna, however, gravity-gradient torques become significant and are a major source of environmental disturbance. For the MMW satellite the calculated torques are even larger than those associated with the effects of atmospheric drag at the 500 km altitude.

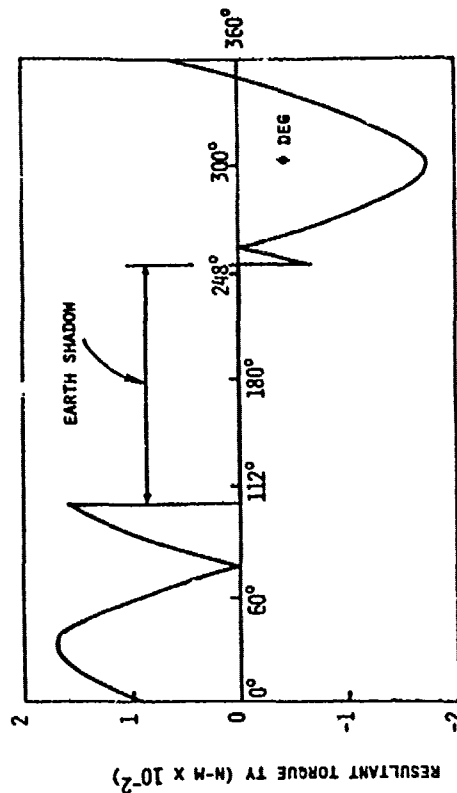
This section discusses the treatment of the effects on an orbiting body of the earth's gravitational field. With proper selection of body axes, the equations for the torques can be reduced to simple expressions. The torques for the MMW spacecraft are evaluated simply in terms of orbit geometry and mass moments-of-inertia. It is interesting to note that the gravity-gradient torques for an earth pointing satellite are almost constant (the MMW antenna is earth pointing), whereas they would vary constantly for an earth orbiting spacecraft that is inertially fixed.

3.5.2 Gravity-Gradient Analysis

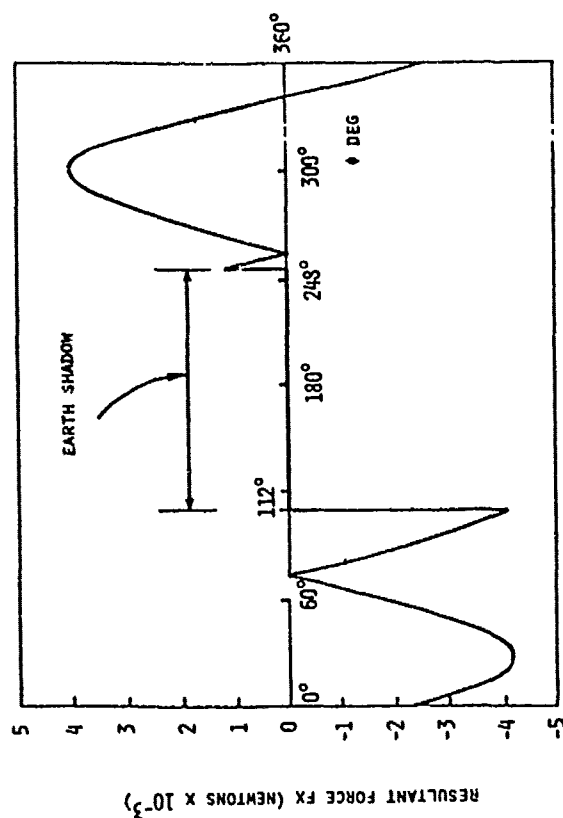
While a rigorous treatment of the effects of gravity-gradient can be quite elaborate if the gravitational field is expressed by an infinite series of harmonics, this approach is less complicated as it takes advantage of a number



SOLAR RADIATION FORCE RESULTANT FZ ABOUT C.M.



SOLAR RADIATION TORQUE RESULTANT ABOUT C.M.



SOLAR RADIATION FORCE RESULTANT FX ABOUT C.M.

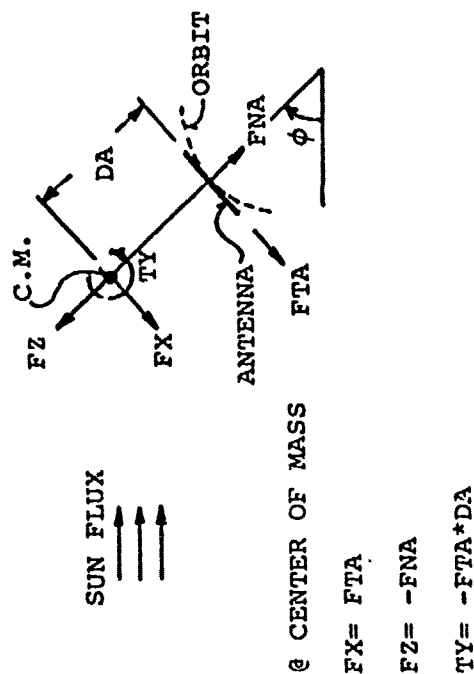


Figure 3-12. Solar radiation resultants.

of legitimate simplifications. The anomalies due to irregularities of the earth mass distribution and its surface features can be disregarded in a first-order estimation. The evaluation of torques accounting at least for the oblateness of the earth is usually recommended, but this approach considers the simple case of a spacecraft in circular orbit about a spherical earth. The derivation of the basic equations for this "ideal" case is presented below.

For a body in a circular orbit of radius, R_o , about the earth, (see Figure 3-13) a reference coordinate system ($\hat{i}_r, \hat{j}_r, \hat{k}_r$) is defined such that \hat{k}_r is always directed radially toward the earth, and its origin coincides with the mass center of the body. The vector radius \vec{R} has components in the reference coordinate frame as follows

$$\begin{aligned}\vec{R} &= R_o \hat{k}_r \\ &= R_x \hat{i}_b + R_y \hat{j}_b + R_z \hat{k}_b\end{aligned}\tag{3-1}$$

The components of the vector \vec{R} in the body axes are obtained from the rotation matrix relating the two systems of axes by use of the Euler angles ψ, θ and ϕ . They are:

$$\begin{aligned}R_x &= R_o \sin \theta \\ R_y &= -R_o \sin \phi \cos \theta \\ R_z &= -R_o \cos \phi \cos \theta\end{aligned}\tag{3-2}$$

If $\vec{\rho}$ denotes the radius vector from the body's center of mass to a generic mass element, dm , it has the form

$$\vec{\rho} = x \hat{i}_b + y \hat{j}_b + z \hat{k}_b\tag{3-3}$$

and the radius vector from the earth's center to this mass element becomes

$$\vec{r} = \vec{R} + \vec{\rho}\tag{3-3}$$

The force due to gravity on a mass element is

$$d\vec{F} = -\frac{\mu dm}{r^3} \vec{r}\tag{3-4}$$

where

$$\begin{aligned}\mu &= GM_e \\ &= g_e R_e^2 \\ &= 398,601 \text{ km}^3/\text{sec}^2\end{aligned}$$

G = universal constant of gravity

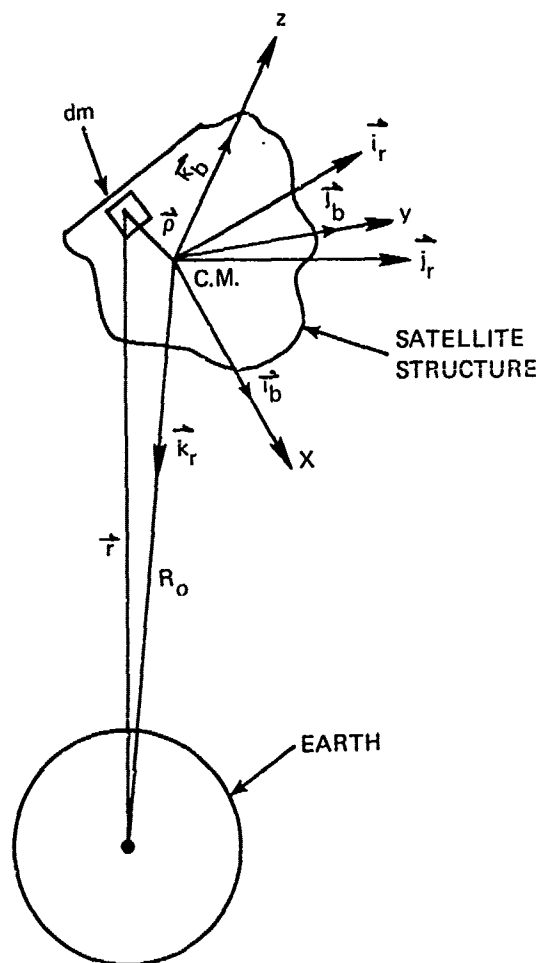


Figure 3-13. Reference and body axes for a body in a circular orbit about the earth.

M_e = mass of earth

g_e = gravity acceleration at earth's surface

R_e = radius of earth

This causes a torque dL about the mass center of the vehicle

$$d\vec{L} = \vec{r} \times d\vec{F} = - \frac{\mu dm}{r^3} (\vec{r} \times \vec{r}) \quad (3-5)$$

Great simplifications of the equations are obtained because the origin of the body axes coincide with the center of mass. Further simplifications can be gained if these same axes are the principal axes of inertia. With these assumptions some algebraic manipulations lead to the final result for the gravitational torques in scalar form:

$$L_x = \frac{3\mu}{2R_o^3} (I_z - I_y) \sin 2\phi \cos^2 \theta \quad (3-6)$$

$$L_y = \frac{3\mu}{2R_o^3} (I_z - I_x) \sin 2\theta \cos \phi \quad (3-7)$$

$$L_z = \frac{3\mu}{2R_o^3} (I_x - I_y) \sin 2\theta \sin \phi \quad (3-8)$$

Here

$$I_x = \int (y^2 + z^2) dm, \text{ etc.}$$

and the product-of-inertia terms

$$I_{xy} = \int xy dm$$

are zero, since the principal axes of inertia are chosen to coincide with the body axes. Note that in the expression of the torques, only two Euler angles (θ , ϕ) appear, because the third angle ψ , a rotation about the \vec{k}_r vector has no effect on the gravitational force on a mass element dm .

3.5.3 MMW Antenna: Gravity-Gradient Torques

The MMW antenna is an earth pointing spacecraft on an assumed circular orbit at an altitude of 500 km. Because of its asymmetric configuration and due to its orientation, the satellite principal axes of inertia do not coincide with the reference coordinate system of the orbit. By inspection of the equations (3-6), (3-7), and (3-8) derived above, it is clear that gravity-gradient torques will therefore be present. Figure 3-14 indicates the relative orientation of the two systems of axes and the orbit parameters needed for the evali-

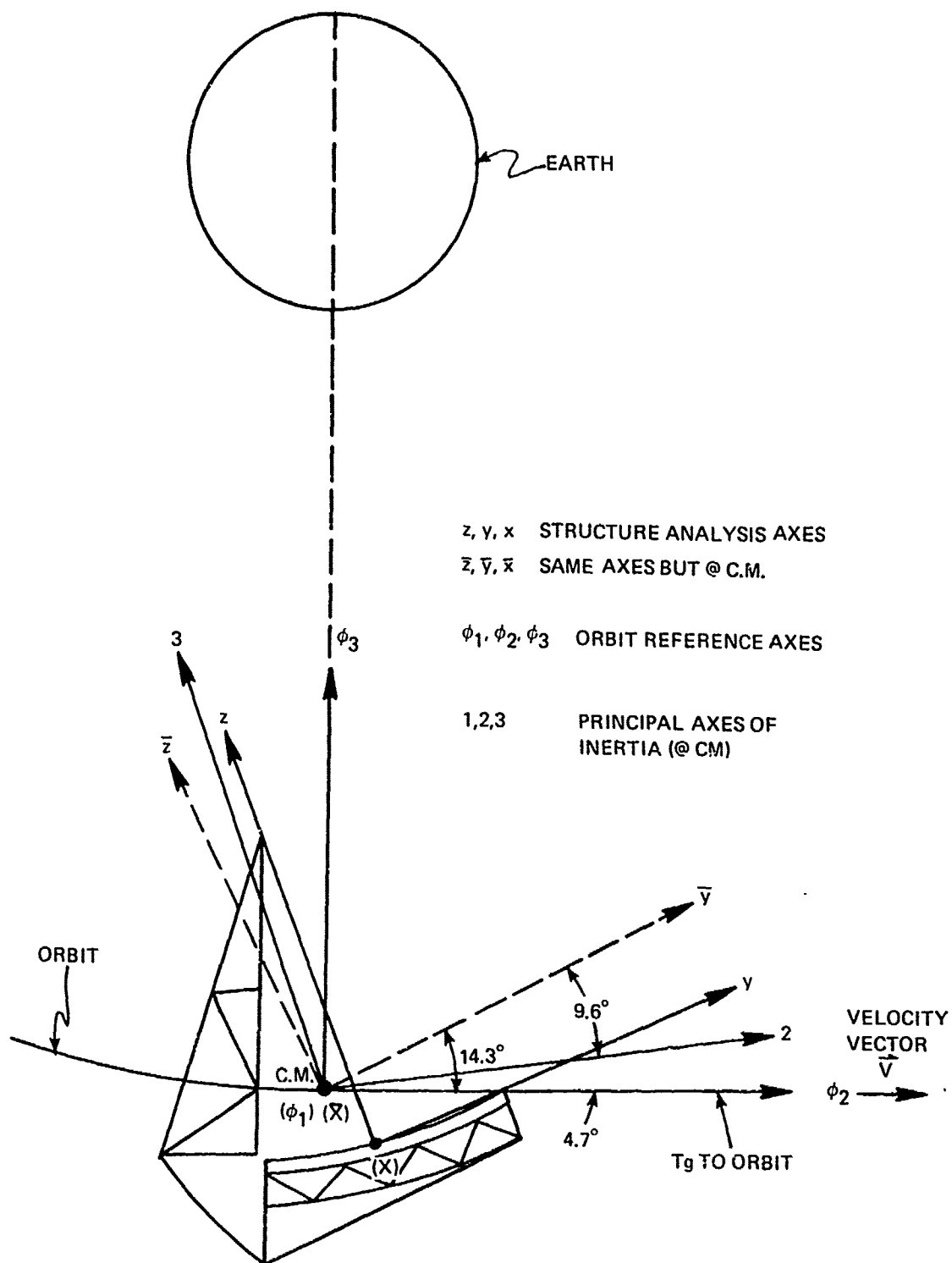
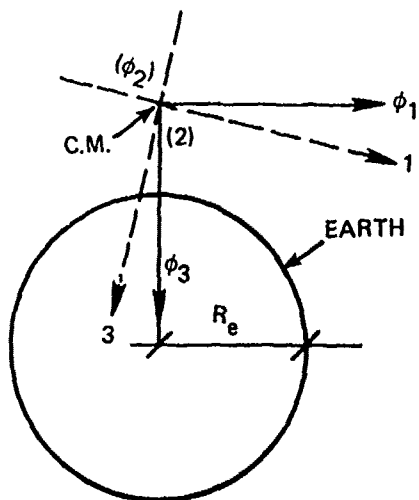


Figure 3-14a. Definition of satellite axes for gravity-gradient torque evaluation.



- ORBIT REFERENCE AXES $\hat{i}_r, \hat{j}_r, \hat{k}_r$ UNIT VECTOR TRIAD
- SATELLITE BODY AXES $\hat{i}_b, \hat{j}_b, \hat{k}_b$ UNIT VECTOR TRIAD
- RELATIVE ORIENTATION $\phi = -4.7^\circ$
 $\theta = 0$
 $\psi = 0$
- I_1, I_2, I_3 SATELLITE PRINCIPAL MASS MOMENTS OF INERTIA

$$T_1 = \frac{3K}{2R^3} (I_3 - I_2) \sin 2\phi \cos^2 \theta$$

$$T_2 = \frac{3K}{2R^3} (I_3 - I_1) \sin 2\theta \cos \phi$$

$$T_3 = \frac{3K}{2R^3} (I_1 - I_2) \sin 2\theta \sin \phi$$

$$R = R_e + h$$

$$= 6378 + 500 = 6878 \text{ km}$$

$$K = 398,601 \text{ km}^3/\text{s}^2 (\equiv \mu \text{ IN TEXT})$$

$$\text{ORBITAL PERIOD } T = 94.6 \text{ min}$$

STEADY STATE TORQUE $T_1 = 0.14 \text{ n-m}$

INCREMENTAL TORQUES FOR PEAK ATTITUDE TOLERANCE OF 2 mr

$$\Delta T_1 = 0.0034 \text{ n-m}$$

$$\Delta T_2 = 0.0015 \text{ n-m}$$

Figure 3-14b. Definition of satellite axes for gravity-gradient torque evaluation.

uation of the torques. Because of the orientation of reference and body axes, the Euler angle θ is equal to zero. As a result, the only gravity-gradient torque that remains is T_1 about the body x_b - axis (same as reference x_r - axis). This disturbing torque is called steady-state as opposed to incremental torques ΔT_1 and ΔT_2 that could be present in case another disturbance misaligns the body with respect to the reference axes. Incremental torques ΔT_1 and ΔT_2 have been estimated for a peak attitude tolerance of 2 mr. The torque T_3 is always zero.

3.6 Dynamic On-Board Disturbance

3.6.1 Disturbance Causes

The disturbances on board the MMW satellite include vibrating equipment such as a cryo-cooler, reaction forces from irregularities in the unbalanced pointing motions of communications antennas and reaction forces from attitude and orbit control systems. In this case both the attitude control and the orbit control are assumed to be done with thrusters. In order to determine if there can be a serious problem due to disturbances it is assumed that thrusters are not throttled, but are turned on and off abruptly. In this situation the thrusters are expected to produce much more disturbance than the other items mentioned above, so in the following only the thrusters are considered.

3.6.2 Summary of Thruster System Requirements

The thrusters are required to counteract the relatively steady drag force and attitude-disturbing torques caused by atmospheric drag, gravity gradient, and solar pressure. Since the only interest at this time is to roughly determine the disturbance which the thrusters cause in the course of maintaining the desired attitude and orbital altitude, no specific control law will be derived, and the requirements on the system will not be specified in any detail. Table 3-4 summarizes the major external disturbance forces and torques acting on the satellite. These have been estimated, as treated in other sections. In the presence of these disturbances the spacecraft attitude must be maintained to a tolerance of ± 2 mrad.

Table 3-4. External disturbance forces and torques

Cause	Drag Force	Torque
Atmospheric Drag		(Axis 1 normal to orbit plane)
Average Solar Activity		(Axis 2 along velocity vector)
Several-Day Average	0.0285 N	$T_1 = 0.0081$ N-m
Peak within an Orbit	0.0760 N	$T_1 = 0.0223$ N-m

Table 3-4 (cont.) External disturbance forces and torques

Cause	Drag Force	Torque
High Solar Activity		
Several-Day Average	0.105 N	$T_1 = 0.030 \text{ N-m}$
Peak within an Orbit	0.210 N	$T_1 = 0.0617 \text{ N-m}$
Solar Radiation Pressure		
Average over an Orbit	$\ll 0.007 \text{ N}$	
Peak within an Orbit	0.007 N	$\text{Max } T_1 = 0.017 \text{ N-m}$
Gravity-Gradient		
(limits shown apply for $ \epsilon_1 \text{ or } \epsilon_2 < 2\text{mrad}$)		$T_1 = 0.140 + 1.7\epsilon_1 =$ $0.140 \pm 0.0034 \text{ N-m}$ $T_2 = 5.8\epsilon_2 = \pm 0.0115 \text{ N-m}$

3.6.3 Control Rationales

The determination of thruster force magnitudes and locations depends on several satellite design decisions. As is shown in Table 3-4 the gravity-gradient torque has a comparatively large steady component tending to rotate the satellite in the orbit plane, due to the fact that, with the mass distribution assumed, the satellite's inertia ellipsoid is tilted in the orbit plane away from the local vertical. It might be practical to redistribute the masses and essentially eliminate the steady component of gravity-gradient torque, and in principle the first-order gradient torques could be made zero, or changed from destabilizing to stabilizing torques.

Similarly it might be possible to align the center of atmospheric drag with the center of gravity to reduce the torque due to the drag force. Neither of these possibilities has been explored at this point, so the results can be considered as conservative assessments. In any case, there is actually no direct propellant penalty for not balancing the torques, since by using single unbalanced thrusters rather than opposing-pair attitude thrusters all attitude control thrust for in-orbit-plane torques contributes to orbit altitude maintenance, which is necessary. (Some penalty can result from requiring a lower thrust level.)

With regard to maintenance of the orbit altitude, two options are possible, and these will be treated in the following two subsections. One is to quasi-continuously maintain the orbit throughout both the operating and non-operating parts of the orbit, using an on-off control of selected thrusters arranged in an array. The average thrust would be controlled to maintain the orbital altitude and the low desired eccentricity. The average point of application within the perimeter of the thruster array would be controlled to maintain the spacecraft within 2 m of the desired attitude.

The other option is to do intermittent orbit corrections, which would be needed every three to ten days according to the estimated orbit decay rate and altitude tolerance. Presumably these corrections could be done in the parts of the orbit when the system is not operating so the disturbance to the antenna structure would not degrade system performance. The attitude control could be done with smaller thrusters, thus causing less disturbance than in the quasi-continuous option.

Both of these options are treated in a very simplified way in the two following subsections, the purpose being to roughly characterize the structure disturbances rather than design the reaction control system.

3.6.4 Quasi-Continuous Orbit Maintenance

As seen in Table 3-5 the average thrust required for orbit maintenance varies from 0.015 N for HSA (high solar activity) to 0.0285 N for ASA (average solar activity) and to much lower values for low solar activity conditions. To properly choose the thruster magnitudes and locations such that, with the above average thrust, the average line of application is located so as to produce the torque needed to control attitude, requires appropriate information of the variabilities of the various forces and torques on the spacecraft. Since the gravity-gradient torque (assumed not to be balanced, as noted previously) is the largest torque component, variation of drag requires that both the magnitude and the point of application of the average thrust be changed. This close coupling between attitude control and orbit control does appear to be quite undesirable, but nonetheless is considered in assessment of possible disturbances to the spacecraft.

The thrust calculations for the two cases noted above are tabulated as follows, assuming all torques are in the same direction.

Table 3-5. Thrust displacement for attitude control

	High Solar Activity	Average Solar Activity
Average thrust over several orbits	0.105 N	0.0285 N
Required Torque		
Atmospheric drag	0.0617	0.0223
Components		
Solar Radiation	0.017	0.017
Gravity Gradient	<u>0.1434</u>	<u>0.1434</u>
Total Torque	0.222 Nm	0.183 Nm
Required displacement from c.g.	$\frac{0.222}{0.105} = 2.1\text{m}$	$\frac{0.183}{0.0285} = 6.4\text{m}$

This gives some idea of the thruster magnitudes and the distance over which the average thrust line must be able to be moved by varying the duty cycle of the several thrusters. Possibly a pair of 0.2 N thrusters located about 2m from the c.g. plus lower thrust units at larger distances above and below the c.g. would be typical design results. Pairs would be spaced laterally for yaw control. For the present purposes it is enough to conclude that

the turning on or off of a thrust of 0.4 N is a reasonable estimate of the disturbance.

The next question is how often such a disturbance may occur. Considering a time interval in which the thrusters are all off, if we assume a to and from excursion $\Delta\theta = 1\text{mr}$ is executed with a torque $T = 0.2\text{ Nm}$ (see Table 3-5) the total time would be

$$t = 2\sqrt{\frac{2\Delta\theta I}{T}} = 2\sqrt{\frac{2(0.001) 1.154 \times 10^6}{0.2}} = 215\text{ sec}$$

If the torque exerted by the thrusters is double the externally applied torque, the thrust duration would be equal to the off time given above. Actually there will be additional transients due to the requirements to control the other spacecraft axes (which have much smaller external torques), but more importantly, it may not be practical to allow $\Delta\theta$ to be so large, allowing for sensor errors and suitable performance margins. Also, if the thrusters torque is rather larger than the externally applied torque, the on time will be proportionately less. In conclusion, it appears that a disturbance model should be the turn-on or turn-off of 0.4 N of thrust at about one minute intervals.

3.6.5 Intermittent Orbit Maintenance

In this case the orbit maintenance burns are done intermittently at three to ten day intervals, during times when the satellite is not required to be operating as a sensor. Therefore the disturbance peak is of no concern, and only has to decay sufficiently before the system must again be operational. The attitude control thrusters can then be placed at a maximum distance from the c.g. so the force levels can be reduced. Using the same external torque values as before, and a thruster torque of double that, if the thruster is placed at the antenna feed (level arm of about 25 meters) the force required is

$$F = \frac{0.4\text{ Nm}}{25\text{ m}} = 0.016\text{ N}$$

This is an order-of-magnitude less, and the time between transients could be the same, about one minute.

To get an idea of the magnitude of thruster required for orbit maintenance, if the drag of 0.105 N over a three day interval is compensated by two burns, each occupying 10 degrees of orbital motion and spaced by 180 degrees around the orbit, the thrust required is given by

$$T = (0.105\text{ N}) \frac{(3\text{ days} \times 24 \times 3600)}{\frac{20^\circ}{360^\circ} \times 95\text{ minutes} \times 60} = 36\text{ N}$$

where the orbital period is 95 minutes. Clearly there is considerable freedom in the choice of such parameters.

Incidentally, the propellant required for orbit maintenance at 500 km altitude is appreciable. The average drag of 0.0285 N implies a loss of about 510 m/sec velocity for a spacecraft of 8800 kg over a year life. For a

specific impulse of 260* sec this means a propellant mass given by

$$m = 8800 \left(e^{\frac{510}{260 \times 9.8}} - 1 \right) = 1950 \text{ kg}$$

It would therefore be of interest to consider raising the orbital altitudes somewhat.

3.6.6 Summary

The specific disturbance values given in the preceding sections are provided for use in an exploratory assessment, and are not to be considered as firm values. As has been noted, the balancing of gravity-gradient would greatly reduce the steady torque, and the torque due to atmospheric drag could also be largely balanced out. In addition, an increase in the orbital altitude would save propellant mass and reduce the drag torque. If the result were to be that thruster disturbances were still inconveniently large, reaction wheel control could be considered with momentum dumping either by small thrusters or by active balancing of the external torques.

*Typical of shuttle vernier RCS engine, at 26 lb thrust.

SECTION 4

STRUCTURAL MODEL AND ANALYSIS

4.1 Introduction and Approach

The approach to the mathematical model of the MMW structure was influenced by both the need for a proper structural representation and the requirements imposed by the evaluation method of antenna performance. It was the intent here to incorporate into the model all those structural characteristics that could significantly affect the antenna behavior. Another driving requirement for this model was the need to represent the reflector surface by a large number of information points. In terms of the mathematical model, such a requirement rapidly increases the size of the system matrices, to a point where the solution becomes both susceptible to errors and abnormally costly. This conflict was easily circumvented by a substructuring approach used in both the static and the dynamic analyses. Since the antenna structure consists of a main assembly supporting 124 panels, identical in the geometry and structural characteristics, a substructuring technique was even more desirable. Once the accuracy problems inherent to the uncoupling procedures have been assessed, the antenna analysis can be reduced to the analysis of two basic structures: (a) a typical panel and (b) the back-up trusses/receiver tower assembly. Although the combination of the distortions of the individual components require additional computation, these calculations are relatively easy since they are simple geometrical manipulations.

The response calculation to the quasi-static loading is deemed "exact". The panels being supported on three kinematic mounts, it is legitimate to uncouple them structurally from the underlying back-up trusses. In the dynamic analyses, however, the same approach leads to some error in the evaluation of the elastic distortions. This error, however, can be satisfactorily reduced if the dynamic characteristics of the panels are such that they can minimize the dynamic coupling. To this end, the design of the panel was concerned with imparting adequate bending stiffness to the structure in order to achieve a specified lowest frequency of approximately 30 Hz. Since the back-up structure will exhibit most of its significant natural frequencies below the panel's fundamental frequency, the strong interaction between these structures is limited to the higher frequencies of the trusses. The corresponding mode shapes, although excited, show significantly smaller amplitudes and are expected to be of negligible consequence.

This section, therefore, describes two structural models. The back-up trusses and the tower represent the first model for which a modal analysis uncovers their dynamic characteristics. The second model is a representation of the typical hexagonal reflector panel. The natural frequencies and mode shapes are presented for three different panel constructions, thus permitting trade-offs for the most desirable selection. The evaluation of the structural responses is presented in Section 5.

4.2 Model Description of Trusses/Tower Assembly

4.2.1 Mathematical Model

The main structure of the MMW antenna includes a grid of trusses forming a spherical surface and a tapered tower frame supporting the receiver array. The mathematical model used is a faithful representation of the actual structure, as evidenced by the large size of the stiffness matrix. However, to keep the number of degrees-of-freedom (DOF) to a reasonable level, the large platform was modelled with axial members whereby only three DOF's are present at each joint. Although the truss member connections usually exhibit good bending capability, this simplification is legitimate since the axial load path is overwhelming in the truss configurations. For the tower, however, frame members were used to insure stability of some joints. The distributed mass from the reflector panels were lumped at only 34 surface joints so that the dynamic problem remained at a tolerable size. While there are 1131 DOF's in the stiffness matrix K , the total number of entries along the diagonal mass matrix M is limited to 141. It is useful to recall that an accurate representation of the elastic properties of a structure requires a more refined mathematical model than the representation of the inertia properties does. This is due to the fact that the inertia properties (or kinetic energy) depend directly on the displacements of the structure, whereas the stiffness properties (or strain energy) are functions of the derivatives of the displacements, and it is well known that the derivatives have larger components of error than the displacements themselves.

The geometrical description of the mathematical model is best understood by considering the plots shown on Figure 4-1. The presence of outriggers at the periphery and the minimum number of diagonal members result in reducing the system structural mass without impairing overall stability. The pattern selected for the orthogonal trusses (in projection) is such that the inter-sections offer hard-points to accept the three kinematic mounts for each reflector panel. The 1.5m deep trusses have a mass of 1 kg/m^2 including an allowance of 0.1 kg/m^2 for the thermal blanket, while the applied mass from the hexagonal graphite-epoxy panels amount to 4 kg/m^2 .

Because of the preliminary nature of this study, only two different member cross-sections have been used in this model: (a) an open thin-wall section for all the truss members and (b) a thin-wall tube for the tower frame elements. The geometry of these cross-sections, the material used and the various dynamic and stability characteristics of the individual members are summarized on Table 4-1.

The tower member lengths range from 5 m to 15 m with most of the members at about 10 m. In this design the thin-wall tube with 10 cm diameter produced a relatively low fundamental frequency of 11.4 Hz for a 10 m long member. The effects of the vibrations of single members in the tower structure are difficult to anticipate at this point, however, it is always possible to use a larger cross-section, or provide intermediate bracing points if this low level of natural frequency becomes a problem. Table 4-1 compares the merits of two

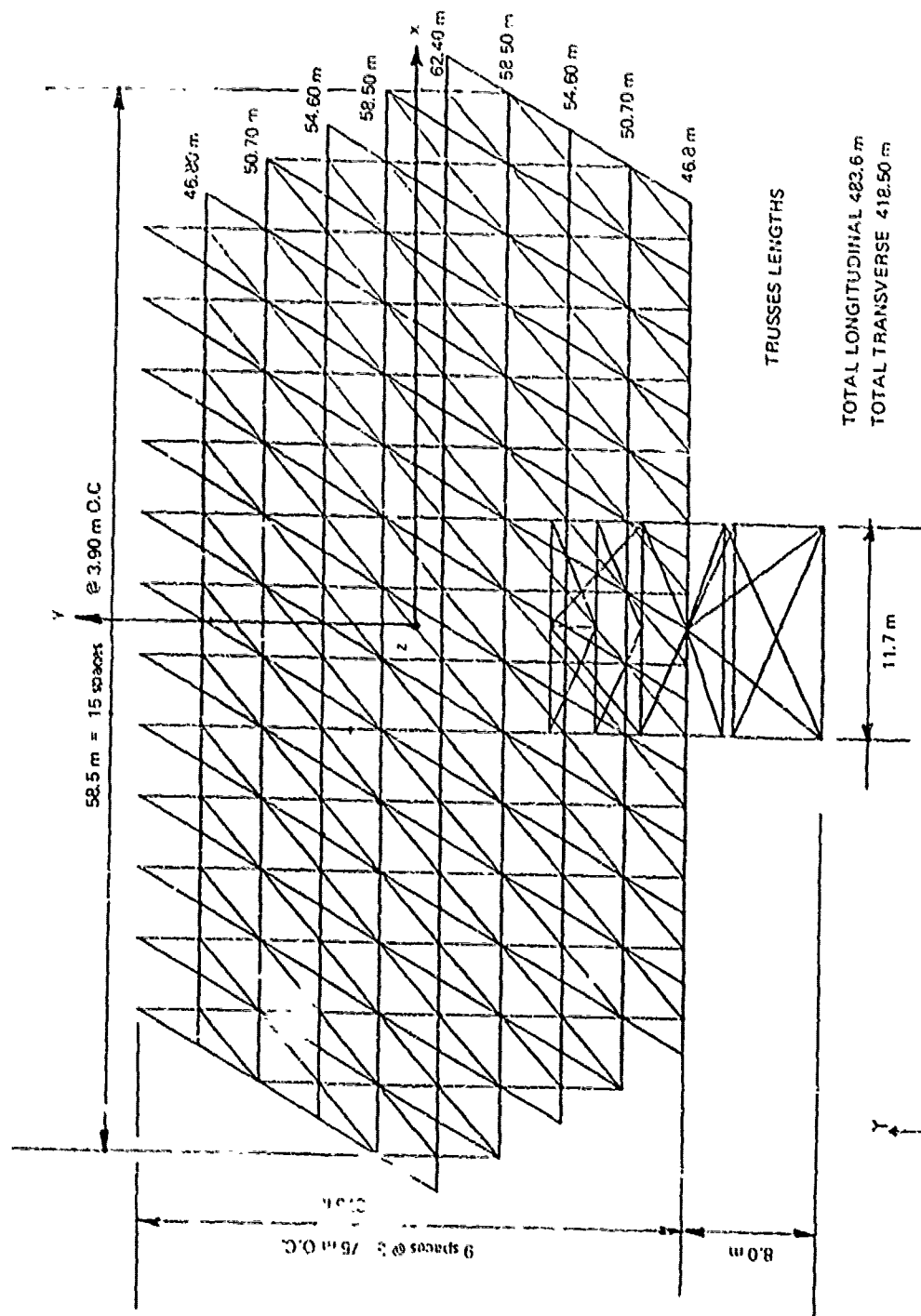


Figure 4-1a. MW antenna mathematical model.

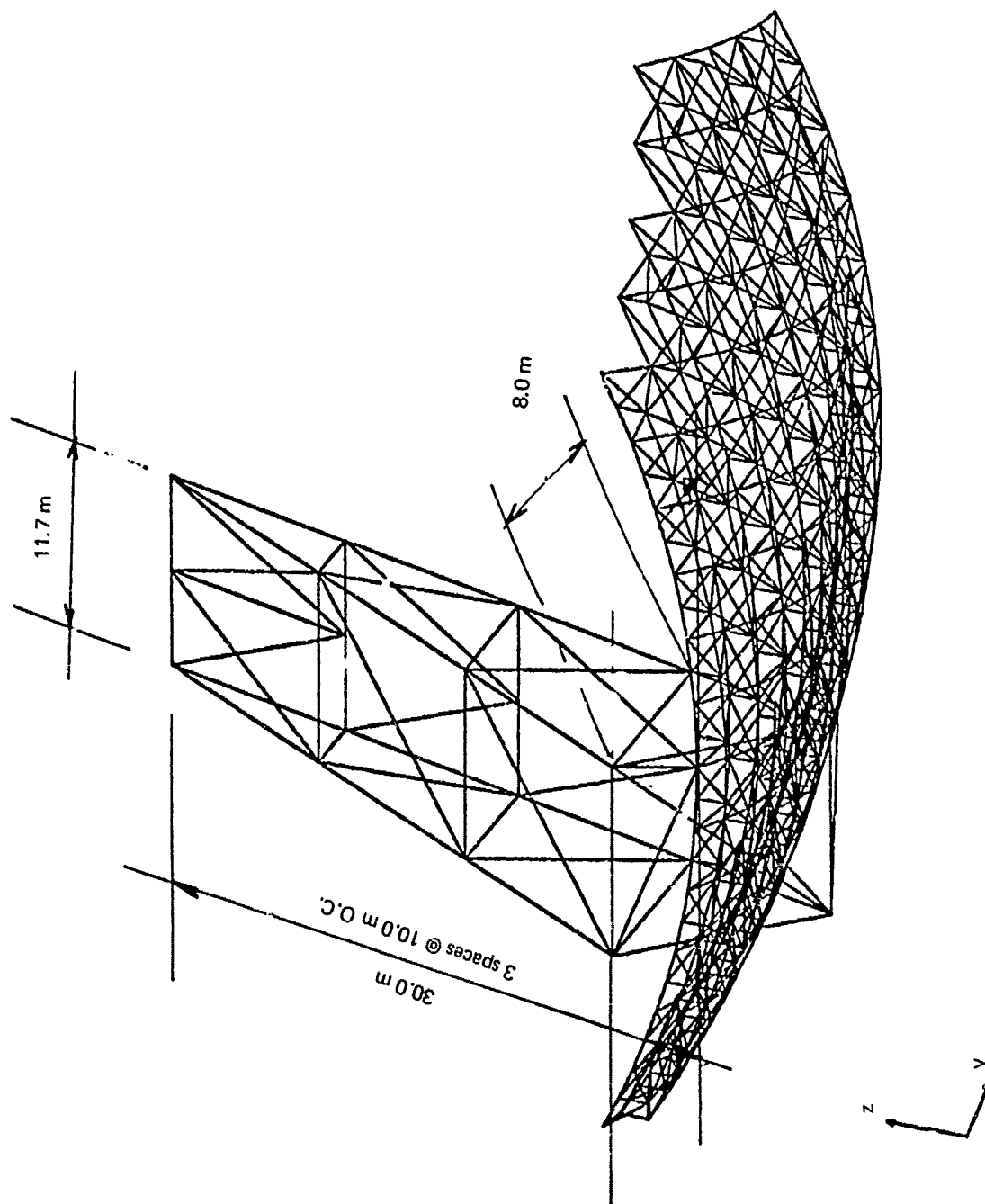
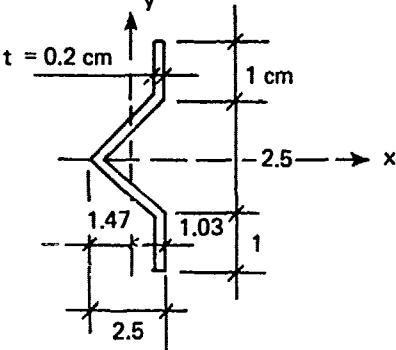
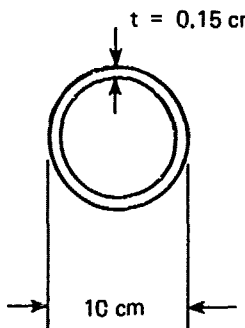
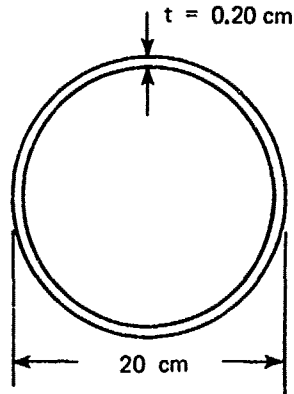


Figure 4-1b. MMW antenna mathematical model.

Table 4-1. Cross-Sectional Properties and Member Characteristics

TRUSS MEMBERS		
<ul style="list-style-type: none"> MATERIAL GRAPHITE-EPOXY 	$E = 14 \times 10^{10} \text{ N/m}^2$ $w = 0.32 \text{ kg/m'}$	
		$A = 1.86 \text{ cm}^2$ $I_x = I_1 = 3.74 \text{ cm}^4$ $I_y = I_2 = 1.38 \text{ cm}^4$ $r_{\min} = r_2 = 0.862 \text{ cm}$
	MAXIMUM LENGTH $L = 5.16 \text{ m}$	
<ul style="list-style-type: none"> FUNDAMENTAL FREQUENCY OVERALL FLEXURAL BUCKLING FLEXURAL-TORSIONAL BUCKLING 		$f = 10.4 \text{ Hz}$ $P_{\text{cr}} = 2800 \text{ N}$ $P_{\text{cr}} = 4400 \text{ N}$
TOWER FRAME MEMBERS		
<ul style="list-style-type: none"> MATERIAL 	GRAPHITE-EPOXY	$E = 14 \times 10^{10} \text{ N/m}^2$
<ul style="list-style-type: none"> CROSS SECTION GEOMETRY 		
<ul style="list-style-type: none"> MAXIMUM MEMBER LENGTH = 15.4 m 		
<ul style="list-style-type: none"> CROSS-SECTIONAL PROPERTIES 	$w = 0.81 \text{ kg/m}$ $A = 4.71 \text{ cm}^2$ $I = 58.9 \text{ cm}^4$ $J = 117.8 \text{ cm}^4$ $r = 3.53 \text{ cm}$	$w = 2.16 \text{ kg/m}$ $A = 12.57 \text{ cm}^2$ $I = 628 \text{ cm}^4$ $J = 1256 \text{ cm}^4$ $r = 7.07 \text{ cm}$
<ul style="list-style-type: none"> FUNDAMENTAL FREQUENCY 	$f = 4.8 \text{ Hz}$	$f = 9.6 \text{ Hz}$
<ul style="list-style-type: none"> FLEXURAL BUCKLING 	$P_{\text{cr}} = 1360 \text{ N}$	$P_{\text{cr}} = 14500 \text{ N}$

tube cross-sections for the maximum member length of 15.4 (tower diagonal diagonal length $(10^2 + 11.7^2)^{1/2} = 15.4$ m.) Note that the tower support members extending below the reflector are even longer in this model, but in reality, they will be braced.

Graphite-epoxy composite was used for all the structural members. The excellent E/ρ ratio (E = modulus of elasticity, ρ = density) coupled with a very low coefficient of thermal expansion have made it a prime candidate for space applications. These desirable characteristics are evidenced when compared to those of other possible candidates are shown in Table 4-2.

4.2.2 Modal Analysis

The mathematical model of the overall MMW antenna structure containing 141 dynamic DOF's (47 times 3 translational masses) was analyzed as a free-free structure. The results of the modal analysis show frequencies ranging from 0.89 Hz to 136 Hz with 60 elastic modes having frequencies below 25 Hz. Since it is realized that the reliability of the results in the higher modes is questionable due to the limitation of the modeling, the first 60 modes (non-rigid body modes below 25 Hz) were used in evaluating both transient and steady-state responses. This deletion is further substantiated by the natural expectation that the higher modes are less significant in response calculation. Table 4-3 describes the nature of the mode shapes associated with the first 10 elastic modes. The plots of some mode shapes shown in Figure 4-2 (a) to (i) can be quite useful to anticipate the seriousness of performance degradation associated with a particular mode. Finally, it should be noted that the natural frequencies of the system are uniformly distributed and that, for this reason, the tuning of a mechanical disturbance to avoid resonance appears nearly impossible.

Table 4-2. Characteristics of other possible material candidates

Material	$E \times 10^{10}$ (n/m ²)	ρ ($\times 10^3$) kg/m ³	E/ρ ($\times 10^6$) m	ν	α ($\times 10^{-6}$) m/m/°K
Aluminum	7.2	2.77	2.7	0.33	23.0
Beryllium	30.3	1.83	16.9	0.025	12.0
Graphite-Epoxy	13.8	1.72	8.2	0.3	0.2
Magnesium	4.5	1.83	2.5	0.35	26.0
Molybdenum	32.4	1.02	3.2	0.307	6.6
Titanium	11.0	4.6	2.4	0.34	7.5

MODE 7
FREQ = 0.891 HZ

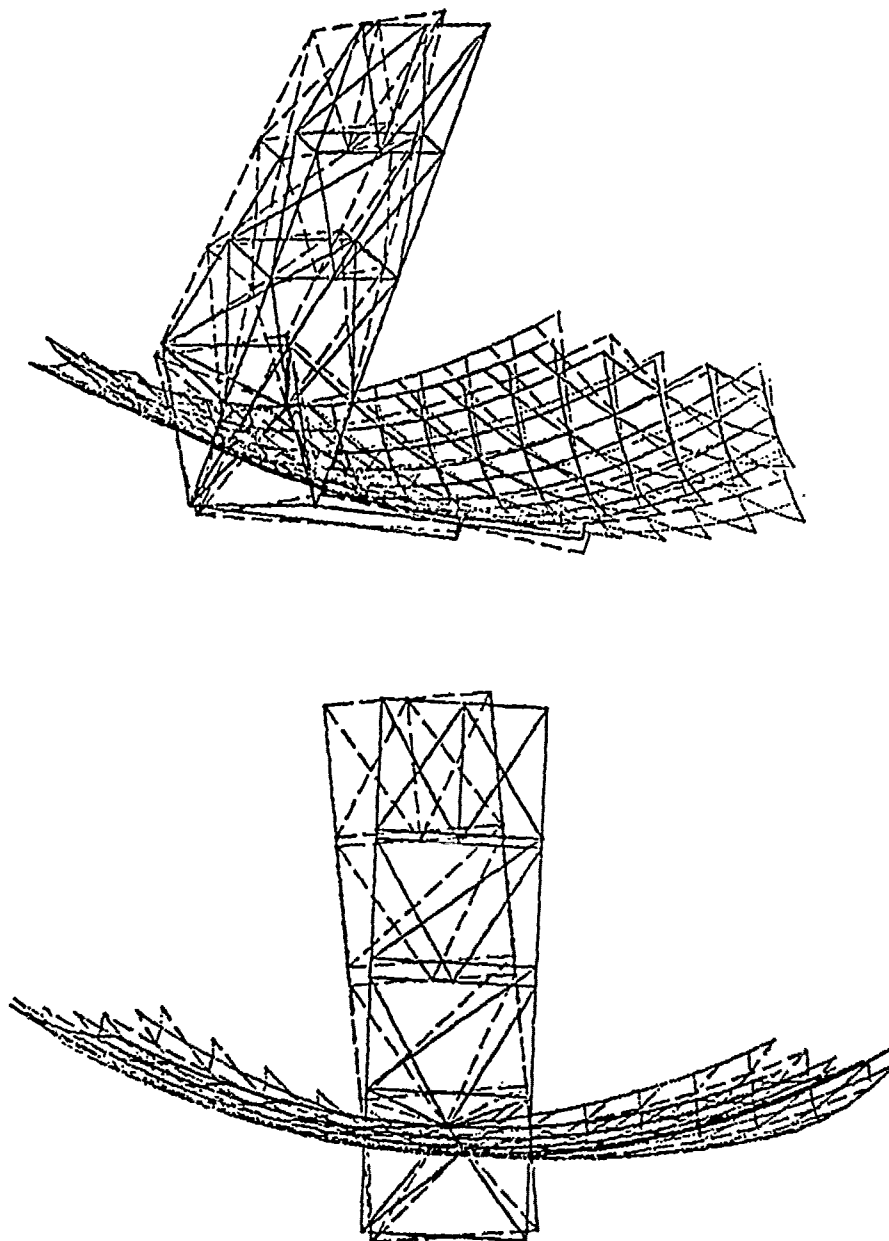


Figure 4-2a. Millimeter wave antenna.

MODE 8
FREQ = 1.453 HZ

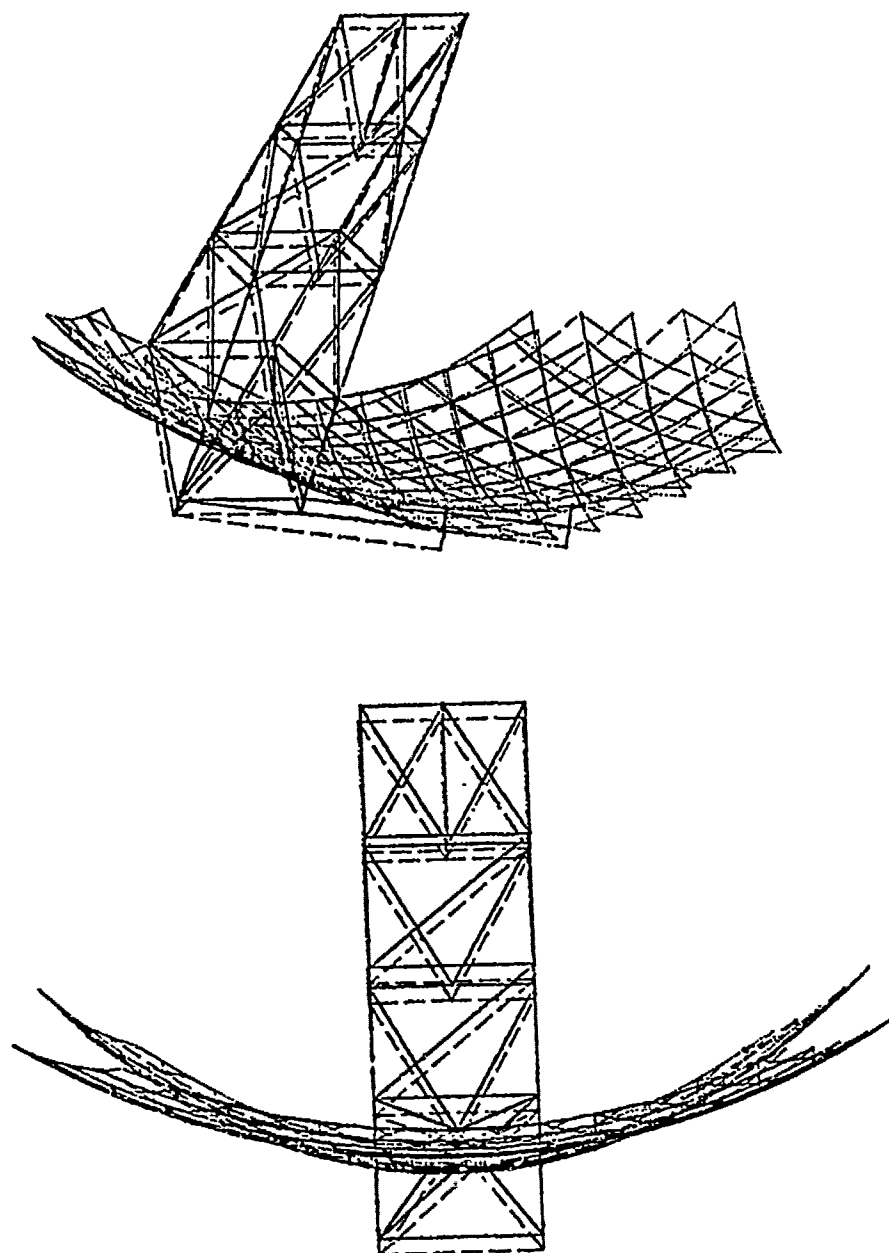


Figure 4-2b. Millimeter wave antenna.

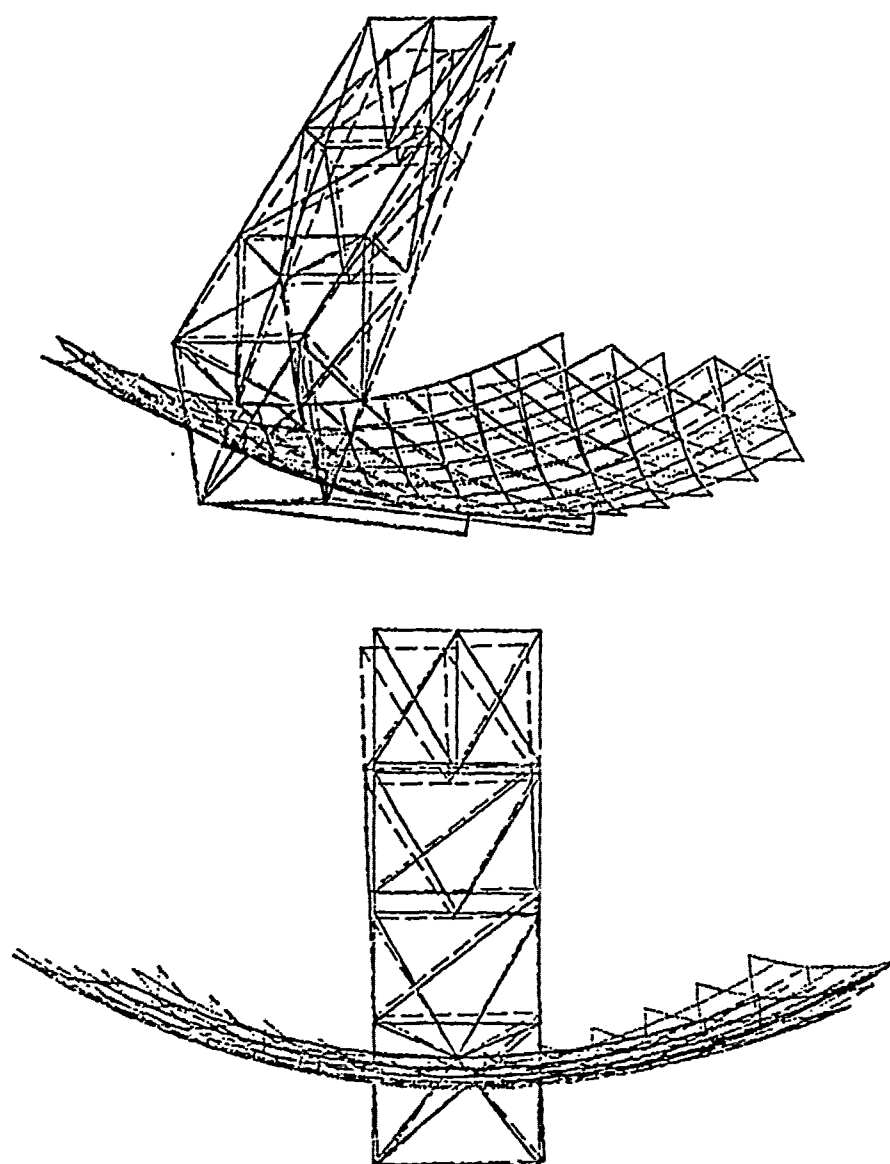


Figure 4-2c. Millimeter wave antenna.

MODE 10
FREQ = 1.819 HZ

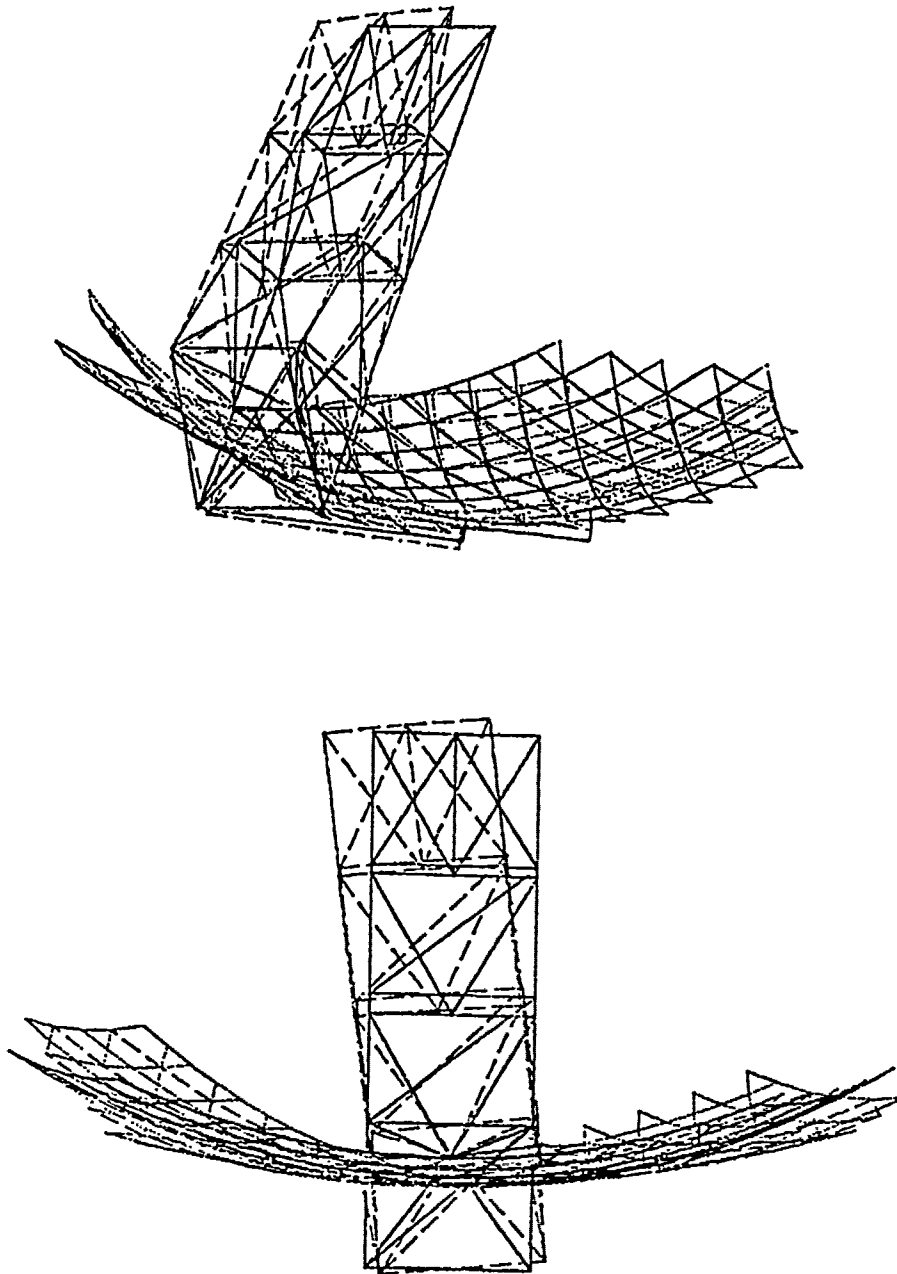


Figure 4-2d. Millimeter wave antenna.

MODE 11
FREQ = 2.702 HZ

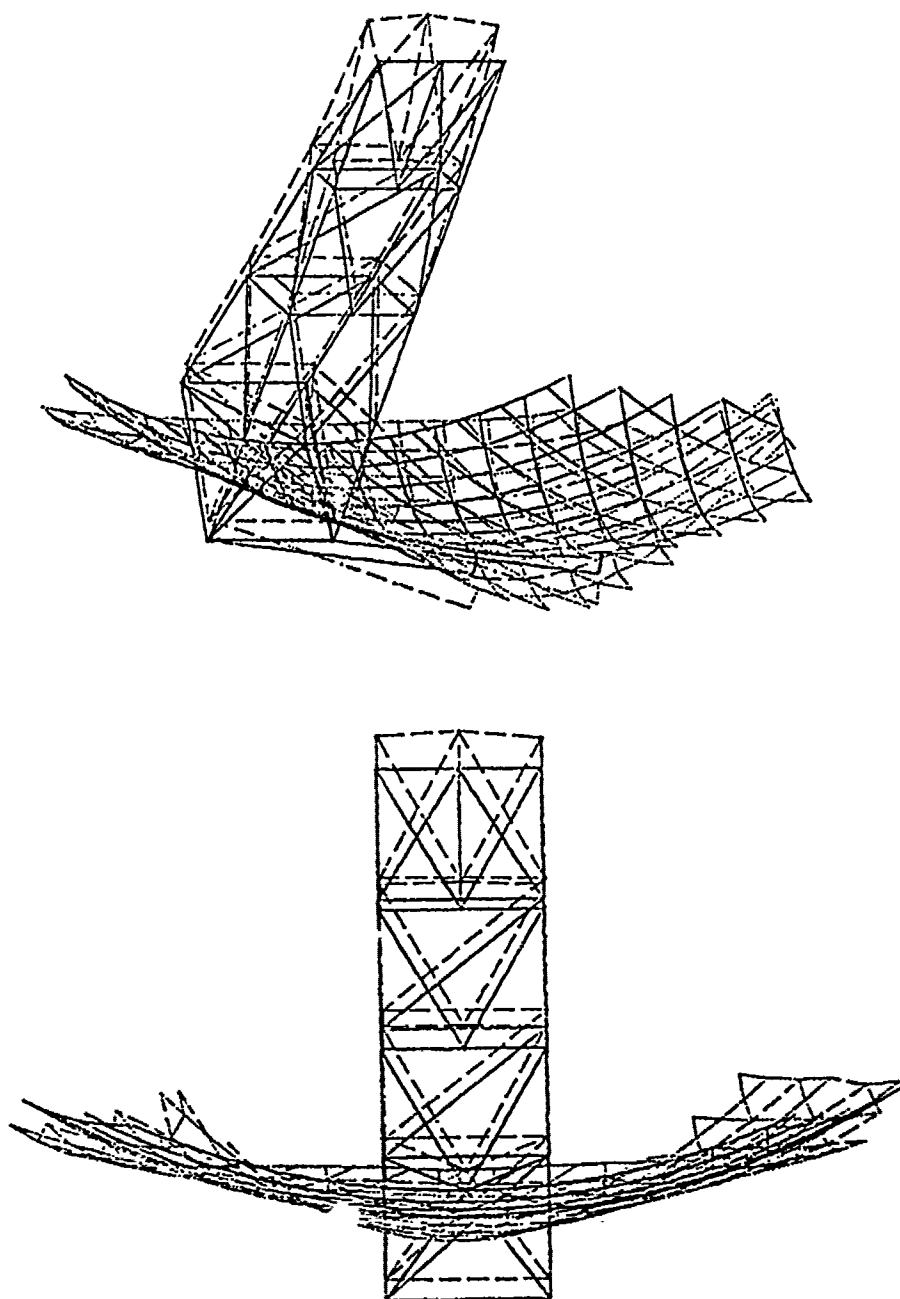


Figure 4-2e. Millimeter wave antenna.

MODE 12
FREQ = 3.448 HZ

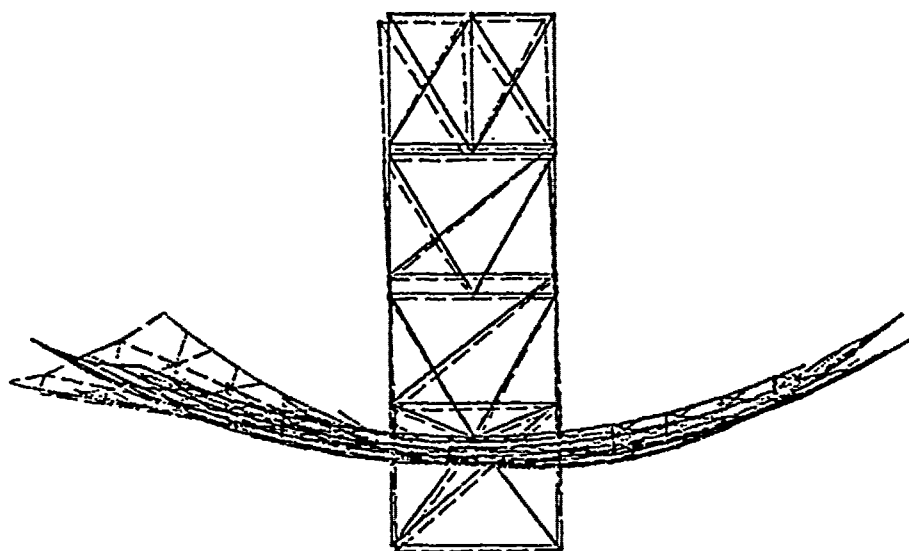
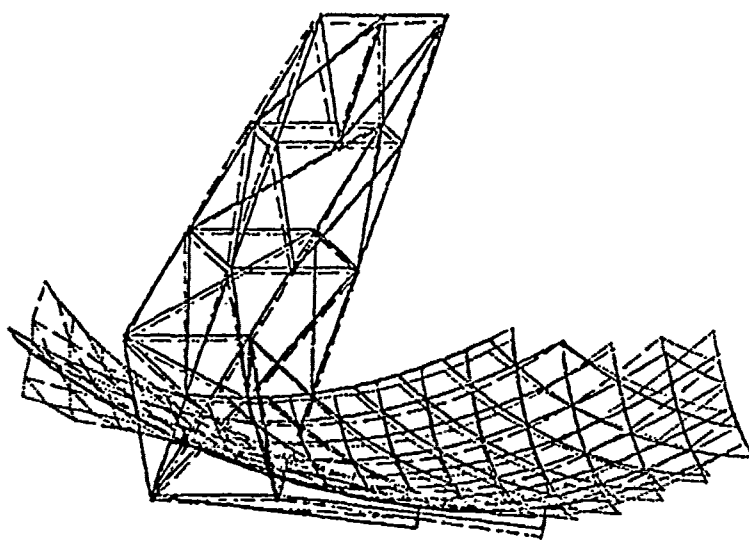


Figure 4-2f. Millimeter wave antenna.

MODE 13
FREQ = 4.165 HZ

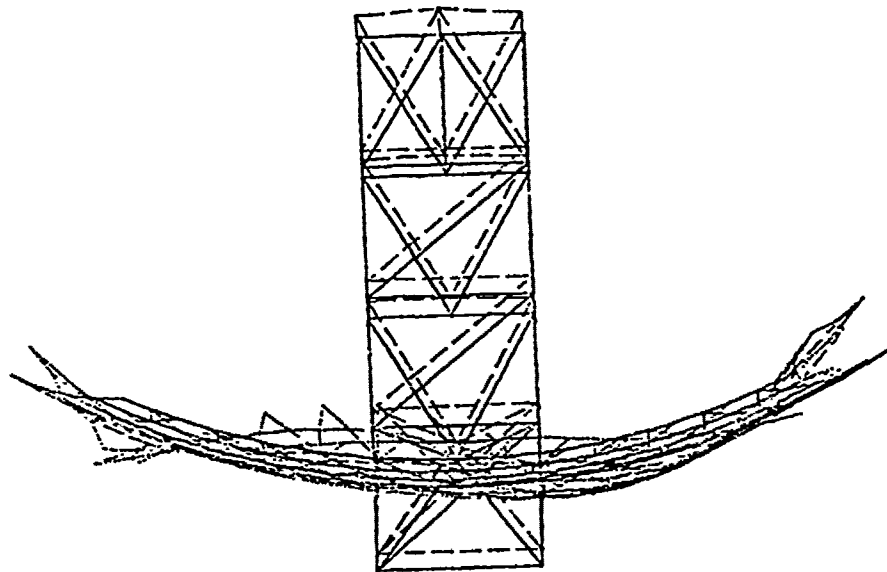
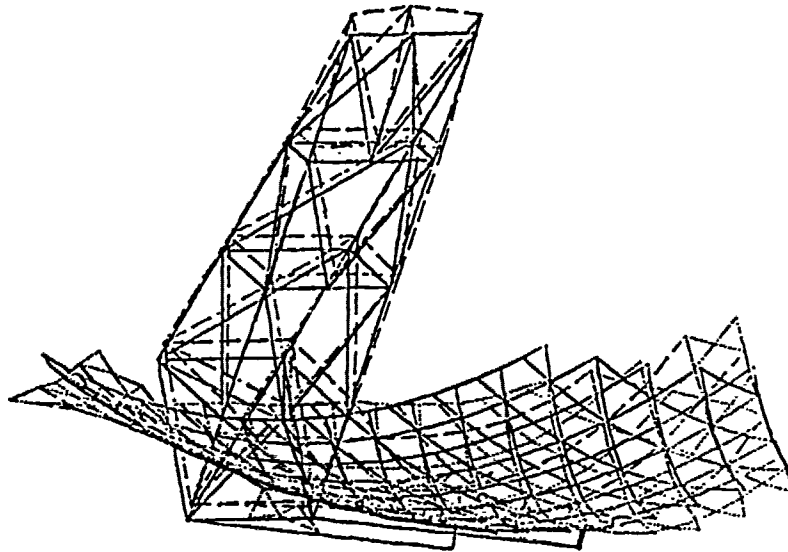


Figure 4-2g. Millimeter wave antenna.

MODE 14
FREQ = 4.865 HZ

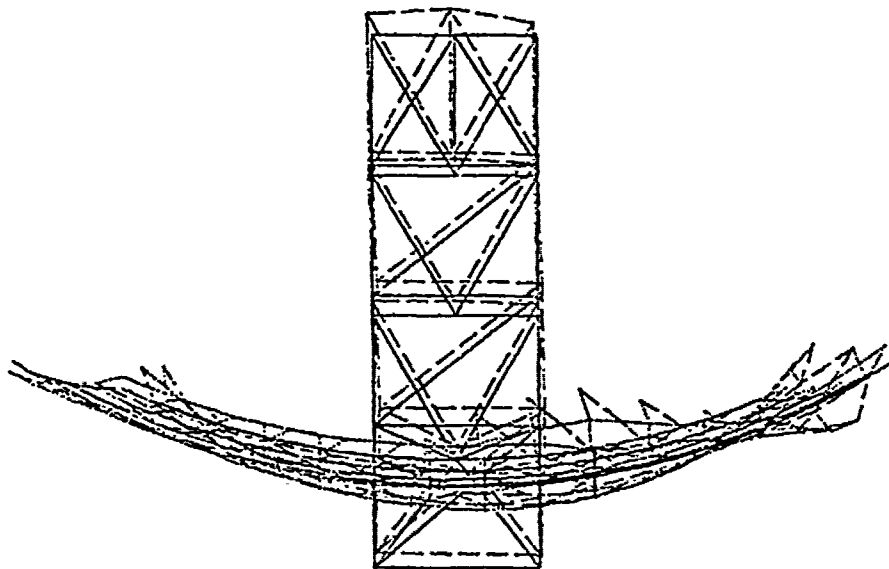
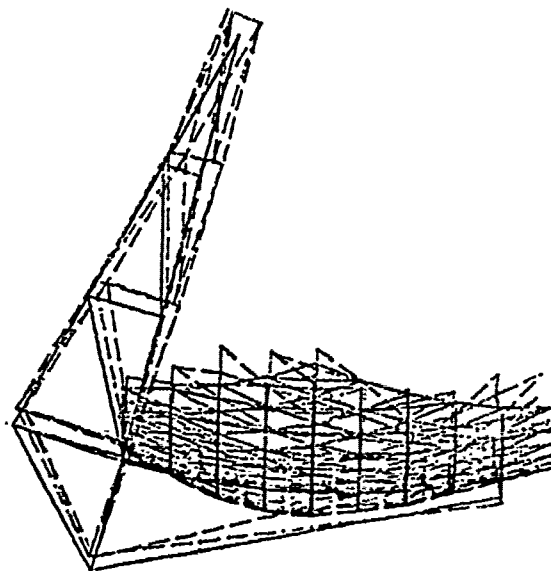


Figure 4-2h. Millimeter wave antenna.

MODE 15
FREQ = 4.893 HZ

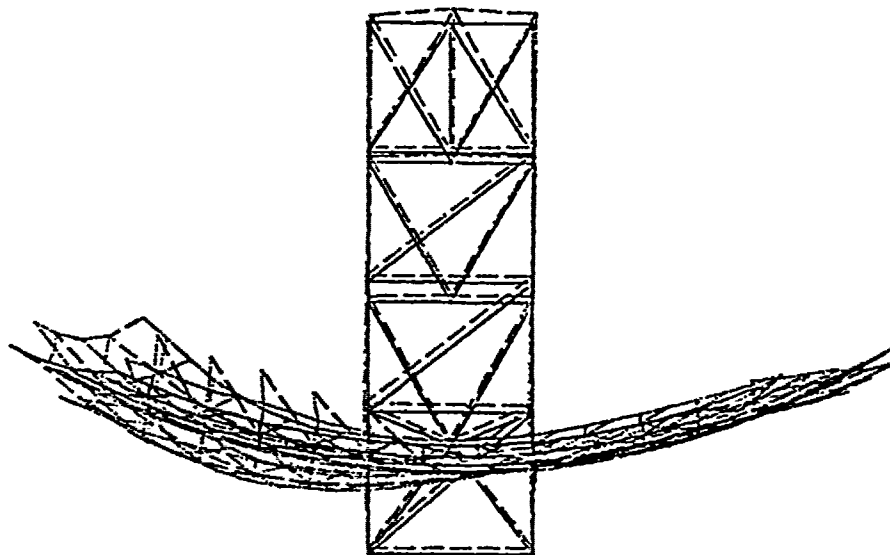
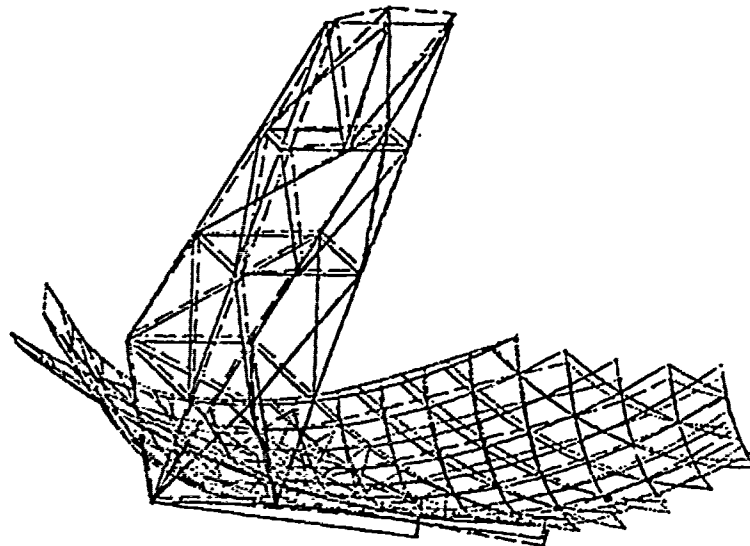


Figure 4-2i. Millimeter wave antenna.

The response calculation to dynamic disturbances were obtained through modal superposition in which a uniform modal damping ratio of 0.005 was assigned to each mode. These results are presented in Section 5.3.

The calculation of the structural responses to quasi-static disturbance such as the thermal loading was obtained by simple inversion of the stiffness matrix K. Before inverting the matrix however, it was necessary to support the structure in order for K to be positive definite. While the distortions of the structural joints are a function of the choice of the support, the arbitrary selection of supports is acceptable since only the relative displacements are of interest. Note that the supports must keep the structure statically determinate (externally). Results of quasi-static loadings are presented in Section 5.2.

Table 4-3. Natural frequencies and mode shapes (MMW)

Mode	Frequency HZ	Description
1-6	0	Rigid body modes
7	0.9	Asymmetric lateral surface bending Lateral tower bending 1st surface torsion mode
8	1.4	1st surface bending mode
9	1.7	1st feed support bending mode
10	1.8	Tower bending - surface twisting
11	2.7	Surface lateral bending
12	3.4	Asymmetric surface bending
13	4.2	Surface bending mode
14	4.9	Surface twist-tower bending and twisting
15	4.9	Asymmetric surface bending
16	5.7	Tower torsion mode

4.3 Panel Design and Analysis

4.3.1 Introduction

In the attempt to design an efficient reflector surface structure for the large area (about 1600 m²) of the MMW antenna, the designer is faced with many

interacting requirements. The selection of a concept is affected by the following driving parameters.

- (1) structural concept: rigid segment or inflatable
- (2) reflector weight and segment size
- (3) required surface accuracy
- (4) expected thermal and dynamic loadings
- (5) active or passive control of surface accuracy
- (6) exposure to adverse environment
- (7) packaging and deployment techniques

Trade-offs among these parameters should converge towards an adequate compromise.

This section deals with a segmented reflector concept, and considers trade-off studies among parameters such as weight, materials, thickness and fundamental frequency for a hexagonally shaped panel of pre-determined size. Three panel designs are presented: (a) a graphite-epoxy egg-crate structure, (b) a honeycomb aluminum sandwich construction and (c) an inflatable such as an air-mat sandwich structure using Dacron weave and drop threads. Since the graphite-epoxy panel appears to fulfill all the requirements, it was chosen to be the candidate for the MMW antenna. The other two concepts have shortcomings that additional study and design manipulations could possibly circumvent.

4.3.2 Hexagonal Panel Design

The choice of a segmented reflector concept appears appropriate for use of the large size of the reflector (approximately 30 m by 60 m) and the rather stringent requirements on the reflector surface accuracy (figure error standard deviation of 0.05 mm) to be maintained by a passive structure. The size of the segment is strongly dependent on the packaging technique whereby all segments must fit together in the most efficient manner in the space allocated by the shuttle cargo bay (cylindrical shape 18.28 m long by 4.57 m in diameter). The form or the shape of the segments must be such that, when assembled, they form a uniform reflector surface. Finally, from a manufacturing point-of-view, it is desirable to fabricate a large number of similar panels, thus improving cost-effectiveness. All these requirements combined to point toward the design of a hexagonal "rigid" panel with a 4.5 m maximum diametrical dimension. The thickness had to be limited to 6 cm so as to allow the back-to-back packaging of 124 panels within a 7.8 m length of the shuttle cargo. Geometrically, the hexagonal panels when deployed and assembled can form the desired surface of an elliptical-torus, and their spatial recurrence facilitates the choice of a pattern for the design of the underlying trusses. Because of these desirable characteristics, the hexagonal shape of the panel remained an invariant in the following trade-off studies. The ultimate choice was based on the merits of a particular material and structural concept responsible for the panel thermal and dynamic characteristics.

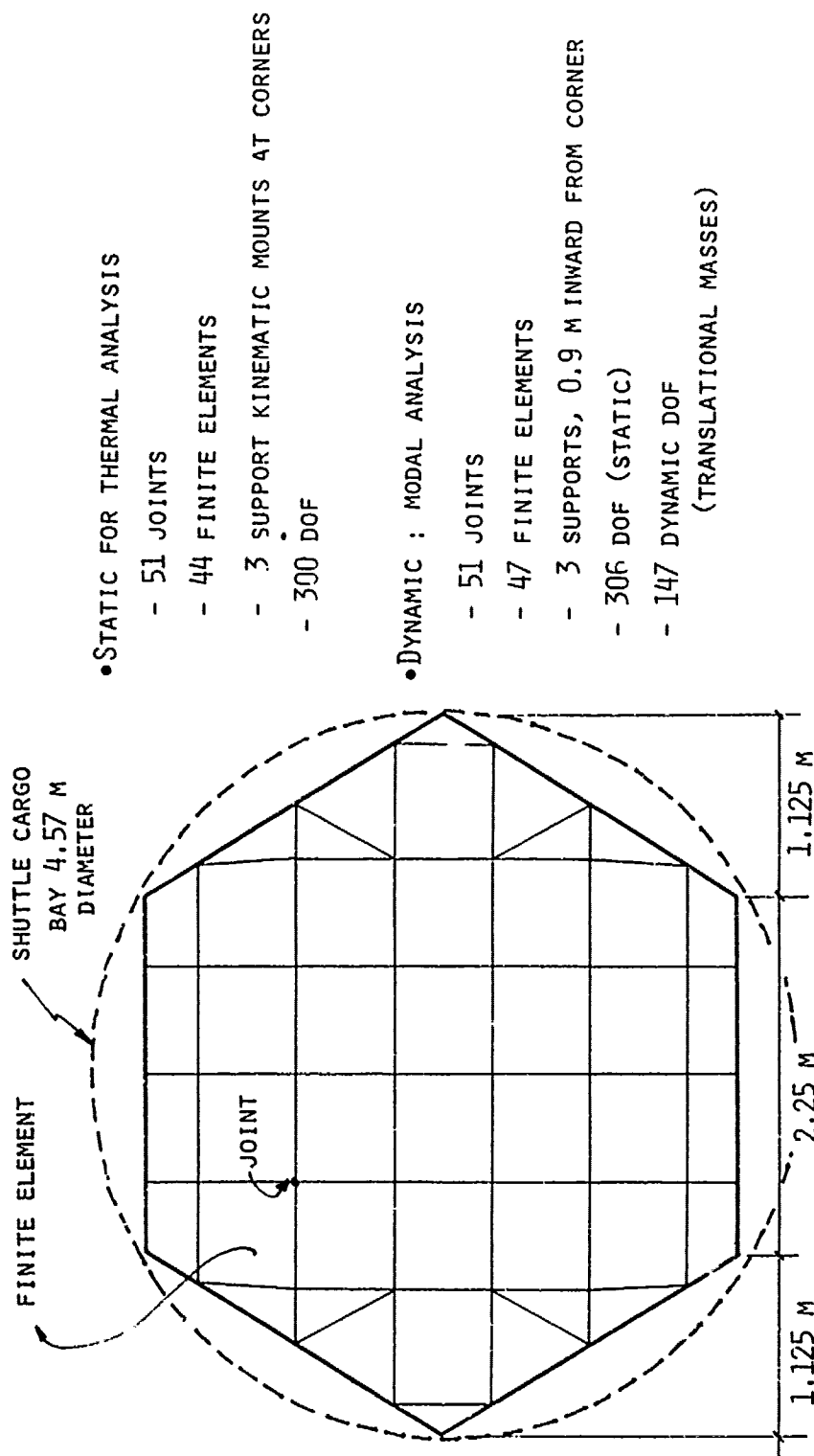
4.3.3 Mathematical Model and Analysis of the Hexagonal Panel

The hexagonal panel was analyzed as a plate represented by 44 finite elements (30 rectangular, 14 triangular elements). The selection of the structural joints was such that they coincide with optical grid points used in the antenna performance evaluation, thus circumventing costly interpolations. The model geometry and its characteristics are given in Figure 4-3. Although the underlying truss configuration offers support points for the "corners" of the hexagons, this choice of support is not optimum for the panel. In this study, the three kinematic mounts are located on radial lines, 0.9 m inward from the corners. This location was chosen because it is very close to the optimum support condition in terms of the high fundamental frequency. Three translational masses at each unrestrained DOF account for the 147 dynamic DOF's.

The mechanical properties of an equivalent plate have been calculated for the three design candidates. The same finite-element model can be used for the three panel construction once the bending and shear stiffness are known and the proper material properties are available. Table 4-4 summarizes the features of the 3 panel candidates and their respective plate stiffness. While the graphite-epoxy egg-crate and the aluminum honeycomb construction concepts are well understood, the inflatable airmat is somewhat unconventional. A brief description of this structural concept and its dominant characteristics is therefore, given below.

Packageability and automatic erectability make inflatable construction especially attractive for satellites and space stations. An example of inflated construction is an inflated fabric plate called Airmat. Airmat, which was developed by Goodyear Aircraft Corporation, consists of two covers of coated, woven material connected by closely spaced flexible fibers called drop cords (or drop threads). The airmat takes on its predetermined configuration as a result of the internal pressure. A theory for the structural analysis of inflatable fabric plates has been developed to provide information on their load-carrying capabilities and structural characteristics. Static tests as well as vibration tests have been performed on inflatable fabric plates in order to assess the validity of the theory. The design of the hexagonal panel using the airmat construction is based on typical values for the choice of airmat geometry, woven material, drop cords and pressure levels. As evidenced by comparing the plate stiffness in Table 4-4, the 12 cm deep airmat exhibits an adequate bending stiffness, but has a very low carrying capability in shear. Since the shear stiffness is proportional to the internal pressure p , an increase in pressure seems reasonable. However, such a move is limited by the amplitude of the surface ripples that could be caused by the deflection of the face sheet between the point supports provided by the drop-threads. A reasonable compromise is therefore needed. Table 4-4 lists the various airmat parameters used in the proposed panel design.

The results of the finite-element model analysis are summarized in Table 4-5. A modal analysis run for each candidate revealed their dynamic characteristics with a list of the first eight natural frequencies. An estimate of their thermal behaviour was obtained on the basis of the thermal model developed in Section 3.2 for the graphite-epoxy panel. Through extrapolations, the maximum thermal gradient ΔT_G in the aluminum honeycomb and the airmat have



•STATIC FOR THERMAL ANALYSIS

- 51 JOINTS
- 44 FINITE ELEMENTS
- 3 SUPPORT KINEMATIC MOUNTS AT CORNERS
- 300 DOF

•DYNAMIC : MODAL ANALYSIS

- 51 JOINTS
- 47 FINITE ELEMENTS
- 3 SUPPORTS, 0.9 M INWARD FROM CORNER
- 306 DOF (STATIC)
- 147 DYNAMIC DOF (TRANSLATIONAL MASSES)

Figure 4-3. Mathematical model of the reflector surface panel.

Table 4-4. Hexagonal reflector panel - design characteristics.

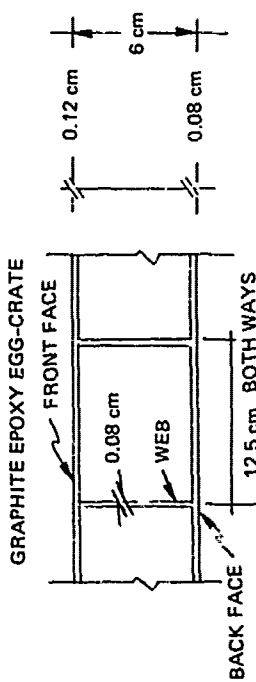
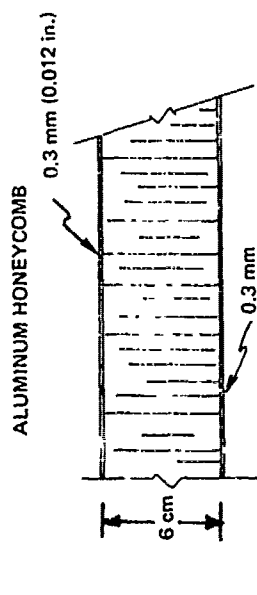
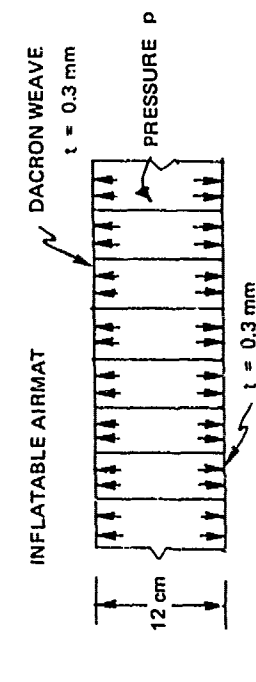
PANEL CONSTRUCTION AND DESIGN FEATURES		BENDING $D_x = D_y$	SHEAR $D_{Qx} = D_{Qy}$
<p>GRAPHITE EPOXY EGG-CRATE</p>  <p>FRONT FACE</p> <p>0.12 cm</p> <p>0.08 cm</p> <p>6 cm</p> <p>0.08 cm</p> <p>12.5 cm BOTH WAYS</p> <p>BACK FACE</p> <p>WEB</p> <p>MATERIAL REMOVED BY HOLES IN WEBS AND BACK FACE FOR LIGHT WEIGHTING (SEE FIGURE 2-5)</p> <p>4.0 kg/m²</p>		18.1 X 10 ⁴	22.4 X 10 ¹⁰
<p>ALUMINUM HONEYCOMB</p>  <p>0.3 mm (0.012 in.)</p> <p>0.3 mm</p> <p>6 cm</p> <p>CORE 3003 - H19 FOIL</p> <p>0.002 in. \approx 0.05 mm THICK</p> <p>3/8 in. CELLS</p> <p>4.5 kg/m²</p>		3.88 X 10 ⁴	11.5 X 10 ⁶
<p>INFLATABLE AIRMAT</p>  <p>DACRON WEAVE</p> <p>t = 0.3 mm</p> <p>PRESSURE p</p> <p>12 cm</p> <p>t = 0.3 mm</p> <p>2.5 kg/m²</p> <ul style="list-style-type: none"> DROPTHEADS A = 0.004 cm² SPACING = 2 cm BOTH WAYS THREAD ϕ = 0.7 mm INTERNAL PRESSURE = 5 psi INFLATED + RIGIDIZED 		0.89 X 10 ⁴	10.2 X 10 ⁴

Table 4-5. Reflector panel designs - thermal and dynamic characteristics

MATERIAL	DESIGN	FREQUENCIES	THERMAL DEFORMATIONS
<p>GRAPHITE - EPOXY</p> <p>$E = 14 \times 10^{10} \text{ N/M}^2$</p> <p>$\rho = 1.72 \times 10^3 \text{ KG/M}^3$</p> <p>$\alpha = 0.2 \text{ TO } 1 \times 10^{-6} / ^\circ\text{K}$</p>	<p>DEPTH = 6 CM</p> <p>MASS = 4.0 KG/CM²</p>	<p>30.6 Hz</p> <p>30.8</p> <p>59.2</p> <p>70.6</p> <p>97.3</p> <p>103.6</p> <p>116.8</p> <p>145.0</p>	<p>$\Delta T_G = 3.1^\circ$</p> <p>MAX = 0.12 MM</p>
<p>ALUMINUM HONEYCOMB</p> <p>$E = 7.2 \times 10^{10} \text{ N/M}^2$</p> <p>$\rho = 2.77 \times 10^3 \text{ KG/M}^3$</p> <p>$\alpha = 23 \times 10^{-6} / ^\circ\text{K}$</p>	<p>DEPTH = 6 CM</p> <p>MASS = 4.5 KG/CM²</p>	<p>14.3 Hz</p> <p>14.4</p> <p>27.8</p> <p>32.5</p> <p>45.7</p> <p>49.9</p> <p>55.6</p> <p>69.2</p>	<p>$\Delta T_G = 1.05^\circ$</p> <p>MAX = 0.91 MM</p>
<p>AIRMAT CONCEPT</p> <p>$E = 41 \times 10^8 \text{ N/M}^2$</p> <p>$\rho = 2 \times 10^3 \text{ KG/M}^3$</p> <p>$\alpha = 7 \times 10^{-6} / ^\circ\text{K}$</p>	<p>DEPTH = 12 CM</p> <p>MASS = 2.4 KG/M²</p> <p>INTERNAL PRESSURE</p> <p>= $35 \times 10^3 \text{ N/M}^2$</p> <p>= 5 PSI</p>	<p>6.3 Hz</p> <p>6.4</p> <p>10.9</p> <p>14.4</p> <p>17.6</p> <p>18.9</p> <p>21.1</p> <p>29.0</p>	<p>$\Delta T_G = 5.7^\circ$</p> <p>MAX = 1.6 MM</p>

been established for an identical thermal flux. The corresponding deflections at the center of the plate are listed in the same Table.

As mentioned above, the egg-crate panel made of graphite-epoxy appears to satisfy both dynamic and thermal requirements and consequently was chosen as the candidate. The aluminum honeycomb design shows a lower fundamental frequency, principally because of its lower modulus of elasticity. It is interesting to note that the thermal gradient is almost 3 times smaller due to the aluminum high conductivity that tends to even out the face sheet temperatures. This, however, is not enough to cancel the effects of the aluminum large coefficient of thermal expansion α . An increase in the panel thickness could improve both its dynamic and thermal characteristics, but it would affect adversely the packaging ratio. The greatest advantage of the airmat concept lies in its high packageability and relatively low mass. Based on perhaps old information (Goodyear Corp. studies date back to the mid-sixties) the design of the airmat does not show great promise. Its ability to minimize the thermal gradient ΔT_G through its thickness is greatly impaired by the presence of only drop threads, thus creating relatively large thermal deformation. These conclusions, based on somewhat old data should not be considered definitive. New studies of the possibilities offered by inflatables, in general, and airmats, in particular, should be undertaken for this kind of structural applications. If the shortcomings in their thermal behavior can be overcome, the inflatables may well prove superior to other concepts, especially because of their initial "flexibility" from a packaging point of view.

The hexagonal panel model approximately represents all 124 reflector panels, and will be used in estimating the absolute thermal distortions of the surface. In order to show the performance degradation as a function of a particular design, the three models will be used. For the dynamic response, the panels are considered to vibrate outside the range of interest and therefore, are assumed to be "rigid". Their deformations of rigid-body nature are imparted by the relative motions of their 3 kinematic mounts (from underlying truss displacements). The results of the response calculations are presented in Section 5.

SECTION 5

RESPONSE EVALUATION

5.1 Introduction and Approach

Section 4 described the mathematical modeling of both the trusses/tower assembly and the hexagonal reflector panels. The structural responses have been evaluated as the geometric combination of the elastic distortions of the component substructures. For the static case, the uncoupling of the reflector panels from the underlying trusses was possible because of the kinematic connection. Each panel was first analysed independently. The rigid-body displacement components associated with deformations of the supporting back-up trusses were added to the elastic distortions. With 124 panels, each having 51 surface points, the deformed reflector surface was finally expressed by three displacement components of 6324 points.

In the response calculation to dynamic disturbance, the 124 reflector panels were assumed to be "rigid". (The rationale for this assumption was discussed in Section 4.) As the back-up trusses vibrate, they move the panels thus imposing rigid-body displacements and rotations on them. The elastic distortions of the panels are disregarded because it is assumed that the amplitudes of panel vibrations are negligible compared to the amplitudes of truss vibrations. The absolute displacements of all 6324 surface points were obtained by evaluating the rigid-body motions of each one of the 124 panels. Figure 5-1 illustrates the steps involved in the computation of the surface displacements. The antenna performance evaluation based on the reflector deformed surface is presented in Section 6.

Section 3 established from a list of disturbances, those that are expected to be predominant in distorting the reflector surface and in affecting the antenna pointing accuracy. The responses calculation therefore was limited to four loadings capable of illustrating the antenna behavior under normal environmental conditions. The only quasi-static loading is the thermal disturbance that corresponds to a 68° sun flux incidence with respect to the z-axis in the X-Z plane of the antenna model. Responses to this loading have been evaluated for the three different panel constructions presented and discussed in Section 4.3. Three dynamic disturbances have been considered: the first two are step-impulse functions associated with the firing of thrusters for two possible attitude control schemes and the third one is a harmonic disturbance simulating a cryo-cooler reciprocating machine. A detailed description of these loading and the associated structural responses are presented below.

5.2 Response to Sun Thermal Flux (68°)

The thermal loading selected for response evaluation corresponds to the time when the satellite emerges from the earth shadow. This time is considered

FOR PANEL k , $k = 1, 2, \dots, 124$:

- (1) ELASTIC DISTORTIONS ON 3 KINEMATIC MOUNT SUPPORTS

$$\delta_i^{el} \quad (i = 1, 50)$$

NOTE: $\delta_i^{el} \equiv 0$ IN DYNAMIC ANALYSIS

- (2) PANEL RIGID BODY DISPLACEMENTS (Δ) AND ROTATIONS (ϕ) FROM BACK-UP TRUSSES DISPLACEMENTS

THEN OBTAIN

$$\delta_i^{RB} \quad (i = 1, 50)$$

- (3) TOTAL DISPLACEMENTS

$$\delta_i^{TOT} = \delta_i^{el} + \delta_i^{RB}$$

- (4) TRANSFORM TO GLOBAL SYSTEM OF AXES

- (5) NEXT PANEL
 $k + 1$

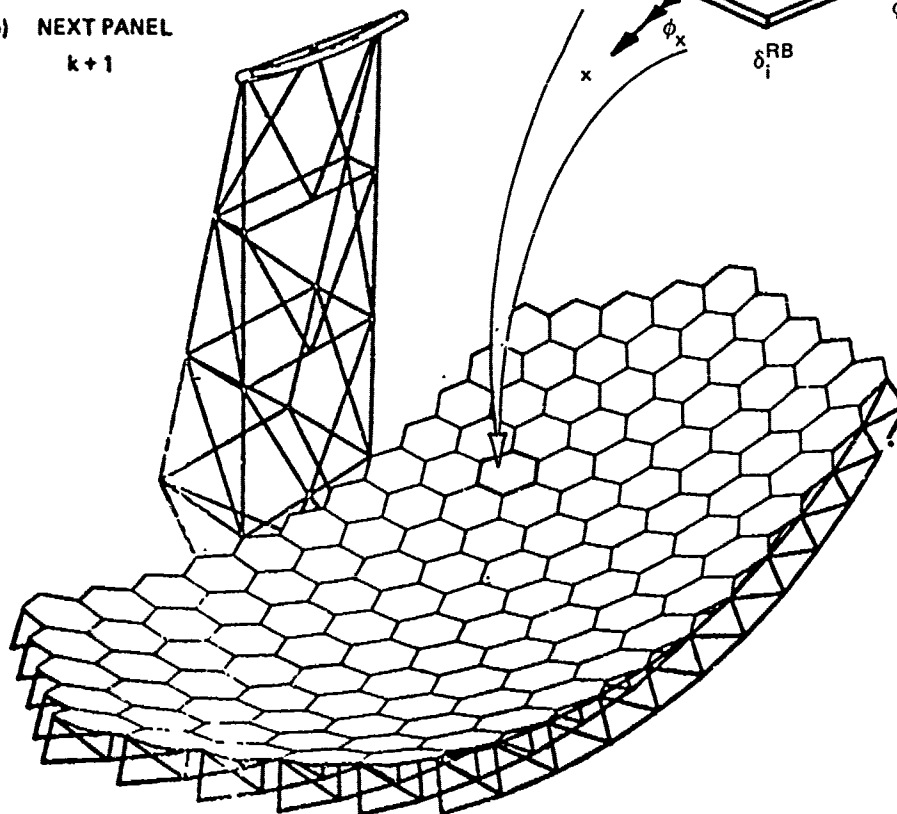
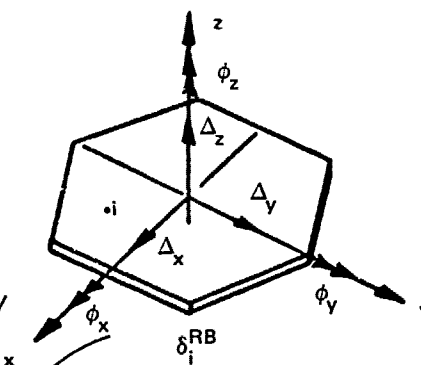
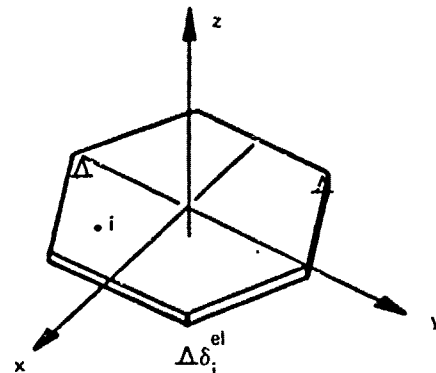
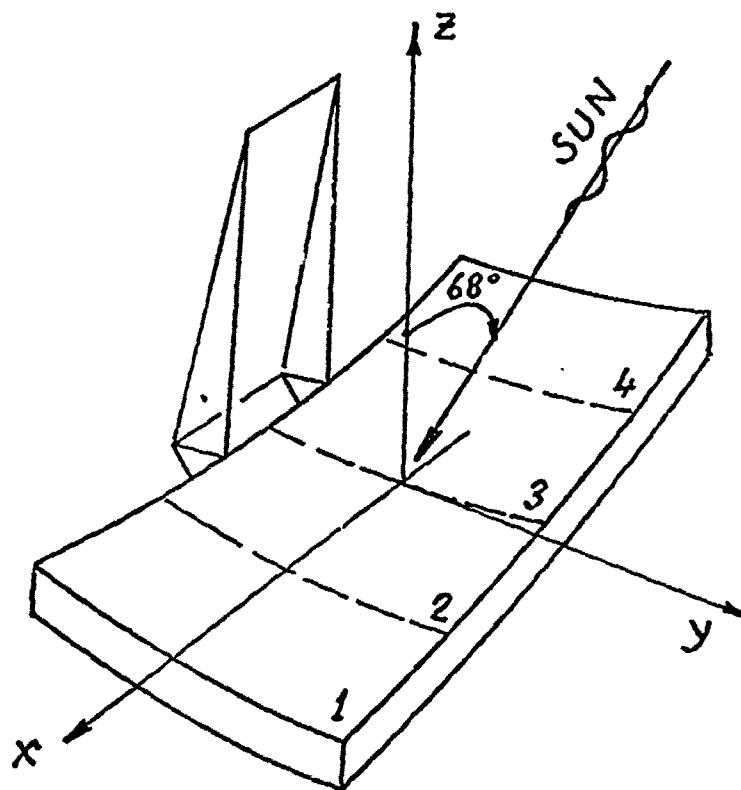


Figure 5-1. Reflector surface distortion calculation.

critical, because it is the only orbital position where the sun impinges directly onto the reflector surface. This condition creates the greatest thermal gradient across the reflector panels. Since the orbit inclination is not definitively known, the sun vector orientation in the X-Z plane was chosen to represent a worst case condition. In addition, due to the curvature of the reflector along its longer dimension (about 60 m) the sun incidence with respect to the various panels shows the widest variation of about 30° from one edge to the other. In order to account for this variation, the reflector surface was arbitrarily divided into four equal width zones of approximately 15 m. The thermal conditions of the structures were assumed to be identical throughout each zone. Although the panels of a zone theoretically are not under exactly the same thermal condition, this restriction was found acceptable and greatly decreased the amount of computations. In a similar manner, the underlying truss assembly was assigned four temperature distributions for the same four 15 m wide zones. Figure 5-2 illustrates schematically the geometry of the zones considered. Since the tower members were not included in this thermal model, information on tower thermal distortions are only approximations in this analysis. A uniform temperature of 220°K was arbitrarily used for the tower members of the model, but a separate analysis for the prediction of tower distortions was carried out based on a special thermal model of the tower and will be presented later in this section.

The thermal response calculations included a static analysis of the hexagonal panel for the four different thermal distributions associated with the four zones. In a parallel analysis, the truss-tower assembly was subjected to four temperature zones as obtained by the thermal model described earlier. The temperatures used in the analysis appear in Table 5-1. The distortions have been computed for an arbitrary reference temperature of 280°K . A special purpose computer program was developed in order to integrate into the overall structure the 124 panel distortions in their proper locations. Each panel was assigned three truss joints for its three support points. Once the truss joints displacements are known, the panel support motions are readily available. On the basis of these displacements, the rigid-body motions of the panel are determined. As a consequence, each panel surface point (there are 51 points per panel) undergoes additional displacements as a function of the panel three rigid-body translations, three rigid-body rotations and location within that panel. The panel distortions finally are computed as the sum of elastic and rigid-body displacements and then expressed in the global coordinate system of the entire reflector. This information was stored on tapes for subsequent use in the performance evaluation. Note that the computation described above was repeated two more times, to evaluate the surface distortions for the aluminum honeycomb panel and the airmat construction. Figure 5-3 depicts the out-of-plane deformations of three longitudinal lines on the reflector surface. A maximum deflection of 0.8 mm is recorded at the reflector edge.

The response of the receiver tower to the sun thermal flux was the subject of a special analysis as explained in Section 3.2. In this case the sun vector was allowed to sweep the Y-Z plane as shown in Figure 5-4. The



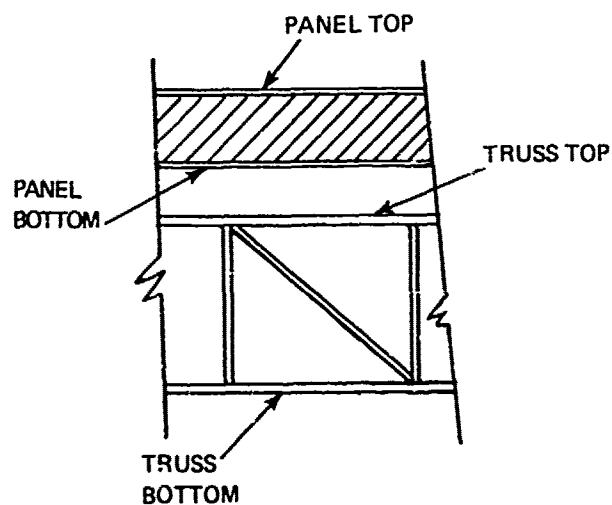
TEMPERATURE DISTRIBUTION

- o Back-Up Trusses: 4 Zones
- o Panels: 4 Zones
 - a) Graphite-epoxy $\alpha = 0.5 \times 10^{-6}/^{\circ}\text{K}$
 - b) Aluminum Honeycomb $\alpha = 23 \times 10^{-6}/^{\circ}\text{K}$
- o Tower: Uniform Temperature Assumed at 220°K

Figure 5-2. Thermal loading for sun at 68° with z-axis.

Table 5-1. Trusses and Panel Temperatures (°K)
(Sun Incidence Angle of 68° with
Respect to Z Axis)

Zone	Trusses		Panels			
	Top	Bottom	Graphite-Epoxy		Aluminum	
			Top	Bottom	Top	Bottom
1	287.3	286.8	288.1	285	286.06	285
2	285.8	285.2	287.0	285	285.68	285
3	284.5	283.9	286.3	285	285.44	285
4	283.4	282.7	285.8	285	285.28	285



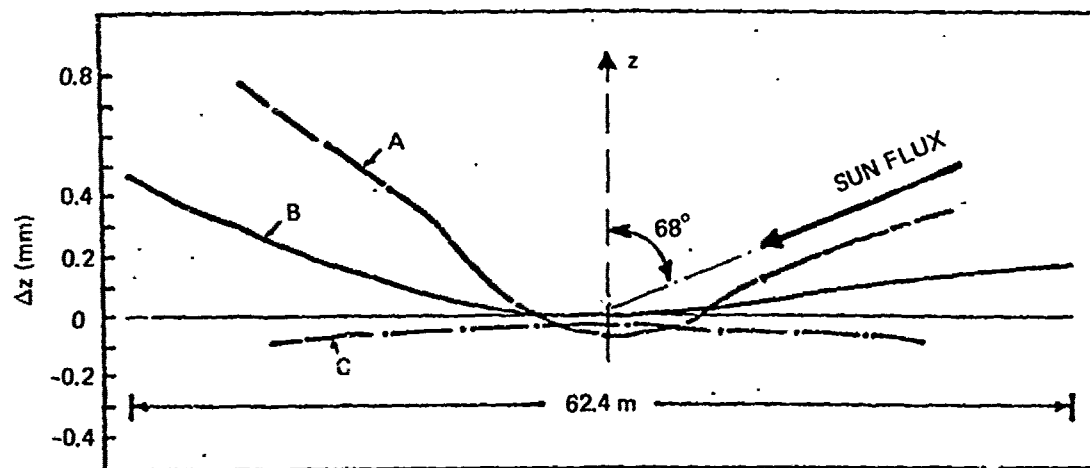
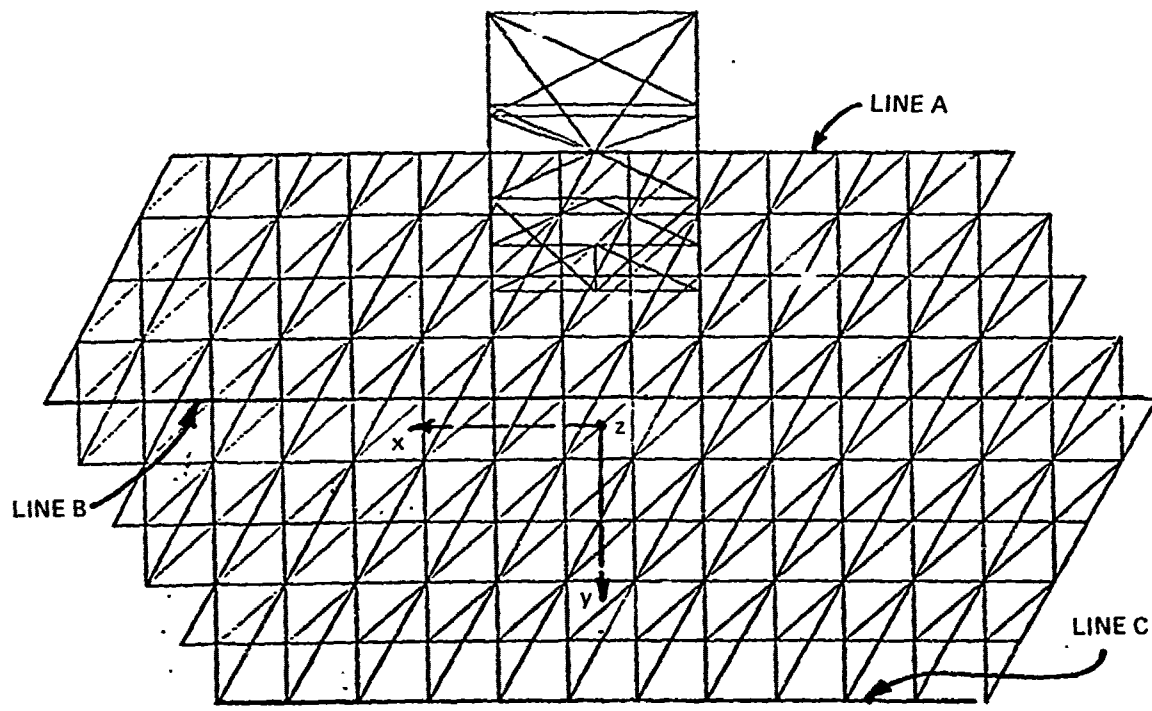


Figure 5-3. Reflector z-displacement of trusses due to thermal loading (68° sun), lines A, B, and C.

shadowing effects of the opaque large reflector were accounted for as well as the shadow that one tower member might have on its neighbor. Since the thermal model was reduced to a planar problem, only the displacement Δy and Δz were calculated. They are expressed in terms of the angle ϕ for the entire 360° sweep. One should note that with respect to a mean value the tower top displacement Δy would vary by ± 0.4 mm while Δz would remain within ± 0.2 mm. Whereas the Δz displacement is acceptable when compared to the 1 mm tolerance, the decenter Δy exceeds by far the stipulated limit of 0.15 mm. In order to alleviate the deleterious effects of the sun on the tower decenter, several possibilities can be suggested. As an example of passive measures, an improvement of the coefficient of thermal expansion by a factor of 3, or possibly a judicious combination of α and ϵ for the various surface quality could reduce Δy sufficiently. As a last resort, it is conceivable to design a semi-active control system that would displace the receiver array according to a predetermined law along the orbital path. While none of these suggestions have been studied in detail, it can be concluded that the implementation of one method or a combination of them should keep the receiver within the tolerable travel. Figure 5-4 illustrates the tower tip displacement histories as a function of sun incidence angle ϕ .

5.3 Approximate Distortion Calculations

The outcome of the thermal response analysis of the mathematical model can be predicted somewhat based on the distortion evaluation of the following ideal case. The problem of the distortion of a homogeneous spherical reflector exposed to a thermal flux can serve to illustrate the relative effects of uniform temperature rise and thermal gradient. Consider a spherical reflector of curvature $1/R$ and having a circular shape of radius a . The plate (thickness h) is homogeneous and the material exhibits a uniform coefficient of thermal expansion α . When exposed to the sun thermal flux, the reflector undergoes deformation that can be essentially attributed to a uniform temperature rise ΔT_u and a thermal gradient ΔT_G across its plate thickness. Figure 5-5 shows the reflector geometry and the expressions for the ΔT_u and ΔT_G as a function of plate geometrical and mechanical properties.

Assuming a free-free structure or equivalently, a plate simply supported along the periphery, the maximum sag δ occurring at the center is expressed by two terms as

$$\delta = \frac{a^2 \alpha}{2} \left(\frac{\Delta T_u}{R} + \frac{\Delta T_G}{h} \right)$$

As expected, a uniform rise in temperature causes a deflection only if there is a curvature $1/R$. In the case of a flat plate, $R = \infty$ and no distortion takes place. The gradient ΔT_G is usually a more significant source of distortions. For a given ΔT_G , the sag δ is inversely proportional to the plate thickness h .

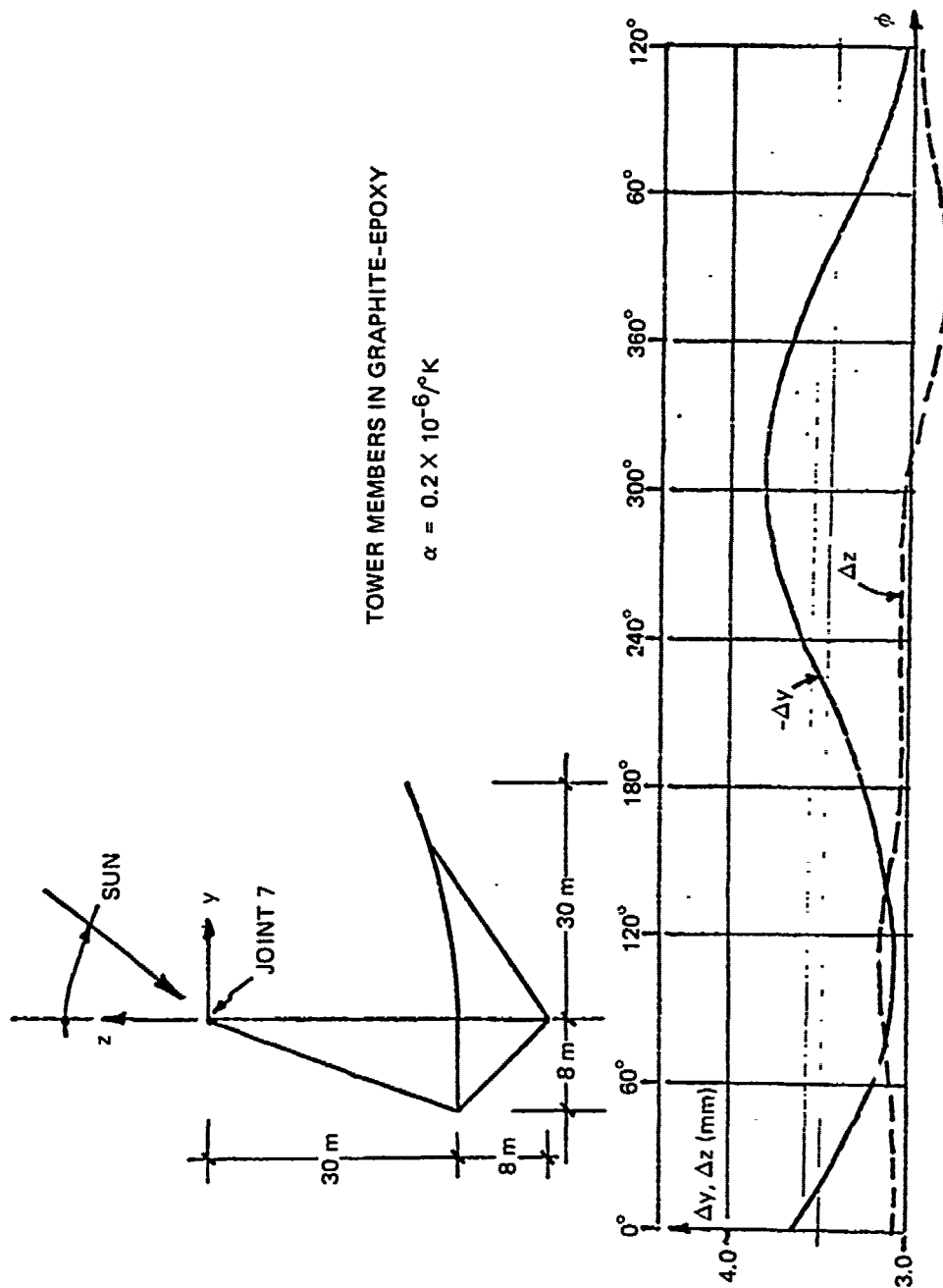


Figure 5-4. Receiver support tower thermal distortions (sun in z-y plane).

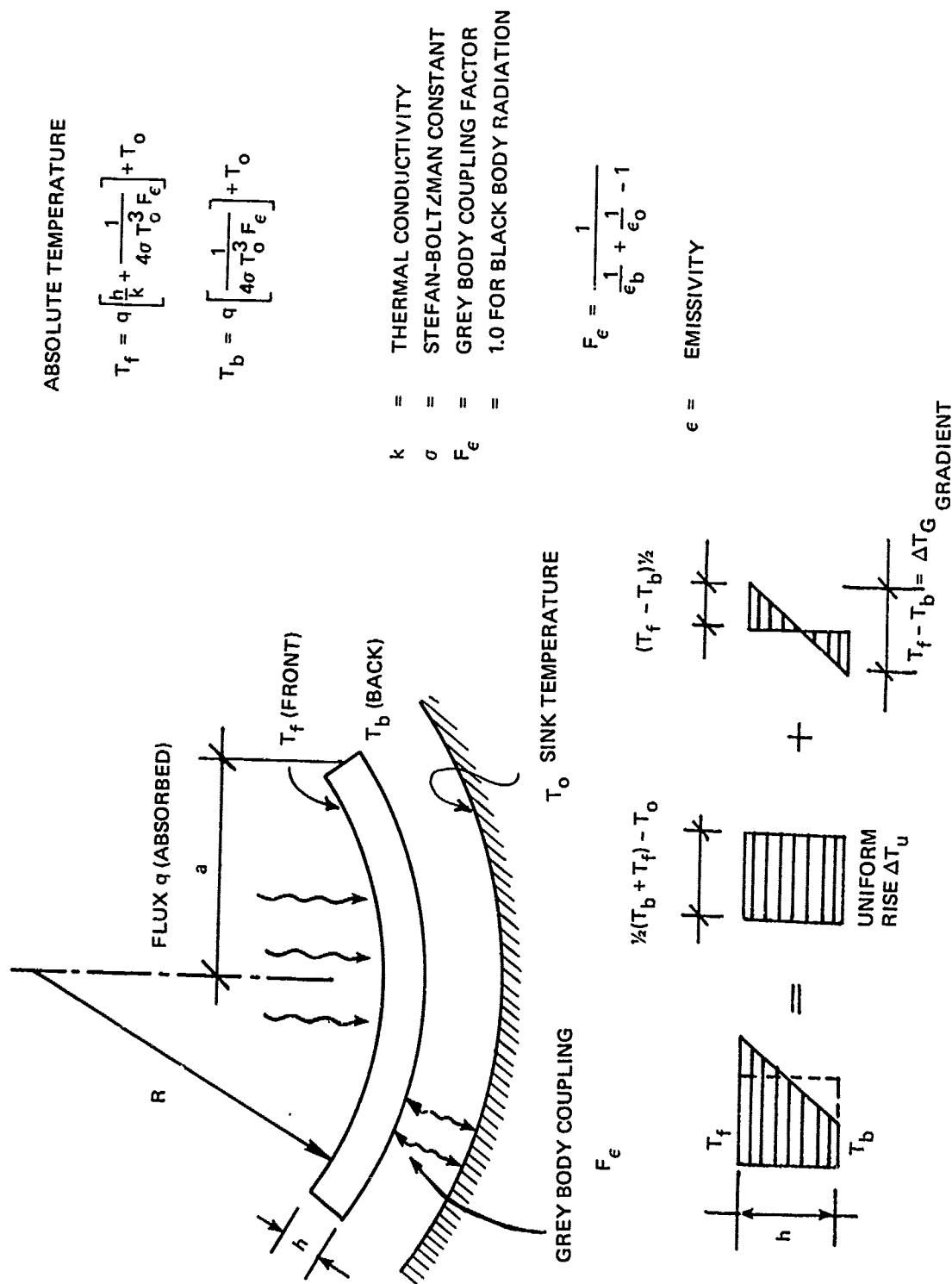


Figure 5-5. Steady-state temperatures on a spherical mirror from a thermal flux.

Applying the expression for δ in the case of an approximate circular plate model of the typical hexagonal panel, the following data, based on thermal model, are used:

$$a = 4.5 \text{ m (0.5)} = 2.25 \text{ m}$$

$$R = 60 \text{ m}$$

$$h = 0.06 \text{ m}$$

$$\alpha = 0.5 \times 10^{-6} \text{ m/m}^\circ\text{K (conservative)}$$

$$\Delta T_u = 40^\circ$$

$$\Delta T_G = 3.1^\circ$$

and

$$\begin{aligned} \delta &= \frac{1}{2}(2.25)^2 \times 0.5 \times 10^{-6} \left[\frac{40}{60} + \frac{3.1}{0.06} \right] \\ &= 0.8 \text{ } \mu\text{m} + 65.4 \text{ } \mu\text{m} \\ &= 66.2 \text{ } \mu\text{m} \\ &= 0.066 \text{ mm} \end{aligned}$$

The numbers show that the contribution of the gradient ΔT_G is overwhelming in the computation of the sag. A large uniform rise, (or fall), such as the one associated with the orbit injection, that is 200° would only cause a sag of $4.2 \text{ } \mu\text{m}$.

5.4 Dynamic Responses

5.4.1 Introduction

The dynamic responses of the antenna surface were obtained through the vibrational distortions of the underlying trusses only, since the surface panels have been assumed to undergo rigid-body motions only. This assumption was made possible by comparing the dynamic characteristics of the truss/tower assembly and the typical surface panels. The natural frequencies of the lower modes of the truss structure, that are predominant in the distortion calculations, fall well below the fundamental frequency of the reflector panel. It is therefore anticipated, that while the trusses vibrate at these low frequencies, the panel would indeed behave as a rigid body. At higher frequencies, the panel is expected to undergo small vibrational distortions, but its rigid-body motions become negligibly small. One should emphasize that these qualitative statements would require substantiation if the calculated distortions are of the order of the allowable ones. In this study, it appears that the dynamic disturbances cause the reflector to distort well within allowable limits.

It was also assumed that the panels could be replaced by only translational masses. While the trusses and the panels can be uncoupled elastically (as was properly done in the static analysis) they remain coupled inertially. Although it can be expected that the panels rotational masses would not affect the responses significantly, additional study would be necessary to substantiate this fact or establish its importance.

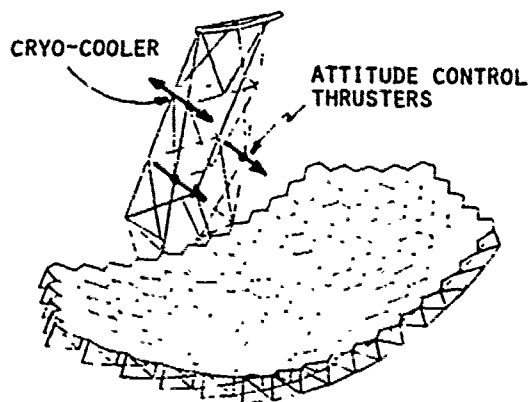
The response calculations have been performed for three dynamic disturbances. As discussed in Section 3.6, the attitude control of the spacecraft can be achieved by two different thruster control laws. One possibility consists of frequent, but small bursts, while another requires two substantial thrusts approximately 180° apart executed once every several days. Figure 5-6 shows the location of the thrusters and the amplitudes of the step-functions used in the evaluation of the responses. The third dynamic disturbance considers a harmonic forcing function that could represent the reciprocating machine of a cryo-cooler. One of the possible designs for the receiver array requires the temperature to be kept at 40°K , and this can only be achieved through the help of an active cooling system. The location for the disturbance was deliberately chosen to produce significant and unsymmetrical distortions (see Figure 5-6). The characteristics of a cryo-cooler with an amplitude of 15 N at a frequency of 10 Hz corresponds to a typical, state-of-the-art machine.

The methods used in evaluating the responses are briefly explained and results presented for selected locations show that the dynamic distortions are relatively small and less serious than the thermal ones.

5.4.2 Dynamic Response to Thrusters Impulses

The firing of the attitude control system thrusters was believed to be one of the critical dynamic disturbances affecting the MMW antenna satellite. The characteristics of the forcing function can be represented mathematically by a step impulse with amplitudes and duration based on the attitude control philosophy presented in Section 3.6. Since the principle of superposition is valid for this time-invariant linear mechanical system, a response to a particular step impulse can be scaled up or down for a similar loading of different amplitude. In other words, the surface distortion computed for the 86 N impulses can be scaled down proportionally for the other impulse loading of 0.4 N.

Owing to the decoupling property of the modal analysis, each mode was considered as a single DOF system. It is instructive to examine the response characteristics of such a system to a step impulse in terms of natural frequency and damping ratio. Figure 5-7 depicts the response function and the expression for the maximum overshoot of the response, its peak time and settling time (5% remaining oscillation about the static deflection) are presented. Since the peak time of the response is inversely proportional to the natural frequency ω , the peak response of the lowest mode (with the smallest ω) occurs after all other modes have peaked. For this reason, the response including the first 53 modes, was calculated for 1.2 seconds, a time corresponding to approximately twice the time to the peak response of the fundamental



- ATTITUDE CONTROL THRUSTERS SIMULATED
BY STEP IMPULSE FUNCTIONS $F(t) \approx F_0 U_S(t)$

A) QUASI-CONTINUOUS ORBIT COMPENSATION

$$F_0 \approx .40 \text{ N}$$

B) INTERMITTENT ORBIT COMPENSATION

W/ 2 BURNS, 180° APART

$$F_0 = 86 \text{ N}$$

- POSSIBLE CRYO-COOLER FOR RECEIVER REFRIGERATION, SIMULATED BY A HARMONIC DISTURBANCE

$$F(t) = F_0 \sin \Omega t$$

$$\text{WITH } F_0 \approx 15 \text{ N}, \Omega \approx 10 \text{ Hz}$$

Figure 5-6. Description of dynamic loadings.

mode. A numerical integration using the Runge-Kutta technique with a time-step size $\Delta t = 0.044$ s calculated each modal response in which a critical damping ratio of 0.005 ($\frac{1}{2}$ percent) was assumed. The superposition of the various modal responses was routinely performed to provide the physical truss displacements as a function of time.

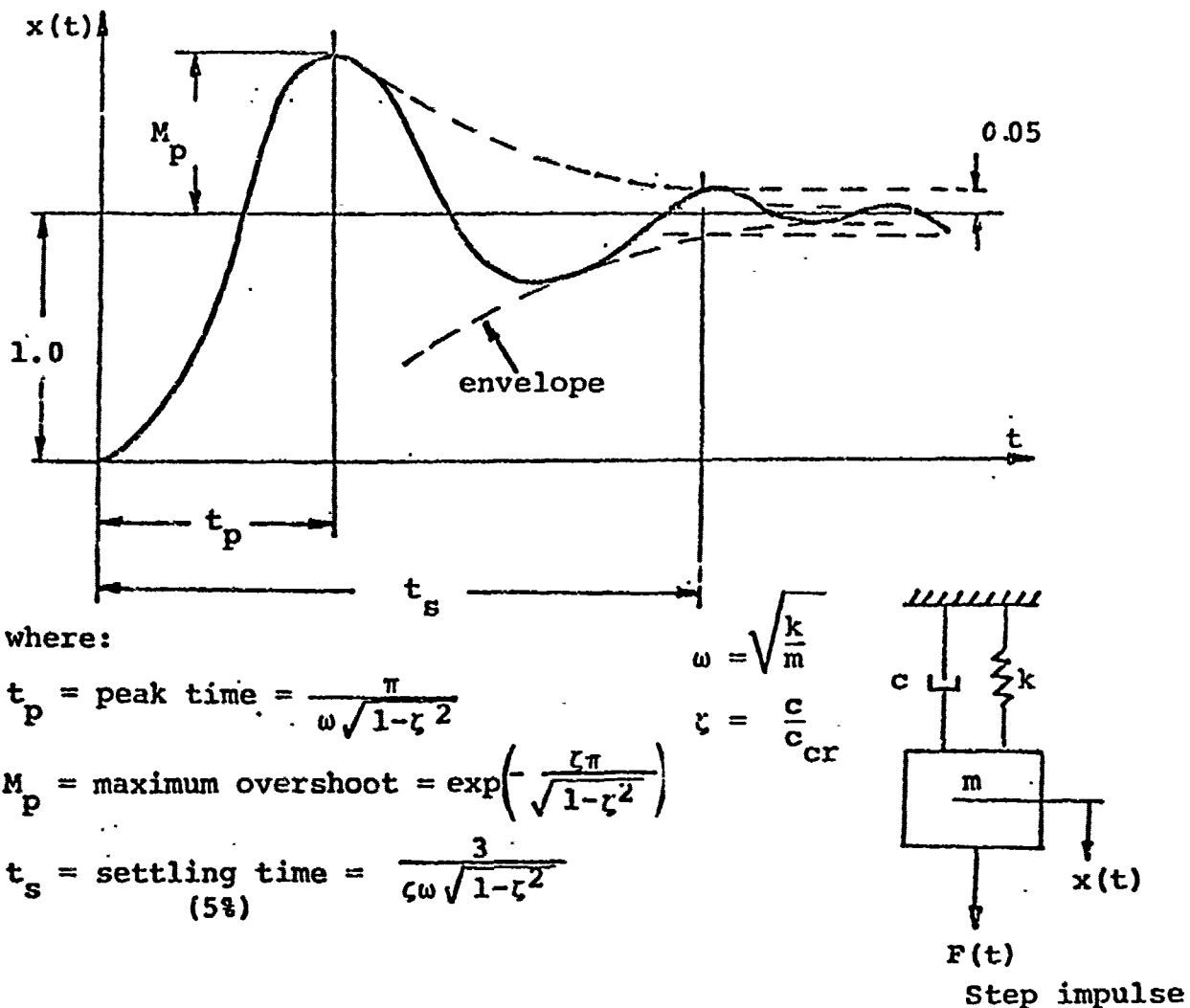


Figure 5-7. Response characteristics to a unit step impulse.

In the evaluation of the structural response to the 86 N thruster step impulse, the integration time was selected such that the responses of all 53 modes under consideration could reach their peak. Because the fundamental frequency is 0.89 Hz, the time of maximum overshoot for this mode is

$$t_p = \frac{\pi}{\omega\sqrt{1-\zeta^2}} = 0.56 \text{ s}$$

and all other modes reach their peak modal response in the interval $0 < t < 0.56 \text{ s}$. Since it is possible that a combination of modal responses can result for a particular DOF in a larger displacement some time after 0.56 s, the integration was carried out to approximately twice as long, i.e., a time $t = 1.2 \text{ s}$. It is reasonable to anticipate that in this interval, the amplitudes of the displacements include their maximum from which they will decrease steadily due to the energy absorption by damping. It is interesting to follow the z-displacement of structural joints along a longitudinal cross-section of the antenna. As expected, several joints reach their maximum z-displacement in the neighborhood of 0.6 to 0.8 s which indicates that the lower modes are predominant for the out-of-plane displacement of the reflector. Figure 5-8 indicates the location of the joints considered and Figure 5-9 shows the corresponding response histories. At the reflector's edge the maximum z-distortion reaches 0.1 mm, while distortions inside the reflector area remain well below 10^{-4} m .

The joints located at the "corners" of the back-up trusses assembly are expected to correspond to the location of maximum dynamic response. Figure 5-10 shows the response histories of these joints where the maximum Δz is approximately 0.16 mm for 3 joints (261, 50, and 270) and 0.22 mm for joint 41. These displacements are used later in the performance evaluation presented in Section 6.

The dynamic response of the tower tip to the 86 N thrusters impulse needs special consideration. Figure 5-11 illustrates the responses for the Δx , Δy , and Δz displacement that can be interpreted as 2 decenters and a defocus. At the start of the response, the maximum decenters of 0.22 mm (x-direction) and 0.32 mm (y-direction) are slightly larger than the tolerance (0.15 mm), while the defocus of 0.06 mm falls below the tolerable 1 mm. Since these displacements decrease with time, they are not considered critical to the antenna performance. Thus, the receiver array motions, as a result of an 86 N thruster's impulse remain acceptable.

It is concluded that even the largest thrust level does not cause unacceptable distortion, so the highest level orbit maintenance thrust need not be restricted to nonoperational parts of the orbit, and the system can operate during the orbit maintenance thrust periods. The lower thrust levels for quasi-continuous orbit maintenance, and the even lower levels for only attitude control likewise do not cause significant antenna deformation.

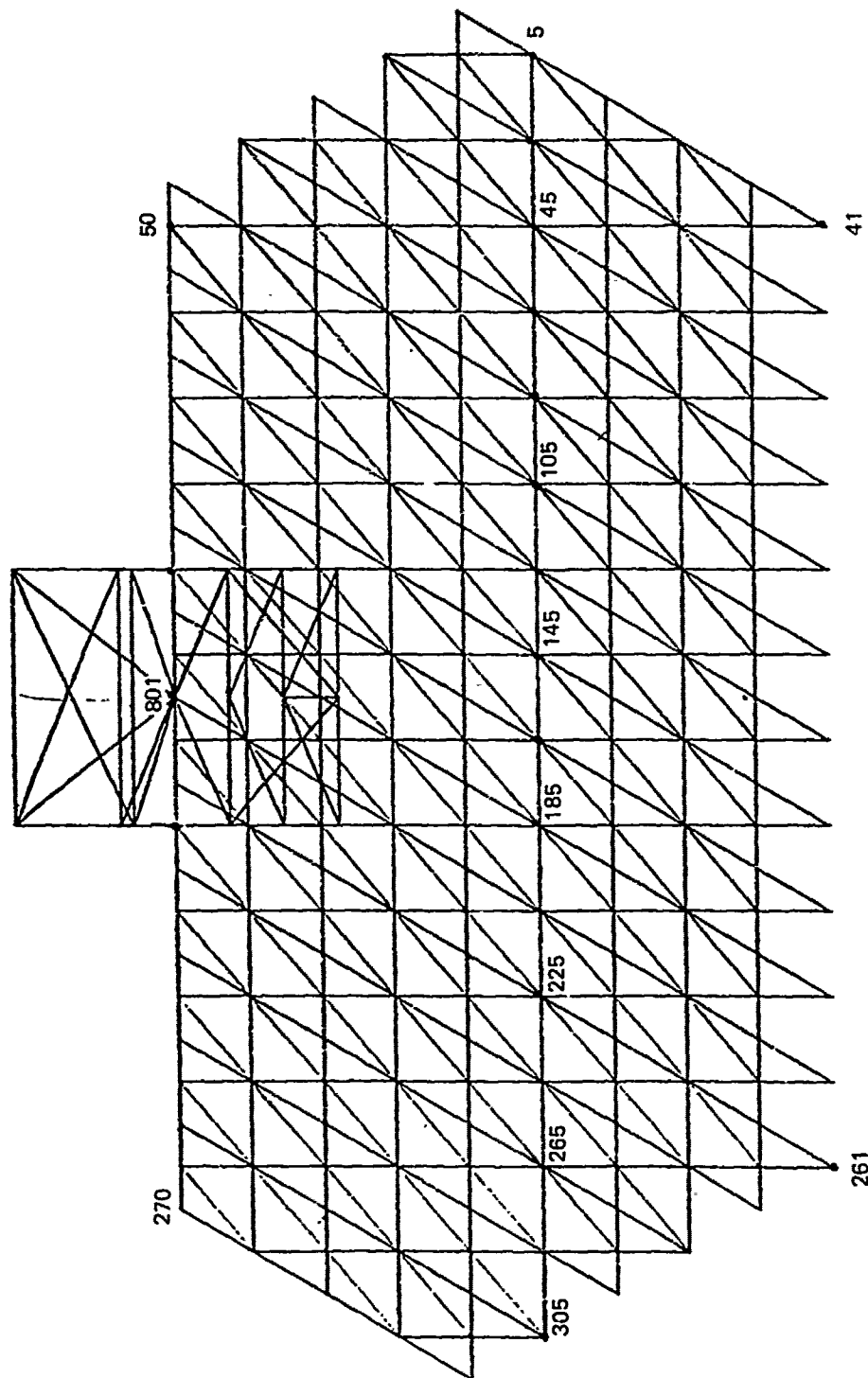


Figure 5-8. Truss/tower model. Joints identification numbers.

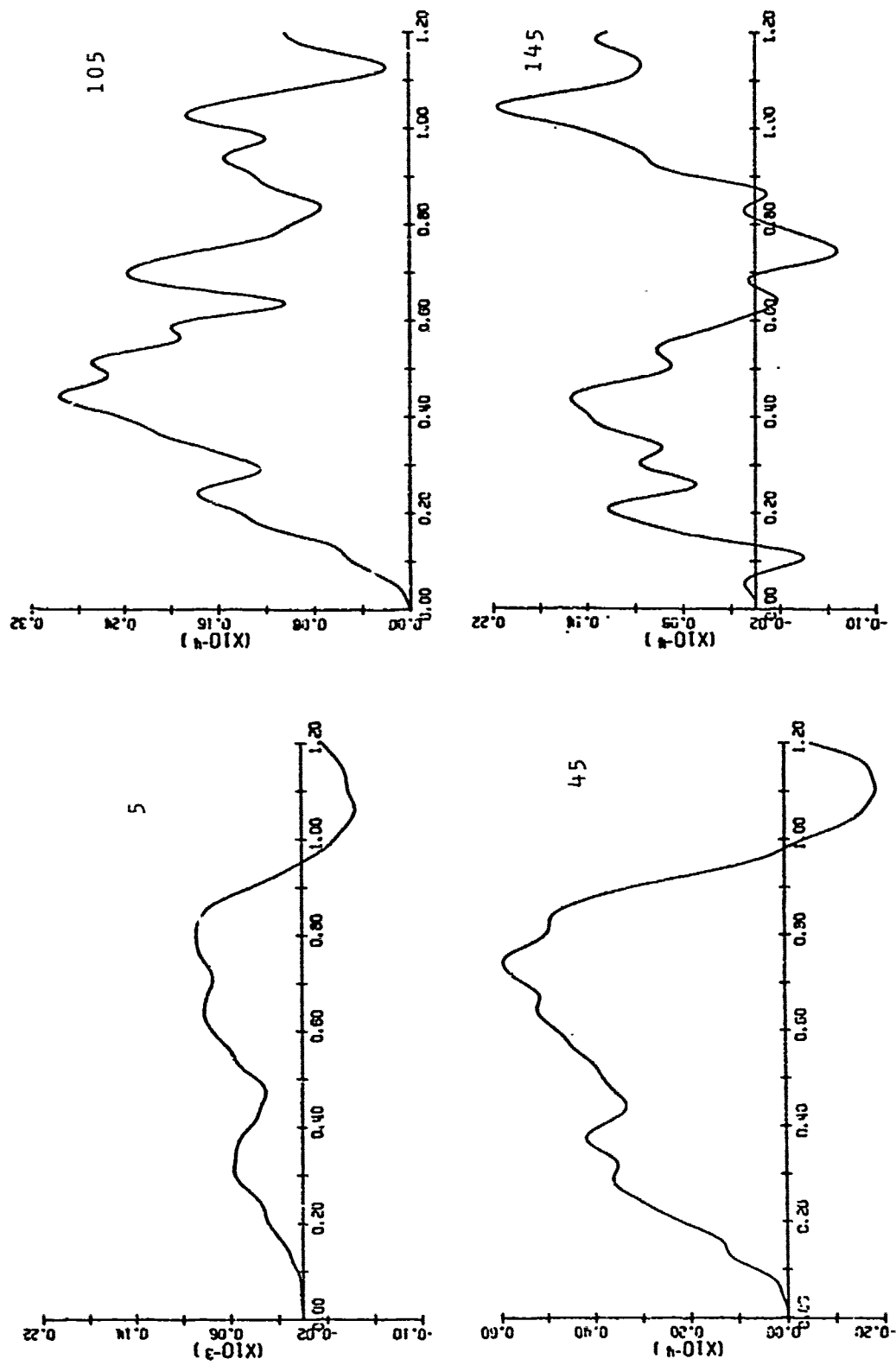


Figure 5-9. z-displacement (m) histories for the first 1.2 s of response to 86 N thiuster's impulse.

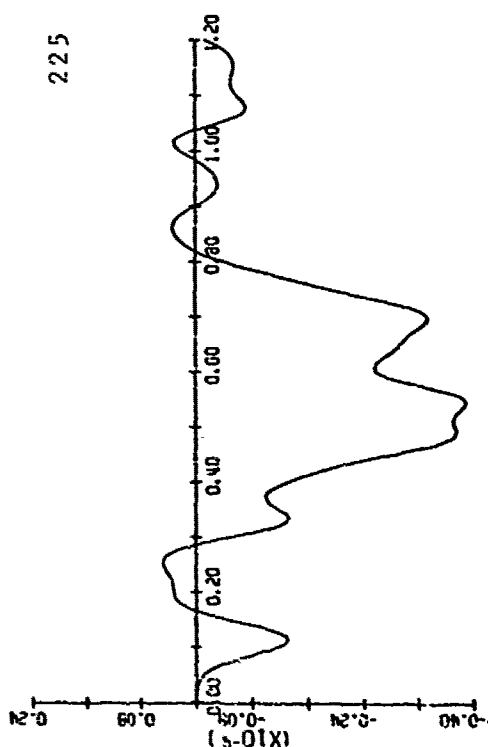
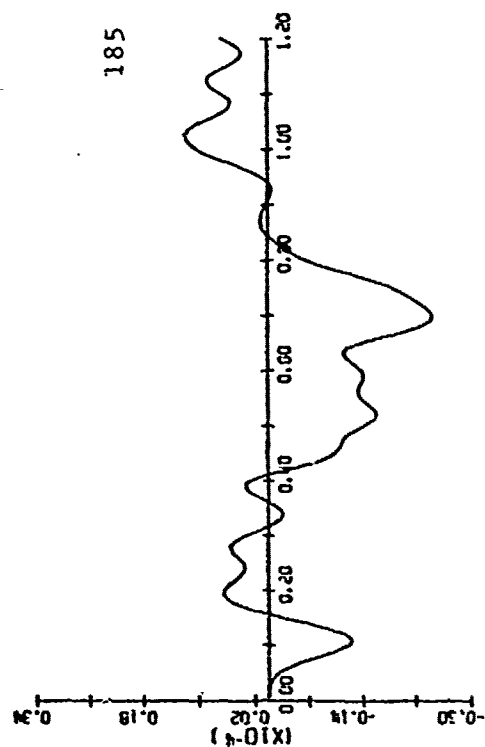
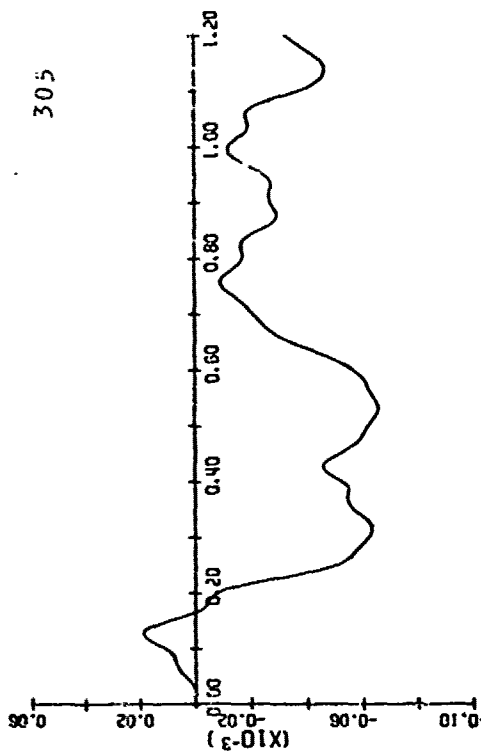
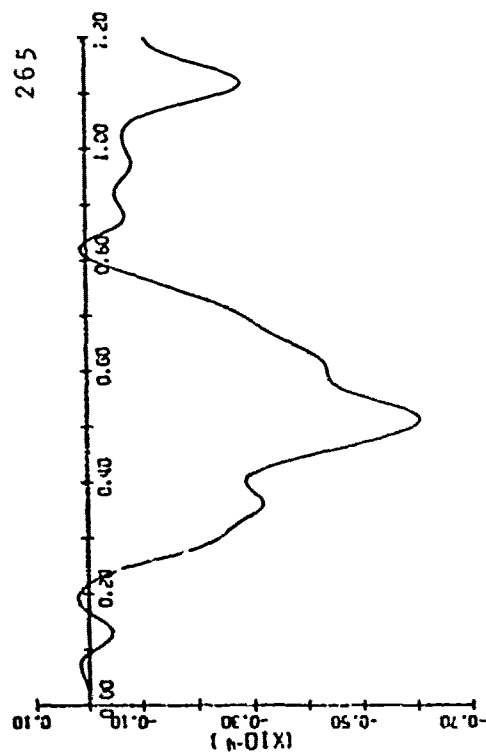


Figure 5-10a. z-displacement (m) histories for the first 1.2 s of response to 86 N thruster's impulse.

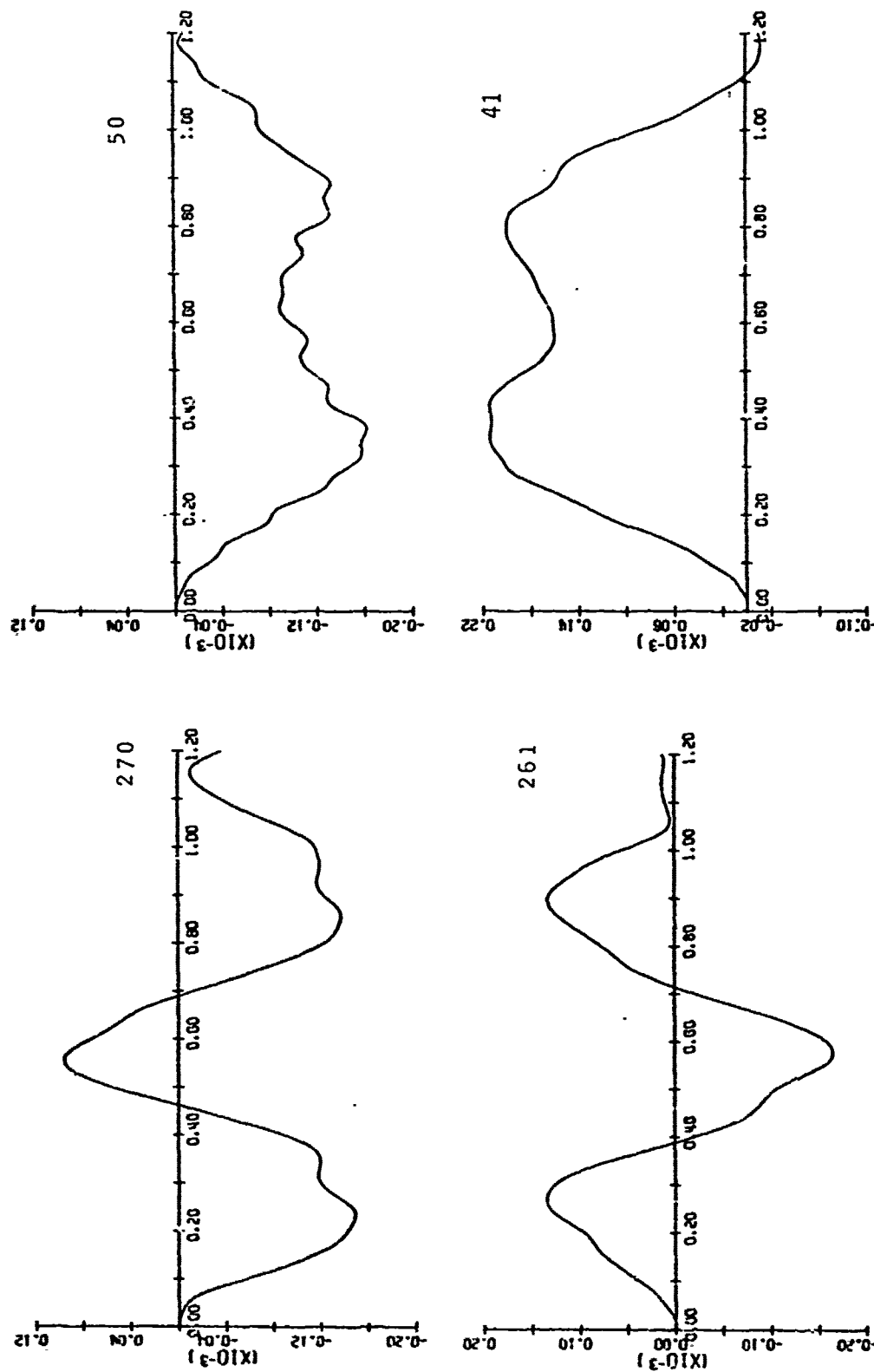


Figure 5-10b. z-displacement (m) histories for the first 1.2 s of response to 86 N thruster's impulse.

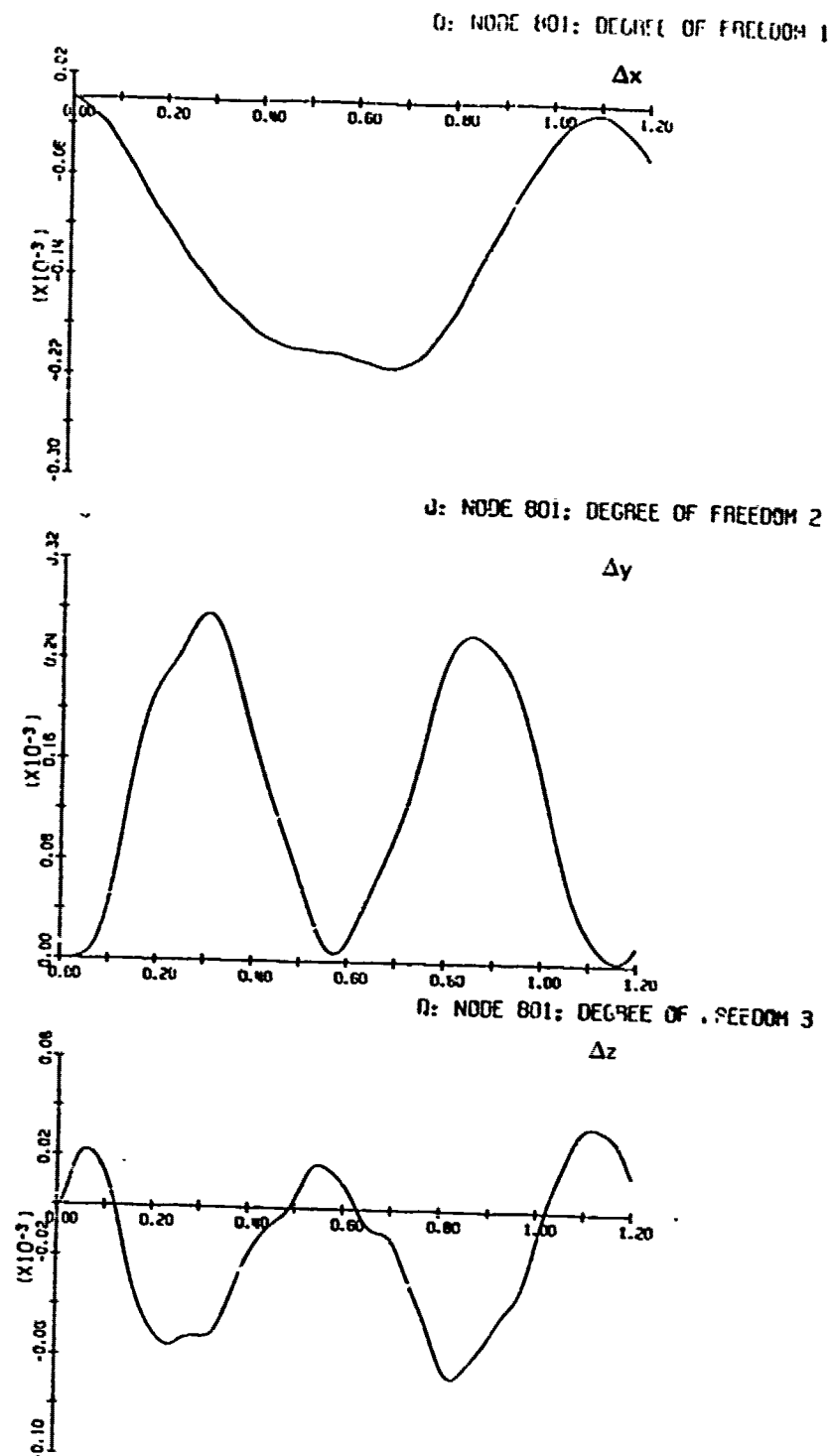


Figure 5-11. Tower tip displacements (m) histories for the first 1.2 s of response to 86 N thruster's impulse.

5.4.3 Steady-State Response to Harmonic Disturbance

The case of the steady-state response to a harmonic forcing-function is of particular interest. When the exciting frequency coincides with a natural-mode frequency of the system, the amplitude of the excited mode tends to grow infinitely large. However, damping places an upper limit that defines the resonance peak. While it is reasonable to anticipate that the largest deflections still occur at the time of the largest amplitude response of the resonant mode when many modes are present, it is of interest to compute the displacements histories along a full cycle of the steady-state response. This approach was followed in the response evaluation of the truss/tower assembly to the harmonic disturbance of 15 N at approximately 10 Hz. To be exact, the forcing frequency was selected to coincide with the system's natural frequency of 9.945 Hz (flexible mode number 22), the closest one to 10 Hz.

In order to establish the steady-state response of the system's physical coordinates, the responses of the individual modes were first evaluated as single DOF systems. It is therefore desirable to examine the response characteristics of a simple oscillator to a sinusoidal forcing function. Figure 5-12 describes the system variables. The expression for the total response including transient and steady-state components is discussed below.

The basic equation of motion of the single DOF system

$$m\ddot{u} + c\dot{u} + ku = p_0 \sin \Omega t \quad (5-1)$$

can be rewritten in the more convenient form

$$\ddot{u} + 2\zeta\omega\dot{u} + \omega^2 u = \frac{p_0}{m} \sin \Omega t \quad (5-2)$$

where

$$\omega = \sqrt{\frac{k}{m}} = \text{natural frequency of the undamped system}$$

$$\Omega = \text{exciting frequency}$$

$$c_{cr} = 2m\omega = \text{critical damping value}$$

$$\zeta = \frac{c}{c_r} = \text{damping ratio}$$

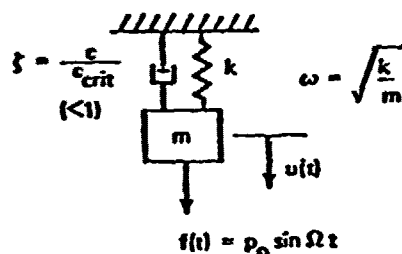


Figure 5-12. Simple oscillator parameter definition.

The general solution including the complementary and particular solution is

$$u(t) = e^{-\zeta\omega t} (A \sin \omega_D t + B \cos \omega_D t) + \frac{p_o}{k} \frac{1}{\left(1 - \left(\frac{\Omega}{\omega}\right)^2\right)^2 + \left(2\zeta\frac{\Omega}{\omega}\right)^2} \left[\left(1 - \left(\frac{\Omega}{\omega}\right)^2\right) \sin \Omega t - 2\zeta \frac{\Omega}{\omega} \cos \Omega t \right] \quad (5-3)$$

where $\omega_D = \omega\sqrt{1-\zeta^2}$ is the damped natural frequency, and A and B could be evaluated for any given initial conditions. The first term of the equation represents the transient response to the loading. Since it damps out quickly according to the exponential $e^{-\zeta\omega t}$ it is of little interest. The steady-state part of the response, at the frequency Ω of the applied loading but out of phase can be rewritten in the following simple form

$$\underset{\substack{\uparrow \\ \text{steady} \\ \text{state}}}{u(t)} = \frac{p_o}{m\omega^2} \left\{ \left[1 - \left(\frac{\Omega}{\omega}\right)^2 \right]^2 + \left[2\zeta\left(\frac{\Omega}{\omega}\right)^2 \right]^2 \right\}^{-1/2} \sin(\Omega t - \theta) \quad (5-4)$$

where the phase angle θ , by which the response lags behind the applied load, is

$$\theta = \tan^{-1} \frac{2\zeta\frac{\Omega}{\omega}}{1 - \left(\frac{\Omega}{\omega}\right)^2} \quad (5-5)$$

for the special case when $\Omega \equiv \omega$, the response reaches a maximum amplitude called the resonance peak, u_{peak}

$$u_{\text{peak}} = \frac{p_o}{2\zeta m\omega^2} \quad (5-6)$$

Each one of the 53 flexible modes considered exhibits the response shown by equation (5-4). While all modes vibrate with the same frequency Ω , they are out of phase with the exciting function by the phase angle θ (equation 5-5). It is a simple task to take an arbitrary time span of $2\pi/\Omega$ corresponding to a full cycle and sum up the contribution of all the modes, including the effects of phase lags. Thus, complete information was obtained for the antenna displacements during the steady-state response. The numerical values used were:

$$p_0 = 15 \text{ N}$$

$$f = 9.945 \text{ Hz}$$

$$\Omega = 62.49 \text{ rad/s}$$

$$\zeta = 0.005 \text{ for all modes}$$

$$\omega_r = \text{natural frequencies } (r = 1, 2, \dots, 53)$$

and the location of the disturbance is shown in Figure 5-6. In using equation (5-4) for the modal response, the amplitude of the forcing function p_0 must be multiplied by the corresponding modal coordinate and the mass m is the generalized mass of that mode. The term $m\omega_r^2$ can be understood to be the spring constant k of the mode r . Although the results included response histories of three displacement components of all the truss/tower assembly joints, it was deemed unnecessary to present them all since they remained negligibly small in terms of antenna performance. Since a tolerance on rms surface deviation was tentatively set at 150 μm , the maximum surface point deviations of about +5 μm are not anticipated to cause any serious performance degradation.

As an illustration, the z -displacement of the reflector centerline (in the long 60 m direction) was plotted for three time snapshots during the steady-state cycle (see Figure 5-13). Also, the z -displacements of the extreme points of the reflector are shown against time for the full 0.1 s period of the steady-state responses. As expected, the responses follow a sinusoidal curve with the same frequency Ω of the excitation, (see Figure 5-14).

The distortions of the tower tip need special attention since they correspond to the location of the receiver array. The three components of displacements Δx , Δy , and Δz of the tower tip center joint 801 are plotted for the same 0.1 s cycle. The maximum distortion for any such component hardly goes beyond 2 μm and thus falls well within the stipulated feed tolerance (allowable $\Delta z = 1000 \mu\text{m}$, $\Delta y = \Delta x = 150 \mu\text{m}$) on defocus and decenter (see Figure 5-15).

In summary, the antenna surface distortions and feed motions resulting from the harmonic disturbance characterizing a cryo-cooler remain well below critical levels. As a consequence, the antenna performance should remain satisfactory for this loading.

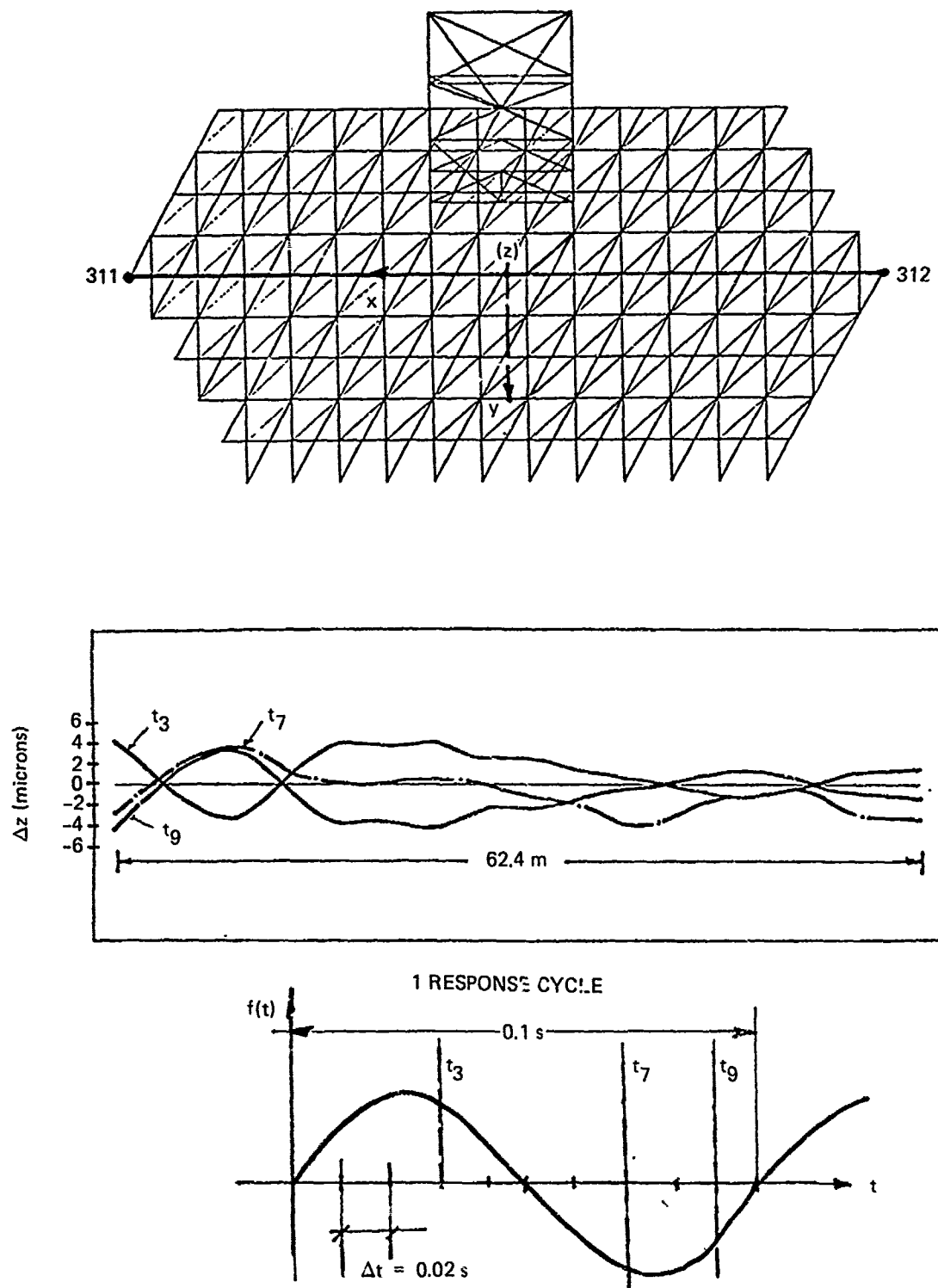


Figure 5-13. Reflector center line response to harmonic disturbance (2 displacements at 3 times).

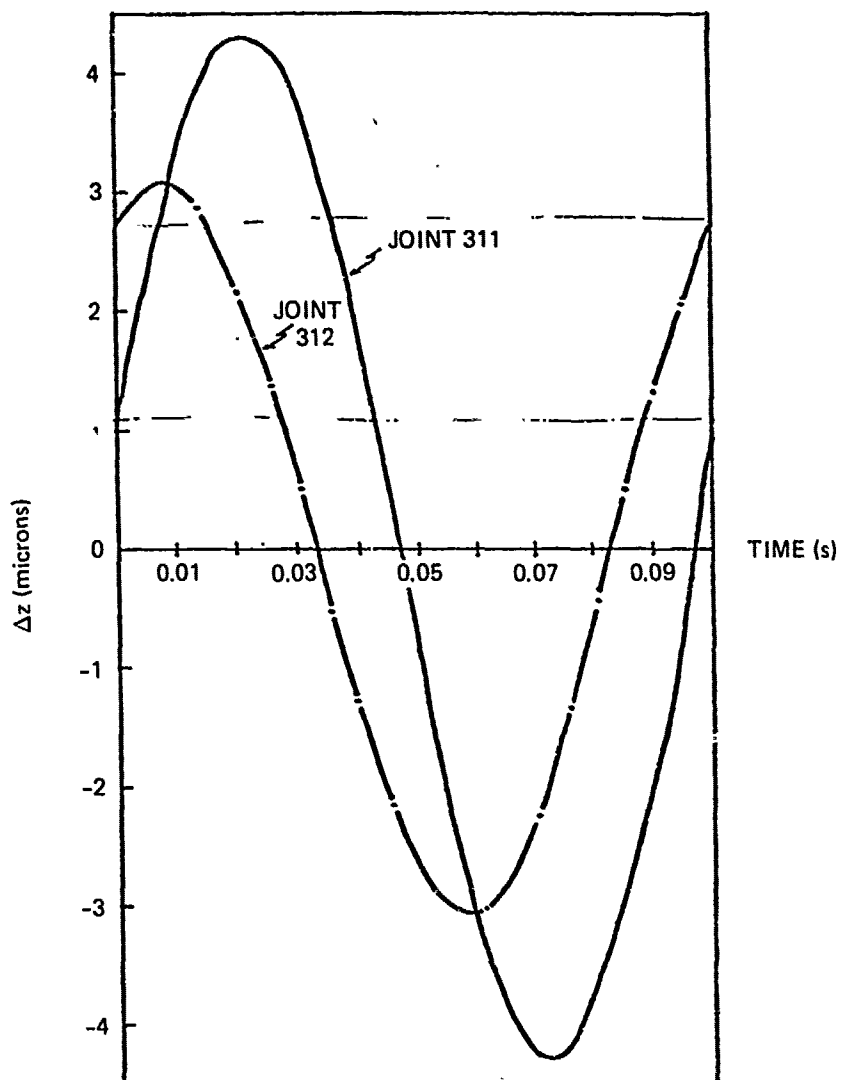


Figure 5-14. Reflector extreme points 311 and 312 Δz steady-state response cycle (0.1 s).
Disturbance: 15 N at 10 Hz.

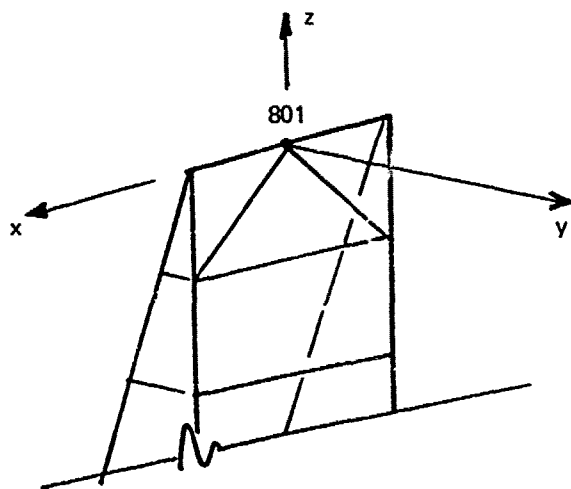
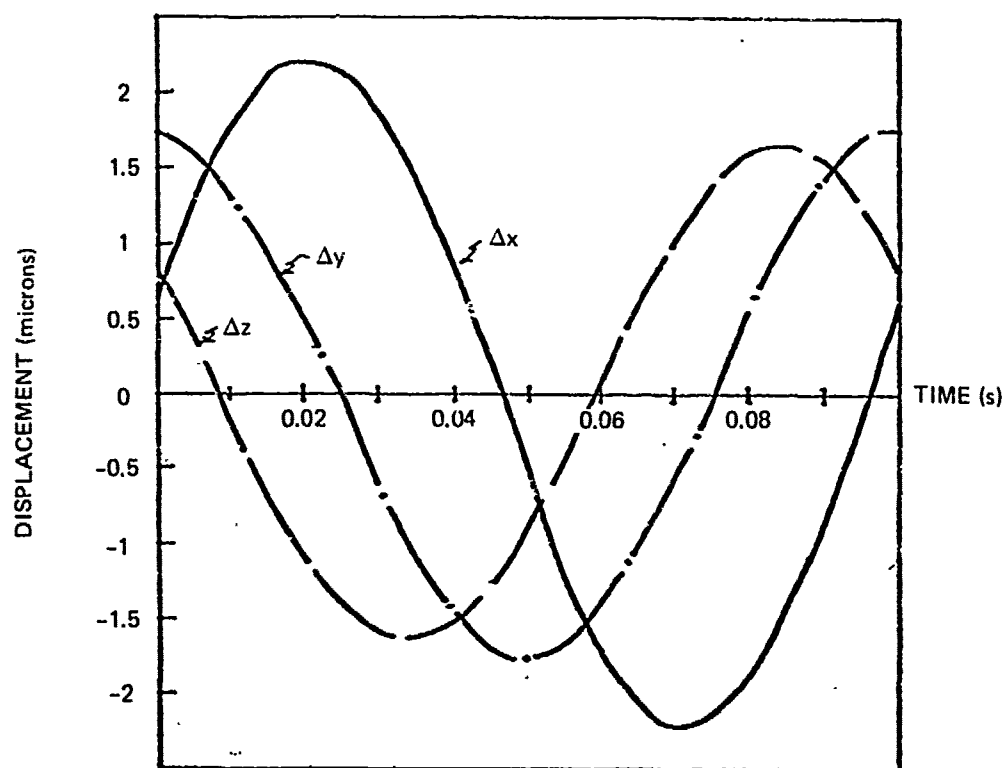


Figure 5-15. Tower tip joint 801 displacements for 1 cycle steady-state response to harmonic excitation (15 N at 10 Hz).

SECTION 6

DEGRADATION OF ANTENNA PERFORMANCE DUE TO SOLAR FLUX

6.1 Introduction

This section describes the degradation of point-spread functions (PSF) of a 30×60 m elliptic torus antenna due to its deformations produced by solar flux. The antenna is assumed to be operating at a wavelength of 3 mm with a cosine feed taper, and the materials considered are graphite-epoxy and aluminum. It is shown that the graphite-epoxy antenna performs much better than the aluminum antenna. Strehl ratios, line-of-sight error (LOS), power on detector, and profiles of the PSFs are given for three regions of the antenna. Airmat antennas were also considered, but owing to their large deformations ($\sim \lambda$) under solar flux, they were not investigated in any detail.

6.2 Antenna Description

Smoke, dust, fog, and clouds frequently prevent satellite-based observation of earth targets with visual and infrared sensors. The ability to penetrate these cover conditions and to perform equally well by night or day makes microwave passive sensing an attractive candidate to significantly extend the capabilities of satellite-based observations beyond their present limitations.

Passive microwave sensors respond to millimeter wave thermal radiation emitted by all objects in proportion to their temperature and surface emissivity. Useful sensing of military targets results predominantly from high contrasts of target emissivity with respect to the background surface. Oxygen and water vapor are the only atmospheric gases with significant absorptions. These combine to establish the clear air transmission windows centered at frequencies 35 GHz, 95 GHz, 140 GHz, and 230 GHz.

The reflector antenna under investigation is an elliptic torus having dimensions of 30×60 m. The feed horns are deployed on a cylindrical surface passing through the focal circle of the ellipses. The other focal circle lies on the surface of the earth. The design of the feed horns provides compensation for the aberration caused by circular cross track reflector profile. Each horn accepts incident energy from approximately half of the reflecting surface and provides for sidelobe control through proper tapering of the energy accepted.

As indicated in Figure 6-1, the antenna is made up of 124 hexagonal segments, the side of a hexagon being 2.25 m. The pupil is assumed to be circular and 30 m in diameter. Its apodization due to tapering of the accepted energy is assumed to be a cosine distribution such that it is unity at the center and zero at the edge of the pupil. The taper distribution outside the pupil was not available, and therefore it was assumed to be zero. The antenna is assumed to be operating at a wavelength of 3 mm corresponding to a frequency of 95 MHz. The system parameters are tabulated in Table 6-1.

Table 6-1. System Parameters

Antenna Shape	Elliptic Torus
Antenna Size	30 × 60 m
Focal Length	30 m
Pupil Diameter	30 m
Taper	Cosine
Wavelength	3 mm

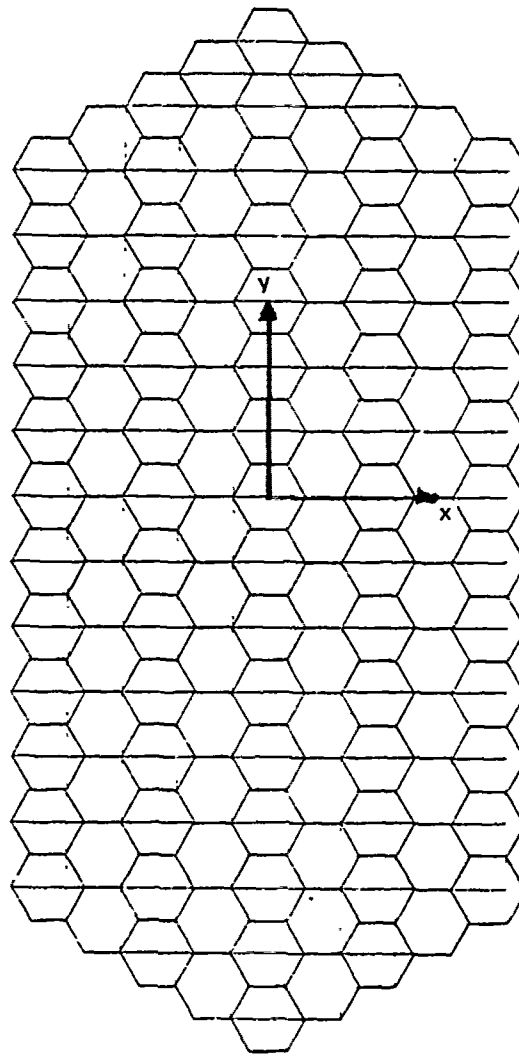


Figure 6-1. Elliptic torus 30 × 60 m segmented antenna. The total number of segments is 124.

6.3 Point-Spread Function Evaluation

The evaluation of the PSF on an imaging system in the presence of thermal and dynamic disturbances is described in "Computer Simulation of a Large Adaptive Optical System", by V. Mahajan and J. Govignon, reprinted from the Proceedings of the Society of Photo-Optical Instrumentation Engineers, January 29-February 1, 1979, Tuscon, Arizona. In this section, the evaluation of the PSF and associated quantities is considered for a circular pupil with cosine apodization.

Assuming an aberration-free antenna in the absence of thermal loading, the point-spread function (PSF), i.e., the irradiance distribution of the image of a point target, in the presence of thermal loading is given by

$$I(x,y) = \frac{1}{\lambda^2 f^2} \left| \iint P(u,v) \exp \left[-\frac{2\pi i}{\lambda f} (xu + yv) \right] du dv \right|^2 \quad (6-1)$$

where λ is the wavelength of the radiation and f is the focal length of the antenna. The effective pupil function $P(u,v)$ at a point (u,v) on the pupil is given by

$$\begin{aligned} P(u,v) &= A_0 \cos \left[\frac{\pi(u^2 + v^2)^{1/2}}{D} \right] \exp \left[\frac{2\pi i}{\lambda} \delta W(u,v) \right], \text{ inside the pupil} \\ &= 0, \text{ outside the pupil} \end{aligned} \quad (6-2)$$

where $D = 30$ m is the diameter of the pupil, A_0^2 is the irradiance at the pupil from the target, the cosine factor represents the feed taper, and δW is the wave aberration function of the antenna. The irradiance distribution $I(x,y)$ is the effective PSF of the antenna system.

To evaluate the diffraction integral in Eq. (6-1), by a discrete Fourier transform, we let

$$\begin{aligned} u &= j\Delta u \\ v &= k\Delta v \\ x &= \ell\Delta x \\ y &= m\Delta y \end{aligned} \quad (6-3)$$

where j, k, ℓ , and m are integers, and $(\Delta u, \Delta v)$ and $(\Delta x, \Delta y)$ are the spatial periods in the pupil and image planes, respectively. Therefore, Eq. (6-1) can be written

$$I(\ell\Delta x, m\Delta y) = \left(\frac{\Delta u \Delta v}{\lambda f} \right)^2 A_0^2 \left| \sum_{jk} P_{jk} \exp \left[-\frac{2\pi i}{\lambda f} (j\ell\Delta x \Delta u + km\Delta y \Delta v) \right] \right|^2 \quad (6-4)$$

where

$$P_{jk} = \frac{1}{A_0} P(j\Delta u, k\Delta v) \quad (6-5)$$

In our fast Fourier transform (FFT) program, the PSF is given by

$$I_{\ell m} = \frac{1}{N^2} \left| \sum_{jk} P_{jk} \exp \left[-2\pi i \left(\frac{j\ell}{N_u} + \frac{km}{N_v} \right) \right] \right|^2 \quad (6-6)$$

where $N_u \times N_v$ is the number of points in the FFT grid and N is the number of points inside the pupil. Note that Eq. (6-6) is normalized in such a way that the irradiance at the center of the image $I_{00} = 1$ when there are no aberrations and the magnitude of the pupil function is constant and equal to unity. Comparing Eqs. (6-4) and (6-6) we find that

$$I(\ell\Delta x, m\Delta y) = \left(\frac{\Delta u \Delta v}{\lambda f} \right)^2 A_0^2 N^2 I_{\ell m} \quad (6-7)$$

$$\Delta x = \lambda f / N_u \Delta u \quad (6-8)$$

$$\Delta y = \lambda f / N_v \Delta v \quad (6-9)$$

For uniform pupil irradiance A_0^2 from the target, the total power in its image is given by

$$\begin{aligned} P_t &= 2\pi A_0^2 \int_0^{D/2} \cos^2(\pi r/D) r dr \\ &= 0.2335 D^2 A_0^2 \end{aligned} \quad (6-10)$$

The fraction of power incident on a detector placed in the image plane is given by

$$P_d = \frac{1}{P_t} \iint_{\text{det}} I(x, y) dx dy \quad (6-11)$$

where the integration is carried over the detector area. If the detector is centered on the aberration-free image center and its size is $2j\Delta x \times 2j\Delta y$, then the fraction of power incident on it may be written

$$P_j = \frac{\Delta x \Delta y}{P_t} \sum_{\ell=-j}^j \sum_{m=-j}^j w_{\ell m} I(\ell\Delta x, m\Delta y) \quad (6-12)$$

where $w_{\ell m}$ are the weights of the integration rule used. Substituting Eqs. (6-7) and (6-10) into Eq. (6-12), we obtain

$$P_j = 4.28 \frac{N^2 \Delta u \Delta v}{N_u N_v D^2} \sum_{\ell=-j}^j \sum_{m=-j}^j w_{\ell m} I_{\ell m} \quad (6-13)$$

6.4 Antenna Aberrations Due to Solar Flux

As indicated in Figure 6-2, the thermal loading from the sun is at a maximum when the antenna, in a 500 km orbit from the surface of the earth, is at an angle of $\pm 68^\circ$ from the line joining the sun and the center of the earth. The antenna is heated nonuniformly and, therefore, deforms causing degradation of its performance. Assume that a certain point \vec{r}_i on the antenna surface moves to \vec{r}'_i because of the thermal loading. Let the displacement of the point be written

$$\delta \vec{r}_i = \vec{r}'_i - \vec{r}_i \quad (6-14)$$

For small $\delta \vec{r}_i$, the corresponding wave aberration contributed to a ray incident at the point \vec{r}_i is given by*

$$\delta W_i = -2\hat{n}_i \cdot \delta \vec{r}_i \cos \theta_i \quad (6-15)$$

where \hat{n}_i is a unit vector along the normal to the antenna surface at the point \vec{r}_i , and θ_i is the angle of incidence of the ray on the undeformed surface.

The wave aberration is positive if the path length is increased and negative if it is decreased. For simplicity, we assume that $\cos \theta_i \approx 1$ so that

$$\delta W_i = -2\hat{n}_i \cdot \delta \vec{r}_i \quad (6-16)$$

We also assume that a point (u,v) on the pupil is identical to a corresponding point on the antenna surface.

In the evaluation of the antenna performance, each hexagonal segment was represented as shown in Figure 6-3, by a periodic array of 30 points. The spatial periods along the u and v axes were $\Delta u = 0.675$ m and $\Delta v = 0.650$ m, respectively. The slight difference in the two spatial periods has to be accommodated in order to achieve continuity of the array from segment to segment. The corresponding distribution of points in a 30 m diameter circular pupil is shown in Figure 6-4.

* V. Mahajan and J. Govignon, "Computer Simulation of a Large Optical System", the Proceedings of the Society of Photo-Optical Instrumentation Engineers, January 29-February 1, 1979, Tuscon, Arizona, p. 440, Eo. 4.

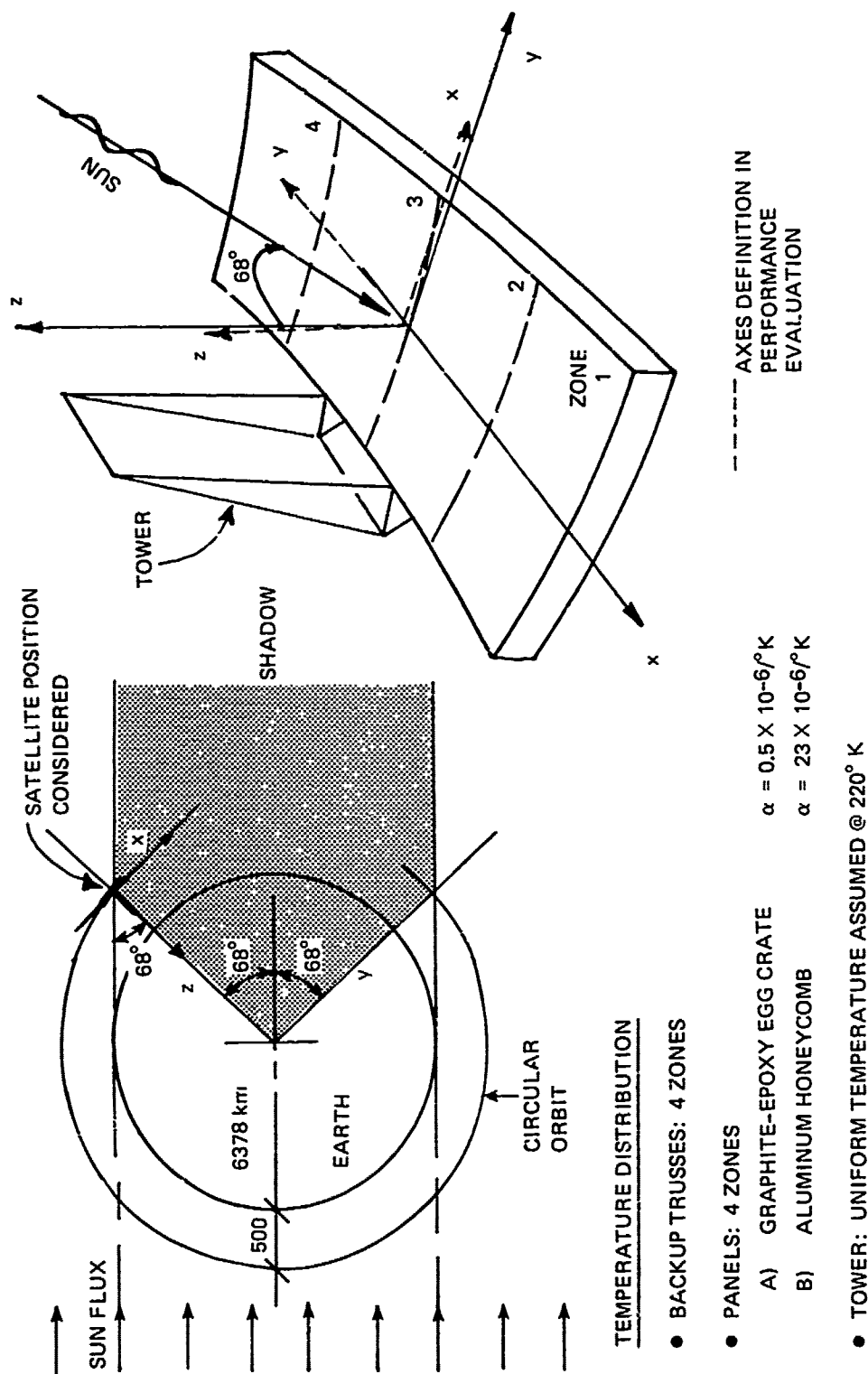


Figure 6-2. Thermal loading due to sun.

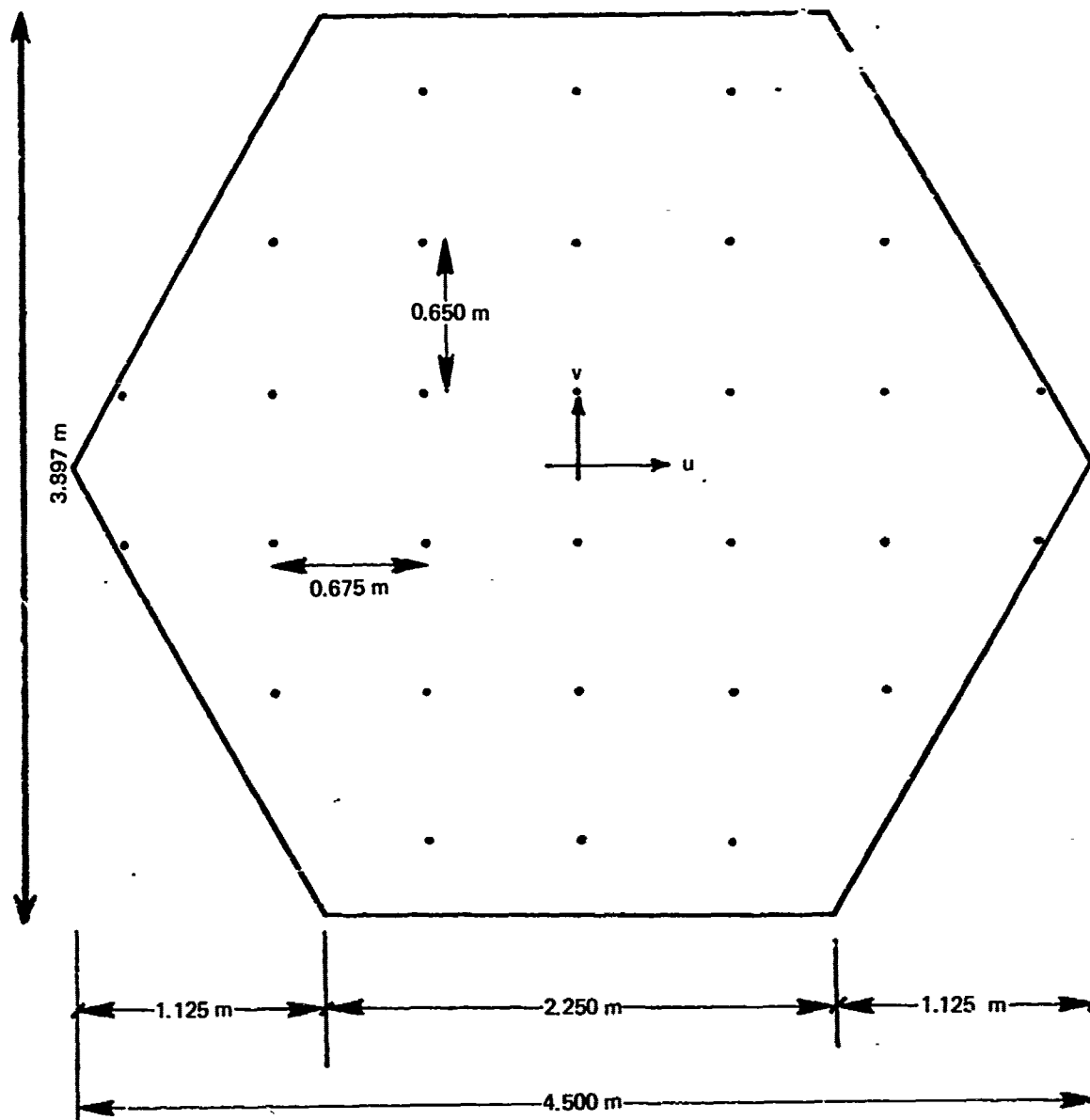


Figure 6-3. Antenna segment showing distribution of points at which deformations were calculated. There are 30 points on a segment.

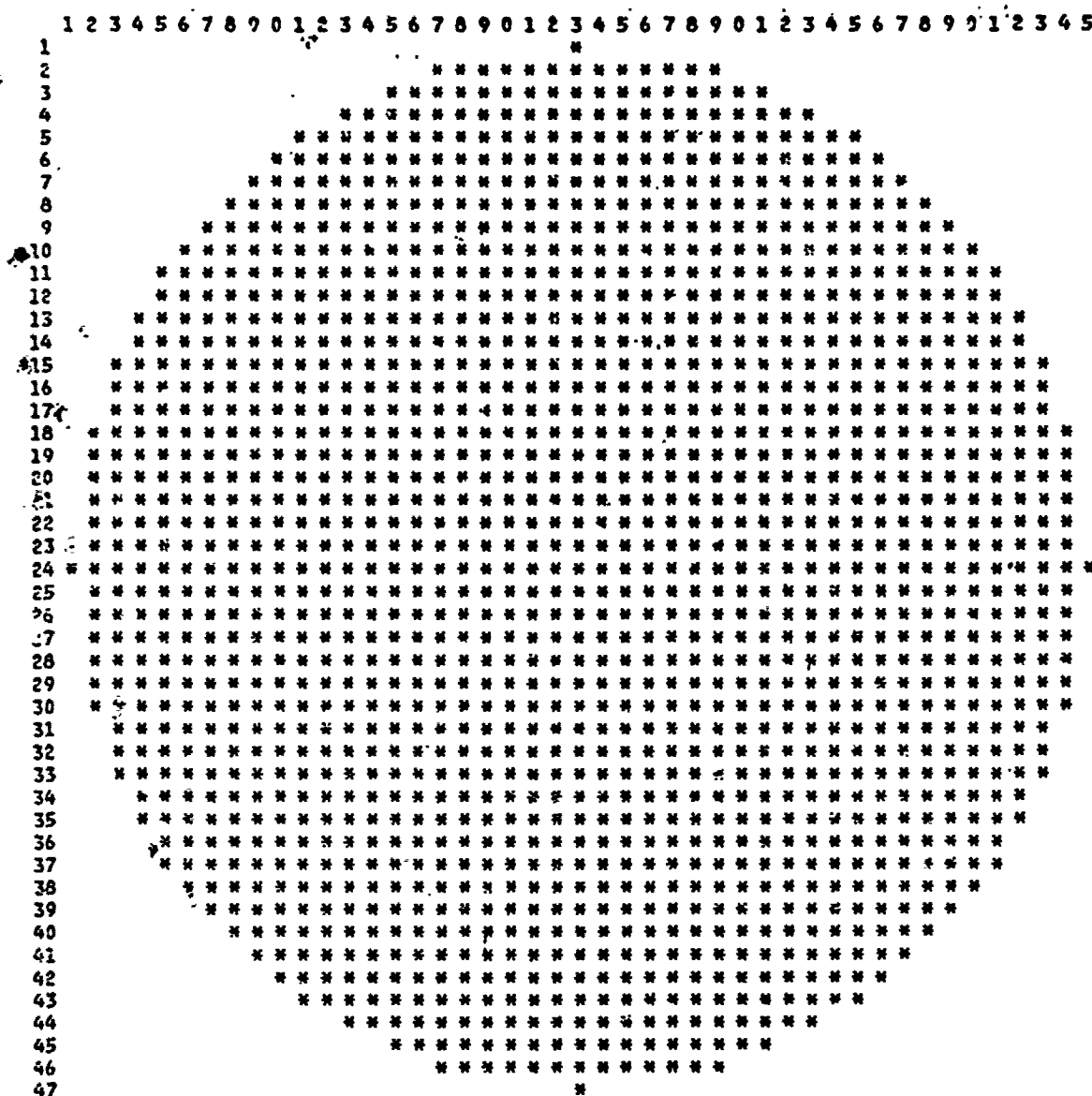


Figure 6-4. Distribution of pupil points. The total number of points inside a circle of 30 m diameter is 1575. The spacings between two adjacent points along the u and v axes are $\Delta u \approx 0.675$ m and $\Delta v = 0.650$ m.

As indicated in Figure 6-2, the antenna was divided into 4 zones. Only one segment within a given zone was analyzed for its faceplate warping due to the solar flux, and all the other segments within that zone were assumed to behave similarly. However, the rigid-body movements of a segment due to the trusses were calculated for each segment. The combined effect of faceplate warping and truss bending gave the net deformation of a segment.

The numbers of points along the u and v axes are chosen to be odd so as to define a center of the pupil and they are equal to 47 and 45, respectively. The total number of points in the pupil are 1575, i.e., $N = 1575$. The deformations due to the solar flux were determined at antenna points lying in an array of 47×97 points. As indicated in Figure 6-5, the center of the pupil was chosen at three different positions:

- (1) (0, 19)
- (2) (0,0)
- (3) (0,-19)

The peak-to-peak and standard deviation of aberration of the whole antenna and portions of it corresponding to pupils centered at the three positions for both graphite-epoxy and aluminum antennas are given in Table 6-2.

Table 6-2. Antenna Aberrations in Millimeters due to Solar Flux

Material	Peak-to-Peak Aberration				Standard Deviation of Aberration			
	Antenna	Pupil Position			Antenna	Pupil Position		
		1	2	3		1	2	3
Graphite-Epoxy	0.94	0.34	0.32	0.70	0.15	0.07	0.05	0.16
Aluminum	1.71	0.54	0.76	1.45	0.30	0.11	0.15	0.28

6.5 Results

The PSFs have been determined by using an FFT grid for which $N_u = N_v = 256$. The various evaluation parameters are tabulated in Table 6-3. The effect of the solar flux on the PSFs is shown in Figures 6-6 and 6-7 for the graphite-epoxy and aluminum antennas, respectively. In these figures, the antenna performance is indicated by two numbers: the Strehl ratio S and the LOS error. The Strehl ratio represents the central irradiance of the PSF relative to its value in the absence of the solar flux. The quantity $100(1 - S)$ is generally referred to as the percent loss in antenna gain. The LOS error was defined as the movement of the location of the peak irradiance of the PSF. Note that the Strehl ratio is degraded significantly in the case of aluminum antenna compared to the graphite-epoxy antenna. Moreover, position 3, which corresponds to maximum solar flux, gives the smallest Strehl ratio in both cases.

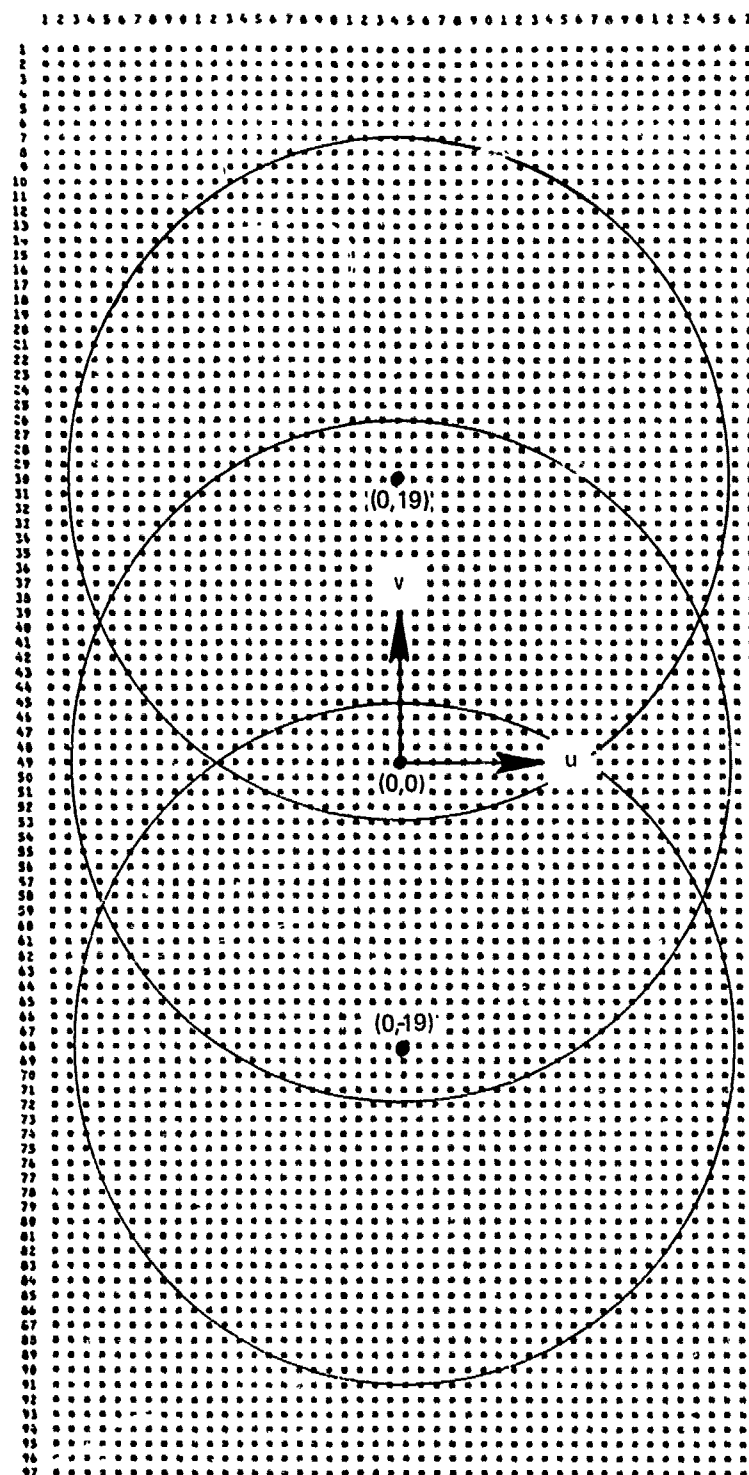


Figure 6-5. Pupil locations on the antenna.

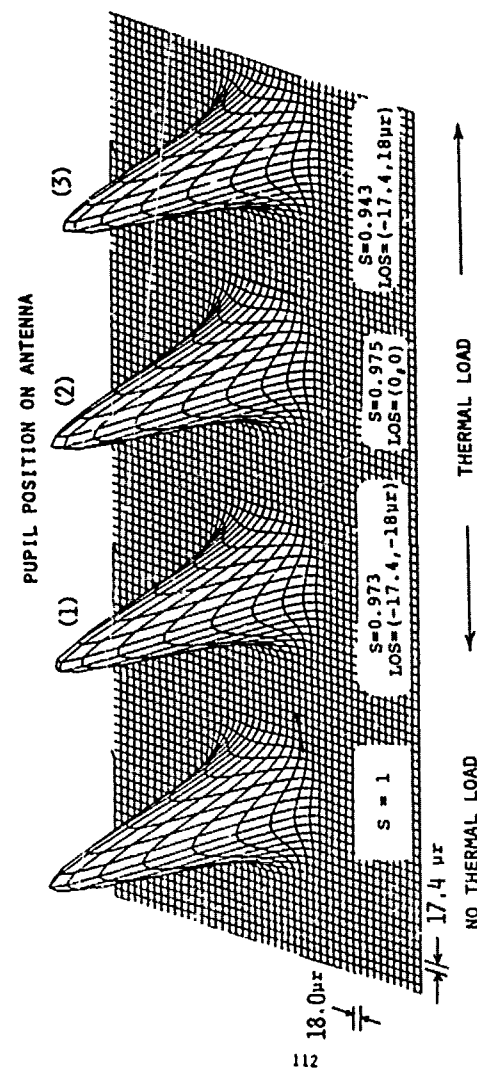


Figure 6-6. Aberration-free and degraded PSFs for graphite-epoxy antenna.

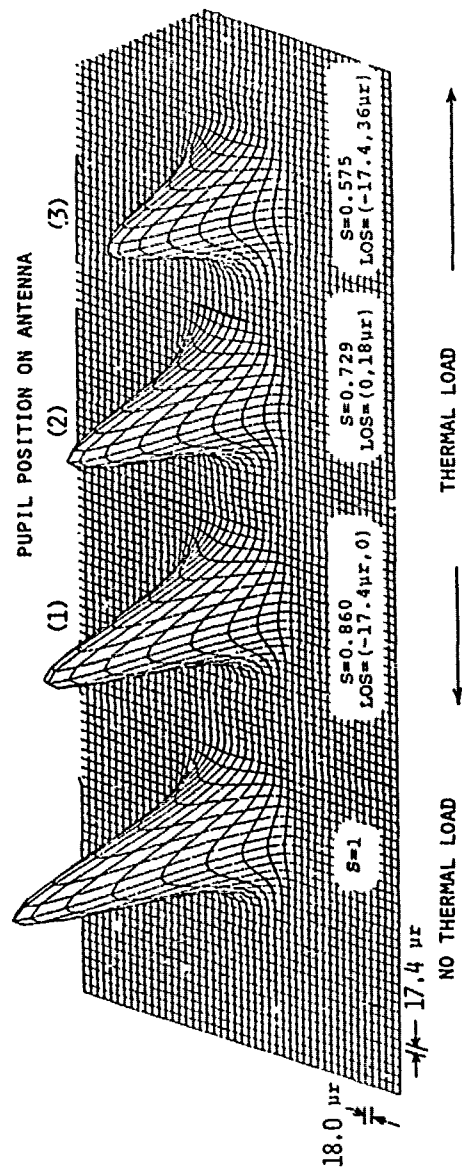


Figure 6-7. Aberration-free and degraded PSFs for aluminum antenna.

Table 6-3. PSF Evaluation Parameters

No. of points in pupil	$N = 1575$
Pupil sampling interval	$\Delta u = 0.675 \text{ m}$ $\Delta v = 0.650 \text{ m}$
PSF sampling interval	$\Delta x = 0.52 \text{ mm}, \Delta \alpha = 17.4 \text{ } \mu\text{rad}$ $\Delta y = 0.54 \text{ mm}, \Delta \beta = 18.0 \text{ } \mu\text{rad}$
FFT grid size	$N_u = 256, N_v = 256$

From Eqs. (6-8) and (6-9) we note that the spatial periods of the PSF data points are given by

$$\begin{aligned}\Delta x &= \frac{\lambda f}{N_u \Delta u} \\ &= 0.52 \text{ mm}\end{aligned}\tag{6-17}$$

and

$$\begin{aligned}\Delta y &= \frac{\lambda f}{N_v \Delta v} \\ &= 0.54 \text{ mm}\end{aligned}\tag{6-18}$$

The corresponding spatial periods in angular units are given by

$$\begin{aligned}\Delta \alpha &= \frac{\Delta x}{f} \\ &= 17.4 \text{ } \mu\text{rad}\end{aligned}\tag{6-19}$$

and

$$\begin{aligned}\Delta \beta &= \frac{\Delta y}{f} \\ &= 18.0 \text{ } \mu\text{rad}\end{aligned}\tag{6-20}$$

Since the FFT grid size is 256×256 the total image area covered by the PSF data is $133 \times 138 \text{ mm}$, or $4.43 \times 4.61 \text{ mrad}$.

The LOS error, which was determined in units of $(\Delta \alpha, \Delta \beta)$, can be determined more accurately by determining the center of the reference sphere with respect to which the variance of the aberrations is minimum. The centroid

of the PSF can also be defined as the LOS. However, in this report the LOS was defined simply as the location of the peak irradiance in the PSF data as determined by the FFT program. It is evident from Figures 6-6 and 6-7 that the LOS error is much larger than the tolerance value of 5 μ rad.

Details of the PSF for a circular pupil with cosine taper are shown in Figure 6-8, where a central profile along the x-axis is plotted. The PSF is normalized so that its value at the center is unity. The linear and angular units of the horizontal scale are 0.52 mm and 17.4 μ rad, as given by Eqs. (6-16) and (6-18), respectively. Figure 6-8 shows approximately 20 sidelobes. Because of the solar flux on the antenna, the irradiance of the sidelobes increases. This is shown in Figures 6-9a through 6-9f for the three pupil positions on the graphite-epoxy antenna. Central profiles along the x and y axes are shown. The linear and angular units of the horizontal scale for the y-profiles are 0.54 mm and 18.0 μ rad, respectively. The principal sidelobes in these profiles, two in the x and one in the y profiles, occur because of the grating effects produced by the segmented nature of the antenna and the manner in which the deformations in a given zone of the antenna were compiled. The irradiance value noted in Figures 6-9a through 6-9f is the maximum value of irradiance in the profile relative to a central value of unity for the aberration-free case. Similar results for the aluminum antenna are shown in Figures 6-10a through 6-10f. These figures show how the sidelobe structure changes. The poor performance of the aluminum antenna is evident from Figure 6-10f. Numerical analyses of these results were not carried out. For example, the irradiance of the far-off sidelobes shown in all of the figures cannot be too accurate because of aliasing in the FFT operation.

The fraction of power P_j incident on a detector in the image plane is shown as a function of detector size j in Figure 6-11. Again, note the significant degradation of detector power (a measure of antenna performance) in the case of the aluminum antenna compared to the graphite-epoxy antenna.

6.6 Discussion and Conclusions

The performance of graphite-epoxy and aluminum antennas operating at a wavelength of 3 mm has been evaluated when they are irradiated by solar radiation. The degradation of the PSFs due to antenna warping caused by solar flux is given in terms of Strehl ratio, LOS error, power on an image-plane detector, and sidelobe structure. It is shown that the LOS error is much above the tolerance value, and that a graphite-epoxy antenna performs much better than an aluminum antenna. Airmat antennas were also considered, but owing to their large deformations ($\sim \lambda$) under solar flux, they were not investigated in any detail.

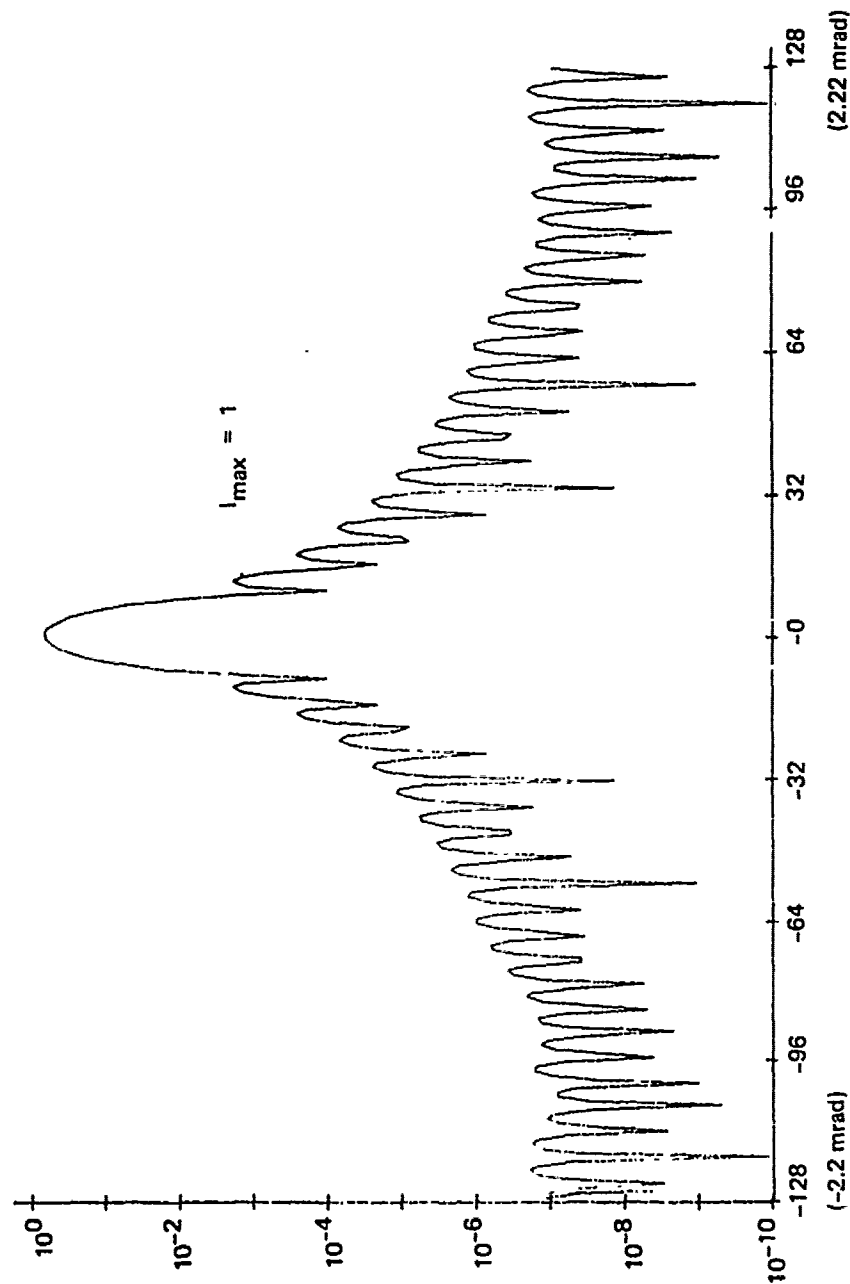


Figure 6-8. PSF profile along the x axis. The central value is unity. The linear and angular units of the horizontal scale are 0.52 mm and 17.4 μ rad, respectively.

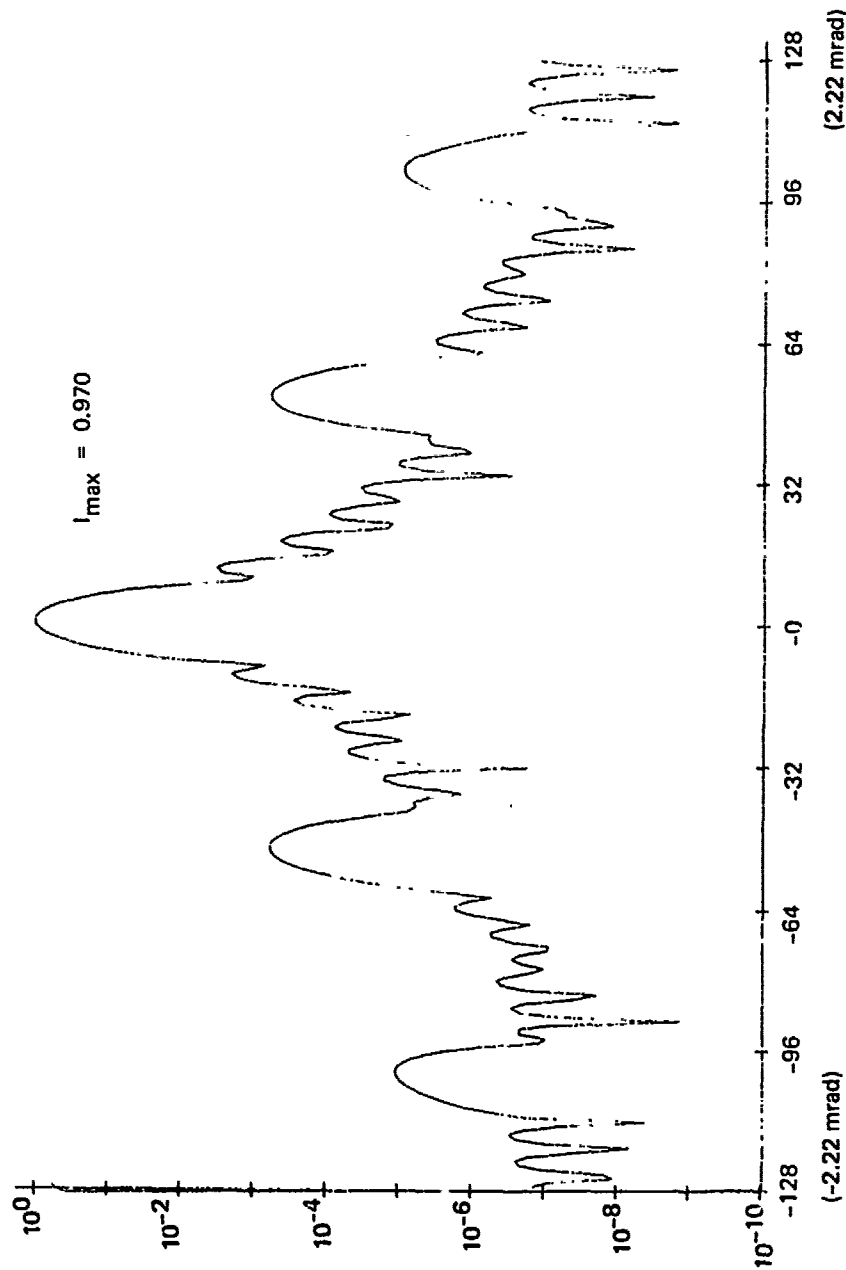


Figure 6-9a. Sidelobe structure for graphite-epoxy antenna under solar flux. PSF x-profile for pupil position 1.

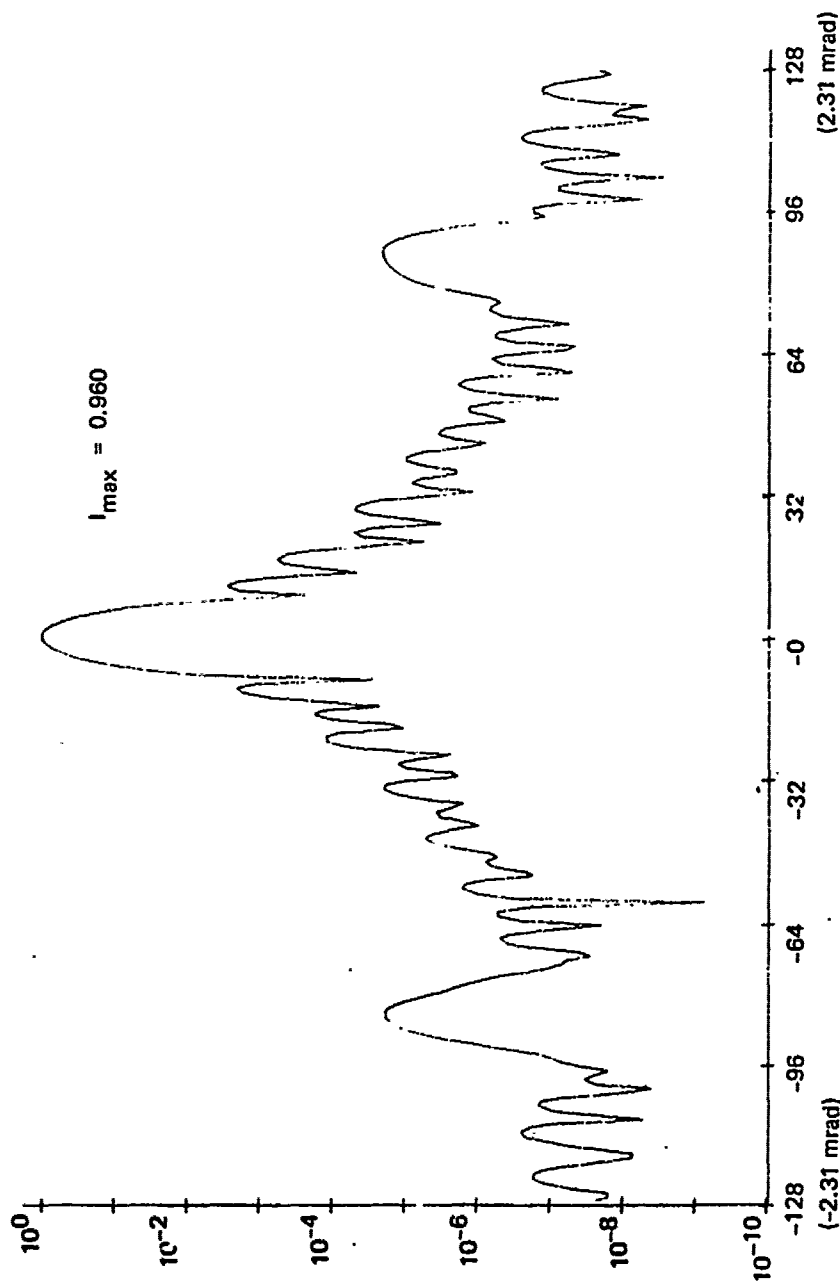


Figure 6-9b. PSF y-profile position 1. The linear and angular units of the horizontal scale are 0.54 mm and 18 μrad , respectively.

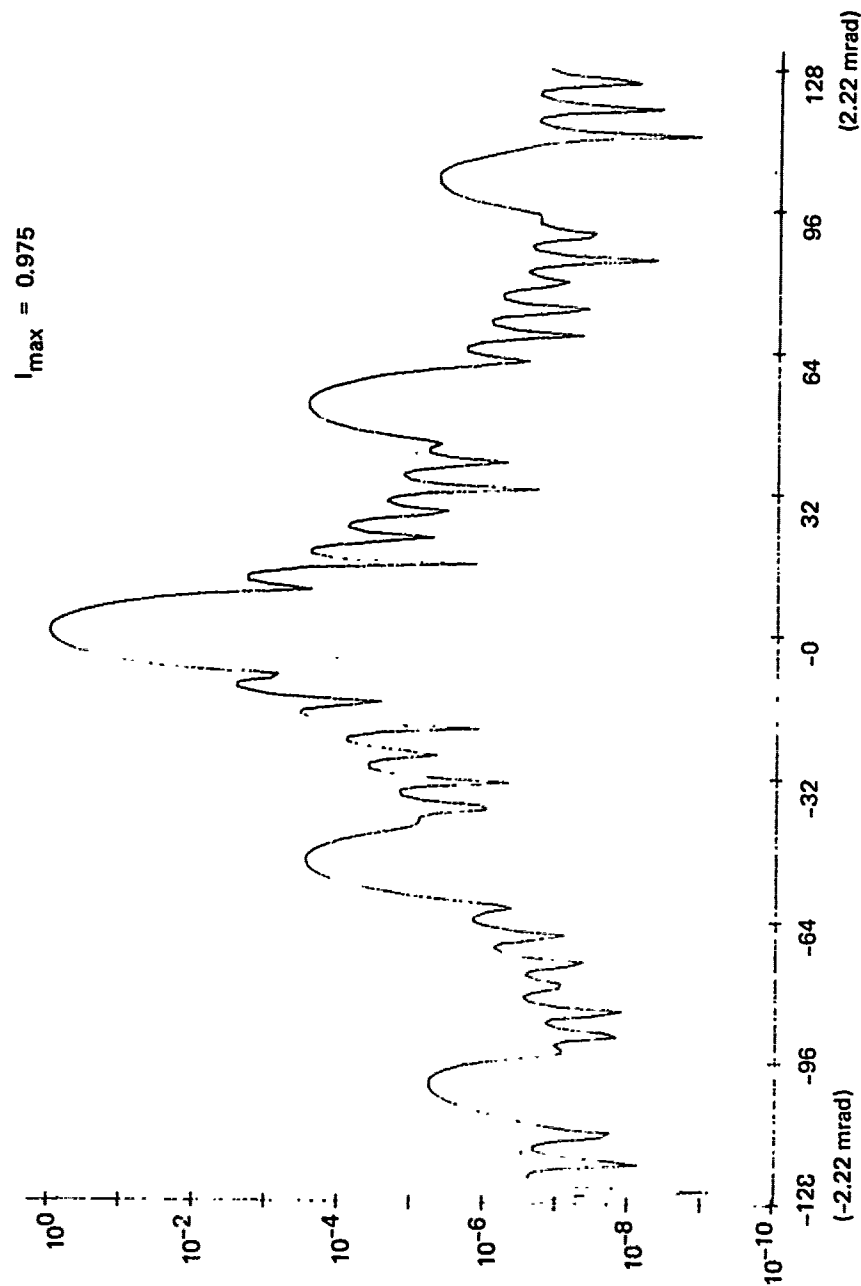


Figure 6-9c. PSF x-profile for pupil position 2.

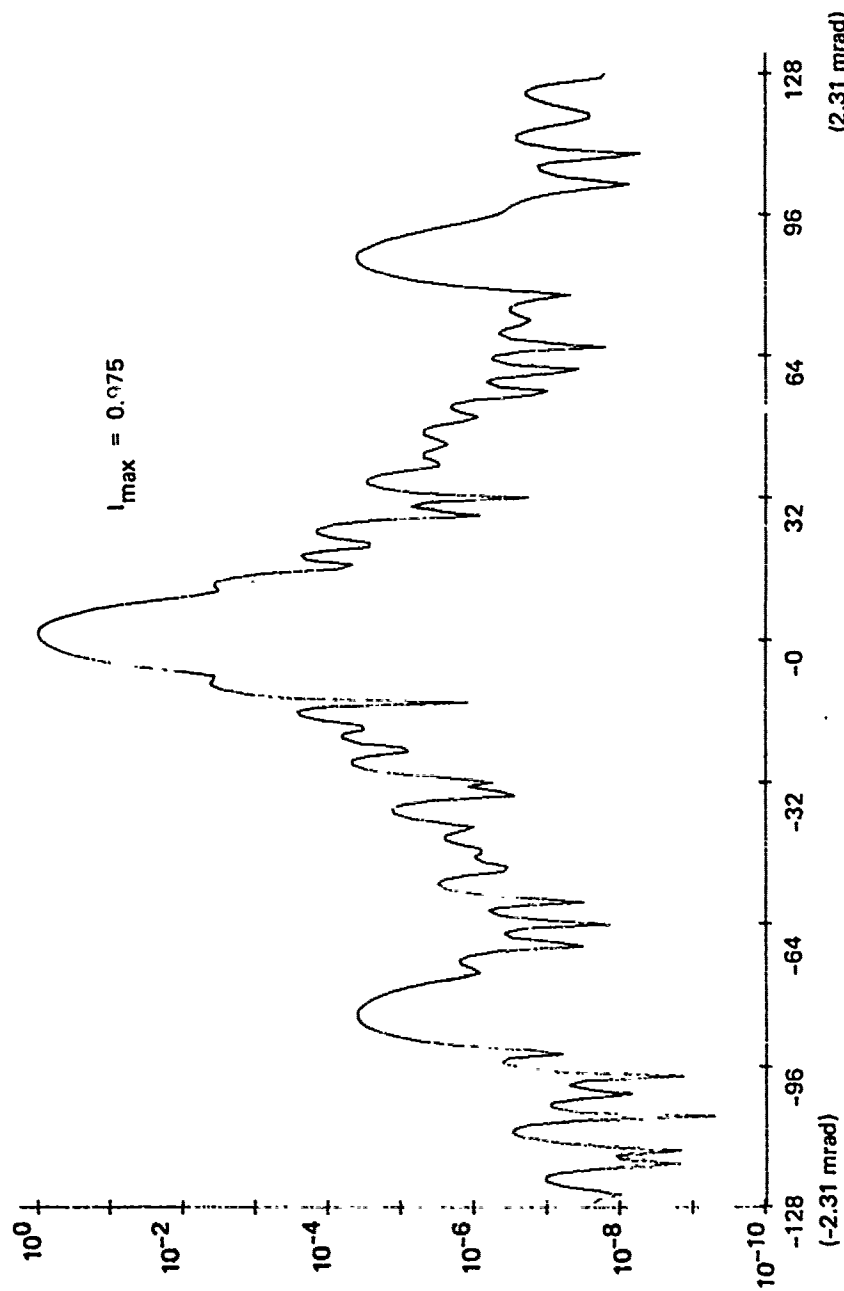


Figure 6-9d. PSF y-profile for pupil position 2.

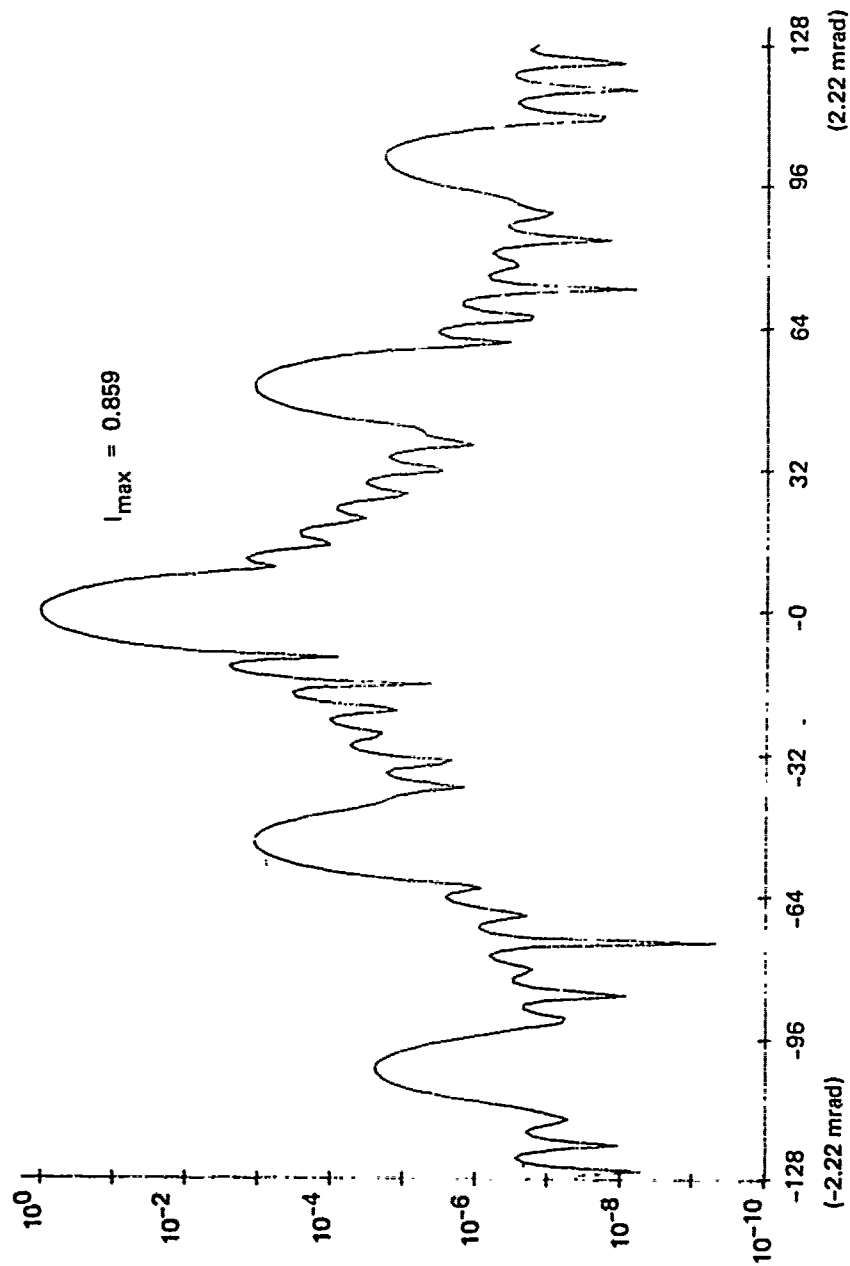


Figure 6-9e. PSF x-profile for pupil position 3.

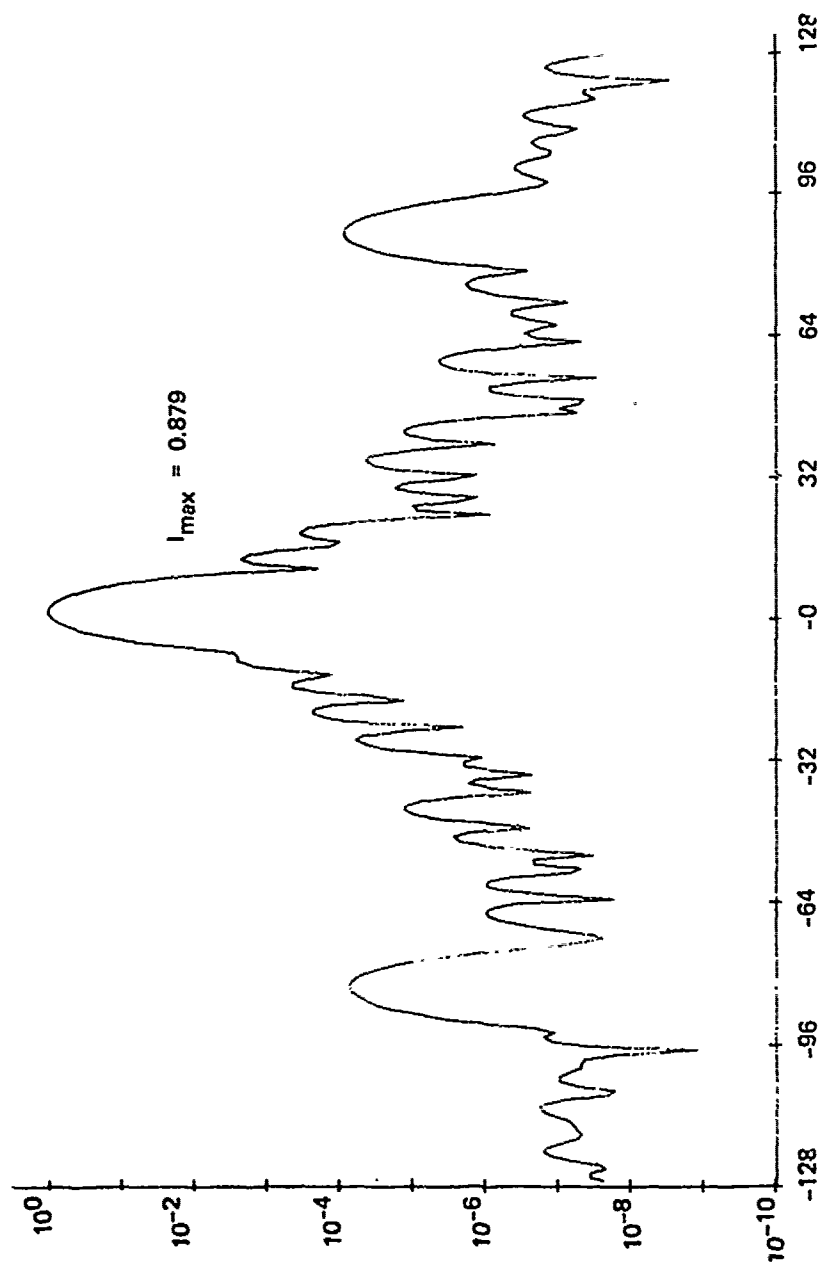


Figure 6-9f. PSF y-profile for pupil position 3.

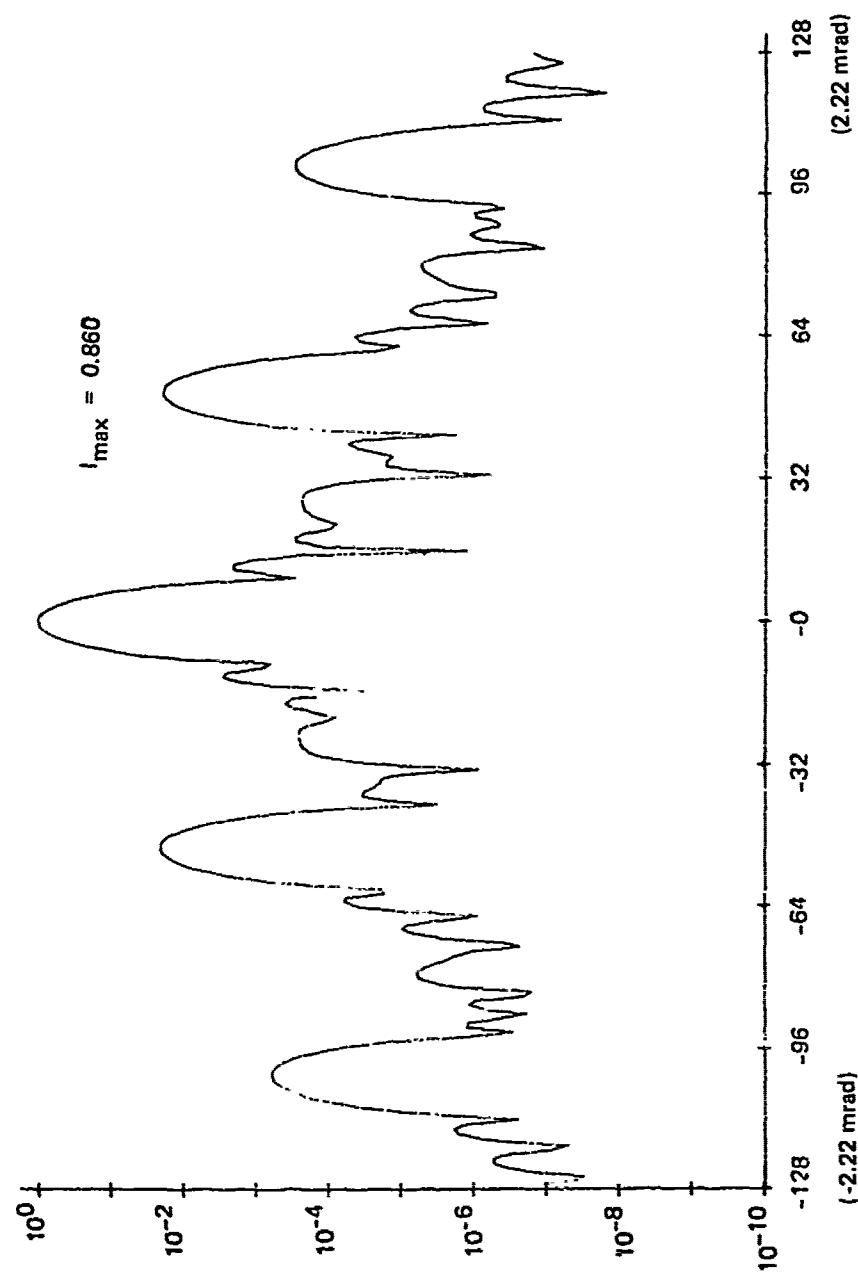


Figure 6-10a. Sidelobe structure for aluminum antenna under solar flux. PSF x-profile for pupil position 1.

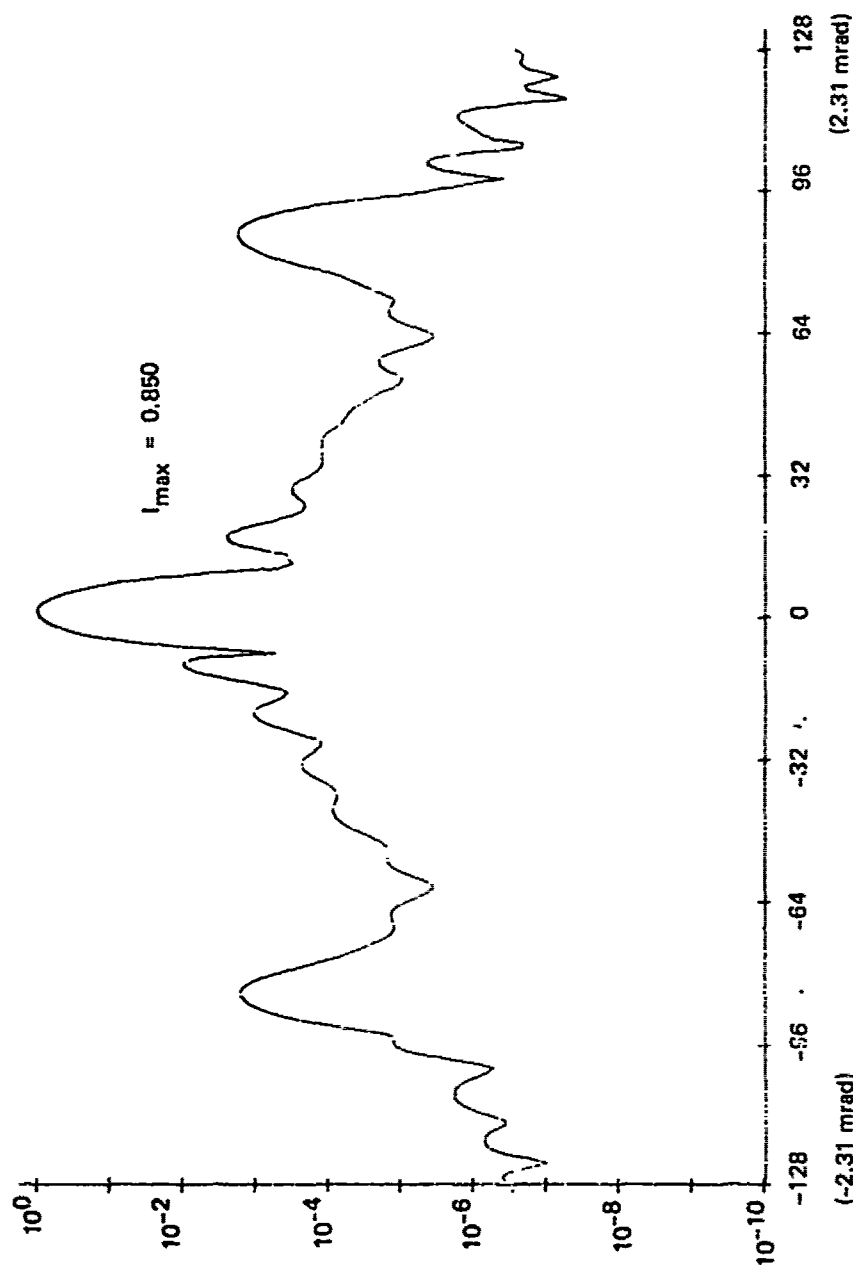


Figure 6-10b. PSF y-profile for pupil position 1.

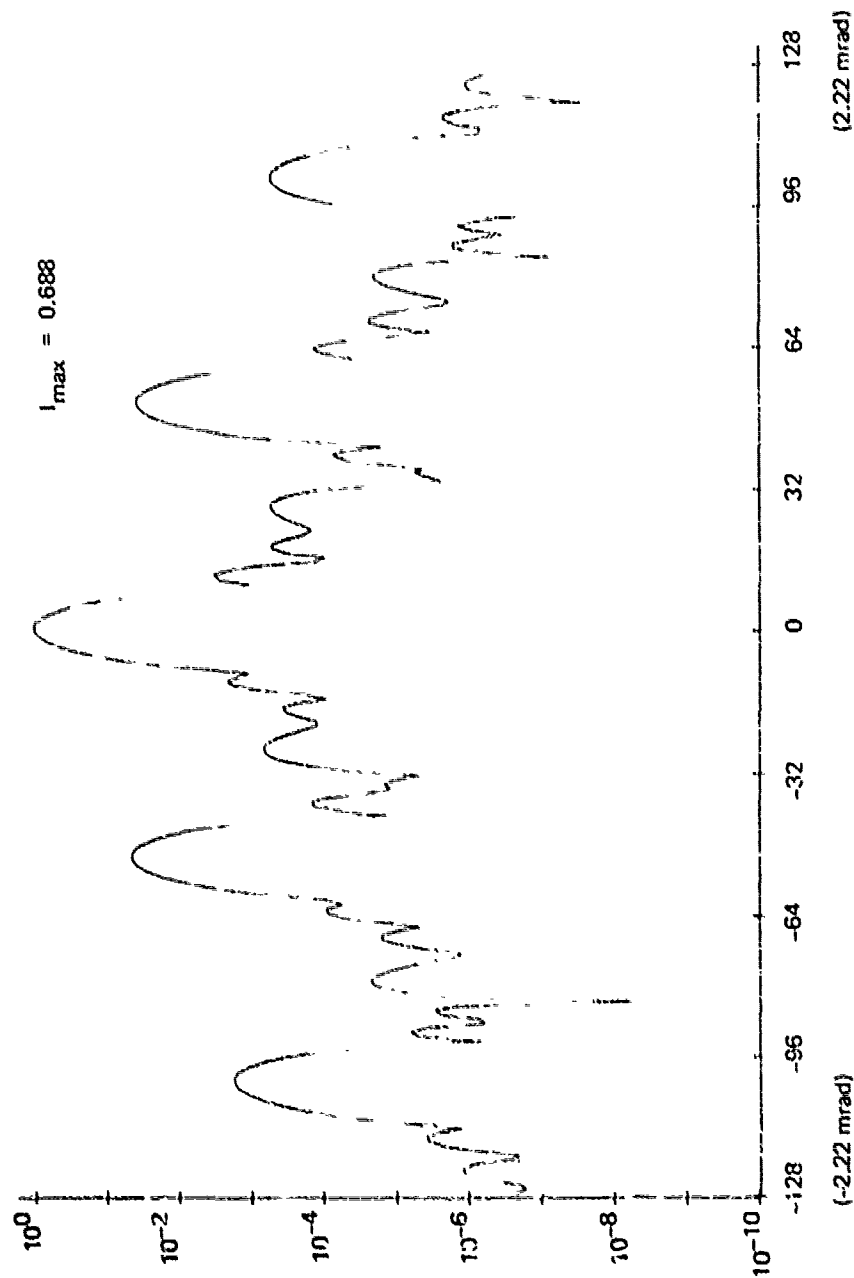


Figure 6-10c. PSF x-profile for pupil position 2.

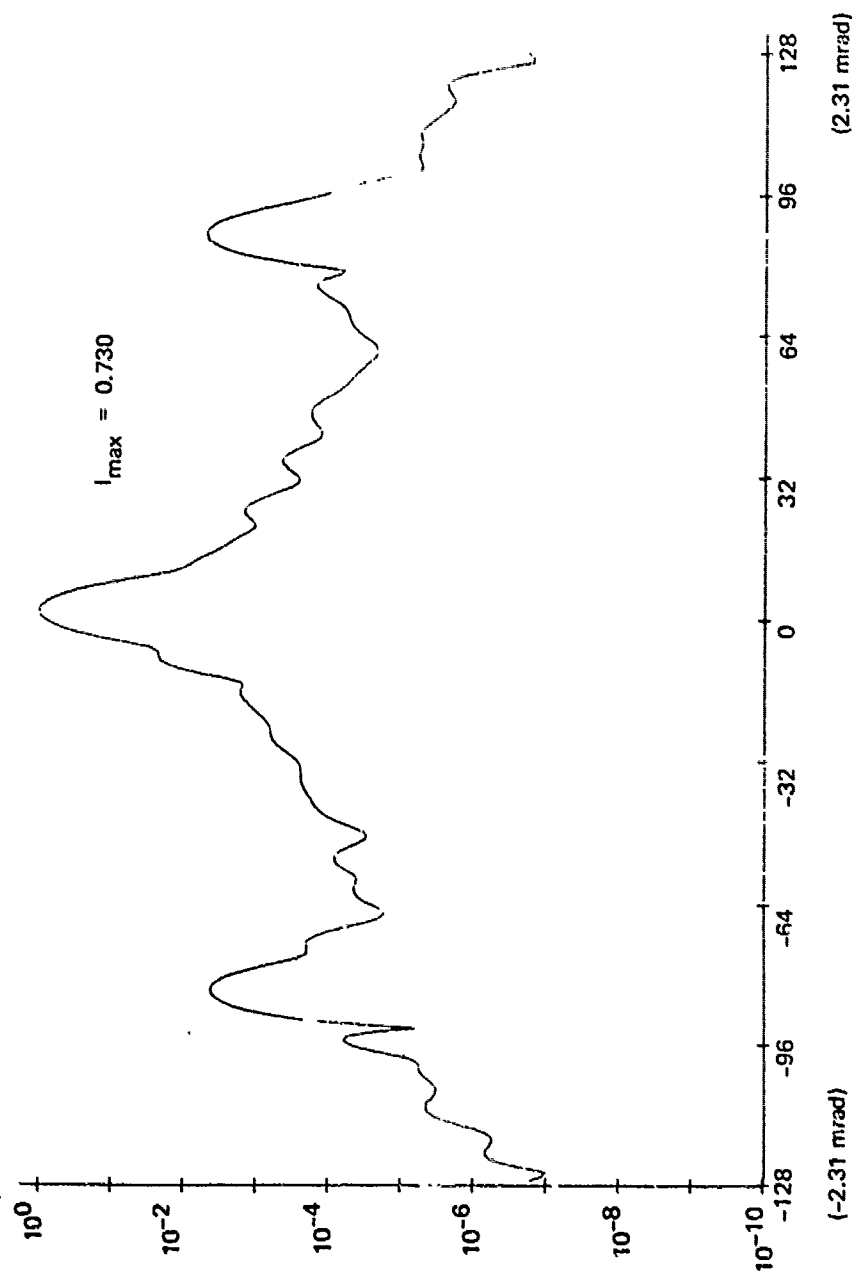


Figure 6-10d. PSF y-profile for pupil position 2.

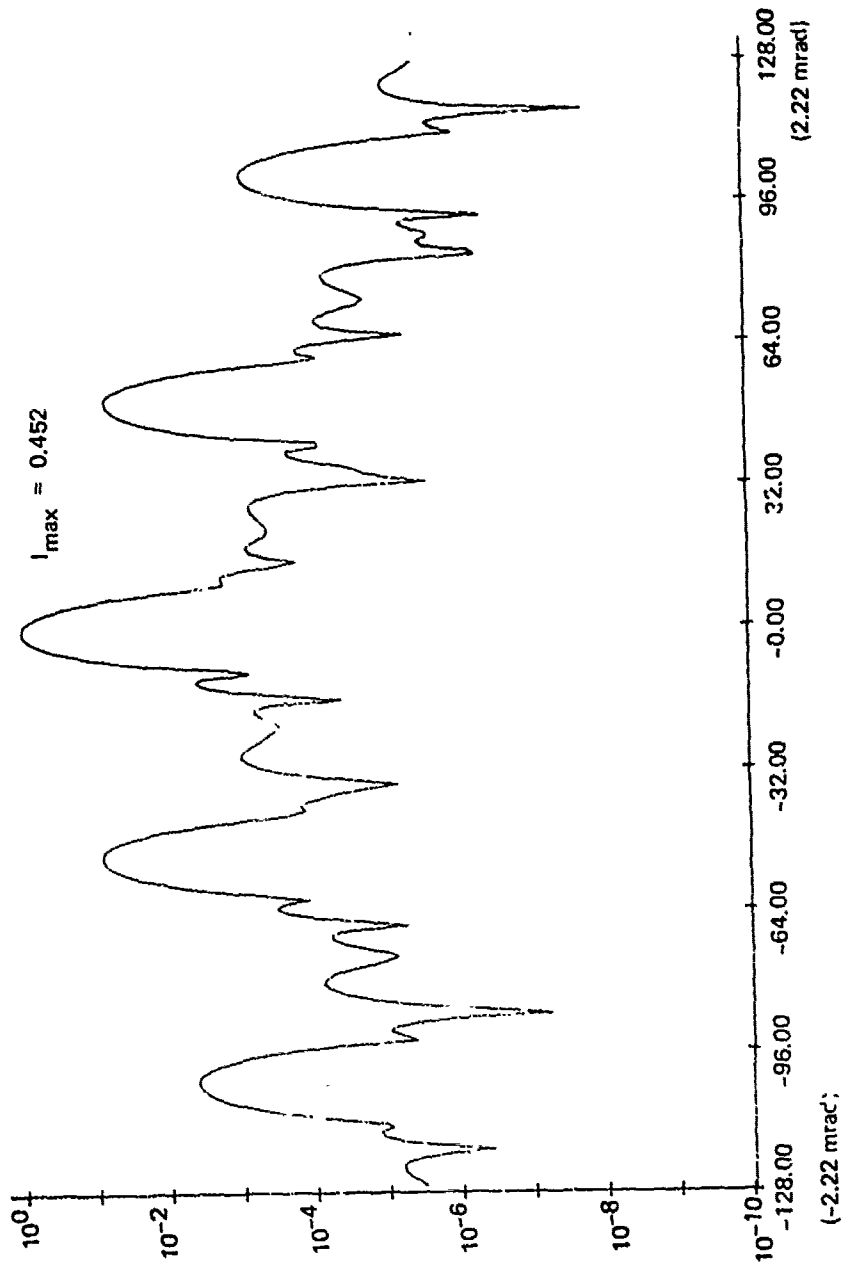


Figure 6-10e. PSF x-profile for pupil position 3.

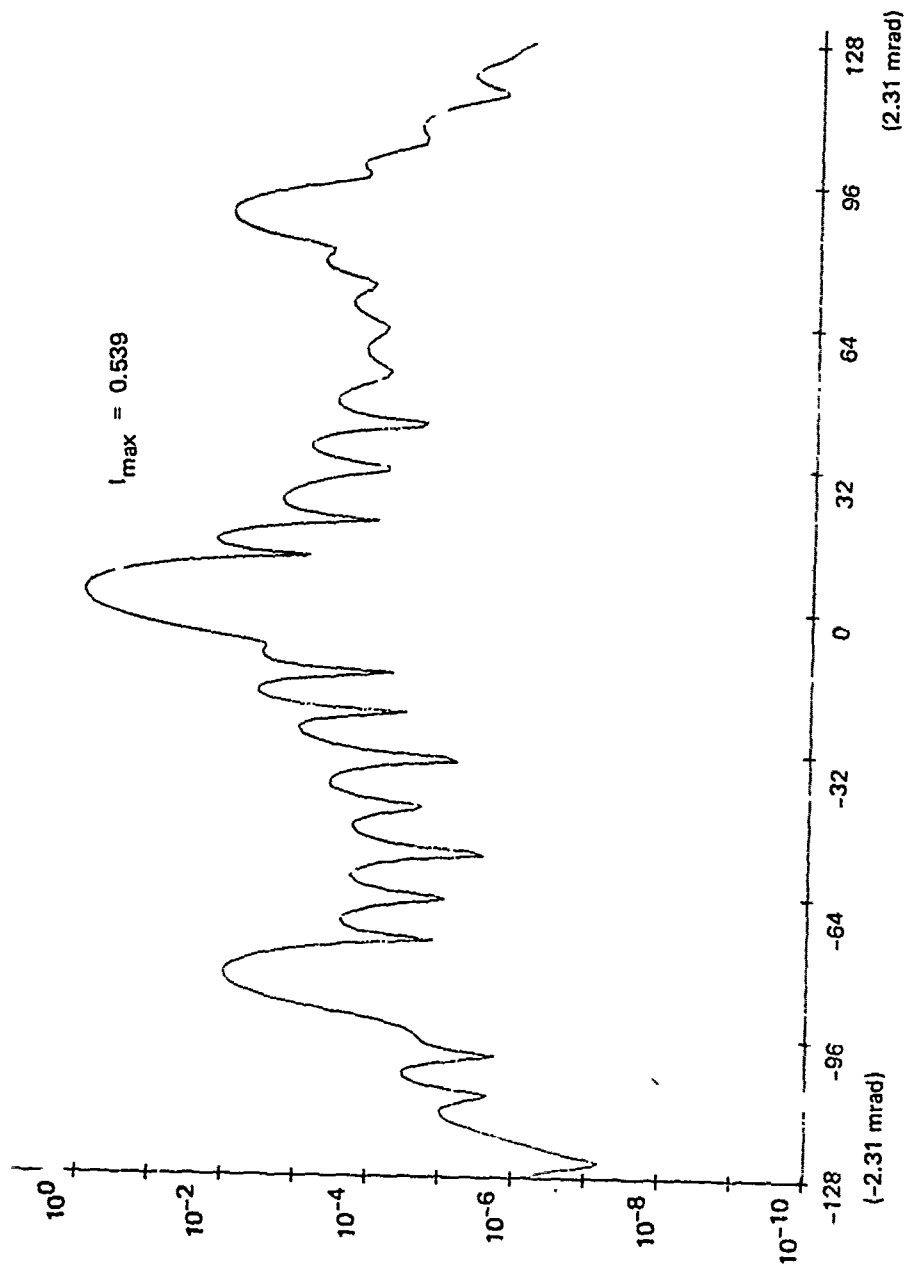


Figure 6-10f. PSF y-profile for pupil position 3.

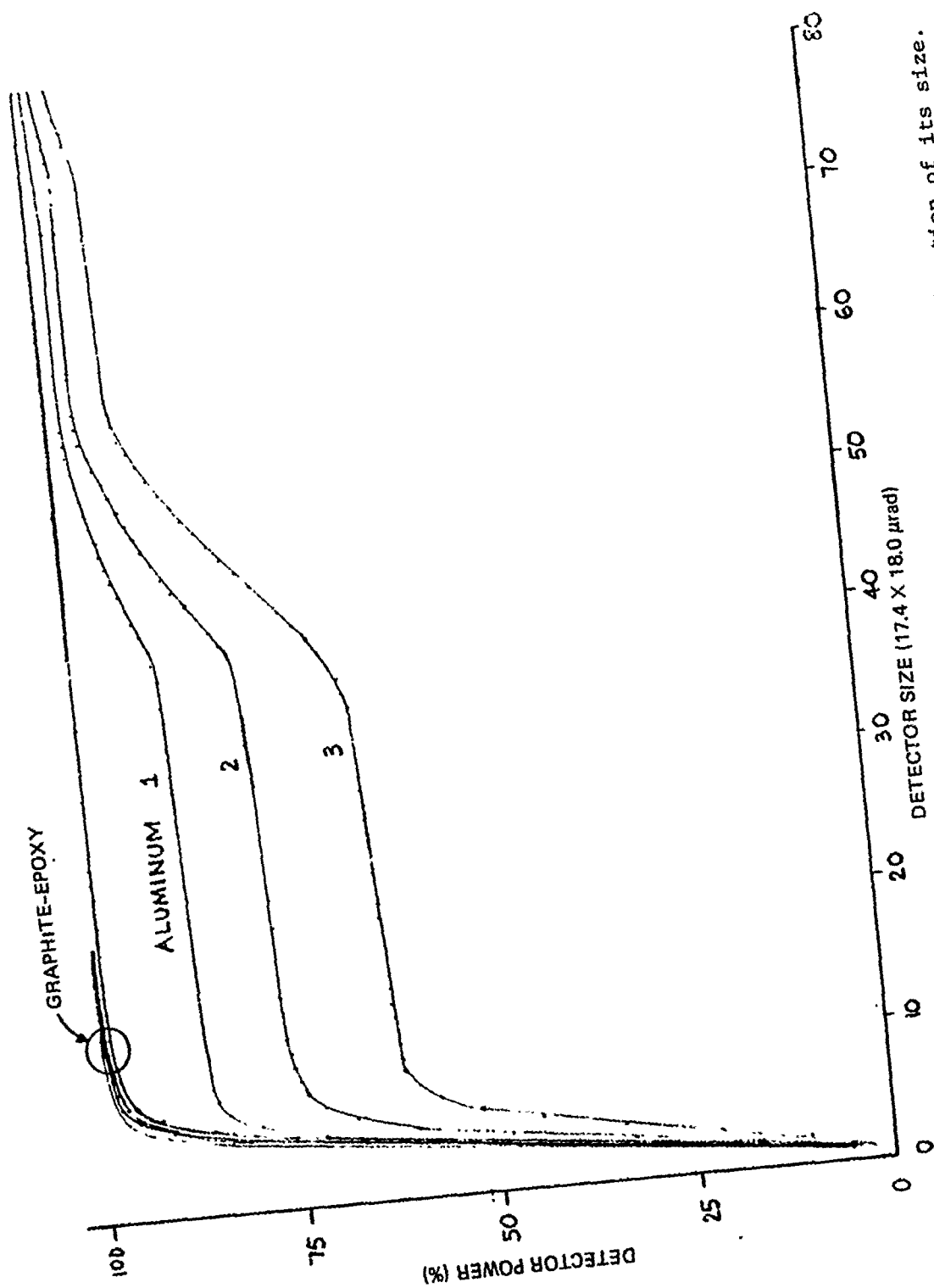


Figure 6-11. PSF power on a centered detector as a function of its size.

SECTION 7

PACKAGING AND DEPLOYMENT

7.1 Introduction and Issues

As the size of the reflector increases and surface accuracy requirements remain relatively stringent, the launching and orbit injection of an entire satellite poses a very challenging problem. The severe size and volume constraints imposed by the cargo bay of the Space Shuttle, in combination with the required high deployment reliability, increase the complexity of the folding and deployment technique. Efficient folding, packaging and stowing of the space structure into a relatively small volume become important factors in the satellite design trade-offs, since they impact all the structural components and may affect their respective performance. (See surface panel design trade-offs in Section 4.3).

The relative merits of folding and deployment concepts can be evaluated as a function of the following parameters

- (1) overall packaging ratio
- (2) design size and concept
 - inflatable
 - variable geometry
 - segmented
- (3) symmetry and components repetitiveness
- (4) folding mechanical complexity
- (5) reliability

The segmentation approach must be considered in close connection with the problems involved with the contemplated mode of in-orbit assembly, including the choice of parking or final orbit. Automated deployment and erection, remotely controlled, computer controlled, or with man-in-the-loop, can be alternatives resulting from trade-offs between cost, design complexity and reliability.

The launch vehicle dynamic characteristics also strongly affect the folding technique which needs to provide the stowed package with protection from the effect of launch acceleration and vibration. Temporary supports and ties can be provided for launch in order to ensure the integrity of satellite components.

The deployment procedure relies on mechanical devices such as hinges, spring flexure joints, locking mechanisms that will undoubtedly increase the design complexity. For a precision structure, trade-offs between performance, reliability and structural deployment complexity must be evaluated. It

appears possible to enhance simplicity by enforcing certain symmetry characteristics of the folding scheme. A reflector, if divided and packaged in a symmetrical manner, provides a desirable repeatability for the algorithm of surface accuracy control of its identical panels. The preservation of symmetry, even if it creates some additional mechanical complexity in deployment, is strongly recommended. Manufacturing complexity and cost are also reduced by the repetitive fabrication of similar reflector panels.

It is evident that the packaging and deployment schemes affect the structural design philosophy. The desirable features for an efficient design of a large deployable structure and the issues associated with the various phases from design to deployment are summarized in Table 7-1. It is apparent that they are strongly interactive, often equivalent, and sometimes complimentary. The overriding need is to maximize the stiffness of the structure by distributing the allocated mass in the most efficient manner. But the design concept must remain amenable to an acceptable packaging technique. This exemplified the need for an integrated approach that ultimately satisfies the simultaneous requirements of performance, packaging, and deployment.

7.2 Packaging Concept for the MMW Antenna Structure

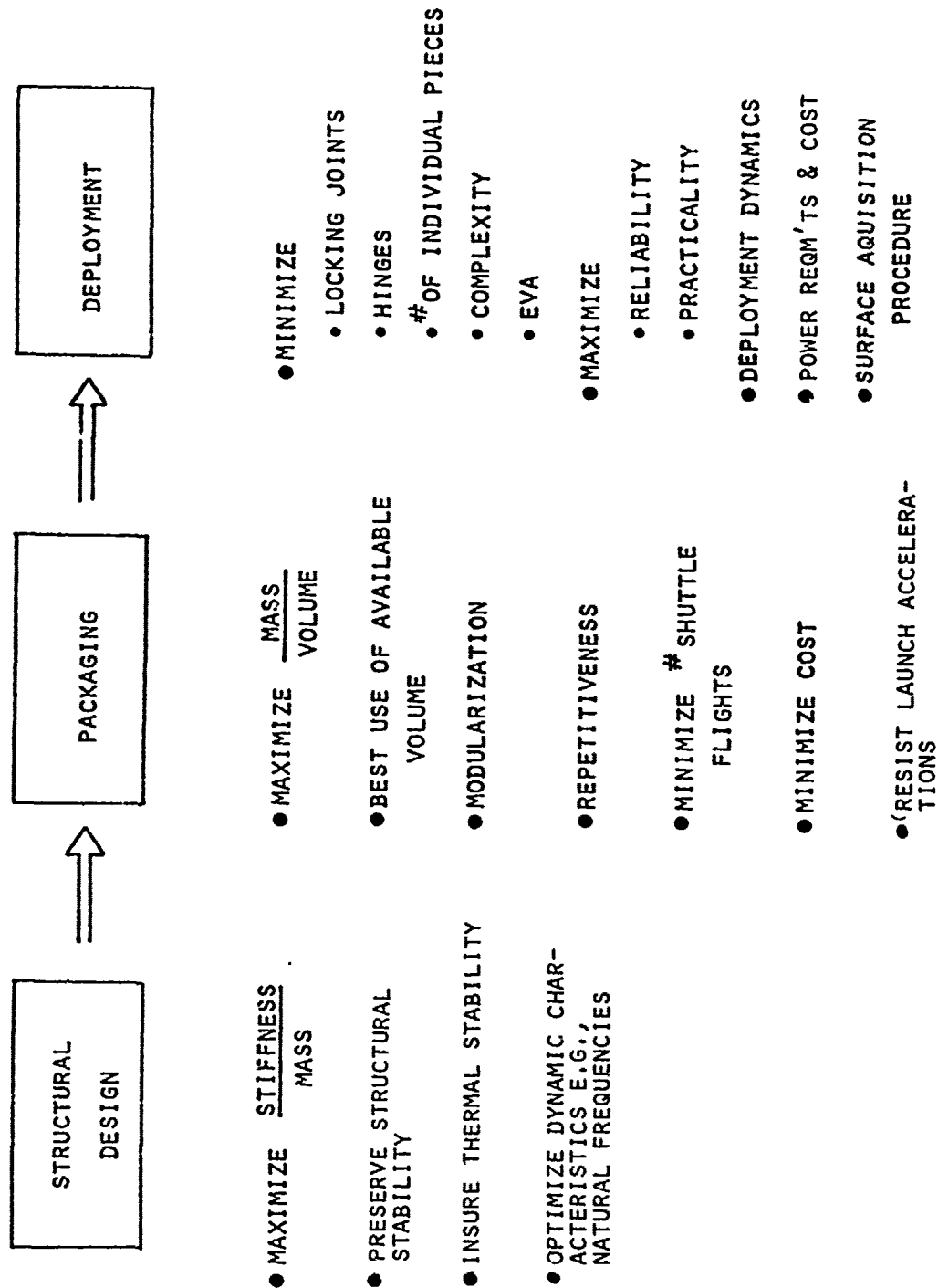
One of the main objectives of this study was to demonstrate that a large MMW antenna performing adequately without the help of active control can be packaged and launched in a single shuttle cargo. It should be realized that the antenna performance relying on passive means of control only translates naturally into increased stiffness and thus, additional mass. In view of the large reflector size and relatively heavy structure, any packaging technique becomes a challenging problem.

While a complete packaging and deployment procedure can not be presented here, an attempt is made to show how it is indeed possible to stow the large MMW antenna structures in a single shuttle cargo bay (the volume available is a cylinder 18.28 m long and 4.57 m in diameter). A procedure for stowing the 124 reflector panels and the packaging of the back-up trusses and other satellite components in the shuttle cargo bay is suggested below.

The reflector panels have been designed as thin curved plates with a hexagonal shape so as to most efficiently use the circular shape of the cargo bay. When stowed back-to-back as "stacked wafers" the 124 panels, 6 cm in thickness, fill up 7.80 m of the cylindrical bay. The first panel in the stack takes up another 8 cm due to its curvature and a spacing of 0.2 cm is allowed between each plate.

The remaining volume is available for the back-up trusses, the tower frame and the various satellite components and hardware. An estimate of the volume required by the packaging of truss sections indicates that it would fit well within the remaining 10.5 m of the cargo. Unlike some folding techniques requiring hinges for the collapsible trusses at every member end, the technique recommended attempts to limit to a minimum the number of movable joints.

Table 7-1. Structural, packaging and deployment issues.



This can be reasonably achieved by using thin-wall open cross-sections for all the truss members. The shape selected is an angle with small lips in order to ensure a reasonable factor of safety against instability. Whereas the traditional tube, (the most efficient axial member) is difficult to pack efficiently, the open section lends itself to a high packaging ratio. While the first truss section has a width of 5 cm, each additional truss can be nested into the previous one, adding only the thin-wall thickness of 0.2 cm and some 0.2 cm clearance to the package. In order to give an idea of the volume required to stow the entire truss work, the longitudinal and transverse 1.5 m deep trusses are assumed to be cut into 10.5 m long sections. Approximately 100 pieces are needed so that they can fit in a parallelepiped of 1.5 m \times 0.40 m \times 10.5 m. The remaining top and bottom diagonals could be stacked as individual members, thus requiring very little space. To be conservative, however, it was assumed that the top and bottom faces were made of 3.9 m deep horizontal trusses. Using the same approach to the packaging of these horizontal trusses, the required volume has dimensions of 3.9 m \times 0.40 m \times 10.5 m.

The members forming the tower frames are thin-wall tubes, 10 cm in diameter. Because of their span, these members have been designed as tubes to exhibit good bending capabilities. Although many simple folding techniques can be advocated, the tubes are simply shown stacked up in some of the remaining available space of the cargo.

Figure 7-1 shows the relative position of the satellite components stowed in the shuttle cargo bay. It can be visualized that the suggested folding procedure still leaves ample room for the additional hardware such as the receiver array package, the communication antennas, the thermal blankets, etc. Although it is possible that a more complete study of this packaging approach could require slightly more volume to accommodate various connection hinges and locking mechanisms, the additional space that would be required is available. It is, therefore, possible to assert that the MMW antenna structure can be packaged into a single shuttle cargo bay.

The use of thin-wall open sections for the truss members presents a number of interesting possibilities for efficient packaging of trusses. Among those considered, Figure 7-2 illustrates the possible folding of an incomplete space truss in which some folded diagonal members make efficient use of the available space between members of the fixed trusses. Although this procedure is preliminary and has shortcomings in terms of structural efficiency (e.g., eccentricities) it is worth pursuing since it may lead to a more automatic deployment while minimizing the number of hinges and ensuring a good packaging ratio.

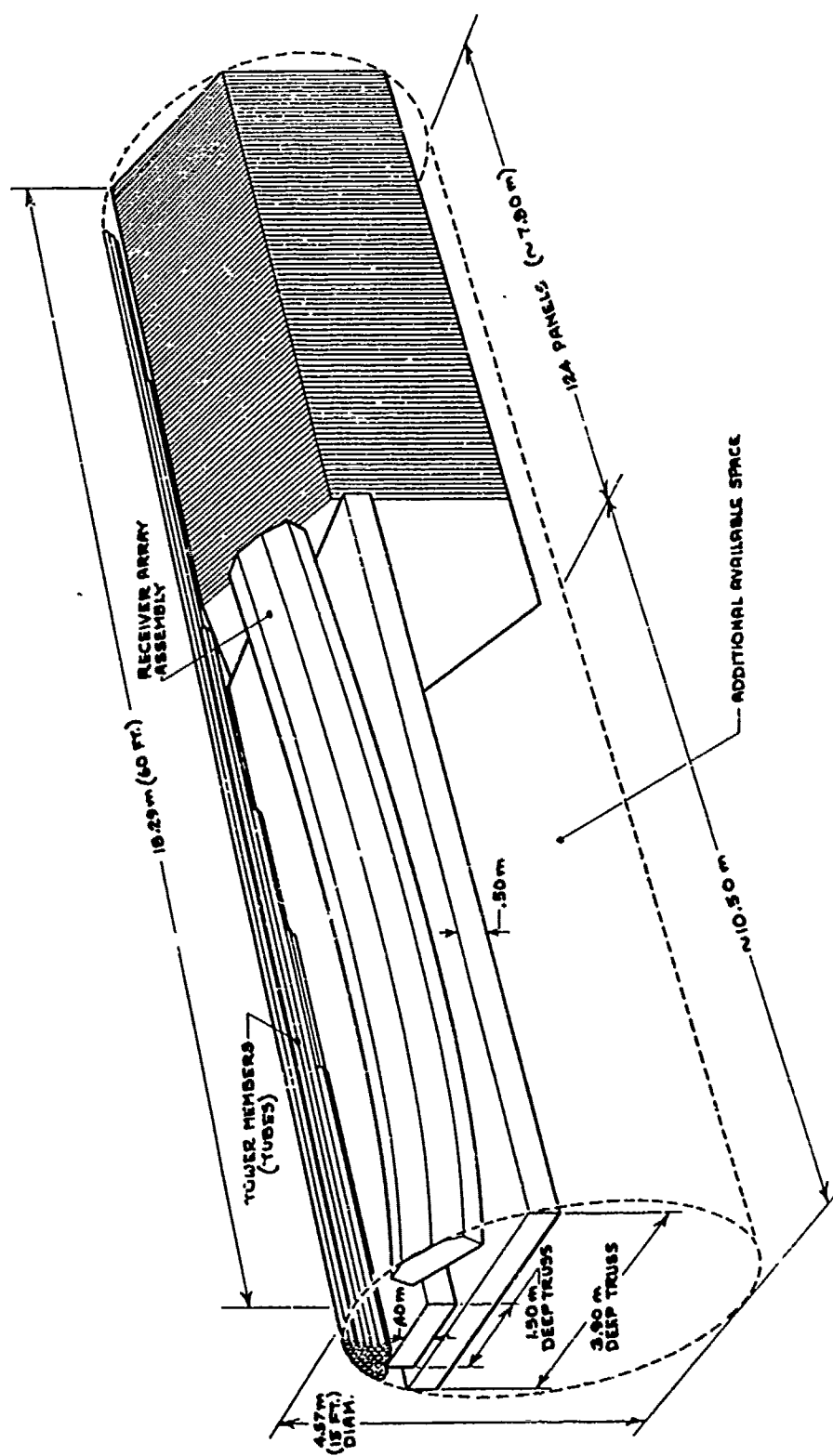


Figure 7-1. MMW antenna packaged in one Shuttle cargo bay.

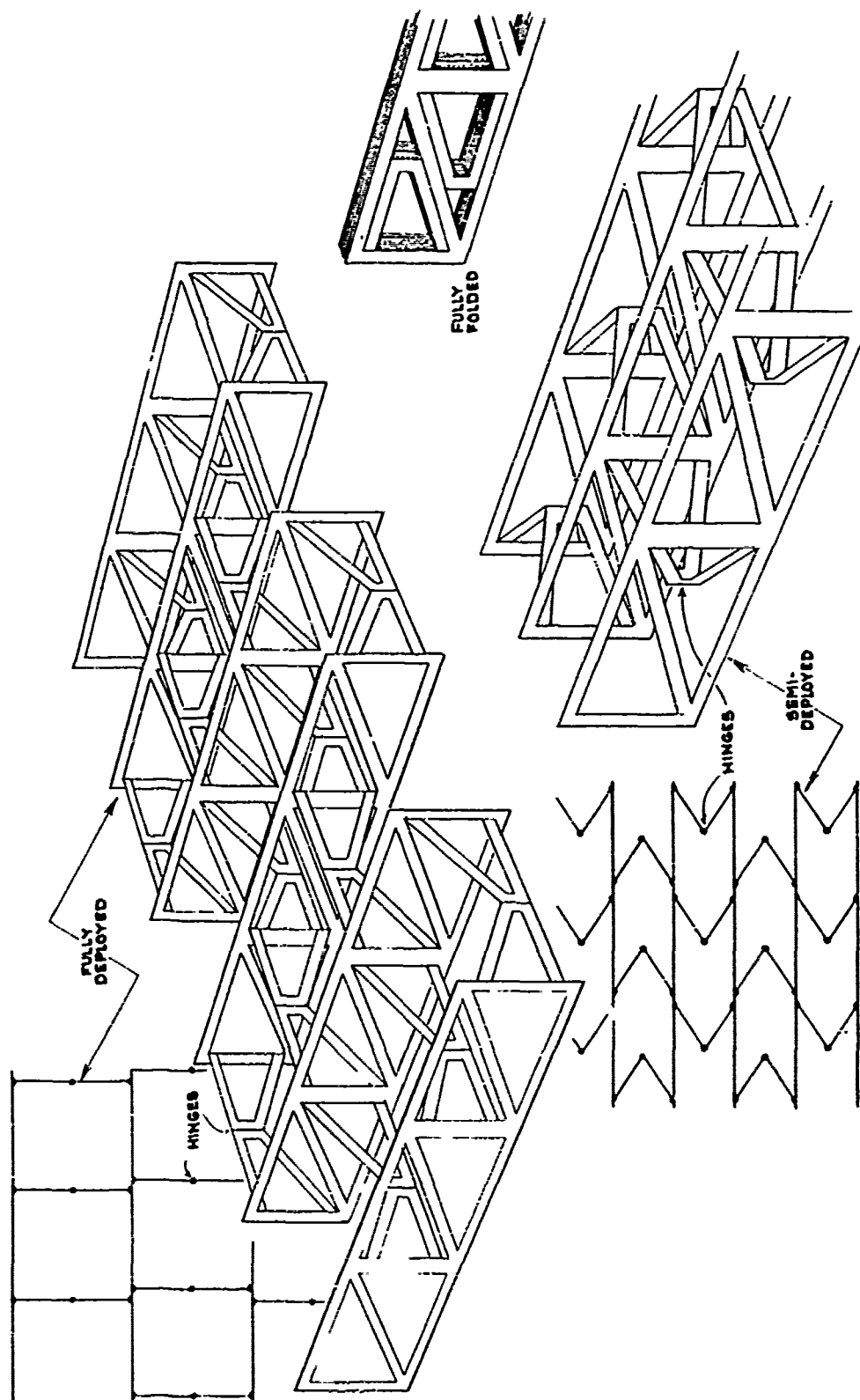


Figure 7-2. Packaging and deployment schemes for back-up vertical trusses (preliminary).

SECTION 8

CONCLUSIONS

The objective of this study was to design an MMW antenna with a structure that would perform adequately under several constraints imposed by various sources. The most important constraints are associated with:

- (1) Orbital environment disturbances.
- (2) Use of passive structural systems only.
- (3) Packageability in a single shuttle cargo bay.

The last two constraints derive from desirable requirements involving simplicity, efficiency, and cost.

The design of the structural components was suggested on the basis of past experience in dealing with a satellite structure of a given size (60 m x 30 m reflector) associated with a stipulated deformational tolerance (on the order of 0.5 mm). A fundamental frequency of 1 Hz for the overall structure was assumed to impart to the satellite enough stiffness such that it would distort within tolerable limits when exposed to the typical environment of a 500 km orbit. But, it is only after going through the entire analysis cycle that the overall merits of the system can be judged. The structure suggested for this analysis appears slightly stiffer than required when exposed to the expected dynamic disturbances. Modifications in design sizes and cross-sectional areas, with corresponding savings in masses can be explored, but other limitations, such as those required by structural stability may possibly become critical in the process. The study showed that the most severe loadings are those associated with the thermal variations of the satellite structures due to the thermal fluxes from the sun, the earth IR and its albedo. The design, therefore, must rely on a material exhibiting a favorable coefficient of thermal expansion such as a graphite-epoxy composite ($\alpha = 0.2 \times 10^{-6}$ m/m°k), and the presence of a thermal shield capable of reducing the temperature excursions and gradients to an acceptable level. It was shown that it is possible with state-of-the-art materials and thermal blanket design techniques to keep the large reflector of the MMW antenna from distorting beyond specified values in the changing thermal environment.

In the trade-off studies for the design of the reflector panels it was found that a graphite-epoxy (G-E) egg-crate structure is by far superior to an aluminum honeycomb, mainly because of the large difference between the CTE (23×10^{-6} m/m°k for aluminum versus 0.2×10^{-6} m/m°k for G-E). The possibilities offered by inflatables such as airmats should be pursued for the design of a reflector panel. In this study, a tentative design showed unacceptable thermal deformations, but there is room for optimization, especially since the restrictions on panel depth that are critical for rigid designs, are almost negligible for inflatables. The receiver tower, however, showed

thermal deformations that can cause an unacceptable LOS error. This fact was expected because no attempt was made to use a thermal shield for the tower. It can be anticipated that with thermal control, these deformations could be brought to a tolerable level. Alternatively, a semi-active control approach could be used, based on the predictability of the slowly changing thermal conditions, to compensate for unacceptable feed movements as the satellite progresses along its orbital path.

As evidenced by the requirements affecting the design of the reflector panel, the issues of packaging and deployment have strongly affected the design of structural components. Segmentation of the large antenna surface was necessary and the hexagonal panels emerged as the best solution for high packaging ratio and efficient surface assemblage. Since they fill up about 42 percent of the shuttle cargo bay, the stowing of the remaining back-up trusses and 30 m tower frame required efficient folding techniques. An attractive approach was suggested for the truss members, where thin-wall open cross sections replaced the traditional circular tube. Once acceptable factors of safety on lateral stability of individual members have been made, nesting of consecutive trusses that can improve the packaging ratio of a factor of approximately 10 can be considered. While a complete packaging method has not been investigated for the back-up trusses, the above approach presents a number of interesting possibilities and should be pursued. On the basis of rough, but conservative estimates, the packaging of the entire antenna (including equipment) into a single shuttle cargo bay is indeed possible.

The study of the representative design for the MMW antenna showed that a reasonable performance can be expected from a structural concept using traditional, state-of-the-art material and design techniques. Of special interest is the simplicity of the system that can operate with a minimum of control, thus increasing reliability. It should be noted that the thermal blanket on the back face of the supporting trusses is a purely passive means of controlling the temperatures. While it is anticipated that kinematic mount actuators for panels are indispensable in the surface acquisition phase of deployment, they should not be necessary during operation thereafter.

The "exact" evaluation of the performance of the MMW antenna was obtained through the processing of the information on the deformational state of the entire structure. In this study, PSF and LOS motions have been calculated for a number of design cases. These values must be assessed by MMW antenna specialists so that performance improvements through structural modifications or additional control can be evaluated. But, as an indirect measure of performance, deformational tolerances also have been set for the rms of reflector surface deviations and the motion of the feed support (decenters and defocus). As mentioned above, the merits of the structural design have been assessed mainly by comparing these deformations to the tolerances and the conclusions based on this comparison.

The desirable simplicity of the system hinges on a relatively stiff structure and, therefore, translates into a substantial amount of mass. (The entire satellite is expected to have a mass of 8800 kg.) This approach using a "heavy and stiff" structure can be contrasted with another solution

involving a "light and very flexible" structure that derives its necessary stiffness from active control means. Using an electrostatically shaped membrane as a reflector is an attractive solution with regard to mass, but requires a sophisticated control system to maintain the surface accuracy of the flexible membrane. The trade-off between the two systems must involve a large number of characteristics that are sometimes difficult to assess. While the total mass and stowed volume are easy to compare, the complexity of the control system and its reliability are examples of features less amenable to resolution.

The choice of a 500 km orbit for the design study was somewhat arbitrary. Although the atmospheric density decreases drastically above an altitude of 300 km and usually does not present a critical problem for small satellites, the large size of the MMW antenna poses an unusual problem for its orbital dynamics. The atmospheric drag forces and associated torques cause a relatively serious orbital decay (in the order of 10 km in a 30-day period) and pointing disturbances must be compensated for. Based on a 5-year life span, the need for approximately 2000 kg in propellant to maintain operations cannot be overlooked. A higher orbit could be considered to alleviate this problem. The present design for use at this altitude should be revised or modified to include structures needed for the support of this additional mass.

COMPUTER SIMULATION OF A LARGE ADAPTIVE OPTICAL SYSTEM

Virendra N. Mahajan and Jacques Govignon
The Charles Stark Draper Laboratory, Inc.
Cambridge, Massachusetts 02139

Abstract

This paper describes a method for evaluating the optical performance of optical systems consisting of large, flexible, actively controlled mirrors in the presence of thermal and dynamic disturbances. The computer simulation described here is divided into four major blocks: optical, thermal, structures, and dynamics. The control aspects are included in the various models used in each block. The output of the simulation is a dynamic point-spread function from which real-time or average quantities such as the line-of-sight error, Strehl ratio, and power in a certain area are calculated. As an example, a two-mirror system that expands a high-power collimated beam and focuses it on a distant plane is considered. The effects of heating of the mirrors are simulated and results on the point-spread function and associated quantities are presented.

1. Introduction

A computer simulation for evaluating the optical performance of large adaptive optical systems is described. Given the optical system design data (e.g., mirror figures, spacings, and sizes), optical ray-trace programs are used to obtain the angles and the points of incidence of the rays on the mirrors and the wave aberrations of the system. The deformations of the optical system (mirror warping and misalignments) due to some disturbance (e.g., thermal loading, or a dynamic disturbance) are calculated by structural programs such as STARDYNE and NASTRAN. Any control aspects of the system are included in this calculation. The residual deformations are given at discrete points on the optical elements, which generally are not the same as the points of incidence of the rays used in optical ray-trace programs. In the simulation, the deformations obtained at structural points are interpolated to obtain the deformations at the optical points.

The wave aberrations produced by these deformations are calculated using the ray-trace data of the undeformed system, and are added to the disturbance-free aberrations of the system to obtain the total wave aberrations of the deformed system. A pupil function is formed from these total aberrations, and using fast Fourier transform (FFT) programs, the point-spread function (PSF) is calculated. The amount of image energy in a certain area, the centroid of the image, and line-of-sight (LOS) error are obtained from the point-spread function. In the case of a dynamic disturbance, both the dynamic and time-averaged PSF and related quantities can be obtained. The image of an incoherent extended object lying in an isoplanatic region of the system can be obtained by convolving the object distribution with the corresponding PSF. However, images of extended objects are not considered in this paper.

An example of a two-mirror system that expands a high-power collimated beam and focuses it on a distant plane is considered. The effects of heating of the mirrors by the beam are simulated and results on the PSF, Strehl ratio, and ensquared power are presented.

2. Disturbance-Free System

Consider a point object at an angle α from the optical axis of an imaging system consisting of m mirrors. The optical performance of the system is evaluated by tracing a certain number of rays. These rays, which represent light emanating from the point object, are distributed uniformly in a square array in the entrance pupil of the system. Depending on the size of the entrance pupil and its associated obscurations, only some of the rays are transmitted by the system. Let N be the number of transmitted rays.

The rays are traced through the system striking the mirrors and finally reaching the exit pupil of the system. We find the end points of all the rays so that the total optical path length travelled by each of them is the same. For example, the path length of all the rays may be equal to that of the ray which starts and ends at the centers of the entrance and exit pupils. Because of obscurations in mirror systems, this ray is usually not physically transmitted by the system, but its optical path length can be calculated as if it were.

The surface passing through the end points of the rays is called the system wavefront for the point object under consideration, i.e., wavefront for a field angle α . If the end points lie on a spherical surface, then we have a spherical wavefront and the system is said to be aberration-free for that field angle. The extent or the boundary of the wavefront is defined by the rays touching the boundary of the exit pupil. The center of curvature of the

spherical wavefront gives the focus of the system for field angle α , i.e., the center of the irradiance distribution. The irradiance distribution is called the PSF.

If the end points of the rays do not lie on a spherical surface, we determine a spherical surface passing through the center of the exit pupil such that the path-length deviations along the rays from it have a minimum variance. These deviations are called wave aberrations or wavefront errors, and their sign convention is such that the aberration corresponding to a certain ray is positive if it has to travel an extra amount to reach the spherical surface. The minimum variance spherical surface is called the reference sphere and its center of curvature is called the best diffraction focus. Let the best diffraction focus be located at $r_F^0(x_F^0, y_F^0, z_F^0; \alpha)$. The surface passing through the best foci for various field angles (point-object positions) is called the focal or the image surface.

Let (u, v, w) be the coordinates of a point where a ray intersects the reference sphere such that $u^2 + v^2 + w^2 = R^2$, where R is the radius of curvature of the reference sphere. If $W^0(u, v; \alpha)$ is the wave aberration and $A(u, v; \alpha)$ is the amplitude** at a point (u, v) in the pupil, then the pupil function of the system is defined by

$$P(u, v; \alpha) = A(u, v; \alpha) \exp \left[\frac{2\pi i}{\lambda} W^0(u, v; \alpha) \right], \quad \text{in the clear region of the pupil} \\ = 0, \quad \text{otherwise} \quad (1)$$

Thus the pupil function is nonzero only in the region of transmitted rays. The amplitude variations in the pupil can be due to a number of sources, e.g., the input wave to the system has amplitude variation or the mirrors have nonuniform reflectivities. In Eq. (1), λ is the wavelength of the object radiation and $i = \sqrt{-1}$.

The irradiance or PSF value at a point $(x, y, 0)$ with respect to r_F^0 , where the (x, y) plane is parallel to the (u, v) plane, is given by¹

$$I(x, y; \alpha) = \frac{1}{\lambda^2 R^2} \left| \int_{-\infty}^{\infty} \int_{-\infty}^{\infty} P(u, v; \alpha) \exp \left[-\frac{2\pi i}{\lambda R} (xu + yv) \right] du dv \right|^2 \quad (2)$$

The integral in Eq. (2) is a Fourier transform of the pupil function. For small angular deviations from angle α , the pupil function and therefore the PSF do not change, except for an overall displacement. The angular extent of the object over which the PSF does not change significantly is called an isoplanatic angle of the system. It is evident that in a computer simulation, a discrete Fourier transform is used, particularly because the aberrations are known at a set of discrete points, the points at which the rays end in the exit pupil. An FFT program is used to evaluate the integral in Eq. (2).

Let $2u$ and $2v$ be the spatial periods of the aberration data points along the u and v axes, respectively. The coordinates (u, v) of a point in the pupil can be written

$$u = j \cdot u \quad v = k \cdot v \quad (3)$$

where j and k are integers. The discrete form of the pupil function in the clear region of the pupil can be written

$$P(u, v; \alpha) = P(j \cdot u, k \cdot v; \alpha) \\ = A(j \cdot u, k \cdot v; \alpha) \exp \left[\frac{2\pi i}{\lambda} W^0(j \cdot u, k \cdot v; \alpha) \right] \quad (4a)$$

* It is assumed throughout that the aberrations are small so that minimization of their variance leads to a better quality image, and the center of the reference sphere is a point of maximum irradiance. In the case of large aberrations, geometrical-optics-based criteria, such as the smallest spot diameter, may be used. In that case there is no distinguishable principal maximum in the PSF, and the LOS may be determined by the centroid of the image rather than the diffraction focus.

** For a point object at a distance z_o from an imaging system with a uniformly illuminated pupil, $A(u, v; \alpha)$ is constant over the pupil and equal to $(P_o/4\pi)^{1/2}/z_o M$, where P_o is the total power radiated uniformly by the object in all directions and M is the pupil magnification, e.g., M is the ratio of the diameters of the exit and entrance pupils.

COMPUTER SIMULATION OF A LARGE ADAPTIVE OPTICAL SYSTEM

Or

$$\begin{aligned} P(u, v; \alpha) &= A_0(\alpha) A_{jk}(\alpha) \exp \left[\frac{2\pi i}{\lambda R} w_{jk}^0(\alpha) \right] \\ &= A_0(\alpha) P_{jk}(\alpha) \end{aligned} \quad (4b)$$

where A_0 is a normalization amplitude factor so that $A_{jk}(\alpha)$ and therefore $P_{jk}(\alpha)$ are dimensionless quantities. The $A_{jk}(\alpha)$ may be chosen such that, for example, the maximum value at a certain point such as the center of the pupil is unity.

If $P_t(\alpha)$ is the total power entering the pupil, it is given by

$$P_t(\alpha) = \iint_{\text{pupil}} |P(u, v; \alpha)|^2 du dv \quad (5)$$

where the integration is carried over the clear region of the pupil. Substituting Eq. (4) into Eq. (5), a discrete form of Eq. (5) can be written

$$\begin{aligned} P_t(\alpha) &= A_0^2(\alpha) \Delta u \Delta v \sum_{j,k} w_{jk} |P_{jk}(\alpha)|^2 \\ &= A_0^2(\alpha) \Delta u \Delta v \sum_{j,k} w_{jk} A_{jk}^2(\alpha) \end{aligned} \quad (6)$$

where w_{jk} are the weights of the integration rule (e.g., trapezoidal, Simpson's, etc.).

For efficient use of the FFT programs, data points with zero pupil function are added in the pupil plane, such that the number of points along the u and v axes are each equal to certain powers of 2. Thus, for example, a grid of $N_u \times N_v$ points is generated, where N_u and N_v are the numbers of rows and columns, respectively, of the data-point matrix, both N_u and N_v being equal to powers of 2. Of the $N_u \times N_v$ data points, only N have a nonzero value of the pupil function.

Let Δx and Δy be spatial periods of data points in the image plane along the x and y axes, respectively. Thus, we may write

$$\begin{aligned} x &= \ell \Delta x \\ y &= m \Delta y \end{aligned} \quad (7)$$

where ℓ and m are integers. Substituting Eq. (3), (4), and (7) into Eq. (2), a discrete form of Eq. (2) can be written

$$I(\ell \Delta x, m \Delta y; \alpha) = \left(\frac{\Delta u \Delta v}{\lambda R} \right)^2 A_0^2(\alpha) \left| \sum_{j,k} P_{jk}(\alpha) \exp \left[-\frac{2\pi i}{\lambda R} (j \ell \Delta x \Delta u + k m \Delta y \Delta v) \right] \right|^2 \quad (8)$$

Both (ℓ, m) and (j, k) pairs form a $N_u \times N_v$ matrix of data points. In our FFT program, the PSF value at an (ℓ, m) data point is given by

$$I_{\ell m}(\alpha) = \frac{1}{N^2} \left| \sum_{j,k} P_{jk}(\alpha) \exp \left[-2\pi i \left(\frac{j \ell}{N_u} + \frac{k m}{N_v} \right) \right] \right|^2 \quad (9)$$

Comparing Eq. (8) and (9), we find that

$$I(\ell \Delta x, m \Delta y; \alpha) = \left(\frac{\Delta u \Delta v}{\lambda R} \right)^2 A_0^2(\alpha) N^2 I_{\ell m}(\alpha) \quad (10)$$

Moreover, the spatial periods in the pupil and image planes are related according to

$$\begin{aligned}\Delta x &= \lambda R / N_u \Delta u \\ \Delta y &= \lambda R / N_v \Delta v\end{aligned}\quad (11)$$

For an exit pupil with extents D_u and D_v along the u and v axes, respectively, Eq. (11) can be written

$$\begin{aligned}\Delta x &= \lambda F_u n_u / N_u \\ \Delta y &= \lambda F_v n_v / N_v\end{aligned}\quad (12)$$

where, for example

$$F_u = R / D_u \quad (13)$$

is the focal ratio of the image along the u axis, and

$$n_u = D_u / \Delta u \quad (14)$$

is the number of rays in a length of D_u . Note that to reduce the spatial periods in the image plane, the matrix dimensions N_u and N_v must be increased. Thus, by merely adding data points with zero values in the pupil plane, a closely spaced distribution of PSF values can be obtained.

From Eq. (9) and (10), the central PSF value can be written

$$I(0,0;\alpha) = \left(\frac{\Delta u \Delta v}{\lambda R} \right)^2 A_0^2(\alpha) \left| \sum_{j,k} P_{jk}(\alpha) \right|^2 \quad (15a)$$

Substituting for $A_0^2(\alpha)$ from Eq. (6), it can also be written

$$I(0,0;\alpha) = \frac{P_t(\alpha) \Delta u \Delta v}{(\lambda R)^2} \frac{\left| \sum_{j,k} P_{jk}(\alpha) \right|^2}{\sum_{j,k} w_{jk} A_{jk}^2(\alpha)} \quad (15b)$$

The fraction of power in a certain area of the image plane can be obtained by integrating the PSF over that area. For example, if a detector is placed in the image plane, the fraction of total image power collected by the detector is given by

$$P_{\text{det}}(\alpha) = \frac{1}{P_t(\alpha)} \iint_{\text{det}} I(x,y;\alpha) dx dy \quad (16)$$

Since the aberration function W is given at a uniformly spaced set of points, the PSF data is also obtained at a uniformly spaced set of points. Therefore, it is convenient to calculate the ensquared power, i.e., the power on a square (or rectangular) detector. For a circular detector, the PSF data has to be interpolated to obtain encircled power. We have shown that for diffraction-limited imaging systems with centrally obscured circular pupils, the difference between corresponding ensquared and encircled powers (square having the same half-width as the radius of the circle) is less than 10% of the total power, regardless of the amount of obscuration or the size of the detector.

Using Eq. (7), a discrete form of Eq. (16) can be written

$$P_{\text{det}}(\alpha) = \frac{\Delta x \Delta y}{P_t(\alpha)} \sum_{\ell, m}^{\text{det}} w_{\ell m} I(\ell \Delta x, m \Delta y; \alpha) \quad (17)$$

where $w_{\ell m}$ are the weights of the integration rule used, and only those (ℓ, m) data points are used in the summation that lie on the detector. Substituting Eq. (6), (10), and (11) into Eq. (17), we obtain

$$P_{\text{det}}(\alpha) = \frac{N^2 \sum_{\ell, m}^{\text{det}} w_{\ell m} I_{\ell m}(\alpha)}{N_u N_v \sum_{j, k} w_{jk} A_{jk}^2(\alpha)} \quad (18)$$

If the light entering the exit pupil has uniform phase and amplitude, i.e., for a spherical wavefront with uniform amplitude across it, we may write using script letters for the pupil function, PSF, and related quantities

$$P(u, v; \alpha) = A_0 \quad (19a)$$

$$P_{jk}(\alpha) = A_{jk}(\alpha) \\ = 1 \text{ [at } N(jk) \text{ points only]} \quad (19b)$$

$$I_m(\alpha) = \frac{1}{N^2} \left| \sum_{j, k} \exp \left[-2\pi i \left(\frac{j}{N_u} + \frac{km}{N_v} \right) \right] \right|^2 \quad (20)$$

$$I(\ell \Delta x, m \Delta y; \alpha) = \left(\frac{N \Delta u \Delta v}{\lambda R} \right)^2 A_0^2(\alpha) I_{\ell m}(\alpha) \quad (21)$$

$$A_0^2(\alpha) = P_t(\alpha) / N^2 u^2 v^2 \quad (22)$$

$$P_{\text{det}}(\alpha) = \frac{N^2}{N_u N_v} \sum_{\ell, m}^{\text{det}} w_{\ell m} I_{\ell m}(\alpha) \quad (23)$$

$$I(0, 0; \alpha) = \left(\frac{N^2 u^2 v^2}{R} \right)^2 A_0^2(\alpha) \quad (24a)$$

$$= \frac{N P_t(\alpha) u^2 v^2}{(R)} \quad (24b)$$

Assuming that the total power entering the pupil when the system wavefront is spherical and the amplitude across it is uniform is the same as when there are aberrations and amplitude variations, we obtain the Strehl ratio* of the degraded image from Eq. (15b) and (24b)

* The Strehl ratio is generally defined as the ratio of central values of a PSF in the presence and absence of aberrations in a system. Here, we generalize this definition to include the degradation of central irradiance due to amplitude variations as well.

$$S(\alpha) = \frac{I(0,0;\alpha)}{I(0,0;\alpha)} = \frac{\left| \sum_{j,k} P_{jk}(\alpha) \right|^2}{N \sum_{j,k} w_{jk} A_{jk}^2(\alpha)} \quad (25)$$

which is less than 1.

3. Disturbed (Deformed) System

Now suppose that the imaging system is disturbed and the mirrors are deformed. Assume that the disturbance is time dependent, although it may contain a time-independent component, e.g., a dynamic disturbance in the presence of a slowly varying thermal disturbance. Consider the state of the optical system at a certain time t , assuming that the control system has restored the system to the best of its ability.

Suppose that a certain point $\vec{r}_{im}(\alpha)$ on the surface of the m th mirror touched by the i th ray is moved by the disturbance and restored by control to a point $\vec{r}'_{im}(\alpha, t)$, so that the residual vector displacement of the point at a time t is given by

$$\delta \vec{r}_{im}(\alpha; t) = \vec{r}'_{im}(\alpha; t) - \vec{r}_{im}(\alpha) \quad (26)$$

For small $\delta \vec{r}$, the corresponding wave aberration contribution to the i th ray is given by (see the Appendix)

$$\delta W_{im}(\alpha; t) = 2[\hat{n}_{im}(\alpha) \cdot \delta \vec{r}_{im}(\alpha; t)] \cos \theta_{im}(\alpha) \quad (27)$$

where \hat{n}_{im} is a unit vector along the normal to the mirror surface at the point \vec{r}_{im} , and θ_{im} is the angle of incidence of the ray on the undeformed mirror. The total aberration contributed by all the mirrors (because of their deformations) to the i th ray is obtained by summing their contributions, i.e.

$$\Delta W(u_i, v_i; \alpha; t) = \sum_m \delta W_{im}(\alpha; t) \quad (28)$$

The total aberration W_i at a point $(u_i, v_i; \alpha)$ in the exit pupil is obtained by adding ΔW_i to the disturbance-free aberration W_i^0 , i.e.

$$W(u_i, v_i; \alpha; t) = W^0(u_i, v_i; \alpha; t) + \Delta W(u_i, v_i; \alpha; t) \quad (29)$$

Given the total aberrations W_i , once again we find a reference sphere such that when the aberrations are measured with respect to it, their variance is minimized. If the center of curvature of this reference sphere is located at $\vec{r}_F(\alpha; t)$, the amount of defocus caused by the disturbance is given by

$$\begin{aligned} \Delta \vec{r}_F(\alpha; t) &= \vec{r}_F(\alpha; t) - \vec{r}_F^0(\alpha) \\ &= [\Delta x_F(\alpha; t), \Delta y_F(\alpha; t), \Delta z_F(\alpha; t)] \end{aligned} \quad (30)$$

where $[\Delta x_F(\alpha; t), \Delta y_F(\alpha; t)]$ is the transverse defocus and $\Delta z_F(\alpha; t)$ is the longitudinal defocus. The transverse defocus represents the LOS error.

Let $W^F(u_i, v_i; \alpha; t)$ be the wave aberration at a point $(u_i, v_i; \alpha)$ in the exit pupil with respect to the reference sphere centered at $\vec{r}_F(\alpha; t)$. Using these aberrations, once again we go through the equations of Section 2 to determine the PSF and ensquared power. By determining $P(\alpha; t)$ at different times, we can calculate the average power or total energy in a certain area during a certain time interval.

Note that the use of the wave aberrations W_1^F implies that the irradiance distribution is centered about the point $\vec{r}_F(\alpha; t)$. This implies that there is an LOS error and longitudinal defocus which are being corrected in real time by the control system. If they are not corrected, the aberrations W_1 of Eq. (29) must be used, i.e., aberrations with respect to a reference sphere centered at (x_F^0, y_F^0, z_F^0) rather than at $(x_F, y_F, z_F; t)$ must be used. If the detector surface for the field of view of the imaging system is planar rather than curved (as determined by the locus of the best diffraction focii), as is often the case (e.g., films) then the (u, v) plane is chosen to be parallel to the detector plane and the reference spheres for various field angles α must be centered on the detector plane.

4. Simulation Architecture

In terms of evaluating the effects of thermal and dynamic disturbances on the optical performance of a large optical system, the simulation as indicated in Figure 1 is divided into four blocks: thermal, structures, dynamics, and optics. Given a certain optical system with its associated structure, the information on any heat sources is used to carry out a thermal analysis. The output of this analysis is the temperature distribution within the system. The temperature distribution is used to determine the deformations of the optical elements. From the material and mechanical properties of the various elements, the structural model determines the eigenmodes and influence matrices (the effect of a disturbance at one point on others) of the system or a subsystem. It also determines the deformations of the mirrors at selected points, which are the nodes of the finite-element structural model, hereafter called structural points. The eigenmodes in conjunction with the dynamics model and the disturbances are used to carry out a dynamics analysis, to determine the movements of the segments of an optical element, or the optical element as a whole, or the system as a whole. The control of figure or rigid-body motion of a segment or whole optical element is included in the structural and dynamics models.

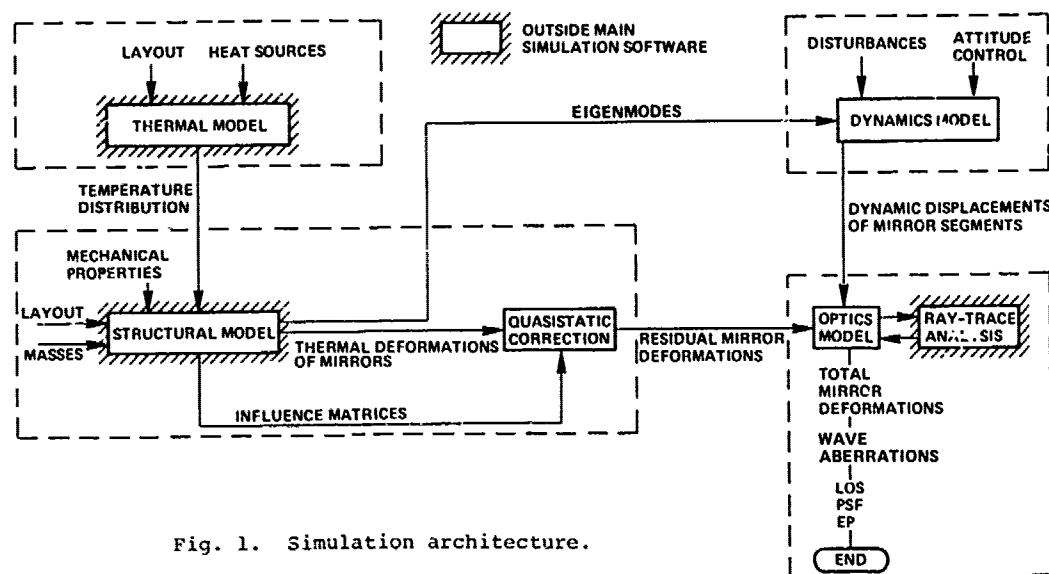


Fig. 1. Simulation architecture.

From the deformations and movements of the optical elements, the optics block determines the LOS error, longitudinal defocus, the image-plane-irradiance distribution and associated quantities. A detailed flow chart of the optics block is given in Figure 2. Note that from the structural and optical points, interpolation coefficients are obtained, which are, of course, time independent. They are used to calculate the deformations at the optical points from those at the structural points. From Eq. (27), we note that we need the deformations along the surface normals, i.e., $\hat{n} \cdot \delta r$, and we interpolate these quantities and not the deformations themselves. This greatly simplifies the calculations because this way we perform a scalar rather than a vectorial interpolation.

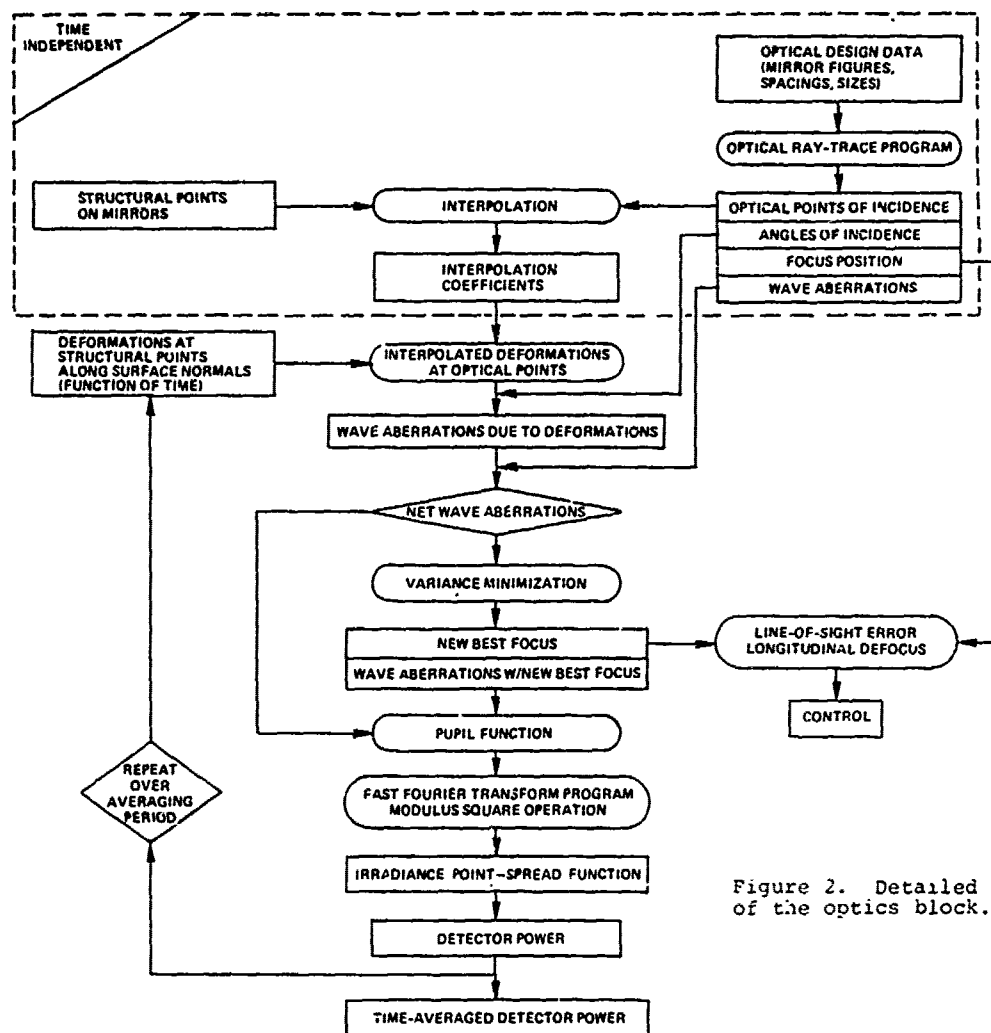


Figure 2. Detailed flow chart of the optics block.

5. Simulation Example and Results

5.1. Disturbance-Free System

A two-mirror optical system has been used as an example for a simulation. As shown in Figure 3, mirrors M_1 and M_2 have diameters of D_1 and D_2 , respectively. The input to the system is a collimated circular beam of uniform amplitude, propagating parallel to the optical axis of the system. The beam, which has a linear obscuration of 0.5, is expanded by the two-mirror system and is focused on the image plane. The collimated beam is equivalent to a point object at infinity, with an additional element near the two-mirror system providing obscuration. The mirror figures and spacing are such that they do not introduce any aberrations, and a perfect image is formed in the image plane.

Since the input beam and the two-mirror system are aberration free, and assuming that the system does not introduce any amplitude variations, the image-plane irradiance distribution (PSF) can be calculated analytically using

$$I(r; \epsilon) = \frac{1}{(1 - \epsilon^2)^2} \left| \frac{2J_1(\pi r/\lambda F)}{\pi r/\lambda F} - \epsilon^2 \frac{2J_1(-\pi r/\lambda F)}{-\pi r/\lambda F} \right|^2 I(0; \epsilon) \quad (31)$$

where the irradiance at the center of the image is given by

$$I(0;c) = \pi(1 - c^2) P_c / 4\lambda^2 F^2 \quad (32)$$

In Eq. (31) and (32), r is the distance of a point in the image plane from the image center, $J_1(\cdot)$ is the first-order Bessel function of the first kind, c , λ , P_c , and F are the linear obscuration, wavelength, total power, and focal ratio of the beam. If D is the diameter of the exit pupil and R the radius of the reference sphere, then $F = R/D$. In the present case, $D = D_2$.

The irradiance distribution in the image plane normalized to its central value is shown in Figure 4. This distribution is circularly symmetric. In Figure 4, the fraction of total power contained in a circular area of a certain radius and the corresponding power in a square area of the same half-width as the radius are also shown.² Note that the difference between the corresponding ensquared and encircled powers P_s and P_c , respectively, which is exaggerated in the figure by a factor of 10, is always less than 9% of the total power.

The distribution of rays in the exit pupil of the system, using a 41×41 array of rays, is shown in Figure 5. Because the beam is circular with a linear obscuration of 0.5, only 952 of the 1681 rays have nonzero amplitude. The 1's in the figure indicate that the amplitude across the beam is uniform. The corresponding image-plane irradiance distribution using a 128×128 FFT grid is shown in Figure 6. The ensquared powers obtained by integrating such a distribution using the trapezoidal rule are listed in Table 1. Semi-analytical results obtained by integrating Eq. (31) are also listed in this table. Note that in going from 64×64 to 128×128 FFT grid, the difference between the semi-analytical results and those obtained by use of the FFT program reduces to less than 5%.

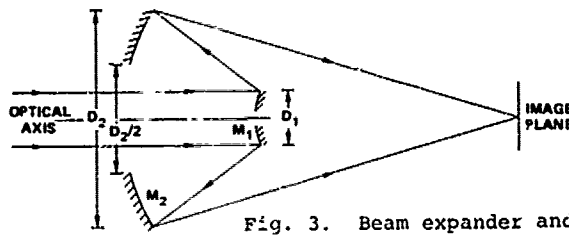


Fig. 3. Beam expander and focusing system.

5.2 Thermal Disturbance (Effects of Mirror Heating)

Assume that the beam entering the two-mirror system is of high power. The mirrors M_1 and M_2 are heated by the beam and therefore deform. The deformations of mirror M_1 along the surface normals are given in Figure 7 at a few typical time instants. Most of the deformation is a change in the radius of curvature and displacement along the optical axis,

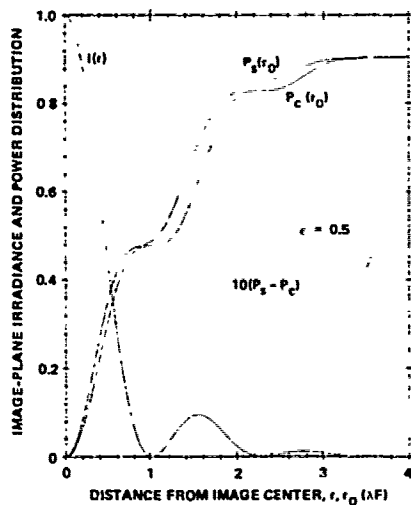


Fig. 4. Normalized image-plane irradiance and power distributions. P_s and P_c are fractions of a total image power in a square of half-width r_0 and a circle of radius r_0 , respectively.

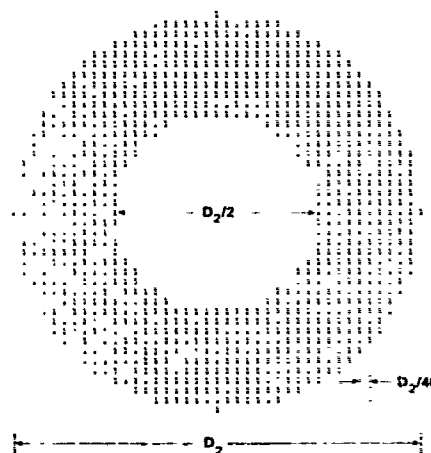


Fig. 5. Distribution of rays in the exit pupil.

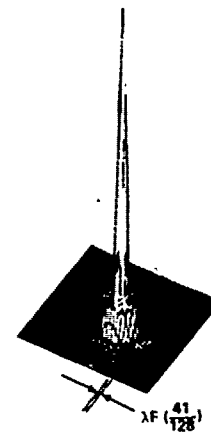


Fig. 6. Image-plane irradiance distribution obtained by using a 128×128 FFT grid.

thus producing a defocus. Since the beam flux density is circularly symmetric, the deformation is also circularly symmetric.

The mirror M_2 has been modeled into 12-degree segments. The mirror is supported along radial lines every 12 degrees by rods. The deformations have been determined along a supported radial line and a free radial line between two supported lines. Because of the circular symmetry of the beam incident on the mirror, deformations along all supported lines are identical; similarly, deformations along all free lines are identical. The deformations along a supported and a free radial line are shown in Figure 8. The details of the deformation calculations which depend on the beam power and the thermal properties of the mirrors are not included here.

The wave aberrations contributed by these mirror deformations are shown in Figure 9 on a 64×64 grid. As stated earlier, most of the error is defocus, i.e., a change in the radius of curvature of the reference sphere. Indeed, as an example, by refocusing (e.g., by translating mirror M_1 along the optical axis), the standard deviation of the wavefront errors at 23 s is reduced to $\lambda/33$.

The image-plane irradiance distribution as a function of time in the absence of refocusing is shown in Figure 10. At 23 s, for example, the Strehl ratio (central irradiance ratio) drops to a value of 0.03. By refocusing, it is brought back to a value of 0.96. The variation of Strehl ratio with time is shown in Figure 11. Whereas with proper focusing the Strehl ratio remains nearly 1, without active focusing it drops rapidly to very small values. When the aberration is a pure defocus, the Strehl ratio for an obscured circular beam is given by"

$$S = \left(\frac{\sin [W_0(1 - \epsilon^2)/\lambda]}{W_0(1 - \epsilon^2)/\lambda} \right)^2 \quad (33)$$

where W_0 is the aberration at the edge of the pupil (beam). Thus the Strehl ratio approaches zero whenever $W_0 = n\lambda/(1 - \epsilon^2)$ waves, where n is an integer. In Figure 11, the Strehl ratio does not become zero, because the aberration is not a pure defocus. This may be seen particularly in the case of mirror M_2 , Figure 8.

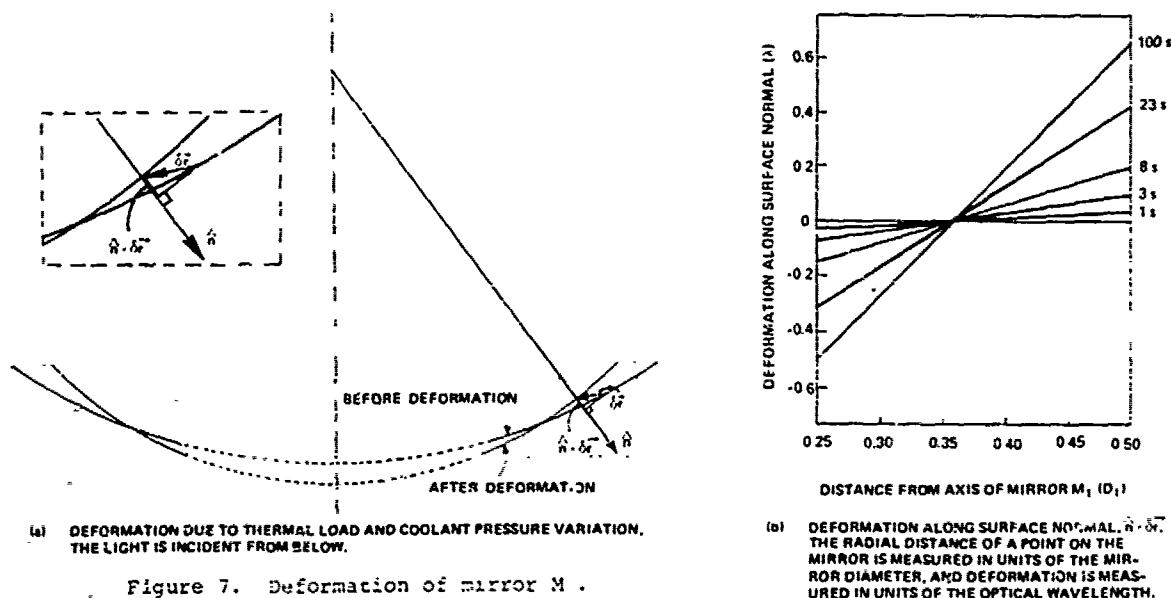


Figure 7. Deformation of mirror M_2 .

Table 1. Ensquared power $P_s(r_0)$ as a function of half-width r_0 in units of λF of a square obtained by integrating Eq. (31) and by using the FFT program and then integrating.

r_0 (in units of λF)	P_s (semi- analytical)	P_s (128 \times 128 FFT)	P_s (64 \times 64 FFT)
0.32	17.7	17.3	
0.64	43.8	41.5	35.0
0.96	48.5	49.0	
1.28	57.5	56.9	59.2
3.60	73.3	71.0	
1.92	81.9	80.7	78.6
2.24	84.3	84.1	
2.56	86.6	86.0	86.5

COMPUTER SIMULATION OF A LARGE ADAPTIVE OPTICAL SYSTEM

The percentage of total power contained in a square area as a function of the half-width of the square *without* and *with* focus correction is shown in Figures 12 and 13, respectively. As expected from the preceding discussion, the ensquared power decreases considerably unless the image is properly focused. In Figure 12, the case of 100 s is also shown. In that case, the amount of defocus is so large that the square areas considered lie practically inside the obscured region of the beam. With focus correction (not shown in Figure 13), a Strehl ratio of 0.78 is obtained, indicating the presence of higher order aberrations, and therefore requiring figure correction of mirrors.

Knowing the longitudinal defocus produced by the disturbance (from minimization of aberration variance and determination of the centers of curvature of the reference spheres in the absence and presence of the disturbance), the movement of mirror M_1 along the optical axis can be determined in order to keep the image focused in the disturbance-free image plane. Because of the symmetry of the mirror deformations, there is no transverse defocus, i.e., no LOS change is produced by the disturbance under consideration.

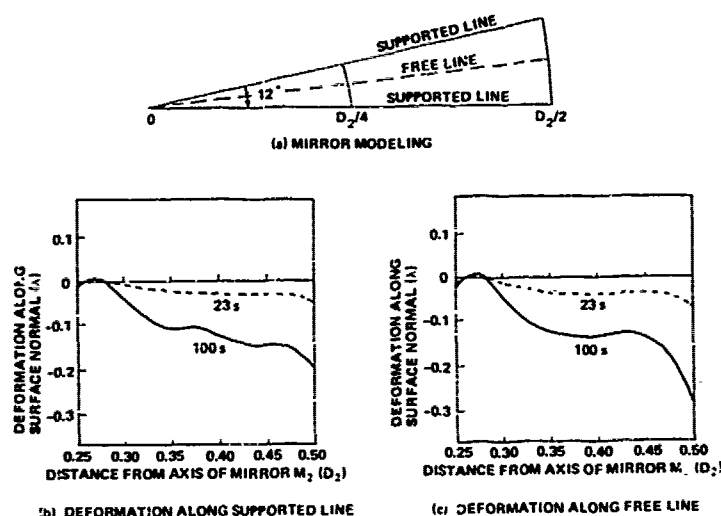


Fig. 8. Model and deformations of mirror M_2 . The distance from the center of the mirror is measured in units of its diameter.

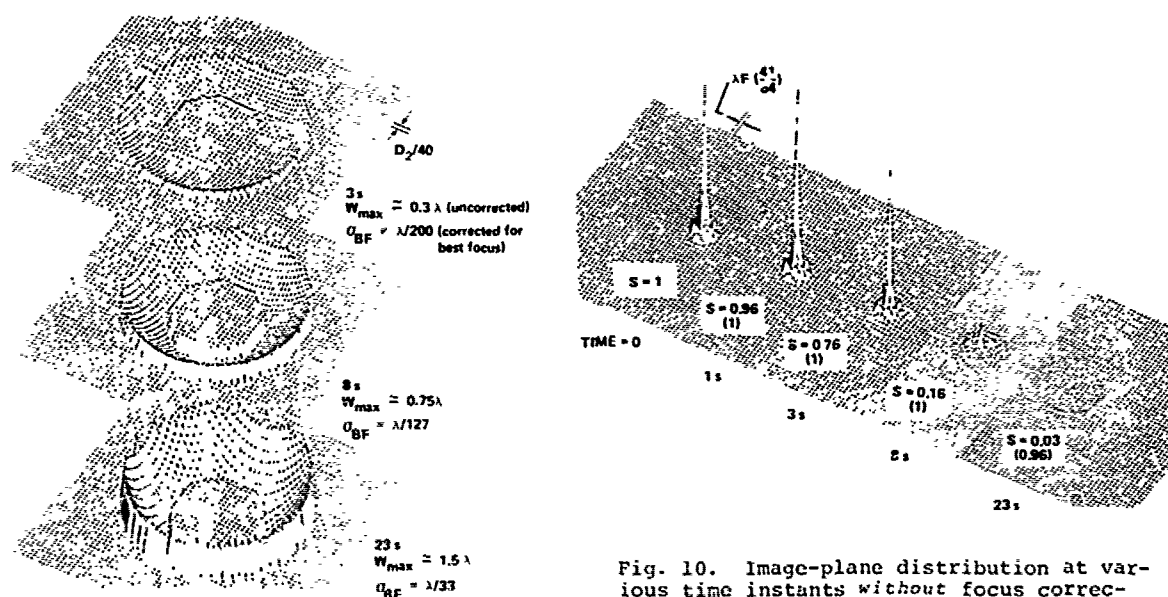


Fig. 9. Wavefront errors at various time instants. Most of the error is defocus.

Fig. 10. Image-plane distribution at various time instants *without* focus correction. S is the Strehl ratio of the image. The parenthetical numbers refer to Strehl ratio obtained with focus correction. A 64×64 FFT grid is used.

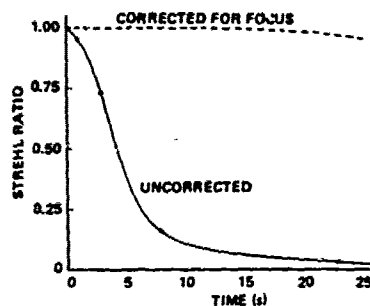


Fig. 11. Strehl ratio as a function of time.

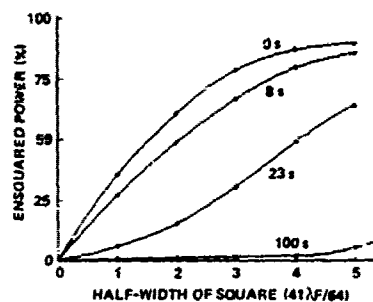


Fig. 12. Ensquared power as a function of half-width of the square at various time instants without focus correction.

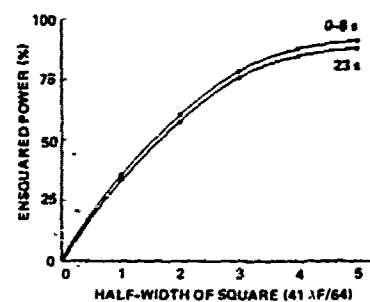


Fig. 13. Ensquared power as a function of half-width of the square at various time instants with active focus correction.

6. Discussion and Conclusions

We have described a computer simulation for determining the optical performance of imaging systems consisting of large, flexible, actively controlled mirrors in the presence of thermal and dynamic disturbances. In the simulation, the deformations of optical elements as determined by structural analysis are converted into optical aberrations using optical data of the undeformed system. Using FFT programs, the simulation determines the dynamic PSFs of the system and real-time or average quantities such as the LOS error, Strehl ratio, and ensquared power.

As an example, a two-mirror system that expands and focuses a collimated centrally obscured circular beam is considered, and the accuracy of the ensquared power calculation is discussed. It is shown that the results obtained are accurate to within a few percent. Next, the beam is assumed to be of high power so that it heats and therefore deforms the mirrors. The optical aberrations produced by the deformations are calculated and it is shown that most of the error can be removed with a focus correction, e.g., by translating one of the mirrors along the optical axis. More complex situations have been handled by the simulation in a similar manner.

Appendix: Relationship Between Mirror Deformation and the Corresponding Wave Aberration

As shown in Figure A-1, consider a ray incident at a point A on an intermediate mirror of an optical system making an angle θ with the normal to the mirror surface. If \hat{u} , \hat{u}' , and \hat{n} are unit vectors along the incident ray, reflected ray, and the surface normal, respectively, we have according to Snell's law

$$\hat{u}' = \hat{u} + 2\hat{n} \cos \theta \quad (A-1)$$

Suppose that when the system is deformed by a disturbance, a portion MN of the mirror under consideration becomes M'M' and that the point A moves to a point A'. The incident ray, the point of incidence, and the reflected ray, all deviate slightly from their nominal positions. Assuming that the mirror is in free space, the wave aberration introduced by the deformation is equal to the difference in path lengths of the "deformed" and "undeformed" rays. For small deformations, the deformed ray (shown dashed in Figure A-1) lies close to the undeformed ray so that their path difference, up to the first order, is equal to the sum of the local variations of the

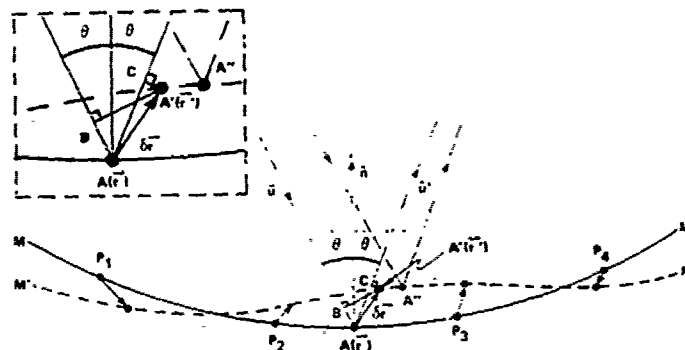


Fig. A-1. Geometry of mirror deformation and wave aberration ($AB + AC$).

path lengths at each deformed mirror. The deformations are considered small if the distances between the points of incidence of the corresponding deformed and undeformed rays on any mirror is a small fraction of the spacing of points of incidence of two adjacent rays of the undeformed system.

From Fermat's principle, the path length of a ray passing through the point A" is stationary. Therefore, in calculating the wave aberration introduced by the deformation, up to the first order, the point A" on the deformed surface can be replaced by the point A' on it. Hence, the wave aberration, which is negative in Figure A-1 because the path length has been reduced, can be written

$$\begin{aligned}\delta W &= -(AB + AC) \\ &= (\hat{u} - \hat{u}') \cdot \delta \vec{r}\end{aligned}\quad (A-2)$$

where if \vec{r} and \vec{r}' are the position vectors of the points A and A', respectively

$$\delta \vec{r} = \vec{r}' - \vec{r} \quad (A-3)$$

Substituting Eq. (A-1) into Eq. (A-2), we obtain

$$\delta W = -2\hat{n} \cdot \delta \vec{r} \cos \theta \quad (A-4)$$

In the simulation, the quantity $\hat{n} \cdot \delta \vec{r}$ is calculated by the structural program at structural points P_1, P_2 , etc., and it is calculated at an optical point such as A by interpolating its values at four neighboring structural points. The angle of incidence θ is obtained from the ray-trace program. The total wave aberration contributed to a certain ray by all the mirrors of a deformed system is obtained by summing the aberrations contributed by each mirror to that ray.

Acknowledgments

The work reported in this paper was sponsored by the U.S. Army Missile Research and Development Command under Contract DAAK40-79-C-0022. Publication of this paper does not constitute approval by the U.S. Army of the findings or conclusions contained herein. It is published for the exchange and stimulation of ideas.

Many persons with different backgrounds have contributed to the simulation described here. The authors gratefully acknowledge helpful discussions with Dr. L. Matson and Mr. F. Scammell. The work in the structures, thermal, and dynamics areas was done by S. Anagnostis, D. Fairbarks, R. Grin, T. Henderson, and the late Dr. J. Canavin. The software work was done by Mr. S. Serben, Ms. F. Satlow, and Dr. W. Koenigsberg. The program was managed by Dr. K. Soosaar and Mr. M. Furey. Encouragement from Drs. C. Thomas and A. Pike of DARPA is also gratefully acknowledged.

References

1. Born, M., and E. Wolf, Principles of Optics, Pergamon, New York, 5th edition, 1975, Section 9.1.
2. Mahajan, V. N., Appl. Opt., Vol. 17, 1978, p. 964.
3. Reference 1, p. 416.
4. Linfoot, E. H., and E. Wolf, Proc. Phys. Soc., Vol. B66, 1953, p. 145.